Petrogenesis of PGE-bearing chromitites in layered intrusions

Vorgelegt von
Felix Emil David Kaufmann

Dissertation
zur Erlangung des akademischen Grades
Doktor der Naturwissenschaften
(Dr. rer. nat.)

Eingereicht im Fachbereich Geowissenschaften
der Freien Universität Berlin

Berlin, Mai 2018

Erster Gutachter
Prof. Dr. Timm John
Institut für Geologische
Wissenschaften
Freie Universität Berlin
Malteserstraße 74–100
12249 Berlin, Germany

Zweiter Gutachter
PD Dr. Lutz Hecht
Museum für Naturkunde
Leibniz-Institut für Evoutions-
und Biodiversitätsforschung
Invalidenstraße 43
10115 Berlin, Germany

Tag der Disputation
13.07.2018

Think it over, think it under

A wise bear
Winnie-the-Pooh

Abstract

Layered intrusions are stratified igneous bodies, which are of outstanding scientific and economic interest. They form due to accumulation of crystals on a solidifying crystal mush and represent 'natural laboratories' providing direct insights into fundamental petrological concepts like crystal accumulation or magma differentiation. In addition to their petrological significance, they host some of the world's most important reserves of base and precious metals, including the platinum-group elements. Among the most prominent, but also most enigmatic, examples of magmatic layers in layered intrusions are Cr-spinel seams or chromitites. Despite the wealth of studies and the long history of research, spanning several decades, the petrogenesis of Cr-spinel layers, i.e. the processes of accumulation and possible subsequent modification, is still incompletely understood and riddles the scientific community till today. This thesis aims to shed some light on this active debate to advance our knowledge and understanding on the petrogenesis of these layers. Therefore, Cr-spinel seams in two case studies, the Bushveld Complex, South Africa and the Rum Layered Intrusion, NW Scotland, were investigated by detailed field observations and micro-analytical examination of the textural and mineral chemical character of the accumulated crystals. These observations were used to elucidate the processes of initial Cr-spinel accumulation and post-cumulus processes, which subsequently modified the primary chemistry and texture.

Post-cumulus processes that modify the original composition or texture of crystals within the crystal mush are known for a long time. Several studies have emphasised the added uncertainty in the interpretation of potentially modified textures and compositions. Thus, this thesis aims to assess post-cumulus changes within the seams to understand the involved mechanism and deduce the original characteristics of cumulus Cr-spinel. Micro-textural analyses of Cr-spinel in the Bushveld Complex reveal two typical textural types, one characterised by small grains, commonly entrapped in oikocrysts and the other by massive, coarse-grained Cr-spinel. While the former kept its original texture due to the protecting oikocrysts, the latter was modified by adcumulus growth and subsequent textural equilibration. In addition, geochemical observations of the oikocrysts reveal that the Cr-spinel layer was an open system, which was infiltrated by a trace element enriched interstitial melt re-equilibrating with the orthopyroxene oikocrysts. Contrary to the layers of the Bushveld Complex, the investigated seams of the Rum Layered Intrusion retained a more primary texture, indicating less adcumulus growth and textural equilibration. Here it is demonstrated that careful examination of Cr-spinel offers a thorough understanding of the processes involved in post-cumulus modifications, which therefore can be used to identify and deduce the primary characteristics of accumulated crystals.

A huge variety of contrasting petrological models are currently discussed to account for almost monomineralic Cr-spinel seams among them are changes in parameter (e.g. change pressure, oxygen fugacity, composition due to mixing, etc.) or mechanical enrichment processes. In this thesis, micro-analytical measurements of Cr-spinel seams were utilised to trace vertical variations across Cr-spinel seams of the Bushveld Complex and lateral variations in the Rum

Layered Intrusion. The compiled data suggest that Cr-spinel accumulation was controlled in both case studies by physico-chemical processes and not by mechanical ones, i.e. neither large-scale crystal settling nor cumulate mobilisation due to Cr-spinel-rich slurries can account for the reported mineral chemistry and texture. Moreover, lateral variations in seam structure and Cr-spinel composition were observed along strike in the Rum Layered Intrusions and to a certain extent in the Bushveld Complex. These variations suggest that the accumulation process was closely linked to repeated influxes of new, primitive magma. These repeated replenishing events within single layers were followed by assimilation of the underlying crystal mush and subsequent fractionation, resulting in the observed lateral and vertical variations.

Kurzfassung

Lagige Intrusionen sind stratiforme magmatische Körper, welche von herausragendem wissenschaftlichen und wirtschaftlichen Interesse sind. Sie entstehen durch Anreicherung von Kristallen auf einem sich verfestigenden Kristallbrei und repräsentieren „natürliche Labore“, die direkte Einsichten in fundamentale petrologische Konzepte wie Kristallanreicherung oder Magmendifferentiation liefern. Allerdings sind sie nicht nur von petrologischer Bedeutung, sondern beinhalten auch weltweit wichtige Reserven für Bunt- und Edelmetalle, wie zum Beispiel die Platingruppenelemente. Eines der wahrscheinlich hervorstechendsten, aber auch rätselhaftesten Beispiele für den magmatischen Lagenbau sind Cr-Spinell-Lagen. Trotz der Fülle an wissenschaftlichen Studien und der langen Historie an aktiver Forschung ist die Petrogenese von diesen Lagen, also der Prozess der primären Anreicherung und der möglichen nachfolgenden postkumulat Veränderung, immer noch nicht verstanden und bleibt damit ein Rätsel in der Wissenschaft. Das Ziel dieser Arbeit ist daher die Petrogenese der Cr-Spinell-Lagen besser zu verstehen. Dafür wurden Lagen in zwei Fallbeispiele ausgewählt: der Bushveld Komplex in Südafrika und die Rum Intrusion, NW Schottland. Beide Intrusionen wurden mit detaillierten Feldbeobachtungen und mikro-analytischen Methoden auf ihren mineralchemischen und texturellen Charakter untersucht. Dank der gesammelten Untersuchungen und Beobachtungen konnte ein genaueres Bild erstellt werden, das die Anreicherung von Cr-Spinell in lagige Intrusionen und die Modifikation des ursprünglichen Charakters erklärt.

Postkumulat Prozesse finden nach der ursprünglichen Anreicherung von Kumuluskristallen statt und können deren primäre Zusammensetzung und Textur beeinträchtigen sowie teils erheblich verändern. Dementsprechend ist es besonders wichtig die Veränderungen zu verstehen und zu bewerten, damit potentielle Unsicherheiten in der Interpretation vermieden werden. Ein Ziel dieser Arbeit ist die postkumulus Veränderungen zu bewerten und dadurch auf die primären Charakteristika der Kumuluskristalle zurückzuschließen. Mikro-texturelle Analysen von Cr-Spinell im Bushveld Komplex zeigen zwei typische, unterschiedliche Texturen: in einem Fall zeigen sich kleine Cr-Spinelle, die typischerweise in poikilitischen Kristallen eingeschlossen sind, während der zweite Fall durch massive, grobkörnige Cr-Spinelle charakterisiert ist. Die erstgenannten Cr-Spinelle behielten ihre ursprüngliche Textur als eingeschlossene Kristalle bei. Die zweite Gruppe wurde durch Adkumulatwachstum und darauffolgende texturelle Equilibrierung nach der Ablagerung verändert. Geochemische Untersuchungen zeigen, dass die Cr-Spinell Lage ein offenes System waren. Die Spurenelementsignaturen der poikilitische Orthopyroxenkristalle weisen auf eine chemische Reequilibrierung mit einer interstitiellen, spurenelementreichen Schmelze hin, die das offene System infiltrierte. Im Gegensatz zu den Cr-Spinell-Lagen des Bushveld Komplexes haben die Lagen der Rum Intrusion ihre ursprüngliche Textur beibehalten. Texturelle Equilibrierung fand hier also nur in einem sehr begrenzten Maße statt. Anhand der beiden Fallstudien kann in dieser Arbeit gezeigt werden, dass eine sorgfältige Charakterisierung der Kumulatchemie und -textur nötig ist, da sie eine Abschätzung der postkumulus Veränderungen sowie Rückschlüsse auf die jeweiligen ursprünglichen Charakteristika der Kumulate ermöglicht.

Verschiedene petrologische Modelle für die Entstehung von fast monominerlischen Cr-Spinell-Lagen werden derzeit diskutiert. Teilweise widersprüchliche Ansätze erklären die Cr-Spinell Anreicherung unter anderem durch Änderungen in Parametern (z.B. Änderung im Druck, Sauerstofffugazität, Temperatur, Magmenzusammensetzung durch Mischung, usw.) oder durch mechanische Anreicherungsprozesse. In dieser Arbeit wurden mikro-analytische Messungen von Cr-Spinell-Lagen verwendet, damit vertikale Variationen entlang der Lagen des Bushveld Komplexes und laterale Variationen in der Rum Intrusion aufgezeichnet werden können. Die zusammengestellten Daten zeigen in beiden Fallstudien eine Anreicherung von Cr-Spinell durch physikalisch-chemische Prozesse statt mechanischer Prozesse. Weder großräumiges Kristallabsaigern noch die Mobilisierung von Kumulaten durch Cr-Spinell-reiche Dichteströme können die beschriebenen Texturen und Mineralchemie erklären. Des Weiteren konnten laterale Variationen in Lagenstruktur und Cr-Spinell Zusammensetzung entlang des Streichens in der Rum Intrusion beobachtet werden. Diese Variationen deuten darauf hin, dass der Anreicherungsprozess eng verknüpft war mit wiederholten Schüben von neuen, primitiven Magmen. Diese Magmenschübe, deren Assimilation des liegenden Kristallbreis und die anschließende Fraktionierung der Magmen, führten schlussendlich zu den beobachteten lateralen und vertikalen Variationen.

Danksagung

Zuallererst möchte ich mich herzlichst bei Lutz Hecht bedanken. Seine Betreuung mit allen Diskussionen, Ratschlägen, Aufmunterungen und Unterstützungen verschiedenster Art haben zum Gelingen dieser Arbeit maßgeblich beigetragen. Danke, dass du mich in dieser Arbeit und in vorausgegangenen Projekten in den letzten sieben Jahren so gutgelaunt und unermüdlich unterstützt hast und meine zaghaften Schritte in die Petrologie und Wissenschaft geführt hast; für deine Offenheit und Unterstützung auch mal vom geplanten Weg abzubiegen und wenn der Umweg zu groß geworden ist, mich wieder sanft in die richtige Richtung zu schubsen. Timm John möchte ich herzlich für die Begutachtung dieser Arbeit danken.

Der AMREP Forschergruppe möchte ich für die gute Zusammenarbeit, die vielen anregenden Diskussionen, die Vermittlung von so viel Wissen und die spannenden und spaßigen Treffen in Südafrika und Deutschland in den vergangenen fast dreieinhalb Jahren danken. Dem BMBF und dem Museum für Naturkunde Berlin möchte ich für die finanzielle Unterstützung des AMREP Projektes danken, die diese Arbeit überhaupt erst ermöglicht haben.

Meinen Kollegen aus der Impakt- und Meteoritenforschung am Museum für Naturkunde Berlin, Robert Luther, Sanni Siegert, Lukas Manske, Nicole Güldemeister, Tomke Fröchtenicht, Tanja Mohr-Westheide, Kirsten Born, Peter Czaja, Kathrin Krahn, Hans-Rudolf Knöfler, Kai Wünnemann, Uwe Reimold, Rita Schmidt und Friederike Schwarz möchte ich für die vergangen Jahre danken, ihr habt mich von wissenschaftlicher und technischer Seite so oft unterstützt und mir die Zeit am Museum so angenehm gemacht. Im Speziellen möchte ich Marie Hoffmann für die unzähligen Diskussionen und die tatkräftige Unterstützung beim Messen und auf Konferenzen danken, Astrid Kowitz für die vielen ‚Aufmunterungen' auf der Stahltreppe und Christopher Hamann für die vielen kleinen Diskussionen, den vielen Kaffee und die kleinen Tipps und Tricks bei LaTeX. Nicht unerwähnt bleiben sollen auch die vielen fachfremden Doktoranden und Freunde am Haus, unter anderem Kristin Mahlow, Nora Lengte-Maaß, Caro Dittrich und viele mehr. Vor allem Leon Hilgers und Vivien Bothe möchte ich danken, ihr beide habt wohl einen nicht zu vernachlässigen Anteil daran, dass ich den Endspurt dieser Arbeit halbwegs gut überstanden und so viel über die Radula, Axolotl, Otter und Biber gelernt habe!

Bei meinen Freunden und Familie möchte ich mich liebevoll bedanken, sie haben wohl selten die Hoffnung aufgegeben, dass vielleicht doch noch was aus mir wird. Dina und Tobi möchte ich für die unzähligen kleinen und großen Dingen, derer es vermessen wäre sie alle aufzuzählen, von ganzem Herzen danken.

Nicht unerwähnt sollen auch die Kaffeebauern rund um die Welt und die deutschen Winzer bleiben. Sie haben mich ‚munter' und ‚beschwingt' durch die Jahre meiner Promotion gebracht. Mein tiefer Dank gehört euch.

Contents

Chapter 1

Introduction

1.1 Layered Intrusion: Petrological and economic treasure troves

Layered intrusions are igneous stratified bodies. Although simple stratification may occur in a wide range of plutonic systems like syenitic intrusions (e.g. Parson, 1979; Hodson, 1998), granitoids (e.g. Barbey, 2009) or sills (e.g. Ripley, 1979; Egorova and Latypov, 2013; Latypov et al., 2015), layered intrusions are unquestioned by far the most prominent examples (Namur et al., 2015) (Fig. 1.1). Layers constituting this stratification are defined by changes in texture, modal proportions (modal layering) and/or chemical composition ('cryptic layering') of minerals in different layers (O'Driscoll and VanTongeren, 2017). Layering can be uniform (i.e. homogeneous across a layer) or non-uniform for example graded changes in mineral modes (Winter, 2009). Thus, at first glance one might misinterpret these layers as sedimentary rocks and many characteristics of sedimentary processes can indeed be observed in layered intrusions. Layered intrusions mainly crystallise from basaltic magmas (Scoates and Wall, 2015) and are of great scientific relevance as they represent 'natural laboratories' helping to understand magmatic system (e.g. Winter, 2009; Boudreau et al., 2016), but also of outstanding economic importance as they are enriched in various base and precious metals (e.g. Lee, 1996; Godel, 2015; Boudreau et al., 2016; O'Driscoll and VanTongeren, 2017).

Layered intrusions can be found around the world on all five continents (Fig. 1.2) and throughout the geological record from the Archean to the Paleogene (Scoates and Wall, 2015) (Table 1.1). Although layered intrusions can potentially form in any tectonic environment, they are generally associated with anorogenic settings and events producing large volumes of basaltic melt (e.g. mantle plumes) (O'Driscoll and VanTongeren, 2017). They show a huge variation in size (few km^2 to tens of thousands of km^2), shape (funnel-shaped, dykes to box-shaped) and to a certain degree in composition. While most layered intrusions have an ultramafic to mafic composition, more evolved exceptions exist like the Ilímaussaq Intrusion in South Greenland, which consist of highly differentiated peralkaline rock suites (Marks and Markl, 2015). Moreover, the process of emplacement can differ significantly. Some layered intrusions like the Kiglapait and the Skaergaard intrusions are interpreted as closed system, i.e. formation by one magma injection and subsequent differentiation (e.g. McBirney, 1996; Morse, 2015; Morse et al., 2017), while other complexes like the Bushveld Complex and the Rum Layered Intrusion are interpreted to have formed as open system due to several replenishing events and more or less assimilation of crustal material involved (e.g. Eales and Cawthorn, 1996; Emeleus et al., 1996; Cawthorn, 2015; Morse et al., 2017). Layered intrusions might not even be restricted to Earth, as Francis (2011) interpreted spectroscopic data collected by the Mars rover Spirit and proposed that the Columbia Hills represent an extraterrestrial

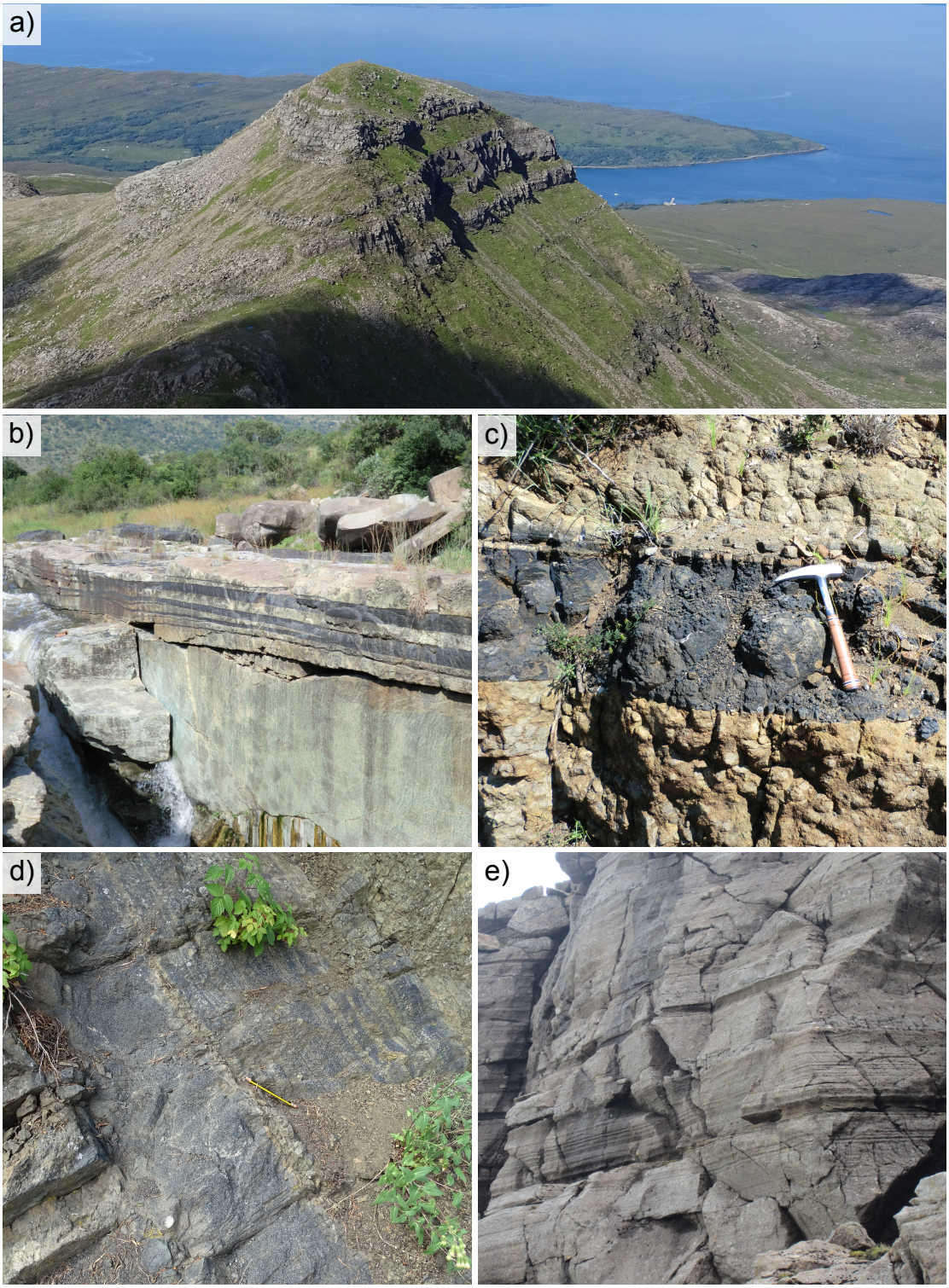

Figure 1.1: Field pictures of different layered intrusions. **a** Rhythmic layering on the Rum Layered Intrusion (Scotland) on the flanks of Hallival. The layers are composed of weathered peridotite and more competent troctolite. **b** UG1 chromitite of the Bushveld Complex (South Africa) at Dwars River. The bifurcating chromitite layers are hosted in anorthosite, the outcrop is ca. 2 m in height, by courtesy of M. Junge. **c** Magnetite layer of the Upper Zone of the Bushveld Complex, by courtesy of M. Junge. **d** Chromitite layer of the Stillwater Complex (Montana, USA). **e** Unit 14 troctolite (Rum Layered Intrusion), with interlayered peridotite, outcrop height is ca. 4 m, by courtesy of L. Hepworth.

layered intrusion with a succession of harzburgites, olivine norites and apatite-bearing norites. Consequently, these variations indicate that neither geologic time, size, shape nor composition are solely responsible for the complex processes that form igneous layering.

Layered intrusions form in magma chambers by accumulation of crystals (termed 'cumulus crystals', Wager et al. 1960) on a solidifying crystal mush ('cumulate') at the chamber floor, roof and/or walls. Consequently, the remaining liquid ('intercumulus' melt) changes its composition by fractionation, especially in closed systems like the Skaergaard Intrusion. Thus, layered intrusions provide direct insights into petrological concepts like crystal accumulation or magma differentiation (e.g. Winter, 2009), which are often limited to experimental observations. However, the complexity of theses natural laboratories challenges the evaluation and interpretation of the respective rocks (Holness et al., 2017d). As a consequence, a number of important questions have been vividly debated since the discovery of layered intrusions, one being the question of the initial process that triggers accumulation of a single cumulus phase to form monomineralic layers (e.g. Cr-spinel layers). Although numerous models exist, their formation is still not yet fully understood (e.g. Maier et al., 2013; Namur et al., 2015; Latypov et al., 2017b). In addition, Sparks et al. (1985) highlighted the importance of post-cumulus processes, which might severely modify the chemistry and texture of the original assemblage and hence add uncertainty to the interpretation of early igneous stages (e.g. Cameron, 1975; Hulbert and von Gruenewaldt, 1985; Barnes, 1986b; Penberthy and Merkle, 1999; Godel et al., 2011; Kaufmann et al., 2018). However, handled "with a healthy degree of caution" (O'Driscoll and VanTongeren, 2017), layered intrusions yield valuable information and thus enhance our general understanding how mafic magma systems in crustal chambers evolve and solidify.

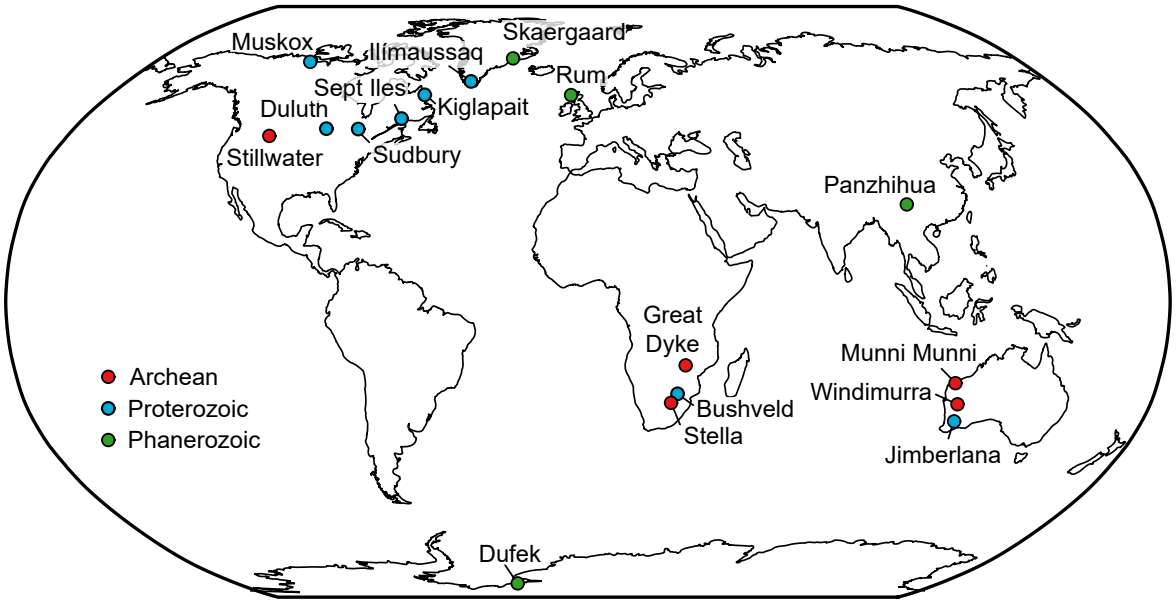

Figure 1.2: Schematic world map with location of some well-known layered intrusions, adapted from O'Driscoll and VanTongeren (2017).

Layered intrusions do not only provide significant scientific wealth, but are also of worldwide economic importance. The major deposits of platinum-group elements (PGE: Ru, Rh, Pd, Os, Ir & Pt) on Earth are hosted in ultramafic to mafic layered intrusions (Godel, 2015). Mining is typically restricted to narrow layers (so-called reefs) enriched in PGE (Godel, 2015) among the most important are the Merensky Reef and the UG2 chromitite layer, both located in the Bushveld Complex, South Africa and the J-M Reef of the Stillwater Complex, USA. Although, PGE mineralised layers can be observed in most complexes, they are typically subeconomic like the Rum Layered Intrusions (e.g. Butcher et al., 1999; Gunn and Styles, 2002; Power et al., 2003; O'Driscoll et al., 2009a). The nature of the processes of PGE enrichment in layered intrusions remains controversial (Godel, 2015; O'Driscoll and VanTongeren, 2017). Layered intrusions are, however, not only enriched in precious metals, but also hold a great potential for base metals, such as Cr, Ni, Ti and V (Lee, 1996; Naldrett, 2004; Godel, 2015; O'Driscoll and VanTongeren, 2017; Maier and Hanski, 2017). The Bushveld Complex for example has massive reserves of V and Ti, providing ca. 18 % of the world's V production (Moskalyk and Alfantazi, 2003; Polyak, 2015) and is the main source for Cr exploitation worldwide (Papp, 2014). The Sudbury Complex, Canada, a layered intrusion originated from an impact event, is extensively mined for Ni (Kuck, 2013). Furthermore, the rather exotic peralkaline Ilímaussaq Intrusion is associated with large reserves of rare-earth elements (REE) and U, thus the intrusion moved into focus of increasing exploration activity over the last years (Marks and Markl, 2015).

Table 1.1: Summary of location and age of some well-known layered intrusions. The two intrusions this thesis focuses on (Bushveld Complex and Rum Layered Intrusions) are highlighted.

Intrusion	Location	Period	Age
Stella	South Africa	Archean	3033 Ma[1]
Windimurra	Western Australia, Australia	Archean	2813 Ma[1]
Stillwater	Montana, USA	Archean	2709 Ma[1]
Munni Munni	Western Australia, Australia	Archean	2625 Ma[2]
Great Dyke	Zimbabwe	Archean	2576 Ma[1]
Jimberlana	Western Australia, Australia	Paleoproterozoic	2411 Ma[3]
Bushveld	**South Africa**	**Paleoproterozoic**	**2057 Ma** [1]
Sudbury	Ontario, Canada	Paleoproterozoic	1849 Ma[4]
Kiglapait	Labrador, Canada	Mesoproterozoic	1305 Ma[1]
Muskox	Nunavut, Canada	Mesoproterozoic	1269 Ma[1]
Duluth	Minnesota, USA	Mesoproterozoic	1099 Ma[1]
Ilímaussaq	Greenland	Mesoproterozoic	1060 Ma[1]
Sept Iles	Québec, Canada	Neoproterozoic	565 Ma[1]
Panzhihua	China	Permian	260 Ma[1]
Dufek	Antarctica	Cretaceous	108 Ma[1]
Rum	**Scotland, UK**	**Paleogene**	**60 Ma** [1]
Skaergaard	Greenland	Paleogene	55 Ma[1]

[1] Scoates and Wall (2015)
[2] Arndt et al. (1991)
[3] Fletcher et al. (1987)
[4] Davis (2008)

1.2 The mineralogy of Cr-spinel in magmatic settings

This thesis aims to advance our knowledge on the formation of Cr-spinel layers[1]. To understand these processes, a general background of the mineralogy of the major constituent of these layers, Cr-spinel, is need and thus summarised in this chapter. The spinel group (AB_2O_4, with A: Mg, Fe^{2+} and B: Al, Cr, Fe^{3+} and Ti) is a typical accessory phase in a wide range of magmatic and metamorphic settings and appears in a wide range of composition (Fig. 1.3). The complex mineral chemistry of this group is especially sensitive to changes in physico-chemical conditions during crystallisation, like changes in melt composition due to mixing and fractionation or changes in pressure, oxygen fugacity or temperature (Allan et al., 1988; Fisk and Bence, 1980). For example, an increase in pressure results in Al enrichment, while increasing oxygen fugacity or decreasing temperature shifts the composition towards Fe^{3+}-rich spinel (i.e. magnetite, magnesioferrite) (Fisk and Bence, 1980). Thus, for a long time spinel was used as as 'petrogenetic indicator' in magmatic systems (e.g. Irvine, 1965; Sack, 1982; Allan et al., 1988; Sack and Ghiorso, 1991; Roeder, 1994; Barnes and Roeder, 2001; Kamenetsky et al., 2001). This holds especially true for Cr-rich spinel, which is stable under a wide range of magmatic conditions and is typically among the first phases to crystallise in ultramafic to mafic systems (Roeder, 1994; Barnes and Roeder, 2001).

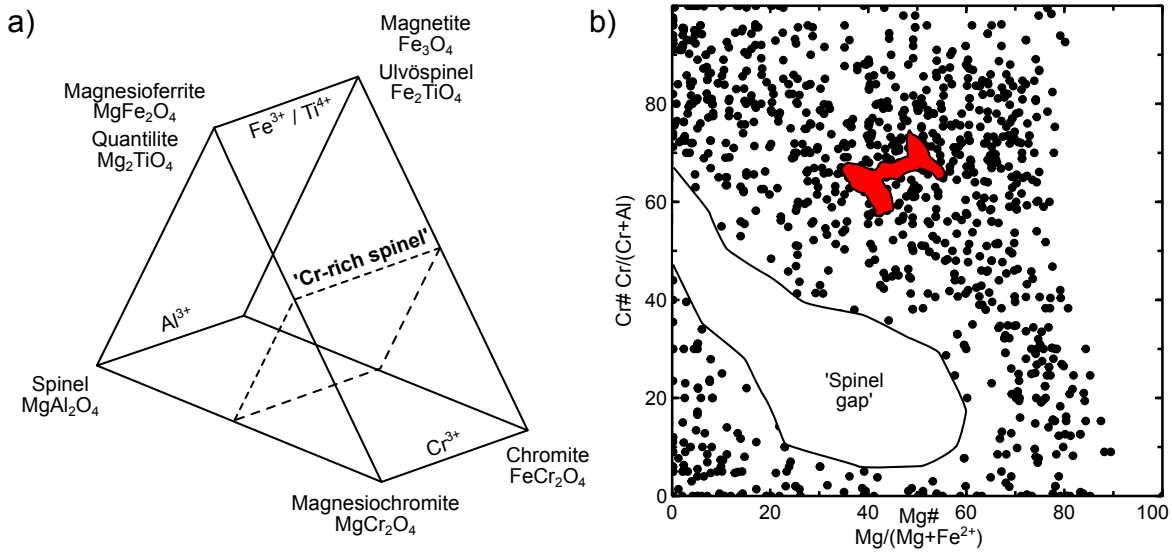

Figure 1.3: **a** Spinel compositional prism, adapted after Haggerty (1991). **b** Spinel chemistry of various terrestrial magmatic locations adapted after Barnes and Roeder (2001). The 'spinel gap' is characterised by a data density minimum between chromite and magnetite, however this gap is not universally present in all magmatic setting (Barnes and Roeder, 2001). The variations in chromitites of the Bushveld Complex are marked by a red field and taken from Naldrett et al. (2012).

Fractionation trends for Cr-spinel have been described for different scenarios. Scowen et al. (1991) mentioned compositional changes for chromite within the Kilauea lava lake, Hawaii.

[1]Although Cr-spinel (Cr-rich spinel *sensu stricto*, $MgAl_2O_4$, where Cr substitutes for Al) and chromite ($FeCr_2O_4$) are different from a crystallographic point of view, the distinction is negligible for the involved petrological processes. Thus, the term Cr-spinel and chromite and the rocks composed of these minerals, Cr-spinel layers and chromitites will be used synonymously throughout this thesis.

Analyses of chromite inclusions in olivine over a time interval of 22 years after the initial eruption revealed an increase in the iron content (Fe^{2+} and Fe^{3+}) and Ti, while Mg, Al and Cr concentrations decreased. The authors also described a close correlation of the Fe/Mg ratio (Mg#, atomic ratio, $Mg/(Mg+Fe^{2+})$) in olivine hosts and chromite inclusions, but attributed this effect to re-equilibration of both phases with the melt, instead to internal re-equilibration between both phases (Scowen et al., 1991). Allan et al. (1988) described similar fractionation trends with decreasing Mg# ratio and an increase in Cr# (atomic ratio, Cr/(Cr+Al)) for Cr-spinel in MORB settings. Naldrett et al. (2009; 2012) described trends in the chromite chemistry for chromitites of the Bushveld Complex. They distinguished two general trends, trend A and B. Trend A is characterised by a decrease of Mg# and an increase in Cr#, similar to the trend described by Allan et al. (1988). Naldrett et al. (2009) proposed that trend A results from a coupled exchange reaction of Cr and Fe^{2+} for Mg and Al. Trend B, which is characterised by a decrease in Cr# and Mg#, results from the fractional crystallisation of orthopyroxene, which leads to an increase of the activity of Al_2O_3 in the melt and a decrease in Cr# in chromite. Further, Cr-spinel is known to readily react and chemically re-equilibrate sub-solidus with the surrounding silicate phases, typically olivine and orthopyroxene (e.g. Roeder and Campbell, 1985; Irvine, 1967; Roeder, 1994). In this reaction Cr-spinel becomes enriched in Cr and Fe, while the silicates take the Mg provided that the system is closed.

In summary, the mineral chemistry of Cr-spinel at magmatic conditions primarily is controlled by the melt composition, while at post-magmatic conditions Cr-spinel chemistry is controlled by the rate of cooling and possible re-equilibration with surrounding silicates (Kamenetsky et al., 2001). However, the authors highlighted that these post-magmatic re-equilibration 'does not, however, obliterate' the magmatic compositional characteristics.

1.2.1 From accessory to major constituent: the process of Cr-spinel accumulation

As aforementioned, Cr-spinel is a typical accessory in a wide range of ultramafic to mafic settings, but it is also famously known to form almost monomineralic layers of Cr-spinel in layered intrusions (Fig. 1.1b). In typical ultramafic to mafic systems, Cr-spinel crystallises in cotectic proportions together with olivine or orthopyroxene (ca. 1–2 vol.%). Therefore, these systems have to undergo changes in crystallisation conditions. Two exemplary scenarios are illustrated in Figure 1.4, how these conditions can be achieved to form Cr-spinel layers. A rapid increase in pressure would shift the composition of melt **A** crystallising anorthite, olivine and spinel in cotectic proportions onto the spinel stability field, which would result in spinel precipitation alone (Fig. 1.4a). Mixing of different magmas is another scenario to account for exclusive Cr-spinel crystallisation (Fig. 1.4b). Based on the ternary system quartz–olivine–chromite Irvine (1975; 1977) proposed that mixing of primitive, intruding magma **B** with either the residual melt **C** or assimilation of crustal melt **D** would shift both intermixed melts $\mathbf{M_1}$ and $\mathbf{M_2}$ onto the chromite stability field. Thus, both mixtures would crystallise chromite as solely liquidus phase.

Besides these two scenarios a huge variety of contrasting petrological models are still discussed heatedly to account for Cr-spinel layer formation. In principle the existing models can be subdivided into the following mechanisms: (1) **gravity-driven crystal settling**,

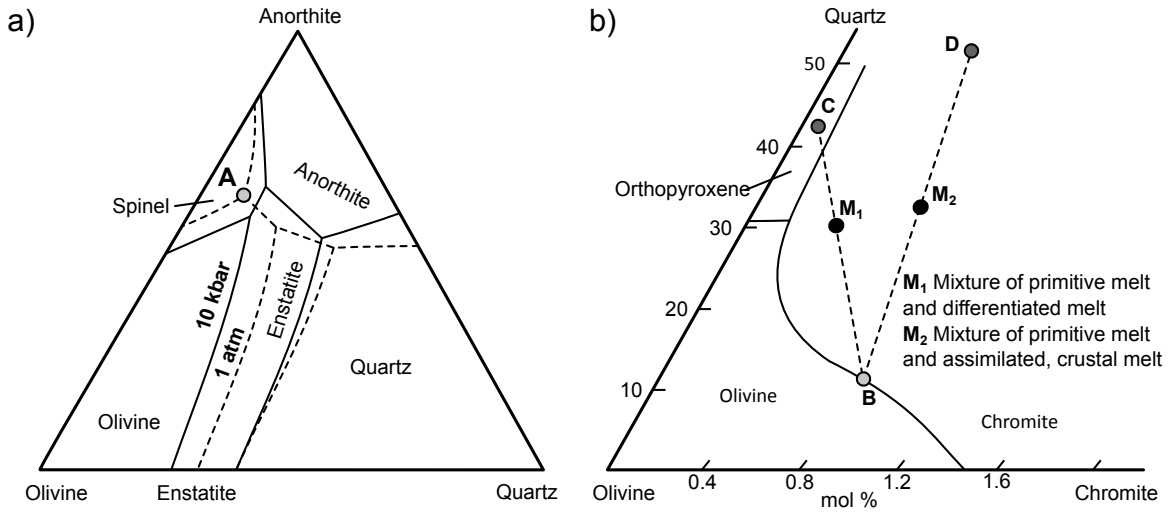

Figure 1.4: **a** Ternary system quartz–olivine–anorthosite, which shows how (Cr-) spinel can precipitated due to changes in pressure, adapted after Naslund and McBirney (1996). **b** Ternary system quartz–olivine–chromite illustrating how magma mixing can produce Cr-spinel layers, adapted after Irvine (1975) and Irvine (1977). See text for further explanation.

(2) ***in situ* crystallisation** at the crystal mush–magma interface and (3) accumulation by **crystal-rich slurries**. A graphic overview of the different models is summarised in Figure 1.5. Crystal settling was the initial idea to accumulate crystals (here Cr-spinel) on the magma chamber floor (Wager and Brown, 1967) to form layers in layered intrusions. Different hypotheses were proposed to initiate the exclusive crystallisation of Cr-spinel (i.e. oversaturation of Cr-spinel), among the most proposed are magma mixing of the residual melt with a primitive magma (Figs. 1.5a, 1.4b) (e.g. Irvine, 1977; Scoon and Teigler, 1994; Naldrett et al., 2009; Campbell et al., 1983), assimilation of crustal material (Figs. 1.5b, 1.4b) (e.g. Schoenberg et al., 1999; Kinnaird et al., 2002; Irvine, 1975; Spandler et al., 2005), fluctuations in pressure (Figs. 1.5c, 1.4a) (e.g. Lipin, 1993; Cawthorn, 2005; Cawthorn, 2011) or Cr-spinel saturation by adiabatic ascent of melts (Fig. 1.5d) (Naldrett et al., 2012; Latypov et al., 2018). However, different authors have pointed out that gravitational accumulation of crystals fails to explain structural features like layers following vertical to overhanging sidewalls (Latypov et al., 2013; Latypov et al., 2017b) or geochemical characteristics like the constancy in mineral chemistry in the footwall and hanging wall (Mondal and Mathez, 2007) and argued for *in situ* crystallisation (e.g. McBirney and Noyes, 1979; Latypov et al., 2013; Latypov et al., 2015; Latypov et al., 2017b). However, these models also require oversaturation of Cr-spinel to initate exclusive crystallisation. O'Driscoll et al. (2009b) and O'Driscoll et al. (2010) proposed that the Cr-spinel layers on the Rum Layered Intrusion formed due to assimilation of the cumulate footwall by influxes of primitive magma (Fig. 1.5e). The assimilation of troctolite by the primitive magma shifted the contaminated primitive magma onto the Spinel stability field, which crystallised mm-thick Cr-spinel layers. Slurries were proposed as a third alternative to the above-mentioned models to form Cr-spinel layers. Here, the crystallisation of Cr-spinel is shifted to an additional deeper magma chamber and Cr-spinel crystals are concentrated prior to the magma emplacement in structural traps. Three different variants are currently discussed (Cawthorn, 2015): (i) emplacement from a deeper staging

chamber (Fig. 1.5f) (e.g. Eales, 2002; Eales and Costin, 2012; Mondal and Mathez, 2007), (ii) mobilisation of cumulate slurries (Fig. 1.5g) in a Bushveld chamber, which was originally much wider (Maier et al., 2013) or (iii) injection of slurries within the cumulate pile (Fig. 1.5h) (e.g. Voordouw et al., 2009; Mungall et al., 2016).

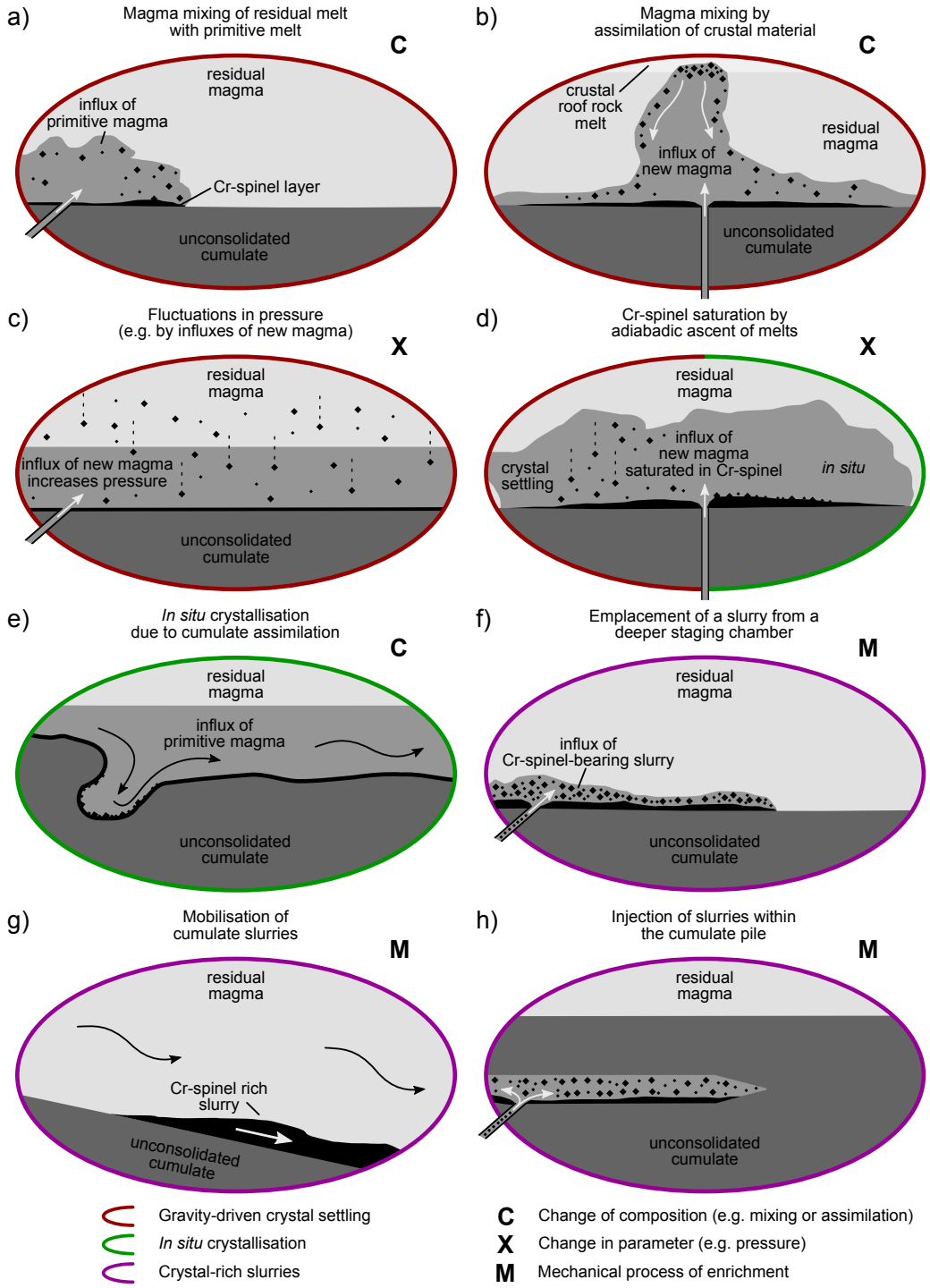

Figure 1.5: Graphic overview of different models to explain the accumulation of Cr-spinel layers, partly adapted after Latypov et al. (2015).

1.3 Thesis Aims and motivation

The presence of Cr-spinel layers in layered intrusions remains a controversial phenomenon in igneous petrology. Despite the long history of research and the wealth of scientific publications, the processes of primary accumulation and subsequent post-cumulus modification of these layers is still enigmatic (Chapter 1.2). This thesis aims to shed light on this debate and to improve the knowledge on processes of Cr-spinel accumulation and post-cumulus modification. Cr-spinel layers of two case studies were selected to study these processes: the Bushveld Complex and the Rum Layered Intrusion. The significant differences in size and age of these two case studies (see Chapter 1.7 for geological background information) offer the opportunity to study similar process on different scales and for different magmatic to post-magmatic conditions. The first case study, the Bushveld Complex, was studied by drill core material covering 5 layers in total, thus providing insights into vertical variations over an extensive interval. Sample material of the second case study, the Rum Layered Intrusions, was collected during a field campaign, which involved detailed mapping and sampling. The outstanding outcrop exposure on Rum offers the possibility to study lateral variations along supposed magma injections in greater detail, which might be too spacious for recognition in layers of the Bushveld Complex. Moreover, due to its smaller size and thickness and its younger age the Rum Layered Intrusion in comparison to the much larger Bushveld Complex exhibited much faster cooling and therefore less post-cumulus changes and post-magmatic alteration (e.g. O'Driscoll et al., 2014). Both case studies were investigated by detailed textural and geochemical micro-analyses to address the following main questions:

What is the significance of post-cumulus modification of Cr-spinel layers?

Soon after the recognition of cumulus theory (Wager et al., 1960; Wager and Brown, 1967), it was realised that post-cumulus processes might severely modify the primary chemistry and texture of accumulated crystals (e.g. Chapter 4; Cameron, 1969; Sparks et al., 1985; Wadsworth, 1985). Here, the effect of post-cumulus modification processes on Cr-spinel layers of both case studies will be summarised and assessed. This will allow to identify primary characteristics of cumulus crystals, which can be used to deduce the primary features of cumulates.

How did magmatic processes result in Cr-spinel cumulus formation: implications from vertical and lateral variations of Cr-spinel layers

As it has been shown in Chapter 1.2.1 the processes of Cr-spinel accumulation remains a puzzling phenomenon and a variety of differing, even contrasting models exist. Vertical and lateral variations will be discussed in this section to contribute to this debate and constrain the primary processes of Cr-spinel accumulation.

1.4 Thesis outline

This cumulative thesis is subdivided into six chapters. Chapter 1 provides an introduction to layered intrusions in general and to the Bushveld Complex and the Rum Layered Intrusion in particular. In addition, it also provides the theoretical background to the factors controlling the mineral chemistry of Cr-spinel in magmatic systems, a brief introduction to the research framework of AMREP, in which this thesis and its respective results were obtained, and a description of the utilised analytical methods. The scientific results of this thesis are given in the following chapters (Chapters 2, 3, 4 and 5). Three of these chapters (Chapters 2, 4 and 5) are self-contained manuscripts, written in collaboration with national and international research colleagues. One manuscript is published in a peer-reviewed journal, two are almost ready for submission. Chapter 3 presents the preliminary results of the evaluation of drill core logs and assays of the Thaba Mine area provided by Cronimet Chrome Mining SA. An overall discussion and conclusion is given in the final chapter (Chapter 6). Chapter 1, 3 and 6 were written particular for this thesis. The following chapters present the main scientific results:

Chapter 2: Kaufmann, F. E. D., Hoffmann, M. C., Bachmann, K., Veksler, I. V., Trumbull, R. B., Hecht, L. Vertical variations in the mineralogy, geochemistry and PGE in the LG and MG chromitites of the northwestern Bushveld Complex, South Africa. Manuscript almost ready for submission to *Economic Geology*.

Chapter 3: Lateral geochemical variations in the Lower Group and Middle Group chromitite layers, Thaba Mine, Bushveld Complex

Chapter 4: Kaufmann, F. E. D., Vukmanovic, Z., Holness, M. B., Hecht, L. (2018). Orthopyroxene oikocrysts in the MG1 chromitite layer of the Bushveld Complex: implications for cumulate formation and recrystallisation. *Contributions to Mineralogy and Petrology* 173.2, 1-20, doi:10.1007/s00410-018-1441-x

Chapter 5: Kaufmann, F. E. D., O'Driscoll, B., Hecht, L. Lateral variations in the Unit 7-8 Cr-spinel seam of the Rum Layered Intrusion, NW Scotland. Manuscript almost ready for submission to *Contributions to Mineralogy and Petrology*.

1.5 Personal contribution

Chapter 2, 4 and 5 were produced in cooperation with national and international colleagues. The contribution of each co-author is outlined below.

Chapter 2
F. E. D. Kaufmann performed all petrographic and geochemical analyses and evaluated the respective data. He wrote the preliminary version of the manuscript. M. C. Hoffmann (now Bundesanstalt für Materialforschung und -prüfung) helped with LA-ICP-MS measurements. K. Bachmann (Helmholtz-Institut Freiberg für Ressourcentechnologie) provided PGM and sulphide MLA data and participated in writing the respective parts of the material and methods section. I. V. Veklser (Helmholtz-Zentrum Potsdam Deutsches GeoForschungsZentrum), R. B. Trumbull (Helmholtz-Zentrum Potsdam Deutsches GeoForschungsZentrum) and L. Hecht (Museum für Naturkunde Berlin) participated in writing of specific parts of the discussion and revision of the manuscript. L. Hecht planned and supervised the research. All co-authors contributed to discussions and L. Hecht, I. V. Veklser and R. B. Trumbull improved focus and clarity of the final manuscript.

Chapter 4
F. E. D. Kaufmann performed all petrographic and geochemical analyses and evaluated the respective data. He wrote the preliminary and final version of the manuscript and managed the manuscript trough the peer review process under the supervision of L. Hecht and M. B. Holness (University of Cambridge). Z. Vukmanovic (University of Cambridge) helped with EBSD data acquisition and interpretation. Z. Vukmanovic and M. B. Holness participated in writing of specific parts of the discussion. All co-authors contributed to discussions and L. Hecht and M. B. Holness improved focus and clarity of the final manuscript.

Chapter 5
F. E. D. Kaufmann collected samples during a field campaign in July 2016 under the guidance of B. O'Driscoll (University of Manchester) and L. Hecht. F. E. D. Kaufmann performed all petrographic and geochemical analyses and evaluated the respective data. He wrote the preliminary version of the manuscript. All co-authors contributed to discussions and L. Hecht and B. O'Driscoll improved focus and clarity of the manuscript.

1.6 The research framework of AMREP

This thesis and its respective results were conducted within the research framework of AMREP (**A**pplied **M**ineralogy for **R**esource **E**fficiency of **P**latinum **M**etals), funded by the German Federal Ministry of Education and Research (BMBF), grant FKZ 033R119C. AMREP is a German-South African project with research partners from both countries, aiming to increase the efficiency and thus sustainable recovery of PGE in chromite ores of the Bushveld Complex, South Africa. PGE are an important resource intensively used in the high-technology industry (e.g. catalysers, fuel cells, medicine, and computers). As already stated in previous sections, the main reserve of PGE worldwide is the Bushveld Complex. Although PGE production is steadily increasing, this also holds true for the industrial demands. Thus, to overcome the potential limiting primary production, recycling and more efficient ways of extraction are needed to keep up with the raising industrial demands.

AMREP combines classical geological and mineralogical data of pristine and weathered ore to define and quantify ore types of differing PGE concentrations and deportments. These findings are used in combination with beneficiation tests for a geometallurgical model, which provides the most efficient way for ore procession and extraction. The Thaba Mine, located in the western Bushveld Complex and operated by Cronimet Chrome Mining SA (Pty) Ltd. serves as case study for AMREP. Currently, the Thaba Mine produces only chromite concentrates for Cr extraction, however, the mined chromitites hold a huge potential in PGE. The working group at the Museum für Naturkunde Berlin mainly contributes to the detailed textural, chemical and three-dimensional characterisation of pristine ores.

1.7 Geological setting and studied sample material

In this thesis, samples from two case studies, the Bushveld Complex and the Rum Layered Intrusion were examined to characterise and understand the petrogenesis of Cr-spinel layers in layered intrusions. Although both intrusions vary significantly in size (65 000 km^2 versus 30 km^2 in areal extent for the Bushveld Complex and the Rum Layered Intrusion, respectively) and age (2057 Ma, Bushveld Complex versus 60 Ma, Rum Layered Intrusion), yet both intrusions comprise Cr-spinel layers of remarkable textural and compositional similarity. The first case study, the Bushveld Complex, was studied by drill core material from the Thaba open pit mine, northwestern Bushveld Complex (Chapters 2, 3 and 4). The second case study, the Rum Layered Intrusion was mapped and sampled during a field campaign to assess the lateral variations of a Cr-spinel layers (Chapter 5).

1.7.1 The Bushveld Complex

The Bushveld Complex, located in the NE of South Africa (Fig. 1.2), is the largest known layered intrusion on Earth and hosts the world's largest known reserves of PGE and chromium. In 2014 the complex accounted for ca. 48 % of the world's production of PGE in general (Loferski 2016) and ca. 44 % of the world's chromium budget (Papp, 2014), thus being by far the largest producer of these elements. The igneous rocks of the Bushveld Complex were first mentioned by Carl Mauch, while Molengraff (1901) was the first to us the term 'Bushveld' (Cawthorn, 2015). Subsequent research in the early years of the 20$^{\text{th}}$ century (e.g. Hall and Humphrey, 1908; Wagner, 1929; Hall, 1932) discovered the great economic potential of the area (Cawthorn, 2015), most notably being the discovery of the world largest PGE host, the Merensky Reef, by the German geologist Hans Merensky in 1924 (Cawthorn, 2015).

The Bushveld Complex is of Proterozoic Age, with a time interval of 2056–2060 Ma for the main emplacement event (see review in Scoates and Wall, 2015) and intruded into sedimentary rocks of the Transvaal Supergroup. The present-day surface covers an area of ca. 65 000 km^2 and a vertical thickness ranging from 7–9 km (Cawthorn, 2015). The South African Committee for Stratigraphy (1980) subdivided the complex into three parts: the ultramafic to mafic Rustenburg Layered Suite (RLS), the Rashoop Granophyre Suite and the Lebowa Granite Suite. The RLS has a saucer-like shape, which dips towards the centre of the intrusion. It comprises four distinct regions, the eastern, western, far western and northern limb, with a fifth one, the southern limb, hidden under sedimentary cover. The western and eastern limbs have an arc-like shape and extend over 200 km (Eales and Cawthorn, 1996). The RLS formed as an open system by several injections of new magma, crustal assimilation and loss of evolved magma due to volcanic eruptions (e.g. Eales et al., 1993; Eales and Cawthorn, 1996; Zeh et al., 2015; Mungall et al., 2016).

Traditionally the RLS is subdivided from bottom to top into the Lower Zone, Critical Zone, Main Zone and Upper Zone, whereas the Critical Zone shows the most pronounced layering of ultramafic to mafic cumulates. According to Hall (1932) the Critical Zone was named based on 'critical' conditions which occurred in the magma chamber (Cawthorn, 2015) and these 'critical' conditions are still not fully understood. The Critical Zone comprises

sequences of pyroxenites-norites-anorthosites and is often further subdivided into the Upper and Lower Critical Zone, where the first appearance of cumulus plagioclase marks the boundary (Cawthorn, 2015). The Critical Zone is also well-known for the occurrence of PGE-bearing chromitite layers of varying thickness. These layers are subdivided into the Lower (LG), Middle (MG) and Upper Group (UG) and are numbered in ascending order, the LG6 is therefore the sixth chromitite of the Lower Group. 13–14 individual chromitite layers are traditionally identified in the RLS: LG1-7, MG1-4 and UG1-3, while the UG3 is restricted to the eastern limb. The LG chromitites are typically hosted in ultramafic cumulates (pyroxenite, harzburgite), while the host rocks of the MG and UG layers show a transition to a more mafic assemblage (pyroxenite, norite, anorthosite). Chromitites are laterally remarkably continuous and can be traced for kilometres along strike, in both the western and the eastern limb.

1.7.2 The Rum Layered Intrusion

The Rum Island on the Inner Hebrides, NW Scotland (Fig. 1.2), hosts the Rum Layered Intrusion, the second investigated complex. Rum is a National Nature Reserve, which is owned by the Scottish National Heritage and is famously known among petrologists for decades (e.g. Harker, 1908) for its diverse geology ranging from Archean gneisses to Paleogene intrusive and effusive igneous bodies including the layered intrusion (Emeleus and Hudson, 1997). Harker was also the first one who studied and mapped the island in great detail (Harker, 1908), while the classic study of Wager and Brown (1961; 1967) recognised the similarity of the layered rocks with those of the Skaergaard Intrusion and laid the cornerstone for numerous studies on the complex (Emeleus and Hudson, 1997). Moreover, the island is the type locality of harrasite, coarse-grained peridotite with branching, skeletal olivine crystals (Harker, 1908; Emeleus and Hudson, 1997).

The Rum Layered Intrusion is a classic example of an ultramafic to mafic layered intrusion (Brown, 1956; Wager and Brown, 1967). It is part of the British Palaeogene Igneous Province and formed in response to the opening of the North Atlantic (Emeleus et al., 1996). The magmas intruded into Upper Proterozoic sedimentary rocks of the Torridon Group (Emeleus and Hudson, 1997). The intrusion is subdivided into the Eastern Layered Intrusion (ELI), Western Layered Intrusion (WLI) and the Central Intrusion (CI). The ELI is typically characterised by large-scale layers (>10 m) comprising olivine and/or plagioclase, while the WLI is generally richer in olivine, layering is less pronounced and mostly characterised by textural changes (Emeleus and Hudson, 1997). The CI, sandwiched between the former mentioned, comprises a melange of large blocks of layered rocks enclosed in thick layers of peridotite and troctolite (Emeleus et al., 1996; Emeleus and Hudson, 1997; Emeleus and Troll, 2011). The ELI is famously known for its magmatic layering, which consists of 16 macro-rhythmic units (Fig. 1.1a) of feldspatic peridotite-troctolite (±olivine gabbro), which can vary considerably in thickness (Brown, 1956; Emeleus et al., 1996). Generally, the units are interpreted to represent pulses of replenishing magmas of picritic to basaltic magma (Emeleus et al., 1996; Upton et al., 2002; O'Driscoll et al., 2009a). Cr-spinel layers occur at the base of some of the macro-rhythmic units. They are typically 2–5 mm thick and can be traced laterally over much of the 2–3 km extent of the ELI (Brown, 1956; Emeleus and

Hudson, 1997). Elevated PGE concentrations have been reported for the Cr-spinel layers of the ELI (Butcher et al., 1999; O'Driscoll et al., 2009a).

1.8 Utilised analytical techniques

Samples from the two case studies described in the previous subchapter were investigated by a large variety of analytical methods to decipher the textural and geochemical evolution of the Cr-spinel layers in layered intrusions.

1.8.1 Textural characterisation

Textural characterisation of the studied sample from the Rum Layered Intrusion and the Bushveld Complex were first studied by classic petrographic observations by optical microscopy. Additional, more in-depth information on the micro-texture was added by crystal size distribution (CSD) measurements of Cr-spinel crystals and electron backscatter diffraction (EBSD) maps and single crystal analyses of Cr-spinel and orthopyroxene on selected samples.

CSD

CSD measurements provide an excellent approach to quantify textural parameters such as the grain size distribution (Higgins, 2006; Higgins, 2015). Here, they were conducted on Cr-spinel grains in Cr-spinel layers of samples of the Bushveld Complex (Chapters 2 and 4) and were carried out using compiled backscattered electron (BSE) images collected at the Museum für Naturkunde Berlin and the program CSDCorrections 1.53 following the methods described in Higgins (2000). Layers were covered with numerous areas on several thin sections to provide a representative data set, different sublithologies were treated separately. BSE images were changed to binary images, grain boundaries were manually outlined, artefacts removed and finally analyzed for their maximum crystal length by the image analysis software ImageJ.

EBSD

EBSD is a powerful tool to unravel the micro-texture of petrological samples, by measuring and mapping the orientation of the crystal lattice (Prior et al., 1999). This is especially important for cubic minerals, because other classical methods like optical microscopy offer only limited insights into the crystallographic properties of cubic crystals (Prior et al., 1999; Vukmanovic et al., 2013; Vukmanovic et al., 2014). EBSD measurements for this thesis (Chapter 4) were performed at the Department of Physics, University of Cambridge. Because EBSD measurement require a smooth and even surface (e.g. Prior et al., 1999), thin sections were polished for 1 h with 0.06 µm colloidal silica (SiO_2 particle dispersion in an alkaline solution), after standard mechanical polishing using diamond paste. Samples were analysed on a FEI sFEG XL30 SEM. The analysed crystallographic dataset was collected, indexed and analysed using Oxford Instruments AZtec acquisition software. EBSD maps and pole figures of crystallographic orientation were constructed using Oxford Instrument Channel 5 software, crystallographic orientation data (pole figures and inverse pole figures) were plotted using

Channel 5 “Mambo” software using lower hemisphere, equal area projections.

1.8.2 Geochemical characterisation

The mineral chemistry of the main cumulus and intercumulus phases (Cr-spinel, plagioclase, orthopyroxene and olivine) was measured by electron microprobe (EMP) for the major element composition and by laser ablation inductively coupled plasma mass spectrometry (LA ICP-MS) for the minor and trace element composition of the respective phases. In addition, the concentration and vertical variations of PGE within the Cr-spinel layers of the Bushveld Complex were analysed and combined with information of the PGE mineral assemblage acquired by mineral liberation analyzer (MLA) data.

EMP

Major element compositions of the main cumulus and intercumulus phases (Cr-spinel, plagioclase, orthopyroxene and olivine) were obtained for sample of the Bushveld Complex (Chapters 2 and 4) and the Rum Layered Intrusion (Chapter 5). EMP analyses were conducted at the Museum für Naturkunde Berlin with a JEOL JXA-8500F EMP equipped with a field emission cathode and five wavelength-dispersive spectrometers. The following typical analytical conditions were used: 20 kV accelerating voltage for Cr-spinel and 15 kV for silicates, 75 and 15 nA beam current for Cr-spinel and silicates respectively and a spot size of 1 µm for Cr-spinel, orthopyroxene and olivine and a defocused beam spot size of 5 µm for plagioclase to minimise the effect of alkali loss. The measured intensities were calibrated against natural minerals of the Smithsonian international standard suite (Jarosewich et al., 1980) and pure metals of the Astimex metal standard. Matrix effects were minimised by a conventional ZAF routine processed by the JEOL series operating system. Accuracy and reproducibility were checked regularly before and after each analysis session by measurements on minerals of the Smithsonian mineral standards. The ferric iron contents of Cr-spinel and orthopyroxene were calculated assuming ideal stoichiometry (Droop, 1987).

LA-ICP-MS

High-precision analyses of trace element compositions of plagioclase, orthopyroxene and olivine were obtained for both case studies (Chapters 2, 4 and 5). LA-ICP-MS analyses were conducted at the Institut für Mineralogie of the Leibniz Universität Hannover (LUH) with a fast scanning-sector field-ICP-MS (ThermoScientific ElementXR) connected to a femtosecond (Ti-sapphire) laser ablation system (further details are given in Oeser et al., 2014; Albrecht et al., 2014). The laser was set to 20–30 Hz, spot size ranged between 40–50 µm in diameter, depending on the crystal size of the analysed mineral phase. The ablation mode was set to raster mode for analyses of coarse-grained minerals and to line mode for analyses of interstitial silicates and rims analyses of cumulus crystals. Each spot was pre-ablated before each measurement to avoid artefacts due to surface contamination. Acquisition times of the background signal and the ablation signal were set to 40 s and 100 s, respectively. Analyses were bracketed every 10–15 measurements by standard reference material NIST610 to monitor

for internal instrumental drift. In addition, silicate reference material (BCR-2G) was measured by multiple analysis. Measured data were processed with the SILLS program (Guillong et al., 2008) and Si concentrations, obtained by EMP analyses, were use for internal calibration of trace element concentration of the respective phases.

Whole-rock PGE concentrations and mineralogy

PGE whole-rock concentrations of Pt, Pd, Ir, Rh, Ru and Au were determined in samples from the ZK135 drill core leftovers (Chapter 2) by the laboratories of the Mintek Analytical Services Division, South Africa. Drill core samples were cut to ca. 5 cm intervals, powdered in agate mills and finally analysed by fire assay with nickel sulfide collector, followed by dissolution and ICP-OES. Reference material SARM 64 was used to determine the accuracy of the analyses. In addition, total S concentrations were measured by LECO combustion analyses. The determination of the PGM identity and distribution was performed on selected samples of drill core material of the Bushveld Complex (Chapter 2) using the MLA instrument at the Helmholtz Institute Freiberg for Resource Technology. The MLA comprises a scanning electron microscope FEI Quanta 650F with two Bruker Quantax X-Flash 5030 energy-dispersive X-ray spectrometers and the MLA 3.1.4 software suite for automated data acquisition.

Chapter 2

Vertical variations in the mineralogy, geochemistry and PGE in the LG and MG chromitites of the northwestern Bushveld Complex, South Africa[1]

Small-scale variations in mineral chemistry, textures and platinum group-element (PGE) mineralization were investigated in the Lower and Middle Group chromitites of the Bushveld Complex, South Africa. Profiles from one drillcore covering 5 major chromitite layers (LG6-MG2) were analyzed by electron microprobe, LA-ICP-MS and whole-rock analysis of the PGE concentrations; textural characterization was performed by crystal size distribution of chromite. The PGE assemblage was also studied by mineral liberation analysis.

Detailed whole-rock analyses of PGE contents along vertical profiles reveal elevated PGE concentrations for all layers. Significant internal variations occur throughout all profiles with enrichments at hanging and/or footwalls. The enriched nature of chromitites in PGE compared to background concentrations of the host pyroxenite is a general feature, independent of the layer thickness. Quantification of the PGE assemblage depicts two principal groups: the LG6, LG6a and MG1 are dominated by the malanite series, laurite and PGE sulfarsenides, while the MG2 and MG2 II layers are characterized by laurite, PGE sulfides and Pt-Fe-Sn and PGE-Sb-Bi-Pb alloys.

Moreover, the results provide strong evidence for textural and compositional post-cumulus changes of the chromitites. Textural analyses by crystal size distribution curves suggest that the primary chromite texture were coarsened by a combination of adcumulus growth and textural equilibration, while compaction of the crystal mush played only a minor role. The mineral composition were also modified by post-cumulus processes, however, contrary to previous studies, we attribute these changes mainly to influxes from outside the layers in an open system, instead of chemical equilibration in a closed one.

[1] A significantly modified version of this chapter was submitted on October 3, 2018 to *Economic Geology* and is currently under review as: Kaufmann, F. E. D., Hoffmann, M. C., Bachmann, K., Veksler, I. V., Trumbull, R. B., Hecht, L. Variations in composition, texture and PGE mineralization in the LG and MG chromitites of the northwestern Bushveld Complex, South Africa.

2.1 Introduction

The Bushveld Complex in South Africa is the largest layered intrusion on earth and it is has the richest endowment in terms of PGE resources, which are mainly hosted in the Merensky Reef and in the underlying UG2 chromitite of the Critical Zone. The chromitite layers are divided into lower LG, middle MG and upper UG groups according to their stratigraphic position. All have anomalously high PGE contents compared to the adjacent silicate layers but the PGE grades in most are subeconomic (although many are mined for Cr). The exception is UG2, which by itself constitutes the world's largest known ore body for PGE. This layer has been extensively studied and there is a wealth of detail on the chemical and mineralogical variations within it (Eales and Cawthorn, 1996; Cawthorn, 2015; Mathez and Mey, 2005; Mondal and Mathez, 2007; Voordouw et al., 2010; Cawthorn, 2011; Junge et al., 2014; Manoochehri et al., 2015; Veksler et al., 2015; Veksler et al., 2018). Another dozen chromitite layers exist in the Critical Zone below the UG2 and these have not received the same attention in the literature. Several studies exist (Cameron, 1969; Cameron, 1977; Cameron, 1980; Eales et al., 1990; Kottke-Levin et al., 2009; Naldrett et al., 2009) but the level of detail is commonly much less than for UG2. In particular, there is less detail about vertical variations in mineral composition and textures within the layers and from one layer to another that can be combined with PGE concentrations and mineralogy. However, the UG2 studies have shown that this level of detail is needed if one attempts to unravel the effects of magmatic processes in forming the layers from those that modify them in the post-cumulus stage (e.g. Junge et al., 2014; Veksler et al., 2018).

This paper presents results of a comprehensive investigation of five chromitite layers in the Lower and Middle Groups (LG6, LG6a, MG1, MG2, MG2II). The work was done on drillcore samples from the Thaba chromium Mine in the northwestern limb of the Bushveld Complex. We report small-scale variations in the major and trace element concentrations of the main cumulus and intercumulus minerals in the seams and add micro-textural information of the chromite from crystal size distribution (CSD) analysis. These compositional and textural observations are used to elucidate the processes of post-cumulus modification of chromitites and discuss the implications on their formation. Finally, we assess the concentrations and vertical variations of PGE within each seam and from one seam to another, and combine this with quantitative data on the PGE mineralogy from mineral liberation analyzer (MLA) data. In this paper we will use the terms layer and seam interchangeably for the chromitites.

2.2 Geologic Setting

The Bushveld Igneous Complex is the largest known intrusion on earth and it has the dimensions qualifying as a Large Igneous Province (ca. 2 000 000 km^3 of magma produced in the time interval of 2056–2060 Ma: Scoates and Wall 2015). The geology of the Bushveld Complex has been reviewed in a number of recent publications and the reader is referred to Cawthorn (2015) for an overview. In simplest terms, the complex is made up of a thick sequence of mafic and ultramafic cumulus layers (Rustenburg Layered Suite or RLS) that is overlain by felsic subvolcanic units that form the roof of the layered complex. The complex is subdivided into four distinct regions or limbs: the eastern, western, far western and northern limb, with a fifth, southern limb, inferred from geophysical data but not exposed. Best known are the western and eastern limbs which each have an arc-like shape extending over 200 km in strike length (Fig. 2.1). Currently separated by younger cover rocks, the eastern and western limbs most likely are connected at depth as shown by geophysical (Webb et al., 2004) and the finding of RLS xenoliths in a younger kimberlite from the center of the complex (Webb et al., 2011). The RLS is subdivided from bottom to top into the Marginal Zone, Lower Zone, Critical Zone, Main Zone and Upper Zone, whereby the Critical Zone stands out from the others due to its pronounced layering of ultramafic-mafic silicate cumulates alternating with nearly monomineralic seams of chromitite, and by the fact that it contains about 70 % of global platinum reserves.

The origin of layering in the RLS, as for other layered mafic intrusions too, remains poorly understood despite decades of research and debate (Namur et al., 2015, and references therein). For the Bushveld Complex specifically, there is consensus on two major points that are relevant for our study: first, all rock layers in the RLS are cumulates and a great deal of magmatic material was lost from the current system presumably to volcanic eruptions; and second, the RLS is the result of multiple injections of magma which remain compositionally similar (tholeiitic basalt) but show clear distinctions in parameters such as Mg number and initial Sr isotope ratio. Related to the discussion of magma recharge vs. magma evolution by fractionation is the question of parental magma composition. The study of fine grained sills and offshoots of the RLS and of chilled margins at the contacts have provided evidence of more than one primary magma composition. For the Critical Zone, the suggested parental composition is a Mg-rich basaltic andesite referred to as B1 (Harmer and Sharpe, 1985; Barnes et al., 2010; Godel et al., 2011; Wilson, 2012).

2.2.1 The Critical Zone and its chromitite layers

The Critical Zone is the subject of this study. It contains 13-14 chromitite layers in its ca. 1000 m thickness whereby the layers are numbered sequentially upwards in each of the three main groups i.e., LG1 to 7, MG1 to 4, and UG1 to 3. Individual layers can vary considerably in thickness from place to place, and they may be single or composite, leading to sub-layers numbered as LG6a. The chromitite layers rarely exceed 1 m in thickness and there are numerous thin chromite stringers of only a few centimeters or millimeters in thickness between the major layers. The LG and lower MG group chromitites are hosted in ultramafic cumulate

rocks (pyroxenite, harzburgite), while the host rocks for the upper MGs and UG layers are more evolved and may contain cumulus plagioclase (as opposed to plagioclase that crystallized from interstitial melt in the crystal mush). The first appearance of cumulus plagioclase marks the transition from the lower to the upper Critical Zones, and this takes place between the MG3 and MG4 layers in the Thaba mine section studied here.

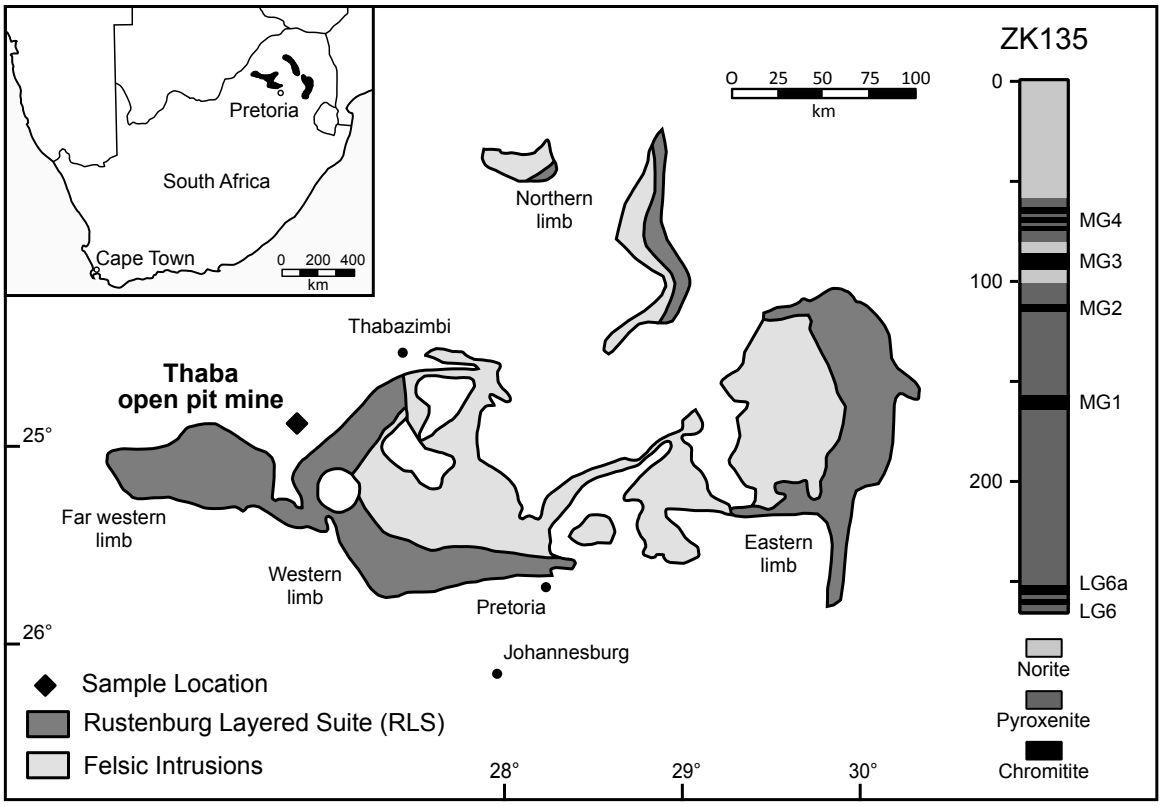

Figure 2.1: Simplified geological map of the Bushveld Complex with sample location, redrawn after Eales and Cawthorn (1996). Simplified lithostratigraphic column of the complete drill core is given on the right.

2.2.2 PGE mineralization in the Critical Zone

In terms of economic geology, chromitite layers are synonymous with chromite deposits. The lower layers of the Critical Zone, from LG6 to MG2, are mined on a large scale and they constitute a major global reserve of metallurgical chromium. However, all chromitite layers also have significant concentrations of platinum-group elements (PGE), which increase in a systematic way upwards, with the Lower and Middle groups ranging between 0.3–4 ppm (Lee and Parry, 1988; Teigler, 1990; Scoon and Teigler, 1994), and from 5 to 11 ppm in the uppermost seams of UG2 and the Merensky Reef stringers (Gain, 1985; von Gruenewaldt et al., 1986). Platinum mining currently takes place only in the highest-grade material of the UG2 and overlying Merensky Reef, but the possibility to recover PGE as a byproduct from the MG layers is under scrutiny.

With some exceptions, information on PGE grade of the LG and MG chromitites refers to the entire seam and little is known about the internal variations. However, several studies of

the UG2 layer have shown that PGE concentrations can vary with height (Hiemstra, 1985; Hiemstra, 1986; von Gruenewaldt et al., 1990; Maier and Barnes, 2008; Voordouw et al., 2009; Voordouw et al., 2010; Junge et al., 2014). Our study is the first to provide within-layer assay data for some of the LG and MG layers.

2.2.3 Chromitites of the Thaba mine and description of the drill cores studied

The Thaba chromium mine is located near Thabazimbi in the northern part of the western limb (Fig. 2.1). The mine currently extracts chromite from the LG6, LG6a, MG1 and MG2 seams in open-cast mining. Samples of these layers were collected from the open pit, but were found to be pervasively altered and weathered since operations do not extend deeper than about 20 meters. This study therefore focused exclusively on drill core material from borehole ZK135 located near the mine workings. A simplified lithostratigraphic log of the core is shown in an inset of Figure 2.1 and the intervals that were sampled for this study (LG6 to MG2) are described in detail below.

ZK135: LG6 to MG2 (Fig. 2.2)

The LG6 chromitite forms a single 55 cm thick layer embedded in feldspathic orthopyroxenite. The lower contact is sharp, orthopyroxene of the footwall pyroxenite overgrowths the chromitite contact. The upper contact shows a gradually transition over 5 cm into the hanging wall pyroxenite. The LG6 layer contains a thin pyroxenite parting in the upper third. Most of the main layer comprises closely packed massive chromitite (85–95 vol.% chromite) with minor amounts of interstitial plagioclase, orthopyroxene and hornblende. Orthopyroxene oikocrysts occur throughout the main layer overgrowing chromite grains. In these, chromite is smaller and less abundant (75 vol.%); these areas are here called spotted chromitites.

The LG6a chromitite begins about 6 m above LG6. It comprises a 14 cm thick, closely packed, massive (86–92 vol.% chromite) main seam and two smaller (2–5 cm) stringers above and below, which are separated from the main layer by pyroxenitic partings containing chromite proportions of 14 and 27 vol.% for the lower and upper parting, respectively. The chromitite stringers contain abundant cumulus orthopyroxene. The orthopyroxene grains in the pyroxenitic parting and the cumulus orthopyroxene in both stringers are aligned parallel to the layering. Massive chromitite is cemented by interstitial plagioclase and minor amounts of orthopyroxene, hornblende and biotite.

The MG1 chromitite is separated from LG6a by about 100 m of feldspar-rich orthopyroxenite. The main MG1 chromitite is 62 cm thick overall (Fig. 2.2) and it contains an intermediate pyroxenite-chromitite transition zone about 15 cm thick (at about 147.35 m) as well as three mm-thick pyroxenitic partings, all parallel to the overall layering. In addition, four mm-thick chromitite stringers occur in the hanging wall pyroxenite. The MG1 pyroxenite footwall is strongly altered for about 10 cm below the contact to the main chromitite layer, where olivine remnants are replaced by orthopyroxene and hydrous silicates. Chromite grains in this altered zone are inclusion-rich, consisting mainly of hornblende and orthopyroxene. The main layer comprises massive chromite (95–98 vol.% chromite) with only minor amounts of interstitial hydrous silicates like biotite and hornblende and orthopyroxene oikocrysts enclosing small

chromite grains. A detailed study of the orthopyroxene oikocrysts in MG1 was published by Kaufmann et al. (2018).

The MG2 chromitite is split into two sublayers in the ZK135 core, designated here as a lower MG2 and an upper MG2 II. Splitting of chromitite seams is common in the Critical Zone, most prominently in the UG1 chromitite (e.g. Voordouw et al., 2009; Latypov et al., 2018). The contact between MG2 and the footwall pyroxenite is sharp and the lowermost 3 cm of MG2 are brecciated. There are three pyroxenite partings in the lower third of MG2 as well as a thin layer of spotted chromitite (Fig. 2.2). All of these features are parallel to the layering. The main MG 2 layer has a lower chromite mode (65–80 vol.% chromite) compared to the underlying LG chromitite layers and it consists of spotted chromitite, which is cemented by orthopyroxene and plagioclase forming larger poikilitic crystals. Centimeter-sized patches of massive chromitite (88–97 vol.% chromite) occur throughout the layer, but are most abundant in the lower third. Chromite in these patches shows 120° triple junctions and smooth curved grain boundaries, interstitial material are hydrous phases like biotite, and hornblende. Above the main layer of massive MG2 chromitite is a thin (2 cm) layer of spotted chromitite with orthopyroxene primocrysts. The MG2 II layer is located about 2 m above MG2, where it is hosted in pegmatoidal pyroxenite consisting of coarse-grained orthopyroxene, interstitial plagioclase and clusters of cm-sized olivine crystals. The chromitite is 14 cm thick and comprises spotted chromitite enclosed in interstitial plagioclase and orthopyroxene poikilitic crystals (55–72 vol.%) as well as patches of massive chromitite (85–90 vol.% chromite). The latter are best developed close to the lower and upper contacts where they are commonly brecciated.

2.3 Analytical Methods

2.3.1 Textural analysis

Crystal size distribution (CSD) analysis of chromite grains from the seams and the contact wall rocks was carried out using compiled backscattered electron (BSE) images from the polished thin-section profiles. After converting BSE images to binary images, chromite grain boundaries were manually outlined and artefacts were removed. The image analysis software ImageJ was used to compile the maximum crystal diameters of chromite grains (a minimum was set to 0.01 mm and these were analyzed by the program CSDCorrections 1.53 following Higgins (2000). A massive fabric, equant chromite shape of 1:1:1 and a roundness of 0.2 were assumed for calculation of CSD histograms by the CSDCorrections software. CSDCorrections was also used to extract the spatial distribution of chromite grains and the regression parameter of the CSD curves, i.e. slope and intercept with the y-axis, of the calculated profiles. The slope in a CSD diagram is defined as the negative reciprocal product of the growth time and the growth rate, while the intercept with the Y-axis corresponds to the nucleation density, both parameters were calculated from regression curves.

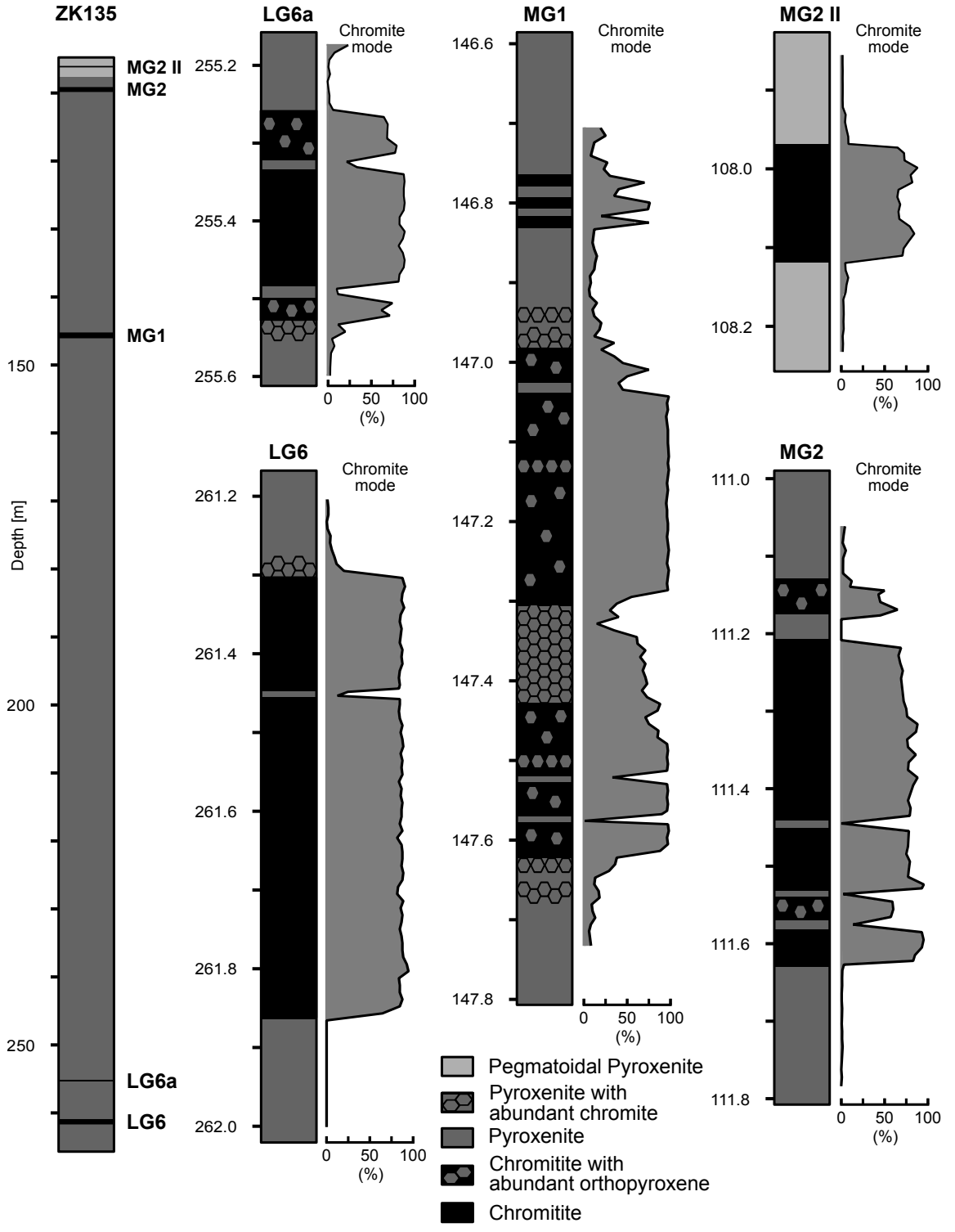

Figure 2.2: Stratigraphic columns and chromite mode of chromitite layers LG6 to MG2.

2.3.2 Mineral compositions

Major-element compositions of chromite, orthopyroxene and plagioclase were analyzed by electron microprobe at the Museum für Naturkunde Berlin with a JEOL JXA-8500F EMP equipped with a field emission cathode and five wavelength-dispersive spectrometers. The analytical conditions are described in detail by Kaufmann et al. (2018) but briefly, a 20 kV

accelerating voltage and 75 nA bean current were used for chromite and 115 kV / 15 nA for the silicate minerals. Chromite and orthopyroxene were analyzed with a 1 µm beam size and for plagioclase a beam size of 5 µm. The ferric iron contents of chromite and pyroxene were calculated assuming ideal stoichiometry (Droop, 1987).

Trace-element concentrations in orthopyroxene and plagioclases were obtained on the same sections used for microprobe by laser ablation ICP-MS at the Institut für Mineralogie of the Leibniz Universität Hannover. The technique employed a ThermoScientific ElementXR sector-field ICP-MS connected to a femtosecond (Ti-sapphire) laser ablation device. Detailed descriptions of trace element analyses are given in Albrecht et al. (2014) and Collinet et al. (2017). The laser operated at 20–30 Hz with a spot size ranging between 40–50 µm in diameter. The ablation was set to raster mode and after pre-ablation at each spot to remove surface contamination, acquisition times of the background and ablation signals were 40 s and 100 s, respectively. The analyses were bracketed every 10–15 measurements by standard reference material NIST610 to monitor instrumental drift. Multiple analysis of silicate reference material (BCR-2G) indicated accuracy and reproducibility of less than 5 %. Data were processed with SILLS program (Guillong et al., 2008) and Si concentrations, obtained by electron microprobe, were used for the internal calibration of trace element concentration for orthopyroxene and plagioclase.

2.3.3 PGE concentrations and mineralogy

The concentrations of Pt, Pd, Ir, Rh, Ru and Au were determined in bulk samples from the ZK135 drill core by fire assay with nickel sulfide collector, followed by dissolution and ICP-OES in the ISO-9000 certified laboratories of the Mintek Analytical Services Division, South Africa (www.mintek.co.za/technical-divisions/analytical-services-asd). The chromitite seams were cut into ca. 5 cm intervals, then powdered in agate mills for analysis. Reference material SARM 64 was used to determine the accuracy of the analyses and inclusion of several duplicates provided a check on repeatability. In addition, S concentrations were measured by LECO combustion analyses.

The identity and distribution of ore mineral in selected samples was determined on the same polished thin sections used for microprobe work with the Mineral Liberation Analyser (MLA) at the Helmholtz Institute Freiberg for Resource Technology (HIF). The MLA comprises a scanning electron microscope FEI Quanta 650F with two Bruker Quantax X-Flash 5030 energy-dispersive X-ray spectrometers and the MLA 3.1.4 software suite for automated data acquisition. Samples were analyzed by the sparse phase liberation (SPL-Lt) mode (Fandrich et al., 2007). Bachmann et al. (2017) give a detailed description of the MLA measurements and data processing.

2.4 Results

2.4.1 Chromite textures and crystal size distribution

Early studies of chromitites in the Critical Zone including Cameron (1969; 1975) established three types of textural relationships between chromite and the rock-forming silicates and these correspond to what we described in the drillcore description of the LG and MG layers above. The first is what Cameron (1975) called intergrain texture, where euhedral chromite grains are interstitial to silicate crystals. This texture, which we here term 'disseminated' is found in pyroxenite partings and in wall rock contacts above and below the chromitite seams (Fig. 2.3a). Cameron (1975) textural type 2 was termed 'nodular' (or 'spotted' in our study), where eudedral to subhedral chromite grains of a similar size to those of type 1 are enclosed in irregular, ovoid, cm-sized oikocrysts of orthopyroxene or plagioclase (Fig. 2.3b). The third textural types of chromite in the seams was termed 'aggregate' by Cameron (1975) and 'massive' in this study. It consists of anhedral chomite intergrowths with little interstitial material (Fig. 2.3c). Whereas Cameron (1975) stated that the nodular texture is 'nearly ubiquitous' in the eastern Bushveld complex, in the Thaba mine on the western limb the 'spotted' texture is rare in the LG6 and LG6a layers, it is present in MG1, and it is most abundant in MG2. The textures of chromite in the 'disseminated', 'spotted' and 'massive' domains are quite different and were treated separately in the measurement and interpretation of crystal size distributions. We obtained CSD data for chromite grains in both the main chromitite layers and the pyroxenitic partings. Care was taken to separate results for partings, oikocrysts and massive layer. The CSD diagrams are shown in Figure 2.4.

Nearly all CSD curves depict lognormal, often slightly upwards-concave shapes. The CSD curves of chromite enclosed in oikocrysts from MG1 is an exception, with a nearly straight shape. The maximum population density in CSD curves of chromite in oikocrysts and disseminated chromite has similar ranges (0.06–0.08 mm), whereas the massive chromite tends to higher values (0.08–0.13). The slopes of the CSD are steep for the spotted texture chromitite and disseminated chromite in partings (larger proportion of smaller crystals) and the curves rotate to shallower slopes and large grain sizes in the massive chromitite texture. Overall, the CSD curves indicate a trend to coarser grain sizes of chromite with increasing height from the LG6 to the MG2 II layer.

Other textural features of the chromitite examined with plots of the 'characteristic length' (-1/slope) versus intercept plot (Fig. 2.5b) reveal microstructural differences within the different layers and the sublithologies. The Thaba mine chromitites show a correlation of decreasing slopes with higher intercepts whereby CSD data for spotted chromitite shows shallower slopes and higher intercepts, and the opposite for massive chromitite. The gray field on Figure 2.5b is beyond the so-called closure limit (Higgins, 2002), where the crystal content of a rock reaches 100 %. The fact that some CSD data from the massive chromitite plot above the closure limit, which is not physically realistic and is attributed to the failure of the CSDCorrection software to correctly calculate the volume percentage of chromitite. Comparison of CSDCorrection calculations with the chromite mode determined by point counting (Fig. 2.5a) shows a good

correlation for volumetric percentages of chromite grains less than about 50, but for larger percentages the CSDCorrection software underestimates the chromite mode.

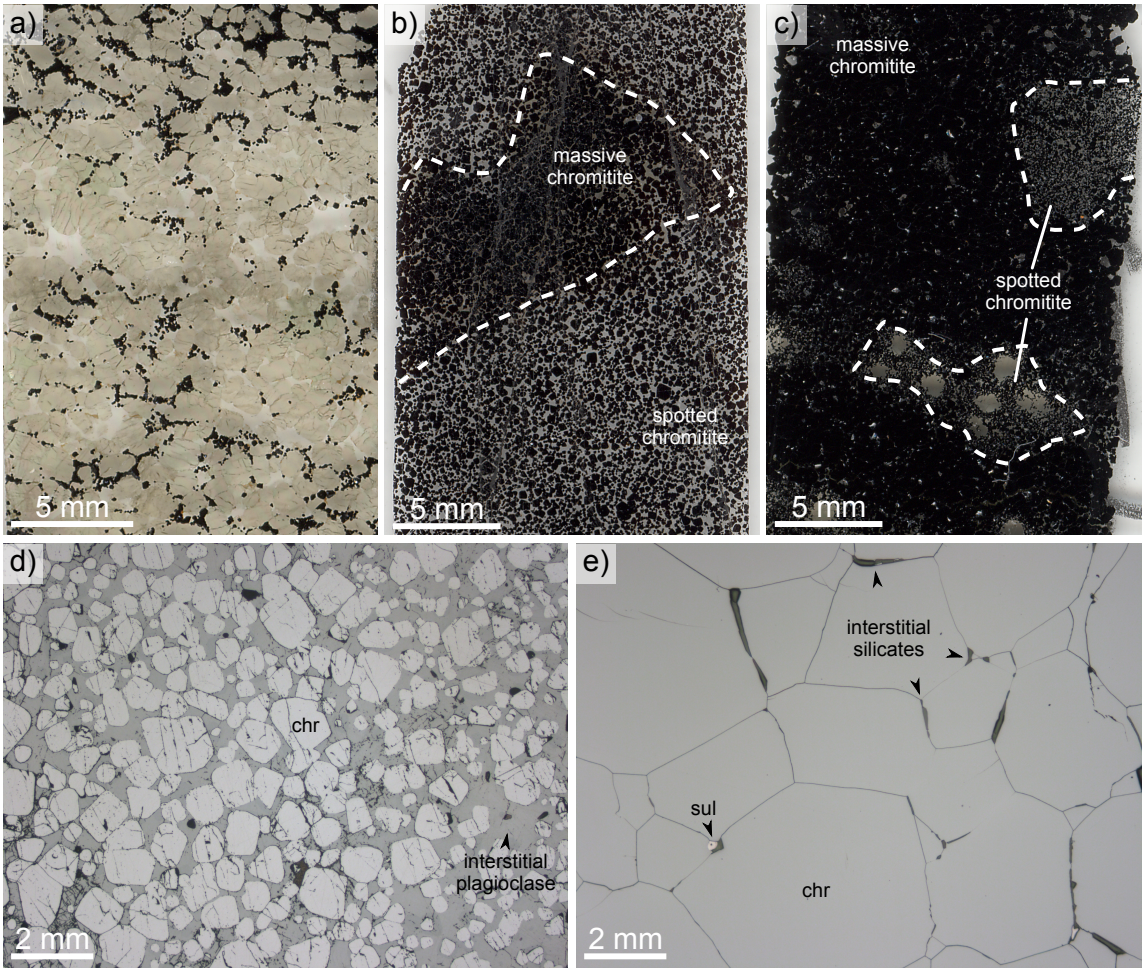

Figure 2.3: Texture types of chromite. **a** Disseminated euhedral chromite interlocked in orthopyroxenite parting. **b** Spotted chromitite of the MG2 layer poikilitic enclosed in plagioclase with marked patches of massive chromitite. **c** Massive chromitite of the MG1 with large, tightly intergrown, anhedral grains, which are almost free of interstitial silicates and marked spotted orthopyroxene oikocrysts. **d** Reflected light photomicrograph of spotted chromitite with interstitial orthopyroxene and plagioclase. **e** Reflected light photomicrograph of massive chromitite.

Finally, the spatial distribution of crystals (nearest-neighbor distance) can be described by the 'R-value', which is used to distinguish different textural-modifying processes like compaction, crystal sorting and overgrowths (Jerram et al., 1996). Figure 2.5c shows the R-value variation with porosity (100 - vol.% chromite). The fields for ordered and clustered distribution as well as the trends for better sorting, compaction, overgrowth and deformational compaction are shown as vector array and are taken from Jerram et al. (1996) and Boorman et al. (2004). The spatial distribution data shows that spotted chromitite has intermediate porosity and R-values ranging between 1.2 and 1.4. Massive chromitite plots in the same R-value range with lower porosity. Thus, the data depict a clear trend of decreasing porosity, while the R-values stay almost constant, which follows the overgrowth vector (Jerram et al., 1996). Disseminated chromite in pyroxenitic partings shows the lowest R-values and the

highest porosity, however these values include cumulus orthopyroxene and thus do not reflect the real porosity.

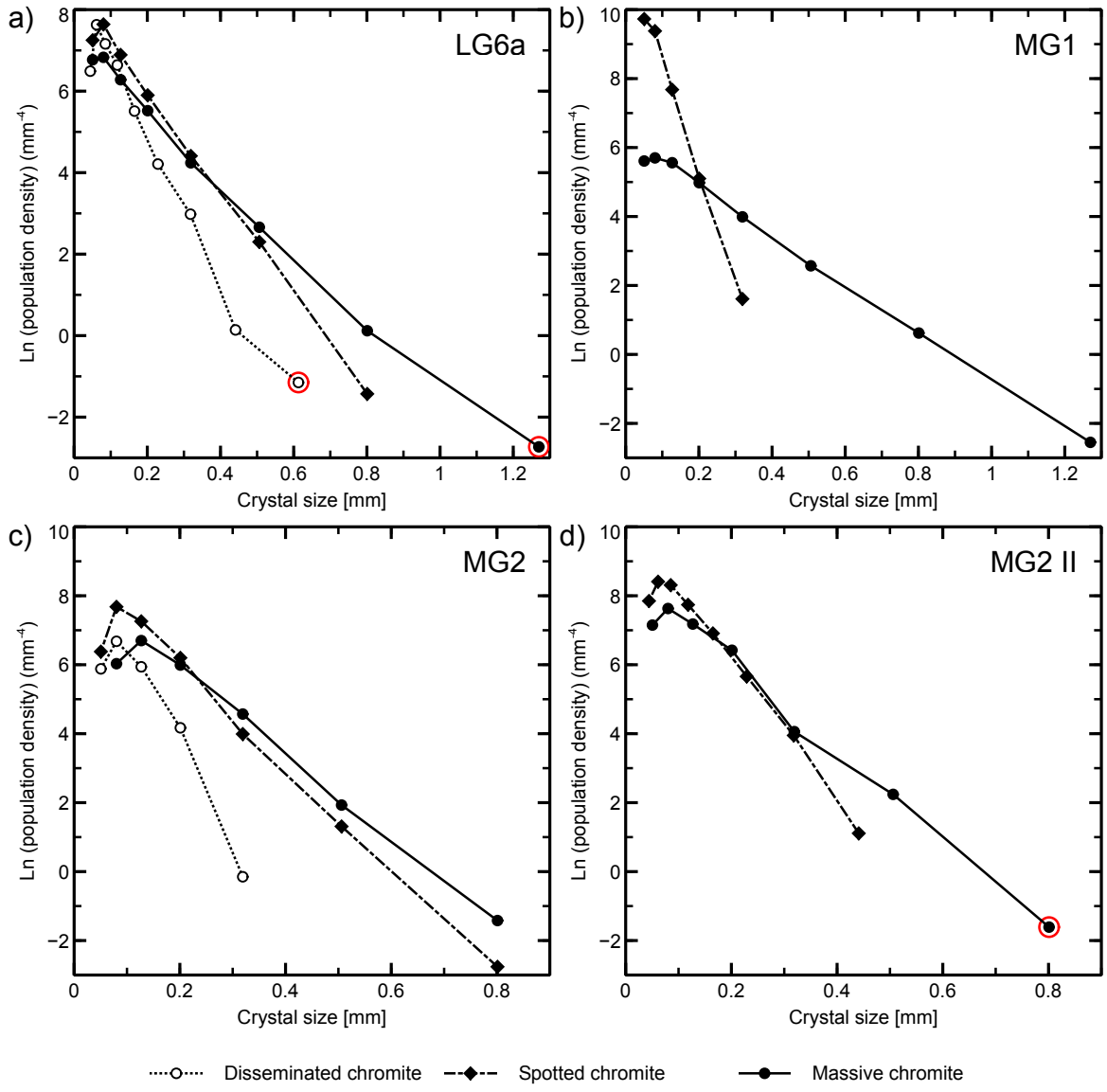

Figure 2.4: Crystal size distribution diagrams for chromite in the LG6 to MG2 II chromitite layers. Points with large uncertainties are marked by a red circle.

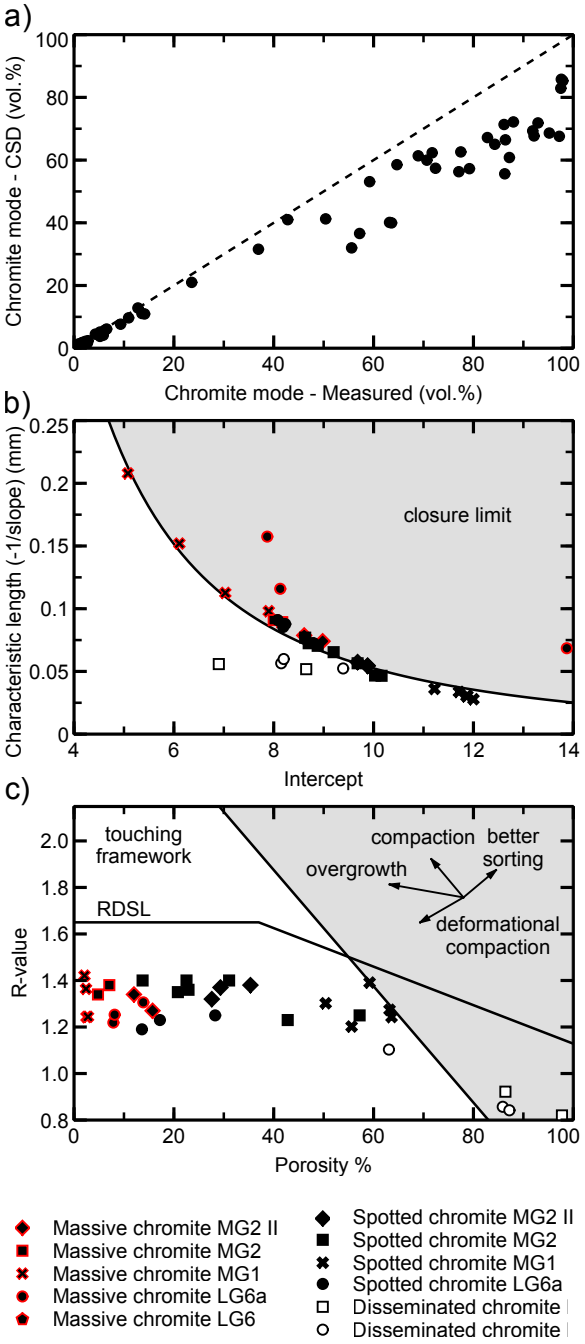

Figure 2.5: **a** Chromite mode measured by CSDCorrection vs chromite mode measured by point counting graph. **b** Characteristic length (-1/slope) plotted against intercept, grey area indicates closure limit for cubic crystals. **c** Porosity vs spatial distribution (R) plot. Shaded area represents a non-touching frame work, Random Sphere Distribution Line (RSDL) and vectors for changes in porosity and R are taken from Jerram et al. (1996).

2.4.2 Chemical composition of the main mineral phases

Chromite

The composition of chromite in the drillcore samples depends mainly on the sublithology (e.g. massive chromitite vs. disseminated chromite in pyroxenite), the modal proportion and the respective position within each layer (Figs. 2.6, 2.7, 2.8). Disseminated chromite in the host rock pyroxenite has lower and more variable Mg# (atomic ratio, $Mg/(Mg+Fe^{2+})$), whereas chromite in chromitites is quite homogeneous, showing a slight decrease in Mg# towards the top for some layers (Figs. 2.7, 2.8). The shift in chromite Mg# from pyroxenite to chromitite is abrupt at sharp contacts (typically at the footwall) and more gradual at the transitional contacts. These contrasts and trends are observed independent of the thickness of chromitite layers; even the thin pyroxenitic partings in chromitite layers show the same abrupt drop in Mg# as the wall rocks. Chromite grains in chromitite have lower and more homogeneous TiO_2 concentrations than those in the pyroxenitic host rocks. In many cases there are vertical trends in chromite composition through the layer (Figs. 2.9, 2.10). For example, the LG6 to MG2 layers show decreasing Cr# and Mg# upwards (Fig. 2.6a). The MG2 II chromitite is exceptional in having higher Mg#, both chromite within the chromitite and disseminated chromite in the host rocks, however, it should be noted that the layer is located in pegmatoidal pyroxenite and clusters of big olivine crystals, contrary to the other layers. Importantly, the composition of chromite is roughly independent of the respective texture, which is especially illustrated by the MG1. Here, chromite crystals within orthopyroxene oikocrysts (55–65 vol.% chromite) and massive chromite (95–98 vol.% chromite) depict an almost similar composition (Fig. 2.6b).

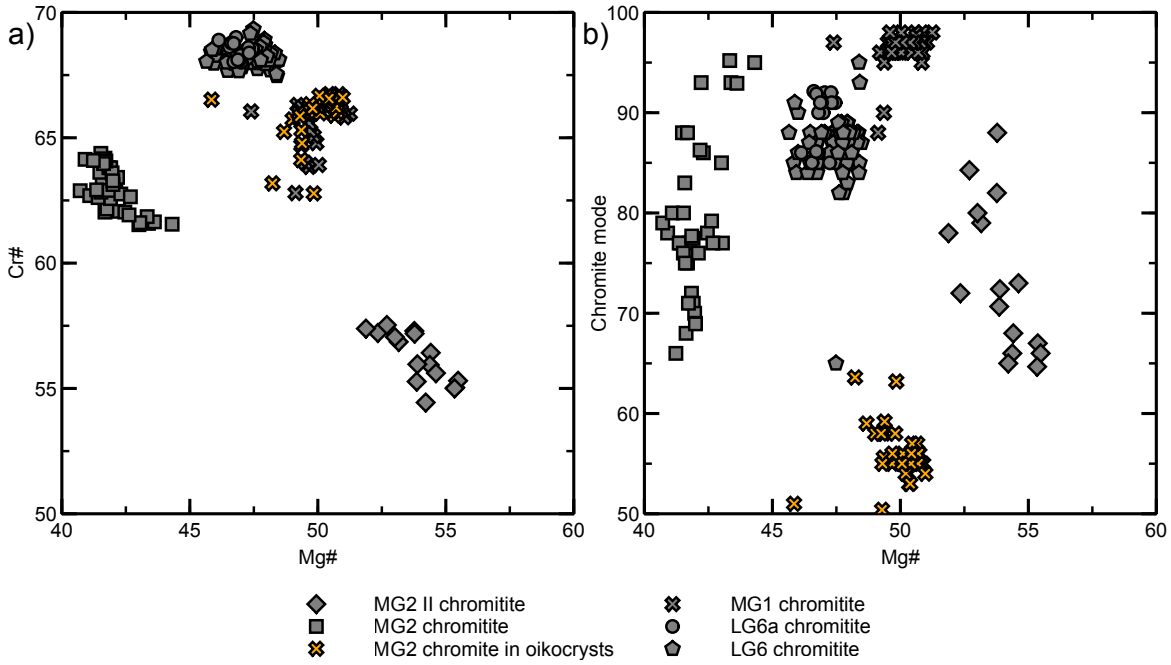

Figure 2.6: Variation in chromite composition across the LG6-MG chromitite layers. Disseminated chromite in the pyroxenite host rocks are omitted for simplification. **a** Cr# vs Mg#. **b** Chromite mode as proxy for extent of textural equilibration vs Mg#.

Orthopyroxene

Orthopyroxene shows clear chemical differences between interstitial orthopyroxene in chromitite and primocrysts in the spotted chromitite and pyroxenite. Orthopyroxene in chromitite is more magnesian than in the pyroxenite, following the trends already described for chromite variations (Figs. 2.7, 2.8). Orthopyroxene trace-element variations are described below.

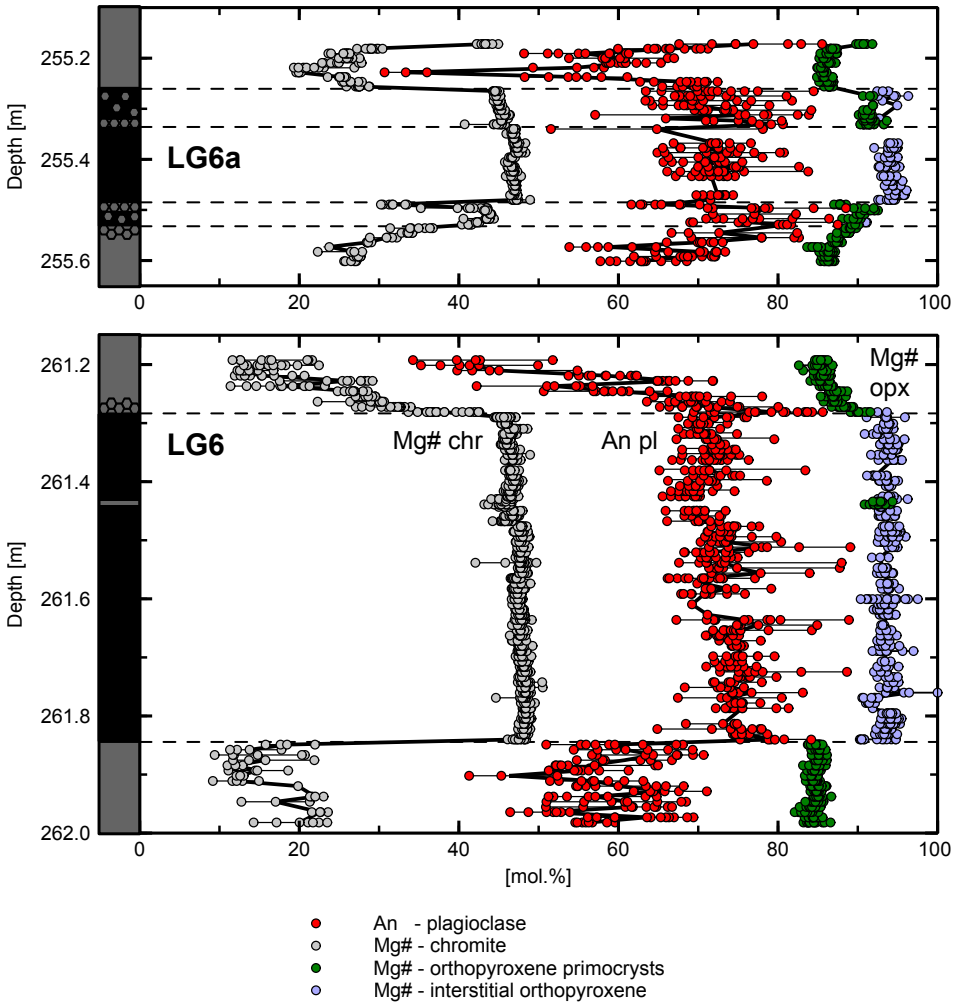

Figure 2.7: Variation in chromite, plagioclase and orthopyroxene mineral chemistry in the LG6 and LG6a chromitite layers. Orthopyroxene chemistry is subdivided in interstitial and primocryst crystals.

Plagioclase

Cumulus plagioclase in the Critical Zone first appears at the level of the MG4 chromitite and in our samples all plagioclase is an interstitial phase. Like the other major phase, plagioclase composition varies with the respective sublithology. Plagioclase in pyroxenite has lower anorthite content (An) than interstitial plagioclase in chromitite, although in both lithologies the compositions vary over a broad range of up to 20 mol % An. The K_2O contents in plagioclase from the chromitite layers tend to increase towards both the footwall and hanging wall relative to the interior of the layer, and like the Mg# variations in chromite

and orthopyroxene, the shift in plagioclase K_2O is sharp at the footwall contacts and more gradual at the hanging contacts (Figs. 2.9, 2.10).

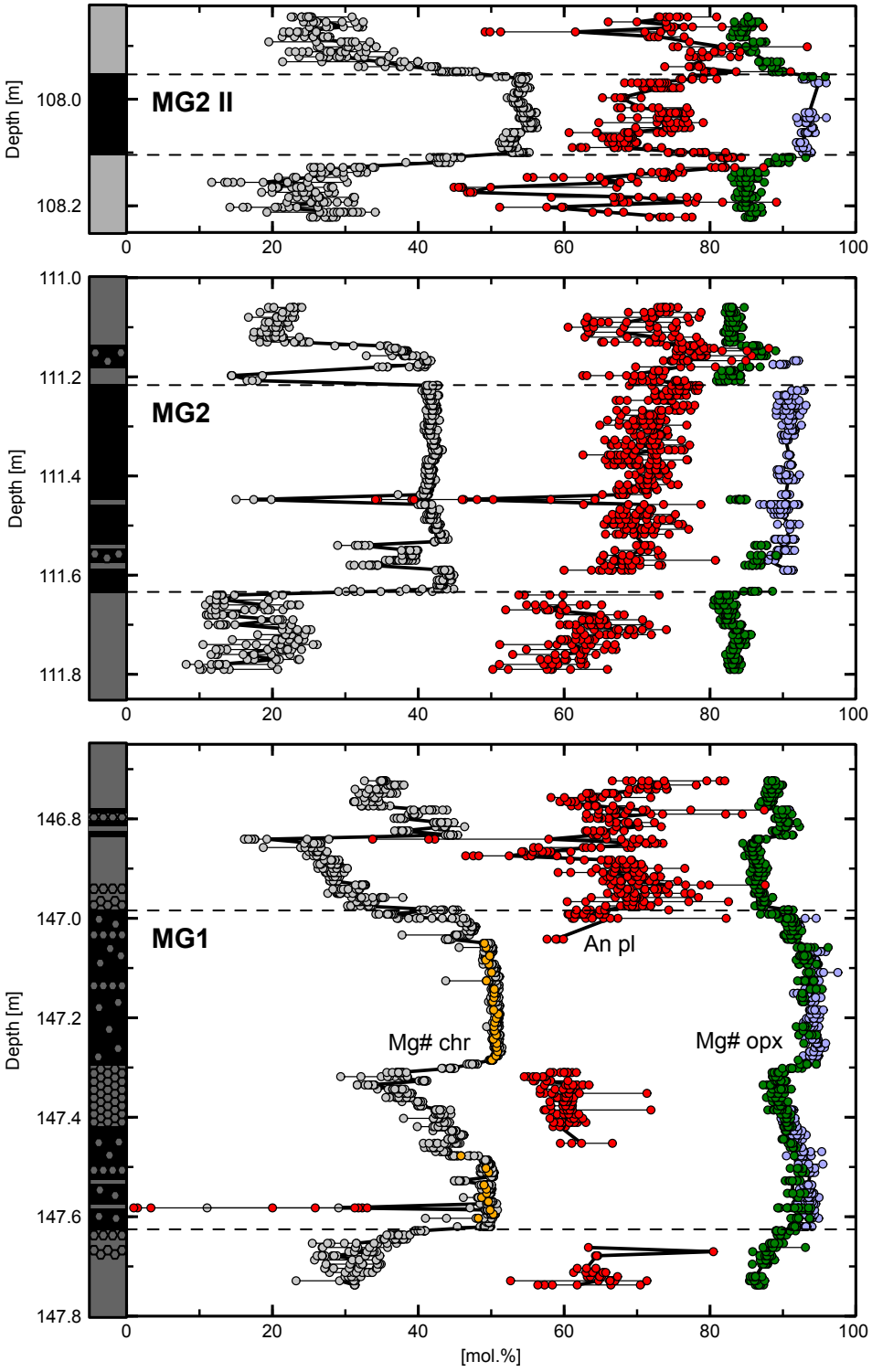

Figure 2.8: Variation in chromite, plagioclase and orthopyroxene composition in the MG1, MG2 and MG2 II chromitite layers. Orange symbols indicate chromite crystals entrapped in oikocrysts.

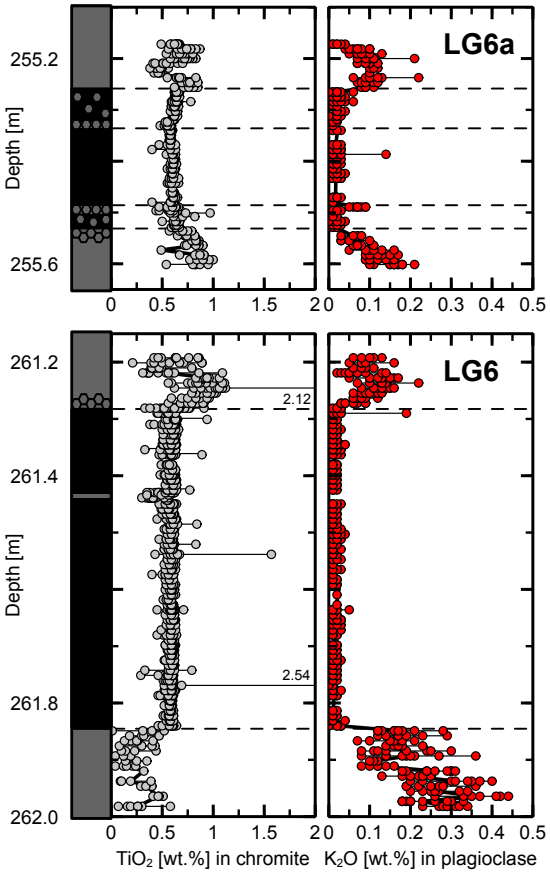

Figure 2.9: Variation in trace element composition for chromite and plagioclase in the LG6 and LG6a chromitite layers.

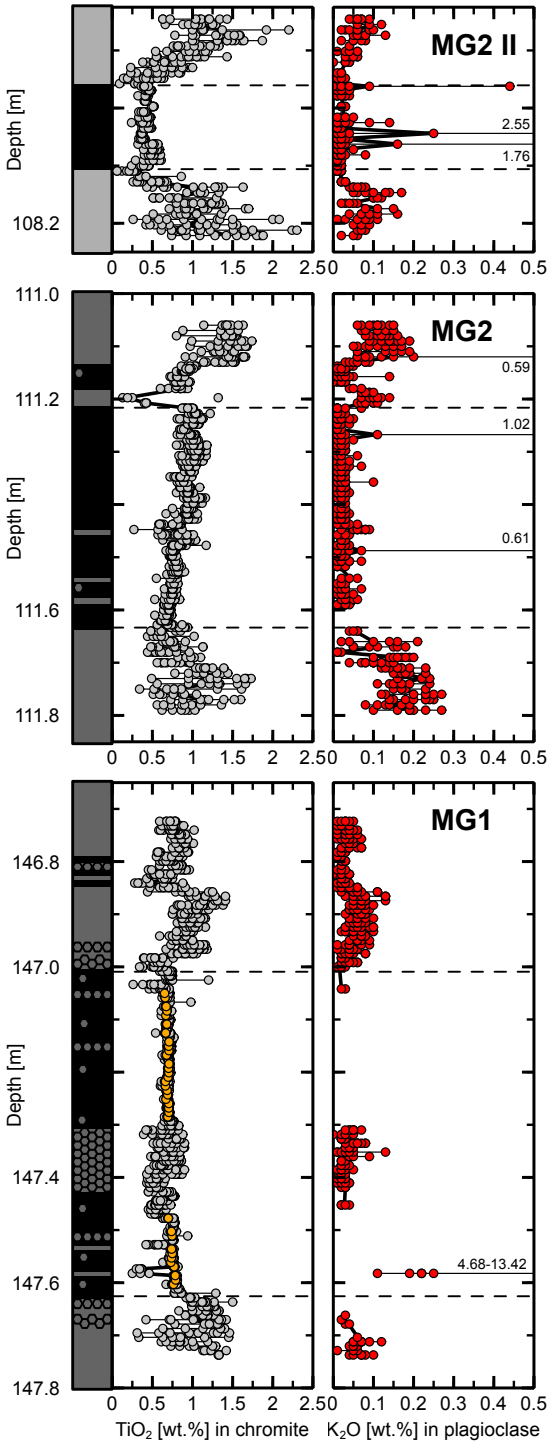

Figure 2.10: Variation in trace element composition for chromite and plagioclase in the MG1, MG2 and MG2 II chromitite layer. Orange symbols indicate chromite crystals entrapped in oikocrysts.

REE concentrations of orthopyroxene and plagioclase

REE concentrations in orthopyroxene and plagioclase were measured by LA-ICPMS in LG6a and MG2 chromitite layers. These two layers were chosen due to their textural diversity. REE concentrations of orthopyroxene of the MG1 chromitite has been discussed in Kaufmann et al. (2018). There was no attempt to make vertical profiles as for the microprobe study, but only selected points to represent the different sub-lithologies present. Our discussion here focuses on the REE composition because of their value in petrologic modelling. The REE patterns for orthopyroxene, normalized to a postulated parental magma B1 (Barnes et al., 2010), are shown in Figure 2.11. There is a difference in REE concentrations in interstitial orthopyroxene in the spotted chromitite and in orthopyroxene cumulus crystals from pyroxenite partings and wall rocks. The interstitial orthopyroxene has lower light REE concentrations compared to the other sublithologies. Moreover, the slope of the REE patterns varies: orthopyroxene in chromitites has a steeper slope towards the light REE. All of the REE patterns show a more or less pronounced negative Eu anomaly. Although continuous profiles were not measured, we find no significant enrichment or depletion in REE from bottom to top of the chromitite layers.

The REE partition coefficients for orthopyroxene and melt depend on temperature and this is shown in Fig. 2.12 by the curves for 800° and 1200 °C following Sun and Liang (2013) and Yao et al. (2012). By plotting the REE contents in orthopyroxene normalized to B1 composition (equivalent to an empirical distribution coefficient) the observed patterns can be directly compared with the predicted curves. There is good agreement in the shape of the observed and predicted patterns but the actual REE concentrations are consistently higher than predicted by simple equilibrium with B1 melt. This offset is attributed to post-cumulus fractionation of intersitial melt in the chromitite layers. Note that the shape of predicted REE patterns changes with temperature, being less steep at 1200° than at 800 °C.

The same approach is taken in displaying plagioclase REE data (Fig. 2.12), normalized to B1 melt composition to compare directly with mineral-melt partition coefficients for plagioclase between 800° and 1200 °C (from Bédard 2006). Plagioclase from all sublithologies in the LG6a samples shows parallel REE patterns and similar concentrations, whereby the plagioclase from partings and host rocks has more variable REE concentrations than in the spotted chromitite. Compared with the predicted REE patterns, the observed data show much higher REE enrichment and steeper slopes. The positive Eu anomaly (not well documented because of very low concentrations of middle and heavy REE) is not predicted by the REE partition models. However, plagioclase from the different sublithologies in MG2 has different and more variable REE concentrations and patterns than in LG6a. Plagioclase in partings and host rock of MG2 is similar to the LG6a plagioclase, whereas interstitial plagioclase in the main chromitite has much lower REE concentrations and plagioclase in spotted chromite has higher ones.

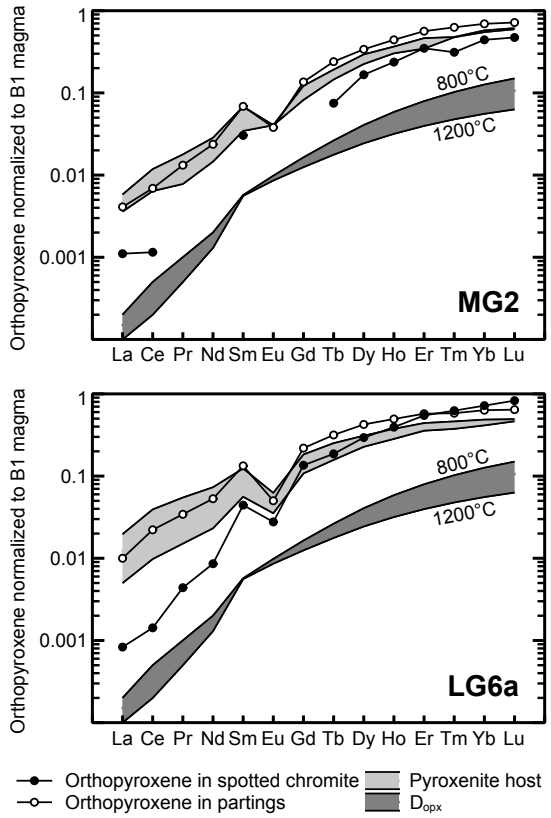

Figure 2.11: Orthopyroxene REE concentrations normalized to B1 magma (Barnes et al., 2010) for the LG6 and MG2 chromitite layers. Calculated partition coefficients (taken from Sun and Liang, 2013; Yao et al., 2012) are plotted for 800 °C and 1200 °C.

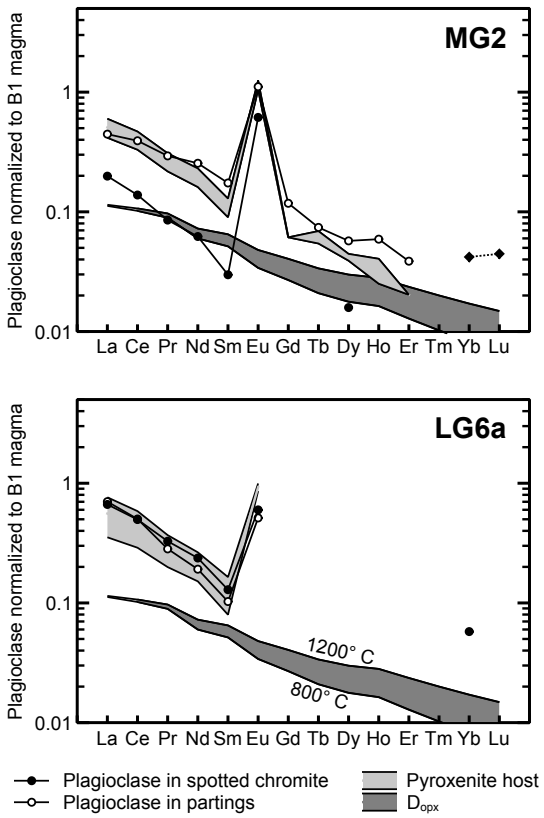

Figure 2.12: Plagioclase REE concentrations normalized to B1 magma (Barnes et al., 2010) for the LG6 and MG2 chromitite layers.Calculated partition coefficients (taken from Bédard, 2006) are plotted for 800 °C and 1200 °C.

2.4.3 PGE geochemistry and petrography of PGE and sulfide minerals

The whole-rock PGE+Au concentrations from 5 cm intervals of drillcore in the LG6, MG1 and MG2 chromitite layers are displayed on Figure 2.13. The average IPGE (Ru+Os+Ir; here Ru+Ir, Os was not measured) concentrations of the layers increase slightly, while the PPGE (Rh+Pt+Pd) contents increases progressively with stratigraphic height from the LG6 to the MG2 (Fig. 2.13a). C1-chrondrite normalized PGE distribution patterns (values taken from McDonough and Sun, 1995) display similar arch-shaped patterns with a peak at the normalized Rh concentrations and a decrease from Rh to Pd for the LG6-MG1 chromitites (Fig. 2.13b). On the contrary, the MG2 and MG2 II display a hump with higher Pt normalized concentrations and a steep drop towards Pd. All chromitite layers have S concentrations below the detection limit of 0.01 wt.%.

PGE concentration profiles along the chromitite layer show the highest concentrations near the bottom and/or upper contact (Figs. 2.14, 2.15). PGE contents are closely associated with the chromitite layers regardless of their specific thickness: the chromitite stringers overlying the MG1 and MG2 have higher concentrations than the enclosing hanging wall pyroxenite, whereas thick pyroxenitic parting in-between the MG1 chromitite depicts lower PGE concentrations. Pt/Pd ratios reveal the already stated differences in PGE geochemistry

of the LG6-MG1 (Fig. 2.14) chromitites compared to the MG2 and MG2 II (Fig. 2.15). The ratios of the former layers follow the concentration profiles, whereas the latter chromitites reveal a constant increase (MG2) or a steady decrease (MG2 II) downwards stratigraphy.

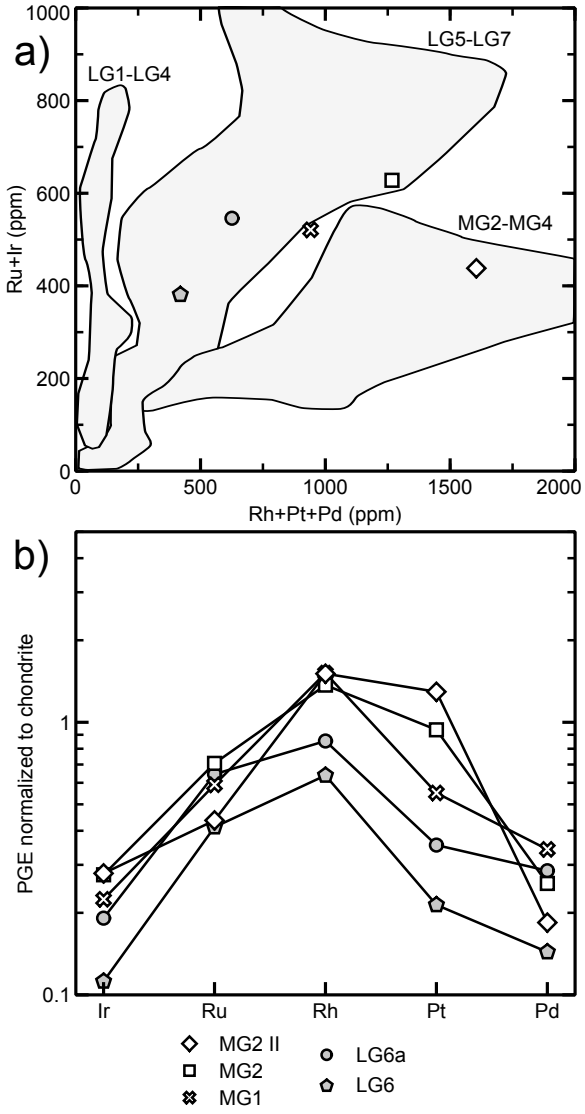

Figure 2.13: PGE distribution of the LG6 to MG2 II chromitites. **a** Averaged Ru+Ir versus Rh+Pt+Pd plot for the LG6-MG2 chromitites with indicated subdivision proposed by Teigler (1990). **b** Average chondrite normalized PGE distribution pattern for the investigated chromitite layers. C1-chondrite values are taken from McDonough and Sun (1995).

The PGM and base-metal sulfide assemblages in selected samples from the chromitite layers were determined by mineral liberation analysis (MLA (Fig. 2.16a). The results are subdivided into the following groups: cooperate-braggite-vysotskite series [(Pt,Pd)S], malanite series [$Cu(Pt,Rh)_2S_4$], PGE-Fe-Sn-alloys, laurite series [$(Ru,Ir,Os)S_2$], PGE sulfarsenides [(Pt,Rh,Ir)AsS] and PGE-Sb-Bi-Pb-alloys. The MLA output includes the areal percentage of the ore minerals as well as the grain count. While PGM assemblage of the LG6 and LG6a is dominated by PGM of the malanite series and laurite, the MG1 assemblage comprises mainly three groups, malanite, laurite and PGE sulfarsenides. The MG2 shows a more diverse PGE

mineralogy, with larger portions of PGE sulfides and additional PGE-Fe-Sn alloys, which are almost absent in the lower layers. The MG2 II is clearly dominated by laurite with additional minor amounts of PGE alloys, both Fe-Sn and Sb-Bi-Pb dominated.

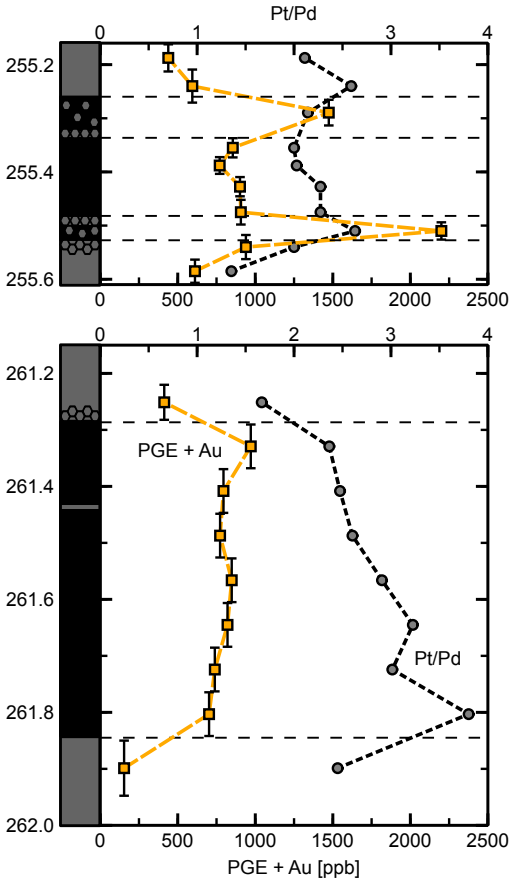

Figure 2.14: Whole rock PGE + Au (yellow symbols) and Pt/Pd ratios (grey symbols) of the LG6 and LG6a chromitites. Vertical bars indicate sample interval.

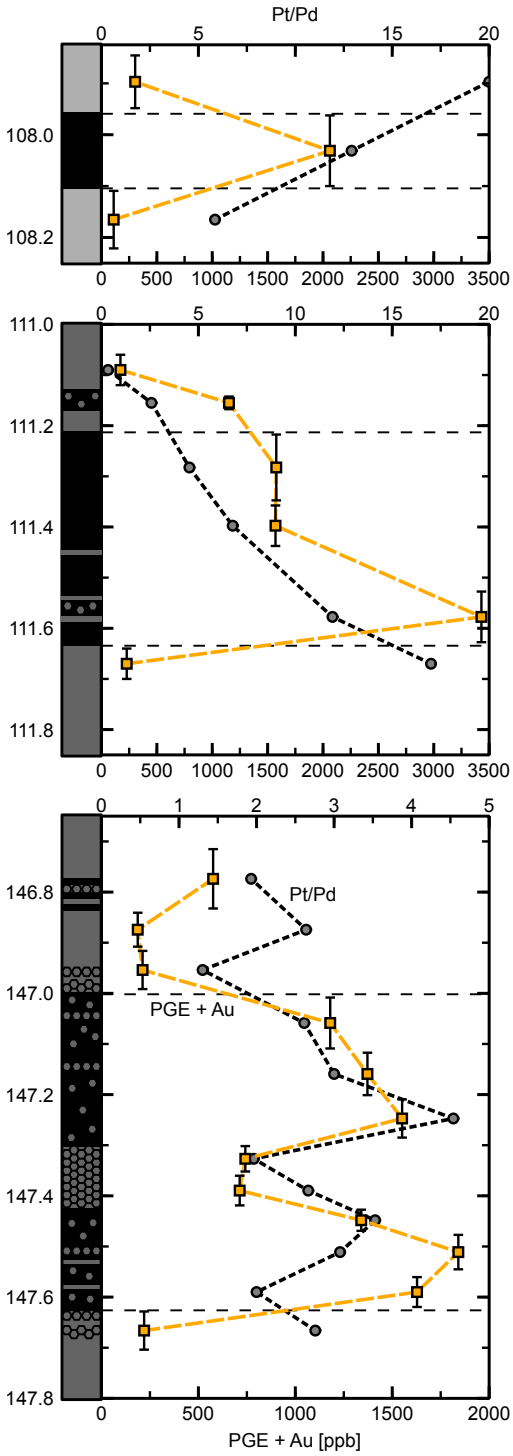

Figure 2.15: Whole rock PGE + Au (yellow symbols) and Pt/Pd ratios (grey symbols) of the MG1, MG2 and MG2 II chromitites. Vertical bars indicate sample interval.

The BMS assemblage was subdived in the following groups: chalcopyrite [$CuFeS_2$], chalcosite [Cu_2S], millerite [NiS], pentlandite [$(Ni,Fe)_9S_8$], pyrite [FeS_2] and pyrrhotite [$Fe_{1-x}S$, x=0 – 0.2], and violarite [$Fe^{2+}Ni_2^{3+}S_4$]. Notably, the MLA data of BMS reveal two different groups (Fig. 2.16b). The first one, which consists of the main LG6 to MG2 layers, is characterized mainly by pentlandite with minor proportions of chalcopyrite, pyrite/pyrrhotite and violarite. Contrary, the second group, the MG2 II, consists mainly of chalcosite, millerite and pentlandite; chalcopyrite, pyrite/pyrrhotite and violarite are absent.

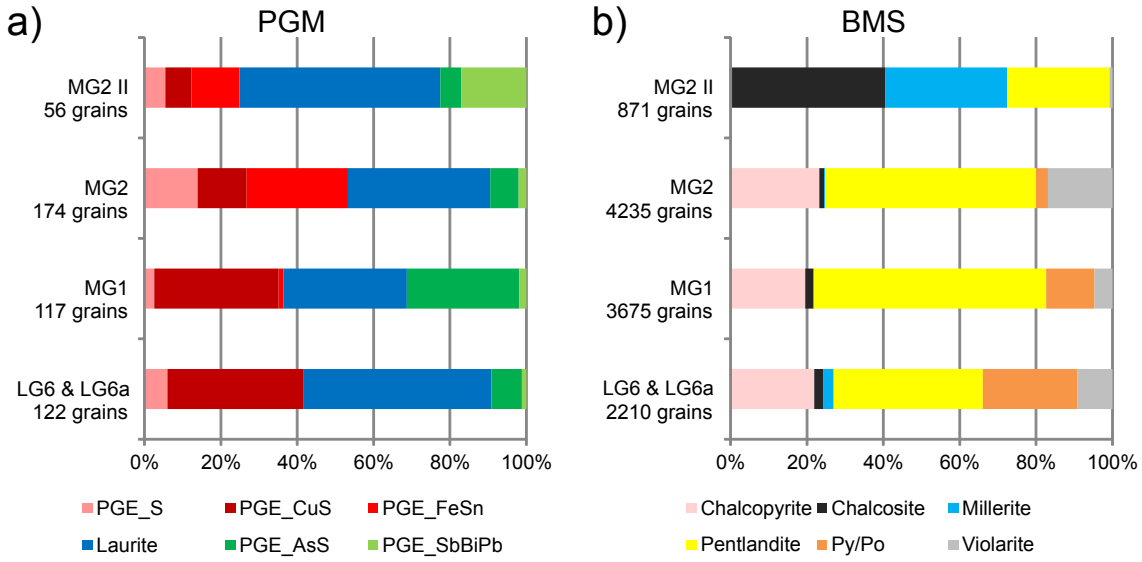

Figure 2.16: Stacked bar plots of **a** PGM proportions (area%) and **b** BMS (area%).

2.5 Discussion

2.5.1 Comparison of chromite and silicate chemistry with other studies of the Critical Zone

Systematic compositional variations of chromite and accompanying minerals, especially orthopyroxene, with stratigraphic height in the Critical Zone have been noted by many workers. A comprehensive early study by Cameron (1977) described compositional variations in mineral compositinos for 26 chromitite layers and sublayers in the eastern limb of the complex. Many of the layers in that study showed the same parallel increase in Mg# and Cr# for chromite in the seams relative to the surrounding pyroxenites, and much more variations in the latter, as we observed in the Thaba LG and MG layers. Naldrett et al. (2012) provided an important summary of chromitite chemical compositions in the Critical Zone that combined information from all sections of the complex and included their PGE variations. The study documented systematic changes in chromite and orthopyroxene compositions upward through the sequence from LG1 to UG2, and emphasized several reversals in trend. For the part of the profile of relevance to this study, Naldrett et al. (2012) found that orthopyroxene and chromite both show systematic decreases Mg# upwards, and this is accompanied by a parallel decrease

in the Cr/(Cr+Al) ratio (Cr#) in chromite. The authors explained these trends by fractional crystallization of mainly orthopyroxene, driving the melt to lower Cr and Mg contents, but higher Al and Fe concentrations. It is worth mentioning that chromite in other layers of the Critical Zone show different trends, whereby the upward decrease in Mg# is matched by an increase in Cr# of chromite. Naldrett et al. (2012) attributed this behavior to a process that prevents depletion of Al in the evolving melt, either recharge of magma or co-precipitation of plagioclase. Our observations from the LG6 to MG2 II layers at Thaba mine are consistent with the other studies. First, chromite and orthopyroxene in chromitite layers has a distinct and more primitive composition compared to those in the host rocks (Figs. 2.7, 2.8). Within the chromitite layers, the minerals show rather relative homogeneous composition (in contrast to the scatter in host rocks) but they show a slight differentiation trend to lower Mg# and Cr# upwards. In the vertical sequence from LG6 to MG2, all main phases follow a general differentiation trend of decreasing Mg# and Cr#. In addition, minor element compositions of chromite and plagioclase follow the described vertical differentiation trend. Thus, TiO_2 concentration in chromite and K_2O in plagioclase gradually increase upwards through the stratigraphy.

2.5.2 Comparison of PGE concentrations and ore minerals with other studies of the Critical Zone

The chromitite layers from the ZK135 core (LG6-MG2) have similar elevated PGE concentrations relative to values reported by Scoon and Teigler (1994) from the same layers in the Union section, which is also in the northwestern limb. The enriched nature of chromitites in PGE compared to background concentrations of the host pyroxenite is a general feature, independent of the layer thickness. Even mm-thick stringers (for instance the stringers overlying the MG1 layer) are enriched in PGE. The reason for this association of PGE with chromitite remains enigmatic (e.g. Godel, 2015).

The PGE distribution in LG6 to MG2 II layers from Thaba mine are compared on Figure 2.13a with data from the nearby Union section reported by Teigler (1990). This plot explores the distinction in enrichment between the IPGE (Y-axis) and PPGE (X-axis). It has been reported that the overall increase in total PGE contents with height in the Critical Zone chromitites is mostly due to higher PPGE contents whereas the IPGE contents stay relatively constant (Lee and Parry, 1988; Naldrett and von Gruenewaldt, 1989; Scoon and Teigler, 1994). This is not the case for the Thaba mine. Here, the LG6 and LG6a from this study agrees with the field for LG5-LG7 of Teigler (1990) but the MG2 and MG2 II layers at Thaba mine have higher IPGE and lower PPGE contents relative to Teigler (1990). Normalized PGE distribution patterns (Fig. 2.13b) illustrate the different geochemical character of the MG2 and MG2 II layer relative to the underlying chromitites more clearly. The LG6-MG1 layers have an arch-shaped pattern with a narrow peak and high normalized Rh concentrations, while the overlying MG2 and MG2 II display broader peak and elevated Pd concentrations. Kottke-Levin et al. (2009) reported similar differences between the MG0-MG1 and the MG2 for the southern part of the eastern limb.

Where researchers have analyzed PGE distribution within single chromitite layers, which has been done mostly for the UG2 layer, it is found that the grades are distributed bimodally, with the highest concentrations at the base and/or upper contact (e.g. McLaren and De Villiers, 1982; Gain, 1985; Voordouw et al., 2009; Voordouw et al., 2010; Junge et al., 2014; Osbahr et al., 2014). The LG and MG layers in the Thabe mine also show significant internal variations and enrichments at hanging and/or footwalls (Figs. 2.14, 2.15).

The variations in the PGE geochemistry are also reflected in the PGM and BMS assemblage (Fig. 2.16). The LG6, LG6a and MG1 chromitite layers depict a similar character, dominated by the malanite series, laurite and PGE sulfarsenides; alloys are largely absent. On the contrary, the MG2 and MG2 II layers depict higher amounts of alloys (Fe-Sn and Sb-Bi-Pb dominated). PGM assemblages of the LG6-MG2 layers were recently reported by Oberthuer et al. (2016) for the western limb and Junge et al. (2016) for the eastern limb. They described similar distribution patterns for the LG6 relative to the LG6 and LG6a layers of the Thaba mine area. The MG1 and MG2 PGM assemblage described by Oberthuer et al. (2016) and Junge et al. (2016) are similar to those of their LG6 layer, on the contrary the PGM distribution of the MG 2 chromitites described by our study differs from those of the LG6, LG6a and MG1 (Fig. 2.13b, 2.16b). Moreover, the PGM and sulphide distribution of the MG2 II differs from those of the underlying chromitites. The MG2 II also depicts a differing chromite composition (Fig. 2.6) and is situated in pegmatoidal pyroxenite, indicating either post-cumulus alteration of the PGM and sulphide assemblage or an more primitive character.

2.5.3 Post-cumulus modification

Textural changes

Post-cumulus modifications of the textures and composition of primary accumulated chromitite are a widely known and reported phenomenon in the Bushveld Complex (e.g. Cameron, 1969; Cameron, 1975; Hulbert and von Gruenewaldt, 1985; Sparks et al., 1985; Nicholson and Mathez, 1991; Penberthy and Merkle, 1999; Kottke-Levin et al., 2009; Junge et al., 2014; Kaufmann et al., 2018). The variety in reported textures in the LG and MG chromitites indicate different degrees of textural modification. The primary texture of a chromitite that is controlled only by the interplay of growth and nucleation rates in a magma is typically modified by mechanical processes like compaction and grain sorting, or by chemical processes of grain coarsening. CSD analyses provide a way to assess the extent of these modifications. The closest approximation to the original cumulus texture may be the chromite grains preserved in orthopyroxene oikocrysts. The CSD curve for chromite in oikocrysts from MG1 (Fig. 2.4g) approximates the straight-line trend expected for simple magmatic crystallization (nucleation-growth rate control). This is in contrast with the CSD curve for nearly monomineralic massive texture of chromitite surrounding the oikocrysts (Fig. 2.4e). That curve is rotated relative to the former one, representing the case of grain coarsening and a reduction in the population density of small crystals (Higgins, 2015).

Compaction in a crystal mush is a process that has been proposed for several layered intrusions (Sparks et al., 1985; Shirley, 1986; Mathez et al., 1997; Meurer and Boudreau, 1998b; Boorman et al., 2004). However, for the Bushveld chromitites, Holness et al. (2017b)

and Holness et al. (2017a) argued that the crystal mush would be too thin for significant mechanical compaction. This can be tested by the CSD results. On a CSD diagram the mechanical reorganization caused by compaction increases the intercept value while the CSD slope stays constant (Higgins, 2002) and continued compaction results in a decrease in the smaller grain fractions. One way to test for compaction, sorting, and other mechanical effects including deformation, is to analyse the spatial distribution of grains, expressed by the R-value and shown in Figure 2.5c plotted against porosity (as 100 - vol.% chromite). Jerram et al. (1996) stated that mechanical compaction (i.e., grain re-arrangement) would increase the R-value, while deformational compaction (grain deformation) leads to a decrease in the R-value. With reference to the vectors on Fig. 2.5c, the distribution of Thaba mine chromite follows the proposed trend for grain overgrowth (i.e., coarsening), and is not consistent with the other processes shown. With respect to deformational compaction, Kaufmann et al. (2018) found no evidence of dislocation creep in the MG1 chromitite. These arguments show that mechanical or deformational compaction was insignificant, or that any evidence of it was erased by textural equilibration related to grain coarsening and overgrowth (i.e. adcumulus growth). This is supported by the spatial distribution plot (Fig. 2.5c) where both the spotted and massive chromite textural types plot parallel to the 'overgrowth' vector, which reflects a reduction in porosity accompanied by a slight increase in the nearest neighbor distance R.

Adcumulus growth was followed by textural equilibration, whereby small crystals are dissolved at the expense of the growth of larger ones. The rate of equilibration is closely correlated with the temperature and the rate of cooling. Crystals held close to the liquidus temperature equilibrate significantly faster than in an undercooled scenario (Higgins, 2002). All CSD curves of massive chromitite show characteristics of textural equilibration, specifically rotation of the curve and reduction in smaller grain size (Fig. 2.5). Textural equilibration also resulted in the smoothing of grain boundaries and 120° triple junctions (Fig. 2.2e) (Thomson, 1887; Bulau et al., 1979; Holness, 2005; Holness et al., 2007). Chromite grains in spotted chromitite show textural equilibration to a lesser extent, because the initial grain size was protected from post-cumulus equilibration due to the surrounding oikocrysts (Kaufmann et al., 2018).

Chemical modification

Classical concepts of cumulate rock petrology envision post-cumulus re-equilibration to start after settling of cumulus crystals effectively stops and the mineral grains are arranged into mechanically stable packing. According to theoretical models of random packing of single grains, this stage is reached at about 50–60 vol.% crystals, which agrees with the observed chromite mode in poikilitic orthopyroxene from MG1 (Kaufmann et al., 2018). As the interstitial melt crystallises with further cooling, grain coarsening and overgrowth develops in parallel with possible mechanical compaction (see previous section), resulting in a fully solidified rock, that commonly has a higher chromite mode. In the case of a slow-cooling intrusion, post-cumulus crystallisation proceeds over a significant temperature interval and then the interstitial melt must re-equilibrate with cumulus crystals in response to the falling temperature. There is an important difference in the chemical evolution of the mineral-melt

system between a cumulate crystal-mush layer and the magma reservoir above it. This is due to the high crystal-to-liquid mass ratio in the former, which imposes more thermal and chemical buffering of mineral-melt reactions than in a liquid-dominated system where crystals are removed by settling (Barnes, 1986b; Meurer and Claeson, 2002; Namur et al., 2014).

The case of a chromitite mush presents a special case where the main cumulus phase (chromite) has an extremely low solubility in the liquid and therefore actively reacts with the liquid and all other cumulus phases. This crystallization sequence of this system has been studied experimentally using the parental B1 magma composition, variable fO_2 and pressures from atmospheric to 0.3 GPa (Cawthorn and Davies, 1983; Sharpe and Irvine, 1983; Barnes, 1986a; Cawthorn and Biggar, 1993). These studies show that the B1 liquid starts to crystallize olivine and Cr-spinel at about 1300 °C, low-Ca pyroxene joins between 1250° and 1210 °C (depending on fO_2 and pressure) and plagioclase appears at 1160–1150 °C. During this sequence, the MgO content in B1 liquid drops from the initial 12–13 wt.% to 4 wt.% at the onset of plagioclase crystallisation, and the solubility of Cr_2O_3 (at fO_2 = FMQ) decreases from an initial 0.15 wt.% to 0.05 wt.% (Barnes, 1986a). These experimentally determined constraints can be used as a reference for post-cumulus crystallisation.

However, the situation in the Bushveld magma chamber was apparently complicated by numerous episodes of magma mixing and recharge that are evidenced, among other things, by variations in Sr isotope compositions and reversals in Mg# of cumulus orthopyroxene throughout the Critical Zone stratigraphy (Kinnaird et al., 2002; Schannor et al., 2018). The important implications of this are that crystallization did not take place in a closed-system as modelled by experiments, and the interstitial liquid in the chromitite layers may have differed from the main B1 melt right from the start of post-cumulus evolution. In any case, evidence is strong that the interstitial liquid in chromitite did not follow the experimentally - determined path of B1 crystallisation. The first sign of this is the absence of interstitial plagioclase in MG1 samples from the ZK135 borehole. Experiments predict plagioclase formation from an evolved interstitial melt and indeed, interstitial plagioclase crystals are observed in the LG6 and MG2 chromitite as well as in the pyroxenite host rocks, but this is not true for MG1 and apparently, either plagioclase did not crystallise at all or was consumed by a peritectic reaction. Note that Kaufmann et al. (2018) reported remnants of olivine in core zones of orthopyroxene oikocrysts, which implies an extensive olivine-orthopyroxene peritectic reaction and is another sign of a distinctly different evolution trend of the interstitial liquid.

The high mass proportion of chromite relative to orthopyroxene and to the intercumulus liquid, at least initially, imposed strong buffering effect on the Fe-Mg exchange between the solid and liquid phases. It was recognised long ago and is demonstrated again in this study that Mg# of both chromite and orthopyroxene are much higher in chromitite layers than in the pyroxenite partings and host rocks within and around them (Figs. 2.7, 2.8). The importance of mass balance for chemical re-equilibration at the post-cumulus stage is emphasized in the concept of the trapped liquid shift effect (Barnes, 1986b; Cawthorn, 2013; Cawthorn, 2015). This effect relates to reaction between the interstitial, 'trapped' liquid and the cumulus crystals. Given the buffering effects on major elements by chromite, pyroxene and plagioclase, the trapped liquid shift effect is best shown by trace elements. The

concentrations of incompatible trace elements in the liquid are by definition higher than in cumulus minerals, and they continue to increase during post-cumulus crystallization. Thus, mineral-liquid re-equilibration and solid state diffusion in the late stages of crystallization may enrich cumulus minerals in incompatible trace elements, and this effect will be greatest for minerals with the lowest mineral-to-liquid mass ratio. Trace element analyses of interstitial orthopyroxene and plagioclase in the LG6a and MG2 layers (Figs. 2.11, 2.12) show that both phases are enriched in REE and other incompatible elements with respect to predicted equilibrium partitioning with the postulated parental B1 magma. The enrichment is generally in agreement with the trapped liquid shift model and similar observations were reported by Cawthorn (1996), Godel et al. (2011), Cawthorn (2013), Veksler et al. (2015; 2018). However, the trapped liquid shift model does not fit all observations and the reason is the assumption of closed system conditions, which, as noted above, is disproved by variations in Sr isotope ratios among other evidence. The study of Thaba mine MG1 by Kaufmann et al. (2018) showed that the incompatible element concentrations in chemically zoned orthopyroxene oikocrysts are inconsistent with crystallisation in a closed system and require influx from outside the layer. In addition, assessment of the chromite composition illustrates the limitations of the trapped liquid shift effect for the investigated layers. In a closed system the extent of chemical re-equilibration depends on the respective amounts of trapped liquid (Barnes, 1986b), which subsequently crystallise intercumulus silicates. However, the chromite composition is mainly independent of the modal proportion of chromite as Figure 2.6b demonstrates.

Another case of open-system behavior discussed in detail by Veksler et al. (2015) is the selective migration of elements across layer boundaries due to electrochemical potential gradients. Reactions of chromite with the liquid and with other solid phases in the mush involve elements with variable valence, most importantly Fe and this may lead to significant electric potential gradients between the mush and surrounding rocks and a driving force for electrochemical transport through the interstitial melt. Such transport will be selective because of differences in the diffusion rates of metal cations and their effectiveness as charge-carriers. Veksler et al. (2015) reported a marked decoupling of alkalis and other incompatible lithophile elements in the UG2 chromitite, and similar features are found in this study, for example the depletion of intercumulus plagioclase in K, and the high An content of the plagioclase oikocrysts in LG6 and LG6a layers (removal of Na).

2.5.4 Relict magmatic features and implications for chromitite formation

From the discussion of post-cumulus modification of textures and mineral compositions described above, we identify the following features that are considered to best reflect the original characteristics of the chromitite crystal layer. It is these features that can be used for discussing the magmatic processes that operated to produce the chromitites and surrounding silicate layers:

1. Mineral composition of chromite within chromitites (Figs. 2.6, 2.7 and 2.8)

2. Lithostratigraphic columns (Fig. 2.2)

3. Textural characteristics, especially CSD curves of massive and spotted chromitite (Figs. 2.4, 2.5)

The chromitite layers in the Bushveld Critical Zone are known to show a generalized upwards fractionation, which is evidenced, among other features, by changes in Mg# of orthopyroxene and Cr# of chromitite. This overall trend is interrupted by repeated reversals linked to replenishing events (Cameron, 1978; Cameron, 1980; Eales and Cawthorn, 1996; Eales and Costin, 2012). More specific to our study, Naldrett et al. (2009) and Naldrett et al. (2012) showed that chromite in the upper LG series (above LG5) and the MG layers display a parallel decrease in Mg# and Cr# upwards, which they termed fractionation trend (see above and Naldrett et al., 2009; Naldrett et al., 2012). In addition, chromite has significant compositional variations within single layers. The LG6 chromitite is characterized by a constant decrease in Mg# upwards, while the LG6a and the MG2 layers show repeated decreasing Mg# and reversals at pyroxenite partings. We suggest that these systematic within-layer variations can hardly be explained by post-cumulus changes, especially considering that chromite forms 60 to 90 vol.% of the rock. Instead, the trends are attributed to magma replenishing events, which caused the initial accumulation of chromite, followed by subsequent differentiation. Similar observations were made by other authors for the UG2 chromitite (Junge et al., 2014; Cawthorn, 2011; Latypov et al., 2017b), who proposed that the UG2 represent a composite layer assembled from multiple magma injections followed by a fractionation interlude. In addition, PGE distribution in LG6 to MG2 II layers shows similar fractionation trends as it has been already discussed above.

Numerous models have been discussed to account for the accumulation of chromitite layers in layered intrusions (Cawthorn, 2015; Namur et al., 2015; Latypov et al., 2017b), however, no consensus has been reached on this debate. The existing models can be subdivided by their emphasis on the following three principal mechanisms: (1) **Gravity-driven crystal settling** from chromite oversaturated magmas due to e.g. magma mixing or fluctuations in pressure (Irvine, 1975; Irvine, 1977; Lipin, 1993; Scoon and Teigler, 1994; Schoenberg et al., 1999; Kinnaird et al., 2002; Cawthorn, 2005; Spandler et al., 2005; Naldrett et al., 2009; Cawthorn, 2011), (2) ***In situ* crystallisation** at the crystal mush-magma interface (O'Driscoll et al., 2010; Latypov et al., 2013; Latypov et al., 2015; Latypov et al., 2017b) and (3) accumulation by **crystal-rich slurries** (Eales, 2000; Mitchell and Scoon, 2007; Mondal and Mathez, 2007; Voordouw et al., 2009; Eales and Costin, 2012; Maier et al., 2013; Mungall et al., 2016). In the following we describe how the observations from LG and MG layers in the Thaba mine help contribute to assessing these hypotheses.

As described above, the within-seam variations especially of the chromite chemistry found in this study, and reported by other workers from the UG2 layer, suggests that chromite crystallized from repeated injections of intruding magma. Moreover, the compositional similarity of chromite in the footwall and hanging wall of chromitite seams questions any model which involve magma mixing, where one would expect a compositionally different hanging wall. Similar observations and conclusions were previously reported and drawn for the UG2 (Mondal and Mathez, 2007; Latypov et al., 2017b). Lithostratigraphic columns

(Fig. 2.2) indicate that the mechanism, which resulted in chromite crystallization, had to operate relatively fast and repeatedly, in order to switch crystallization 'on' and 'off' and thus form distinct mm-thick pyroxenitic partings within the main chromitite and small chromitite stringers in the silicate host rocks. Again, this feature can be explained by repeated magma replenishing events. Additional constrains can be identified by textural assessments of chromite enclosed in oikocrysts, which preserved their original grain size (Kaufmann et al., 2018), reveal no systematic change in grain size across the chromitite layers (e.g. fining upwards). However, systematic fining upwards would be expected for chromite accumulation by crystal slurries (Maier and Barnes, 2008; Eales and Costin, 2012; Maier et al., 2013) or crystal settling on a large intrusion-wide scale and thus contradict such models.

Taken all chemical and textural evidence from the Thaba LG and MG layers together, we conclude that accumulation of chromite fits neither the cumulate slurry model, nor the idea of crystal settling on a large scale from a single magma chamber, nor does dominated magma mixing fit the observations from the investigated layers. Compositional variations in the chromite chemistry indicate repeated replenishing events within single layers followed by subsequent fractionation. We envisage an evolving system where chromite crystallization was repeatedly initiated by events of magma replenishment from a 'staging chamber' deeper in the crust or upper mantle (e.g. Eales, 2002; Harris et al., 2005; Roelofse and Ashwal, 2012; Zeh et al., 2015). Latypov et al. (2017; 2018) proposed that the pressure drop during ascent of magma (B1) from a staging chamber might be enough to shift phase relations in the basaltic system and trigger chromite crystallization. This model offers a suitable explanation for many of the chromitite characteristics and, importantly, it does not rely on a km-thick magma column as in many simple models of the Bushveld Complex (Cawthorn and Walraven, 1998). Instead, it favors relatively thin layers of magma overlying the cumulate successions, which become expelled from the magma chamber. This interpretation is also consistent with studies on silicic magma bodies which are typically interpreted as reservoir comprising a crystal mush with only small proportions of liquid magma (Blundy and Annen, 2016; Cashman et al., 2017; Cooper, 2017).

2.6 Summary and conclusions

Detailed vertical variation in mineral chemistry, texture and PGE enrichment and assemblage along 5 layers of the LG and MG chromitites were reported. Our integrated approach offers insights in the textural and compositional petrogenesis and mineralization of chromitites of the Bushveld Complex.

All chromitites depict elevated whole-rock PGE concentrations, regardless of their specific thickness, even mm-thick stringers are enriched in PGE compared to their silicate host rocks. These concentrations increase upwards stratigraphy following the fractionation trend illustrated by the mineral chemistry of chromite. PGE concentration profiles are typically arch-shaped along the chromitite layers with highest concentrations near the bottom and/or upper contacts. The variations in PGE concentrations are reflected in the PGE assemblage,

quantified by MLA. Two principal groups could be distinguished: the LG6, LG6 and MG1 are characterized by malanite, laurite and PGE sulfarsenides, while the MG2 and MG2 II layers are dominated by laurite, PGE sulfides and Pt-Fe-Sn and PGE-Sb-Bi-Pb alloys. The reason for these variations might be the post-cumulus redistribution of PGE and BMS in the chromitite crystal mush.

Variations in composition and texture along all layers suggest that post-cumulus changes played an important role in the petrogenesis of the investigated chromitites and could be of economic importance due to possible redistribution PGE. Two typical types of chromite texture were described, spotted chromitite, where chromite crystals are overgrown by silicate oikocrysts and coarse-grained, which comprises large parts of the MG2 and MG2 II layers and massive chromitite, which is the dominated type in the LG and MG1 layers. Textural analyses by CSD curves and spatial distribution data suggest that the latter type were coarsened by a combination of adcumulus growth and textural equilibration. Contrary, the spotted chromites were protected by oikocrysts and thus retained their original size. Spatial distribution data indicates that compaction of the crystal mush played only a minor role. Chemical re-equilibration of cumulus crystals with the interstitial liquid have been proposed for different layers in the Bushveld Complex. Similar changes were observed in the LG and MG chromitites. However, contrary to previous studies, we attribute these post-cumulus modifications to influxes of different melts from outside the layers in an open system, instead of chemical re-equilibration in a closed one.

2.7 Acknowledgements

This research was supported by the German Federal Ministry of Education and Research (BMBF) in the framework of the R&D cooperative project AMREP (applied mineralogy for resource efficiency of platinum metals). This study was made possible by drill cores provided by Cronimet Chrome Mining SA (Pty) Ltd. We thank M. Hill and the Cronimet staff for access to mine data and for permission to publish the results. We are grateful to K. Born and P. Czaja for their support at the SEM and electron microprobe at the Museum für Naturkunde Berlin, assistance with the LA-ICP-MS analyses at the Leibniz University of Hannover by M. Oeser-Rabe and S. Schuth is highly appreciated. Helpful discussions with L.N. Hepworth on parts of an early version of the manuscript are greatly acknowledged.

Chapter 3

Lateral geochemical variations in the Lower Group and Middle Group chromitites, Thaba Mine, Bushveld Complex

3.1 Introduction

Chromitite layers of the Lower Group (LG) and Middle Group (MG) of the Bushveld Complex are the world's main reserves of Cr. In addition, all layers have typically elevated concentrations of Platinum-group elements (PGE), although these concentrations are currently subeconomic (e.g. Naldrett and von Gruenewaldt, 1989; Scoon and Teigler, 1994). This study focuses on the lateral geochemical variations of the upper LG and lower MG chromitites of the Thaba Mine area. The Thaba Mine, located in the north-western part of the Bushveld Complex (Fig. 2.1), is currently operating on Chromium extraction of the upper LG and lower MG chromitites, although the potential to extract PGE as by-product is investigated in the joined project of AMREP.

The chromitite layers of the Busvheld Complex are typically described as lateral continuous (e.g. Eales and Cawthorn, 1996; Cawthorn, 2015), however lateral changes in the structural and compositional character of chromitites have previously been described (e.g. Klemm et al., 1985; Scoon and Teigler, 1995), here, the authors argued for repeated replenishment events. Thus, tracing lateral changes might offer valuable insights into the magmatic events involved in the chromitite petrogenesis and were investigated in this study by evaluation and interpretation of a drill core and assay data set.

3.2 Study material

This study is based on an extensive data set provided by Cronimet Chrome Mining (Pty.) Ltd., which consists of core logs of over 400 drill cores and assays of the LG6, LG6a and MG chromitites. The LG and MG chromitites in the Thaba Mine dip to the southeast with angles between 15°–27°, are well developed and of rather constant thickness. The investigated chromitite layers crop out in the north-eastern part of the Thaba mine, where the open pit is currently in operation. This area is also severely weathered ('weathered zone'), thus any chemical data should be evaluated with caution. Towards the south chromitites reach depth of ca. 650 m (Fig. 3.1). The complete mining area covers ca. 14 km along strike (SW to NE) and ca. 2 km along dip (SE to NW) and is cut by several faults and dykes, an IRUP (Iron-Rich Ultramafic Pegmatite, e.g. Scoon and Mitchell, 1994) is located in the north-eastern part of the mine. For this study the Thaba mine area was subdivided into five sectors (I–V, from the

SW to the NE), which are separated by faults and the IRUP (Fig. 3.1). Drill core samples of the LG6, LG6a, MG1 and MG2 layers were analysed for the main elements (Cr, Fe, Si, Mg, Al, Ca and P) and PGE (without Os). Assays were conducted on crushed chromitite whole rock samples including pyroxenitic partings, therefore analyses with SiO_2 concentrations exceeding 10 wt.% were omitted to ensure comparability within the data set.

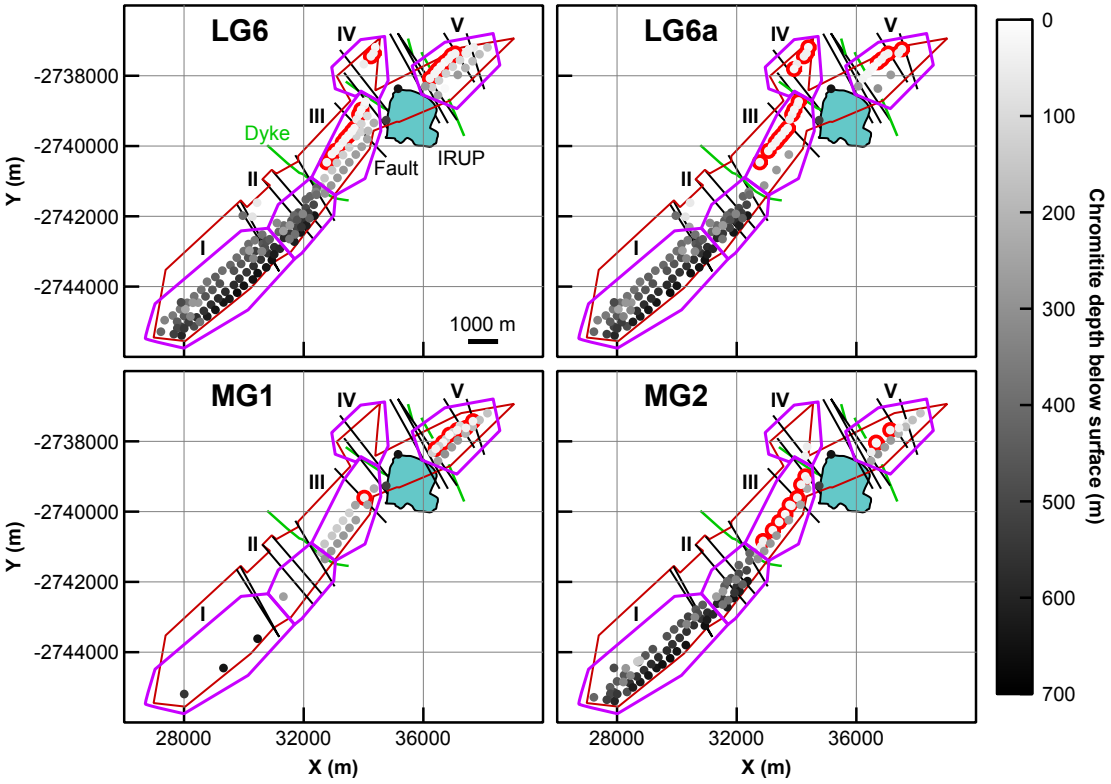

Figure 3.1: Chromitite depth of the investigated layers. Chromitites crop out in the northern part and dip to the southeast. They are cut by several faults, dykes and an IRUP. Chromitites close to the surface (<40 m), which are in the potentially weathered zone are marked by red circles.

3.3 Results and Conclusion

Caluclated whole-rock Mg# (atomic ratio, $Mg/(Mg+Fe^{tot})$) and Cr# (atomic ratio, Cr/(Cr+Al)) are rather uniform in the LG6 and LG6a, with exceptions in the weathered zone (Figs. 3.2 and 3.3), which has lower Mg#. Contrary, assays of the MG2 show that sector III has a differing composition. Here, calculated Mg# are lower and Cr# depict higher values. However, this geochemical difference is only apparent in a few drill cores below the weathered zone, thus these differences should be treated cautiously. The source for these lateral variation remains uncertain, but could possibly be explained by changes in the chromite chemistry or different modal contents of intercumulus silicates. The typical intercumulus assemblage consists of plagioclase and orthopyroxene (Chapter 2), thus an increase in the proportions of intercumulus silicates would result in Si enrichment. However, Si concentrations are rather uniform in the MG2 (Figs. 3.4), suggesting a change in chromite composition. The reason for these changes could be lateral variations in the thickness of the magma sheet on-top of the crystal mush. These changes would result in compositional changes in crystallising chromite.

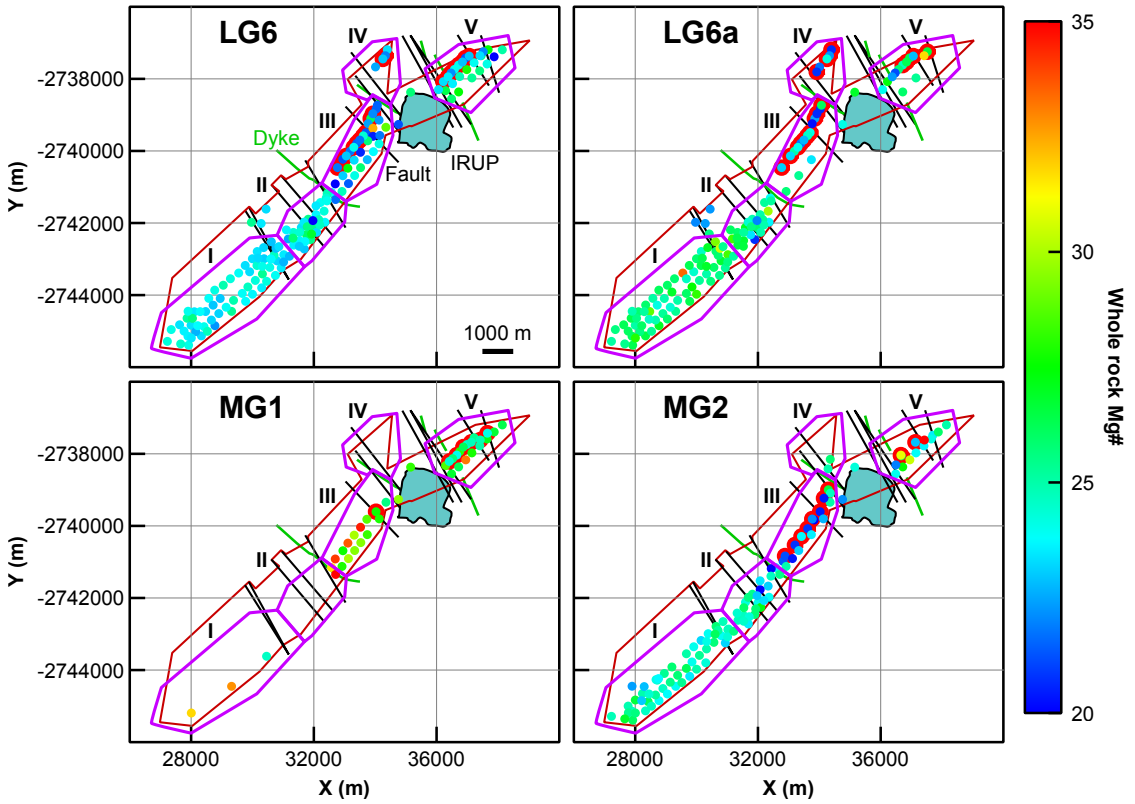

Figure 3.2: Whole-rock Mg# of the LG6-MG2 chromitite layers, chromitites close to the surface (<40 m), which are in the potentially weathered zone are marked by red circles.

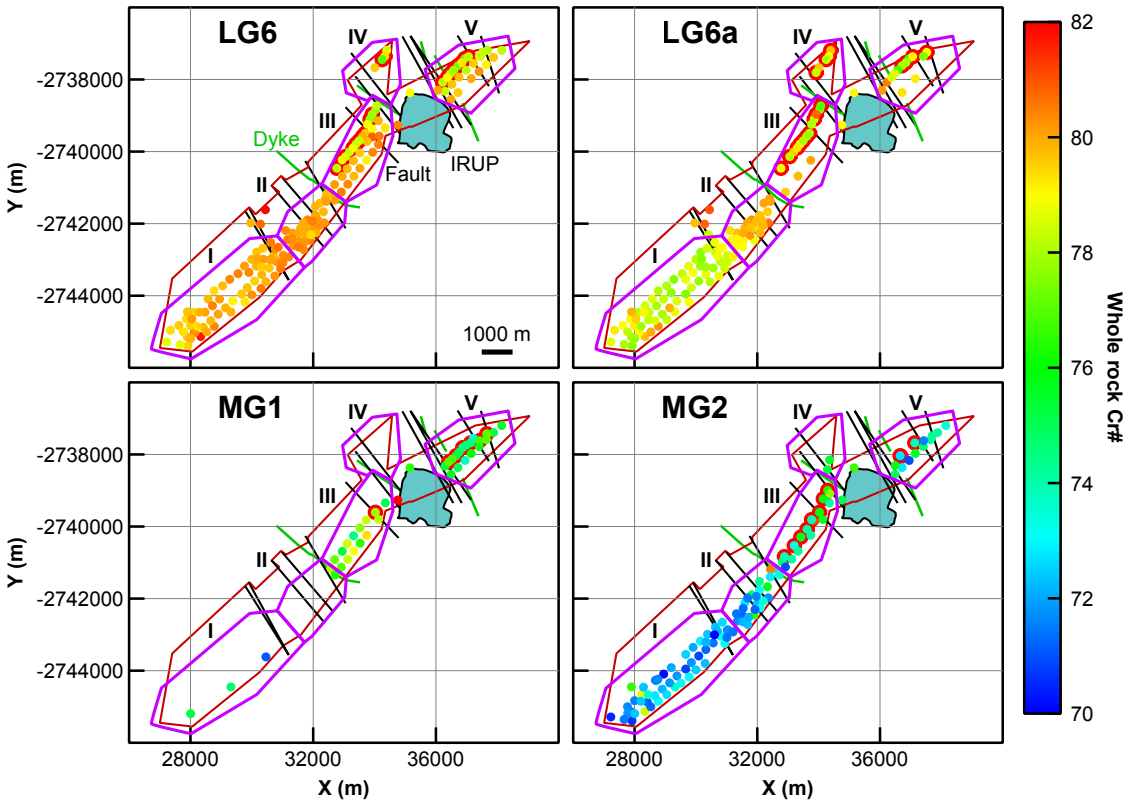

Figure 3.3: Whole-rock Cr# of the LG6-MG2 chromitite layers, chromitites close to the surface (<40 m), which are in the potentially weathered zone are marked by red circles.

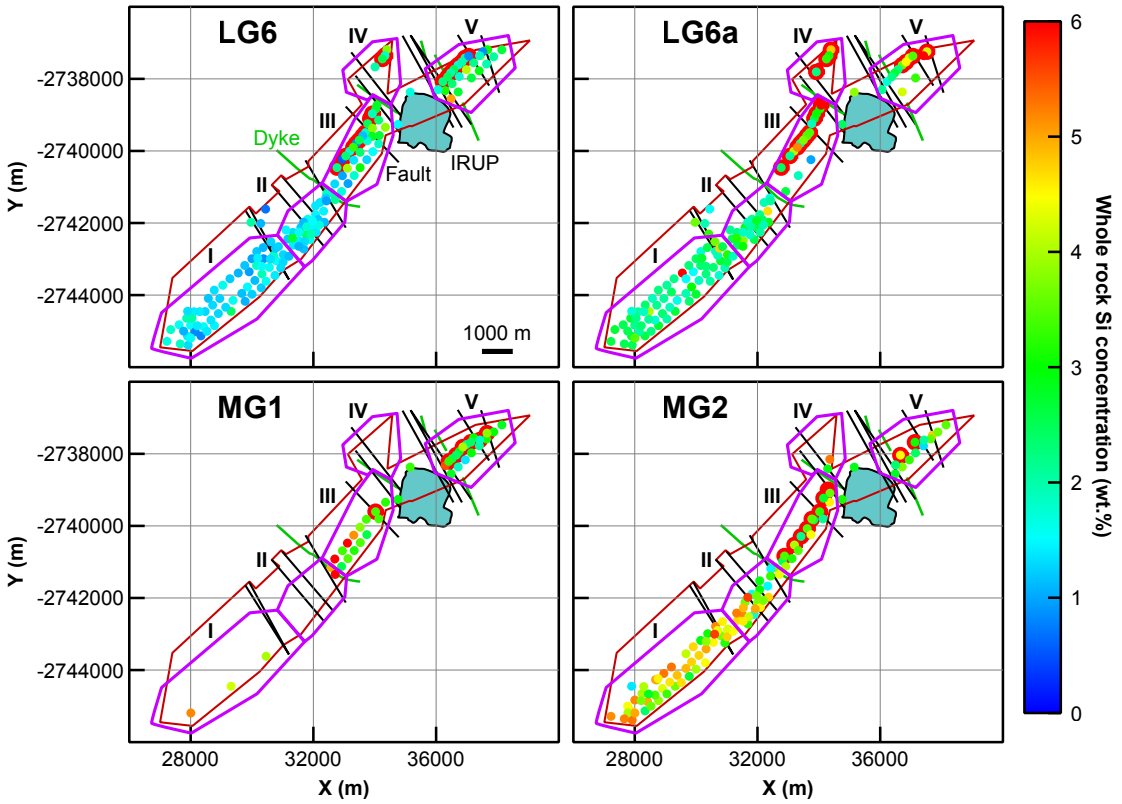

Figure 3.4: Whole-rock Si concentrations of the LG6-MG2 chromitite layers, chromitites close to the surface (<40 m),which are in the potentially weathered zone are marked by red circles.

Whole-rock PGE concentrations generally increase upwards stratigraphy, which has already been described in detail in Chapter 2, suggesting increasing PGE concentrations in the magma due to fractionation. They are uniformly developed throughout all chromitite layers with an exception in sector V of the MG2, which has elevated grades compared to the southern part (sector I–IV) of the Thaba Mine area (Fig. 3.5). Figure. 3.6 indicates a clear correlation of Pt/Pd ratios with the weathered zone, close to the surface. Mobilisation of Pd in chromitite layers of the Thaba mine has recently been described by supergene redistribution (Oppermann et al., 2017), offering a suitable explanation for the described correlation.

P concentrations of the LG6-MG2 chromitites reveal two principal trends (Fig. 3.7): (1) assays in the weathered zone, near the surface (<40 m) to the northeast depict relative higher levels of P in all layers (sector III–V), due to P enrichment by weathering processes (e.g. Smeck, 1973; Cross and Schlesinger, 1995; Hartmann et al., 2014). (2) A general increase in P concentrations to the southwest (sector I & II) is apparent in the LG6 and MG2 layer. Primary P concentrations in layered rocks were used as proxy for the amount of trapped interstitial liquid (e.g. Tegner et al., 2009), because they are incompatible in the cumulus assemblage of the Bushveld Complex before the crystallisation of apatite in the Upper Zone (Cawthorn and Walsh, 1988). Tegner et al. (2009) described vertical variations in P concentrations in the Skaergaard Intrusion and proposed that increasing compaction of the crystal mush results in a decrease in the P contents. Si concentrations in the investigated chromitites (Fig. 3.4), reveal a similar increase in Si (intercumulus silicates) for the MG2 chromitite layer towards

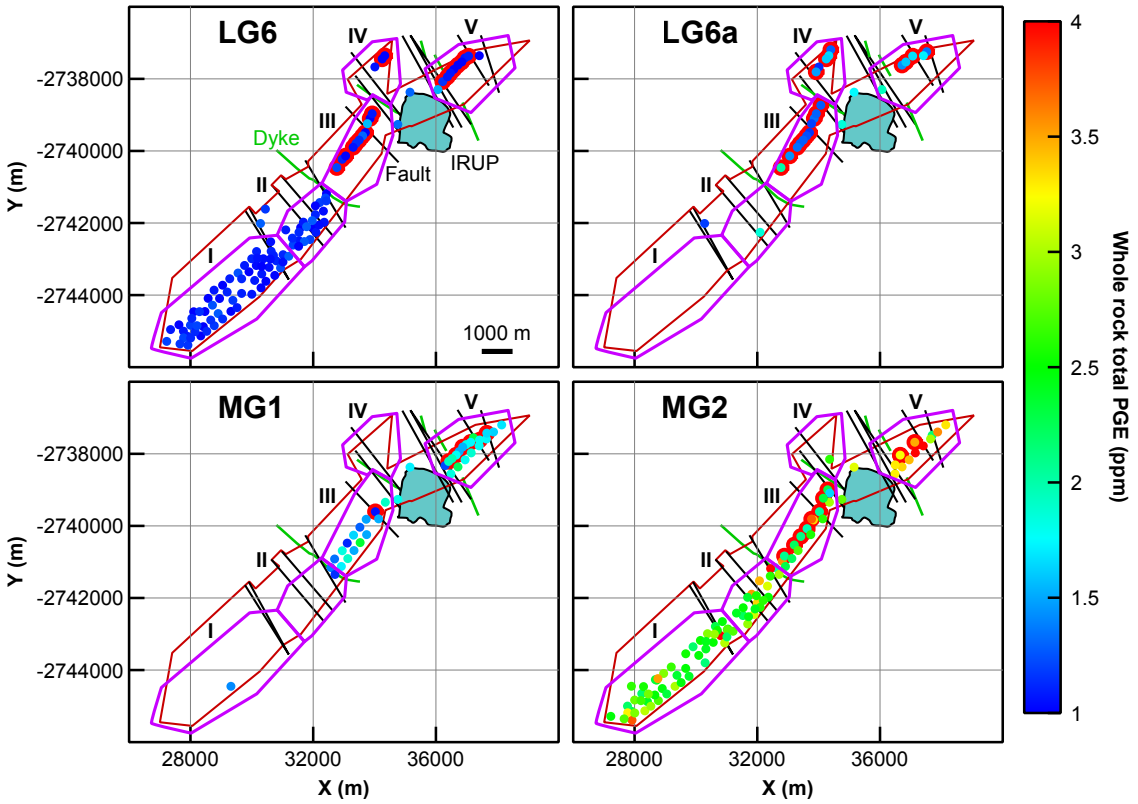

Figure 3.5: Whole-rock total PGE concentrations of the LG6-MG2 chromitite layers, chromitites close to the surface (<40 m), which are in the potentially weathered zone are marked by red circles.

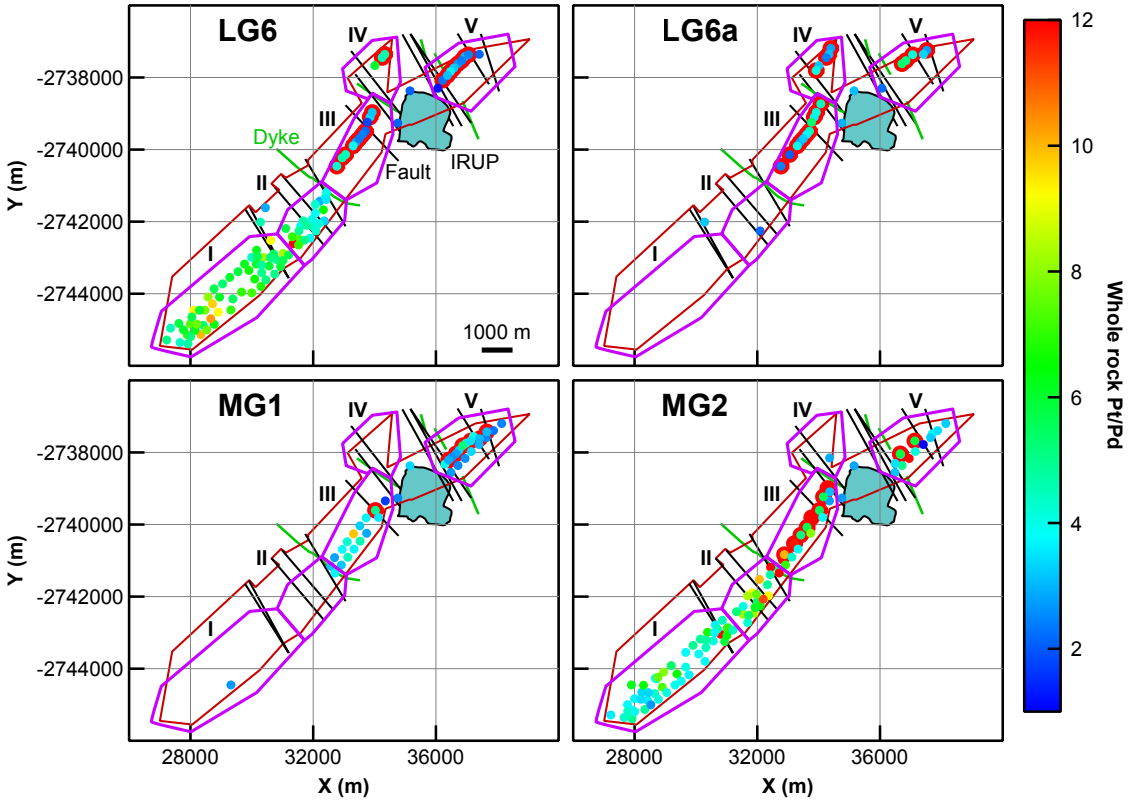

Figure 3.6: Whole-rock Pt/Pd ratios of the LG6-MG2 chromitite layers, chromitites close to the surface (<40 m), which are in the potentially weathered zone are marked by red circles.

the sectors I & II. However, Si concentrations in the LG6 reveal a contrary behaviour with decreasing Si concentrations towards these sectors. Following the line of arguments of Tegner et al. (2009), the observed lateral P and Si variations in the MG2 could indicate that the sectors III–V exhibited higher compaction due to a higher cumulate load, which resulted in a reduction of the intercumulus liquid. However, it should be noted that the findings of this thesis (Chapters 2 and 4) and by Holness et al. (2017a) indicate that compaction played only a minor role in the Critical Zone of the Bushveld Complex, and thus, the changes in cumulate load were likely to be minor. However, further investigations are needed to verify the intercumulus texture and assemblage of drill core sample of the different sectors, especially for the LG6 chromitite.

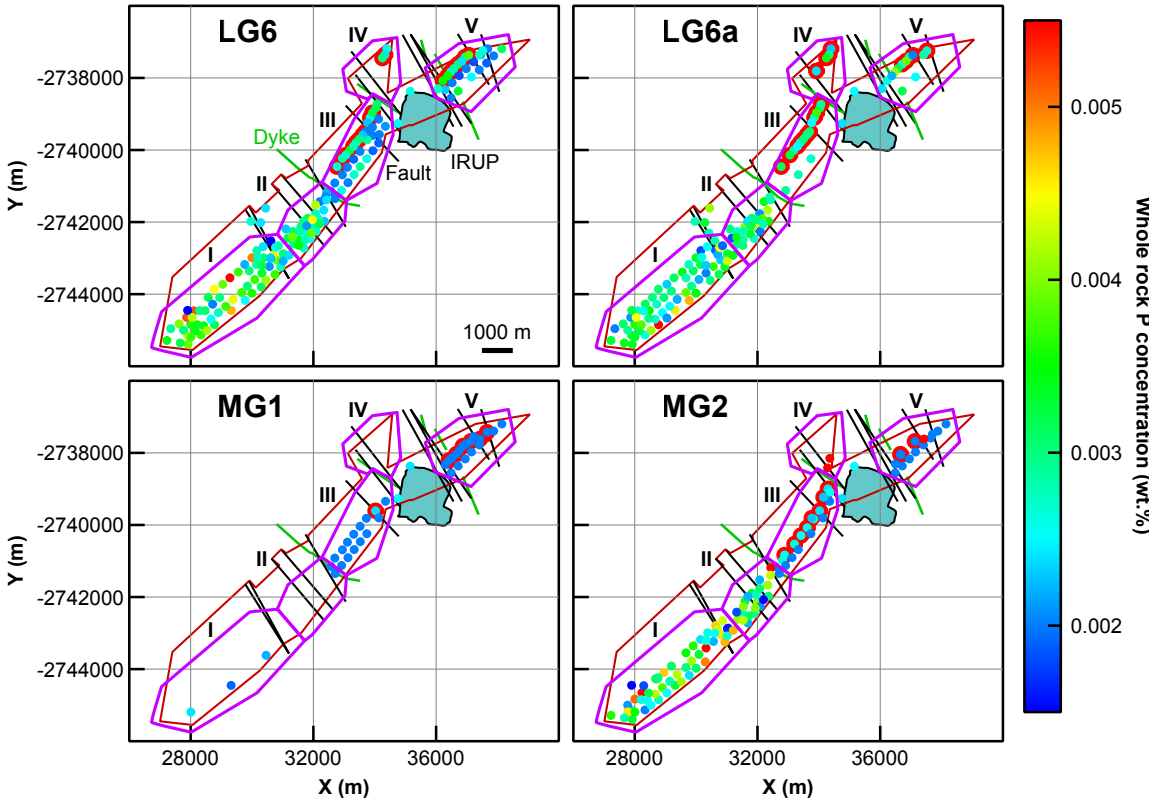

Figure 3.7: Whole-rock P concentrations of the LG6-MG2 chromitite layers, chromitites close to the surface (<40 m), which are in the potentially weathered zone are marked by red circles.

Taken together, the results of this chapter show lateral geochemical variations in the upper LG and lower MG chromitites over a large area (>10 km). While some variations (e.g. P) are likely to result from post-cumulus changes, the variations in Mg# and Cr# can probably be explained by primary magmatic processes, which is confirmed by previous studies (e.g. Klemm et al., 1985; Scoon and Teigler, 1995). The changes in chromite composition are attributed to variations in the thickness of the overlying magma.

3.4 Acknowledgements

This manuscript is based on drill core logs provided by Cronimet Chrome Mining SA (Pty) Ltd. I am grateful to M. Hill and the Cronimet staff for access to mine data and for permission to publish the results. Discussions with I. V. Veskler and R. B. Trumbull are highly acknowledged.

Chapter 4

Clues on post-cumulus recrystallisation by orthopyroxene oikocrysts in the MG1 chromitite of the Bushveld Complex [1]

Two typical mineral textures of the MG1 chromitite of the Bushveld Complex, South Africa, were observed; one characterised by abundant orthopyroxene oikocrysts, and the other by coarse-grained granular chromitite with only minor amounts of interstitial material. Oikocrysts form elongate clusters of several crystals aligned parallel to the layering, and typically have subhedral, almost chromite-free, core zones containing remnants of olivine. The core zones are surrounded by poikilitic aureoles overgrowing euhedral to subhedral chromite chadacrysts. Chromite grains show no preferred crystal orientation, whereas orthopyroxene grains forming clusters commonly share the same crystallographic orientation. Oikocryst core zones have lower Mg# and higher concentrations of incompatible trace elements compared to their poikilitic aureoles. Core zones are relatively enriched in REE compared to a postulated parental magma (B1) and did not crystallise in equilibrium with the surrounding minerals, whereas the composition of the poikilitic orthopyroxene is consistent with growth from the B1 magma.

These observations cannot be explained by the classic cumulus and post-cumulus models of oikocryst formation. Instead, we suggest that the oikocryst core zones in the MG1 chromitite layer formed by peritectic replacement of olivine primocrysts by reaction with an upwards-percolating melt enriched in incompatible trace elements. Poikilitic overgrowth on oikocryst core zones occurred in equilibrium with a basaltic melt of B1 composition near the magma–crystal mush interface. Finally, adcumulus crystallisation followed by grain growth resulted in the surrounding granular chromitite.

[1] This chapter has been published as: Kaufmann, F. E. D., Vukmanovic, Z., Holness M. B., Hecht, L. (2018). Orthopyroxene oikocrysts in the MG1 chromitite layer of the Bushveld Complex: implications for cumulate formation and recrystallisation, *Contributions to Mineralogy and Petrology* 173(2), 1–20, DOI:`https://doi.org/10.1007/s00410-018-1441-x`.

4.1 Introduction

Despite the long history of research and the wealth of scientific publications, the mechanisms by which layering forms in mafic intrusions are not well understood. Due to their ubiquity in cumulate rocks and their ability to preserve different stages of the solidification process, the microstructural and geochemical study of oikocrysts can contribute to our understanding of layering mechanisms (Namur et al., 2015, and references therein).

Oikocrysts are large crystals that enclose smaller crystals (chadacrysts) to form a poikilitic texture. Many different minerals form oikocrysts, such as pyroxene (e.g. this study Cameron, 1969; Cameron, 1975; Ulmer and Gold, 1982; Campbell, 1987; Mathison, 1987; Barnes et al., 2016), plagioclase (e.g. Cameron, 1969), olivine (e.g. Maier, 1995) and hornblende (e.g. Meurer and Claeson, 2002; Ivanic et al., 2015). The formation of poikilitic textures are dependent on differences in the nucleation rate (Wager, 1961) and/or the growth rate (Vernon, 2004, page 106) of the different minerals: oikocrysts form if one mineral has a lower nucleation rate but higher growth rate than co-accumulating crystals of another phase.

There are two main hypotheses to explain the formation of oikocrysts. Early work was based on the hypothesis that oikocrysts form in the post-cumulus stage by the solidification of interstitial liquid (Wager et al., 1960), whereas recent studies argue that the absence of compositional zonation and the similarity of composition of the oikocrysts and nearby primocrysts of the same phase point to the oikocrysts being cumulus grains (Campbell, 1968; Mathison, 1987; Tegner and Wilson, 1995; Barnes et al., 2016).

In this study, we report the results of an investigation of oikocrysts in a chromitite layer of the Rustenburg Layered Suite of the Bushveld Intrusion, South Africa. Our approach integrates the microstructural and geochemical evolution of the orthopyroxene oikocrysts, using electron back-scatter diffraction (EBSD), electron microprobe analysis (EMP) and LA-ICP-MS. These different analytical approaches lead to a model by which we explain the formation of orthopyroxene oikocrysts by reactive replacement of olivine primocrysts by an upwards-percolating melt, followed by poikilitic overgrowth of oikocryst cores from a more primitive melt. Post-cumulus growth and textural modification resulted in the observed composition and microstructure of the granular chromitite.

4.2 Geological setting

The Bushveld Complex, located in the NE of South Africa (Fig. 4.1) is the largest known plutonic complex on Earth, hosting the world's greatest reserves of platinum-group elements, chromium and vanadium. It is of Proterozoic age (Scoates and Friedman, 2008; Scoates and Wall, 2015) and intruded into sedimentary rocks of the Transvaal Supergroup. It covers an area of over 65 000 km^2 and ranges in thickness from 7–9 km (Eales and Cawthorn, 1996; Cawthorn, 2015). According to the South African Committee for Stratigraphy South African Committee for Stratigraphy (1980), the complex is divided into the ultramafic-mafic Rustenburg Layered

Suite and the felsic Lebowa Granite and Rashoop Granophyre. The Rustenburg Layered Suite has a saucer-like shape dipping gently towards the centre of the complex.

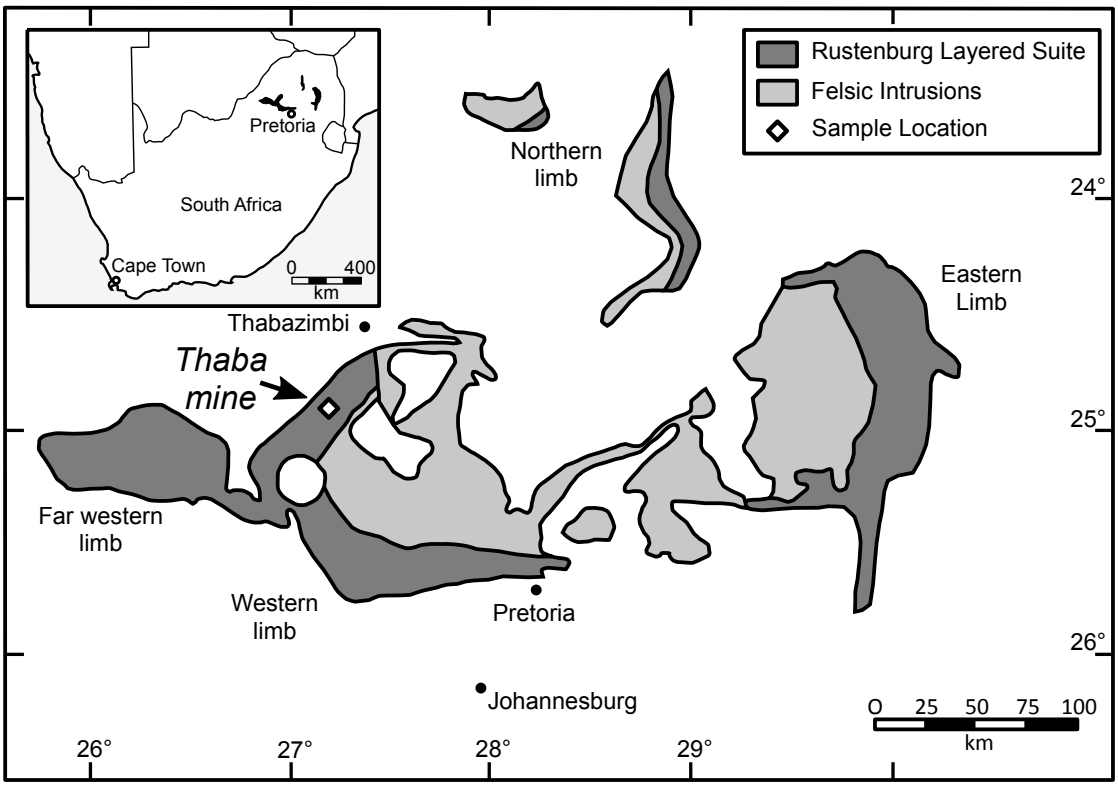

Figure 4.1: Schematic geological map of the Bushveld Complex with sample location (after Eales and Cawthorn, 1996)

The compositions of the parental magmas of the Rustenburg Layered Suite have been estimated from fine-grained sills and chilled margins (Harmer and Sharpe, 1985; Barnes et al., 2010; Godel et al., 2011; Wilson, 2012). Three different parental magmas have been proposed: an Mg-rich basaltic andesite known as B1, and tholeiitic basalts known as B2 and B3. The suite is subdivided from bottom to top into the Lower Zone, Critical Zone, Main Zone and Upper Zone. The B1 magma is suggested to have formed the Lower Zone and Lower Critical Zone.

Chromitite layers occur throughout the Critical Zone. They are subdivided into the Lower (LG), Middle (MG) and Upper (UG) groups. Each group is numbered from bottom to top; thus the MG1 layer is the first chromitite of the Middle Group. Chromitites vary in thickness from ∼1 m to small stringers only cm to mm thick. Chromitites may contain pyroxenitic layers, known as partings.

Scientific publications on chromitite layers in the Rustenburg Layered Suite are mainly focussed on the UG2 chromitite, which is the richest in platinum-group elements. However, the MG layers have also been the subject of many published studies (e.g. Cameron, 1969; Cameron, 1977; Cameron, 1980; Lee and Parry, 1988; Eales et al., 1990; Teigler, 1990; Merkle, 1992; Scoon and Teigler, 1994; Kottke-Levin et al., 2009; Naldrett et al., 2009; Junge et al., 2016; Oberthuer et al., 2016). Published studies of mineral chemistry (Cameron, 1977;

Cameron, 1980; Eales et al., 1990; Kottke-Levin et al., 2009) concentrated on the broader successions of the LG and MG chromitites and their adjacent host rocks, proposing a range of different mechanisms of chromitite genesis such as externally-controlled changes in confining pressure (Cameron, 1977; Cameron, 1980), and reaction of the resident magma with influxes of primitive magma (Eales et al., 1990). Cameron (1969) focused on possible post-cumulus changes in chromitite layers, providing a textural description of orthopyroxene oikocrysts similar to those investigated in this study. More detailed investigations have been conducted on the platinum-group element and platinum-group mineral concentration and distribution (Lee and Parry, 1988; Teigler, 1990; Merkle, 1992; Scoon and Teigler, 1994; Junge et al., 2016; Oberthuer et al., 2016).

4.3 Sample material and analytical methods

Sample material comes from drill core ZK135 from the Thaba open pit mine (Fig. 4.1), which covers the LG6 to MG2 chromitite layers and their host rocks. Core material was provided by Cronimet Chrome Mining SA (Pty) Ltd. In this section of stratigraphy, the MG1 chromitite is 62 cm thick, embedded in pyroxenite with an intermediate ca. 15 cm thick pyroxenite-chromitite transition zone (Fig. 4.2a). This study focuses on the cm-sized orthopyroxene oikocrysts that occur in the lower and upper part of the MG1 chromitite layer (Fig. 4.2b, c).

For textural characterisation, the central chadacryst-free regions of 45 oikocrysts were outlined on thin section scans, and the program ImageJ was used to measure major and minor axis length, size, orientation, and spatial distribution. We term this region the oikocryst 'core zone', defined as the central chadacryst-free area that is surrounded by orthopyroxene containing abundant small idiomorphic chromite grains, which varies from 1.3–1.6 mm across. The core zone can comprise several subgrains with different crystallographic orientations, which were treated separately for the alignment analysis. The extent of any preferred alignment of non-equant oikocryst core zones was calculated using the program CSDCorrections 1.53 by Higgins (2000) (see Meurer and Boudreau (1998a) and Boorman et al. (2004) for further information), which provides the alignment factor: this ranges from 0 (no statistically significant alignment) to 100 (perfect alignment of grains). Crystal size distributions (CSD) were measured both for chromite grains enclosed in the poikilitic pyroxenite and for chromite in granular chromitite. For this, we used compiled backscattered electron (BSE) images and the program CSDCorrections 1.53 following the methods of Higgins (2000). The following input parameters were used for the calculation of the CSD histograms: maximum grain diameter (minimum diameter of chromite grains was set to 0.01 mm), a massive fabric, chromite shape of 1:1:1 and a roundness of 0.2.

After standard mechanical polishing using diamond paste, thin sections were polished for 1 h with 0.06 µm colloidal silica (SiO_2 particle dispersion in an alkaline solution) at the University of Cambridge, UK. Samples were analysed on a FEI sFEG XL30 SEM at the Department of Physics, University of Cambridge. All crystallographic datasets were collected, indexed

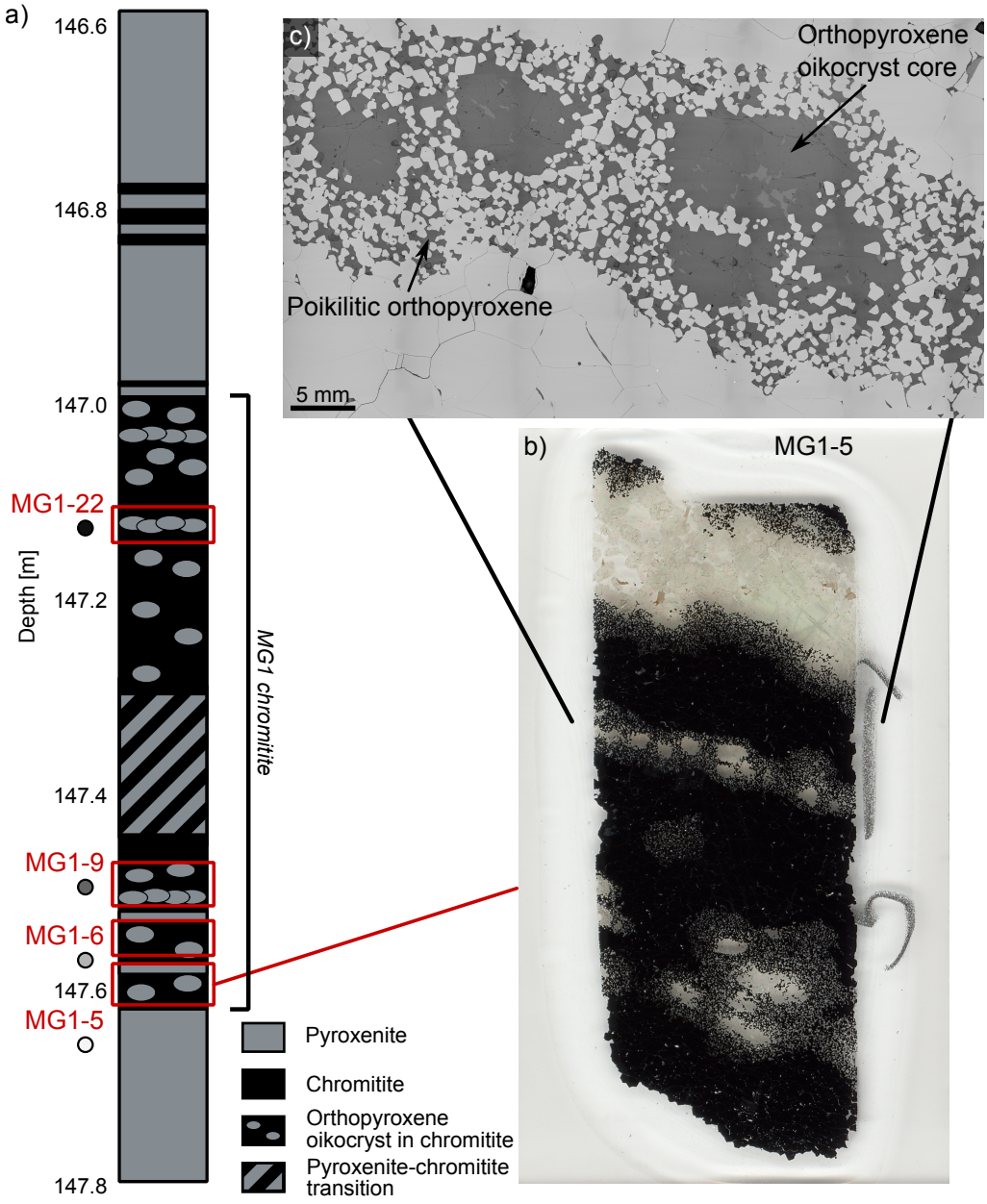

Figure 4.2: **a** Lithostratigraphic column of the MG1 chromitite layer with investigated areas (red boxes) and marker colour used in the following figures. **b** Photograph of petrographic thin section with typical appearance of orthopyroxene oikocrysts. **c** Composed backscattered electron image of oikocrysts forming a layer parallel to the overall layering.

and analysed using Oxford Instruments AZtec acquisition software, set to detect 6 bands, 60 Hough transforms, 75 reflectors, and at 4x4 binning. Whole thin section EBSD was carried out using 15 µm step size. EBSD maps and pole figures of crystallographic orientation were constructed using Oxford Instrument Channel 5 software. Inverse pole figure maps represent the orientation of the crystal lattice along specific directions of the sample reference frame (Y-X). Crystallographic orientation data (pole figures and inverse pole figures) were plotted using Channel 5 'Mambo' software using lower hemisphere, equal area projections. Data are reported with respect to an arbitrarily assigned X-Y reference frame. Chromite density

contour diagrams are calculated on point per grain pole figures, using half width of 20° and cluster size of 10°.

EMP analyses were carried out at the Museum für Naturkunde Berlin with a JEOL JXA-8500F EMP equipped with a field emission cathode and five wavelength-dispersive spectrometers. The following analytical conditions were used: 20 kV accelerating voltage for chromite and 15 kV for pyroxene measurements, 75 and 15 nA beam current for chromite and pyroxene respectively. The spot size was set to 1 µm for chromite and 2 µm for pyroxene. The measured intensities were calibrated against natural minerals of the Smithsonian international standard suite Jarosewich et al. (1980) and pure metals of the Astimex metal standard. Matrix effects were minimised by a conventional ZAF routine processed by the JEOL series operating system. Accuracy and reproducibility were checked regularly before and after each analysis session by measurements of minerals of the Smithsonian mineral standards (Chromite, USNM 117075; Augite, USNM 122142; Hypersthene USNM 746, Jarosewich et al., 1980), which revealed deviations of <2 %. The ferric iron content of chromite and pyroxene was calculated assuming ideal stoichiometry.

LA-ICP-MS analyses for trace element concentrations in orthopyroxene were conducted at the Institut für Mineralogie of the Leibniz Universität Hannover (LUH) with a fast scanning-sector field-ICP-MS (ThermoScientific ElementXR) connected to a femtosecond (Ti-sapphire) laser ablation system. Details of the fs-LA system are given in Oeser et al. (2014) and Lazarov and Horn (2015). In our study, the laser operated at 20–30 Hz, with a spot size ranging between 40–50 µm. The ablation mode was set to raster mode for analyses in the oikocryst cores and to line mode for analyses at the rims and in poikilitic orthopyroxene. Acquisition times of the background signal and the ablation signal were set to 40 s and 100 s, respectively. Sample surfaces of each spot were pre-ablated before measurement to avoid artefacts due to surface contamination. Analyses were bracketed every 10–15 measurements by standard reference material NIST610 to correct for internal instrumental drift. Si concentrations, obtained by EMP analyses, were used for the internal calibration of trace element concentration for orthopyroxene. Further testing of the accuracy and reproducibility was undertaken by measuring silicate reference material (BCR-2G), indicating accuracy and reproducibility of 1–5 %. Further information about trace element analyses by fs-LA-ICP-MS at the LUH is given in Lazarov and Horn (2015) and Lazarov and Horn (2015). Data processing was performed with the SILLS program (Guillong et al., 2008).

4.4 Results

4.4.1 Petrography

The MG 1 chromitite layer comprises granular chromitite, with only minor amounts of interstitial material, surrounding large isolated orthopyroxene oikocrysts characterised by an inclusion-free core zone that is typically ovoid. The proportion of chromite decreases from the uppermost part of the chromitite into the hanging wall, which is formed of cumulus orthopyroxene, 1–10 vol.% chromite, and minor amounts of interstitial plagioclase

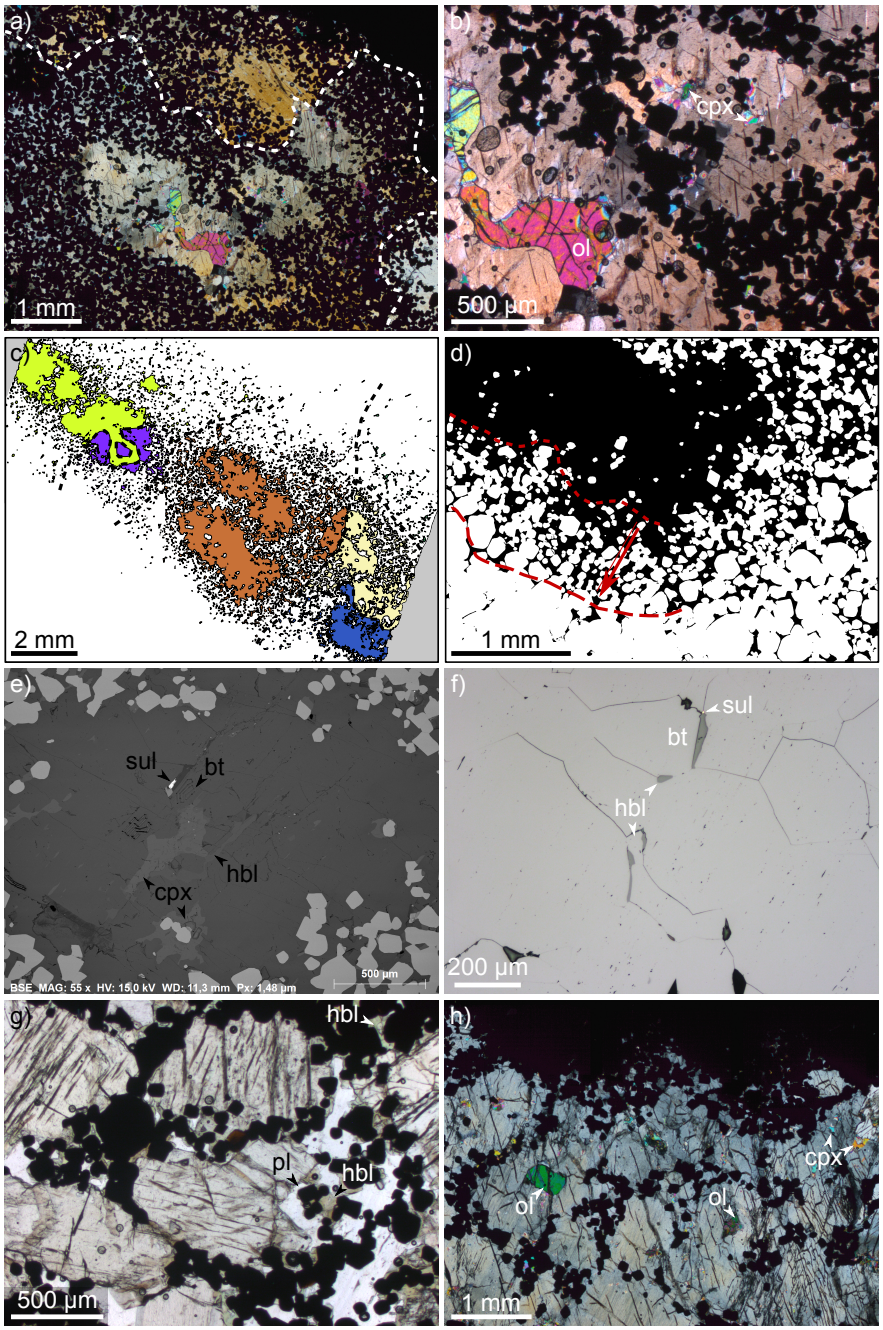

Figure 4.3: Photomicrographs in crossed polarised light. Note that the thin sections are ~100 µm thick and therefore minerals show birefringence colours of higher than usual order. **a** Overview of oikocryst cluster consisting of three different orthopyroxene crystals. Grain boundaries of orthopyroxene with same crystallographic orientation are illustrated by dashed lines. **b** Olivine (ol) and clinopyroxene (cpx) inclusions in orthopyroxene oikocryst core zone. **c** Sketch of oikocryst layer, showing the complex relationships between orthopyroxene crystals (each coloured differently). **d** Sketch of poikilitic aureole. The arrow indicates the increase in grain size for chromite from the core zone (upper part) to the granular chromitite (lower part). **e** Backscattered electron image of oikocryst cores with sulphide (sul), biotite, hornblende and clinopyroxene inclusions. Note that hydrous silicates are oriented parallel to the cleavage of the orthopyroxene. **f** Reflected light photomicrographs of granular chromitite. Chromite shows 120° triple junctions and smooth curved grain boundaries. Interstitial phases consist mainly of hornblende (hbl) and biotite (bt). **g** Chromitite-pyroxenite transition in plain polarised light with cumulus orthopyroxene and interstitial plagioclase (pl) and hornblende. **h** Footwall pyroxenite consisting of pegmatoidal orthopyroxene overgrowing the chromite framework.

and clinopyroxene. The chromitite layer contains three mm-thick pyroxenitic partings parallel to the overall layering, while four additional mm-thick chromitite layers are embedded in the hanging wall pyroxenite. The footwall of the MG1 is a feldspathic pyroxenite, and is separated from the overlying main chromitite layer by a heavily altered coarse-grained chromite-rich (10–25 vol.%) pyroxenite with remnants of olivine overgrown by orthopyroxene.

The poikilitic aureoles surrounding the inclusion-free core zones contain 50–60 vol.% euhedral to subhedral chromite grains. Although most oikocrysts have chadacryst-free core zones, some do not: we ascribe this to a 2D cut effect. Oikocrysts are either isolated or form clusters of several crystals elongated parallel to the layering (Fig. 4.3a). The grain boundaries between different crystals of orthopyroxene do not always correspond to the apparent margins of the oikocrysts. Importantly, the orthopyroxene in adjacent oikocrysts is commonly in optical continuity, and the grain boundaries between adjacent crystals may pass through an oikocryst (Fig. 4.3c). Oikocryst core zones are not always entirely inclusion-free but may contain small grains of chromite, olivine, clinopyroxene and, rarely, biotite and hornblende. The olivine inclusions are commonly lobate, with a shape entirely unlike that expected for primocrysts (Fig. 4.3b). Some exsolution lamellae of clinopyroxene are present (Fig. 4.3b, e). Hydrous silicate inclusions follow the orthopyroxene cleavage and are restricted to the lower part of the MG1.

Chromite grains show a wide range of grain sizes: the few grains in the oikocryst core zones are 0.02–0.15 mm across, in contrast to those in the outer poikilitic aureoles which are 0.06–0.3 mm, whereas the massive chromitite grains are 0.4–1.1 mm across. Chadacrysts generally increase in size outwards from the oikocryst core (Fig. 4.3d). The chromitite hosting the oikocryst has a granular texture (Fig. 4.3f) with <5 vol.% interstitial material, which is mainly biotite, hornblende and serpentine. Minor amounts of apatite and sulphides are present. Chromite in granular chromitite has 120° triple junctions and smoothly curved grain boundaries. Plagioclase is absent throughout the chromitite seam (upper and lower part) but is present in the chromitite-pyroxenite transition, which comprises cumulus orthopyroxene with interstitial plagioclase and hornblende (Fig. 4.3g). The pyroxenite immediately underlying the chromitite has similar microstructural characteristics to the oikocrystic layers in the chromitite: the chromite framework is overgrown by coarse-grained orthopyroxene enclosing olivine in the former cores.

4.4.2 Microstructural analysis

The average aspect ratio of oikocryst cores is 1.80 (± 0.51 S.D.), and they display a systematic alignment (Fig. 4.2b), with an alignment factor of 73 (on the basis of 45 grains). By comparison with Meurer and Boudreau (1998a), the uncertainty on this value is likely to be in the range ± 2–3. The general dip of the shape preferred orientation of the oikocryst core zones is parallel to the overall layering (15°± 22° S.D. from the horizontal borehole).

Independent of their size, chromite crystals, either those enclosed by oikocrysts or those outside oikocrysts, show no overall crystallographic preferred orientation (CPO, Fig. 4.4). However, small groups or clusters of grains in both the coarse-grained band and where enclosed by orthopyroxene oikocrysts occasionally show similar crystallographic orientations along a

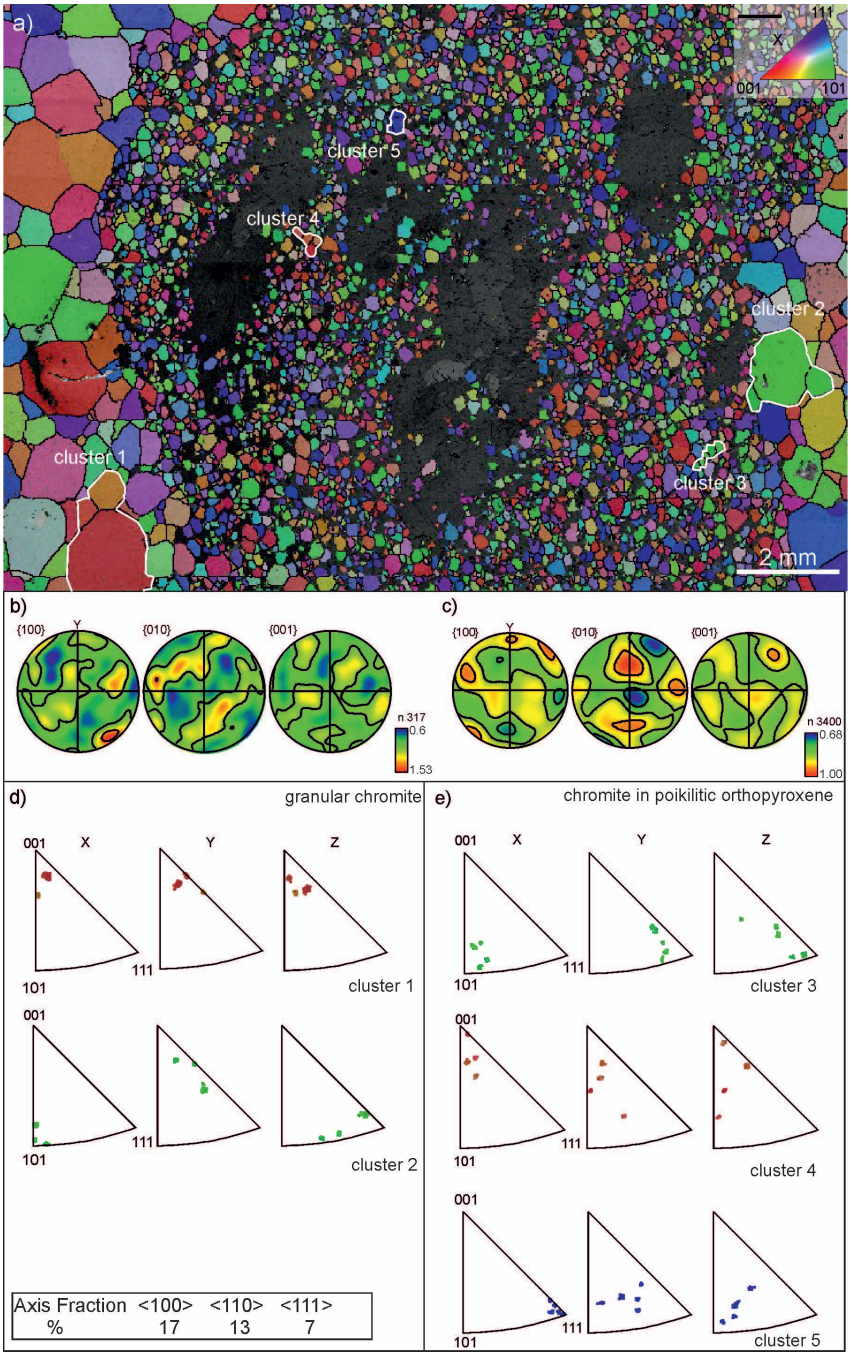

Figure 4.4: **a** EBSD inverse pole figure map of chromite grains of the lower part of the MG1, superimposed on a band contrast map. The inverse pole figure map represents the orientation of crystal planes relative to the x-direction of the sample reference frame. The colour scheme is given in the inverse pole figure legend (see inset). White lines outline clusters of chromite crystal with similar crystallographic orientations along the y-direction of the sample reference frame. **b** Density contour diagram (point per grain pole figure) of chromite crystals in poikilitic orthopyroxene. **c** Density contour diagram (point per grain pole figure) of granular chromite calculated with half width of 20° and cluster size of 10°. Both pole figures shown in **b** and **c** are plotted using a lower hemisphere, equal area projection. **d** Inverse pole figure of granular chromite clusters (clusters 1 and 2). **e** Folded inverse pole figure of chromite clusters within the poikilitic orthopyroxene (clusters 3 and 4). Each cluster contains 4 chromite grains. Folded inverse pole figures are plotted using a lower hemisphere, equal area projections. The fraction of the different shared axes is calculated using colour thresholding to identify clusters and presented as an area fraction of all the chromitite grains shown in the EBSD map in **a**.

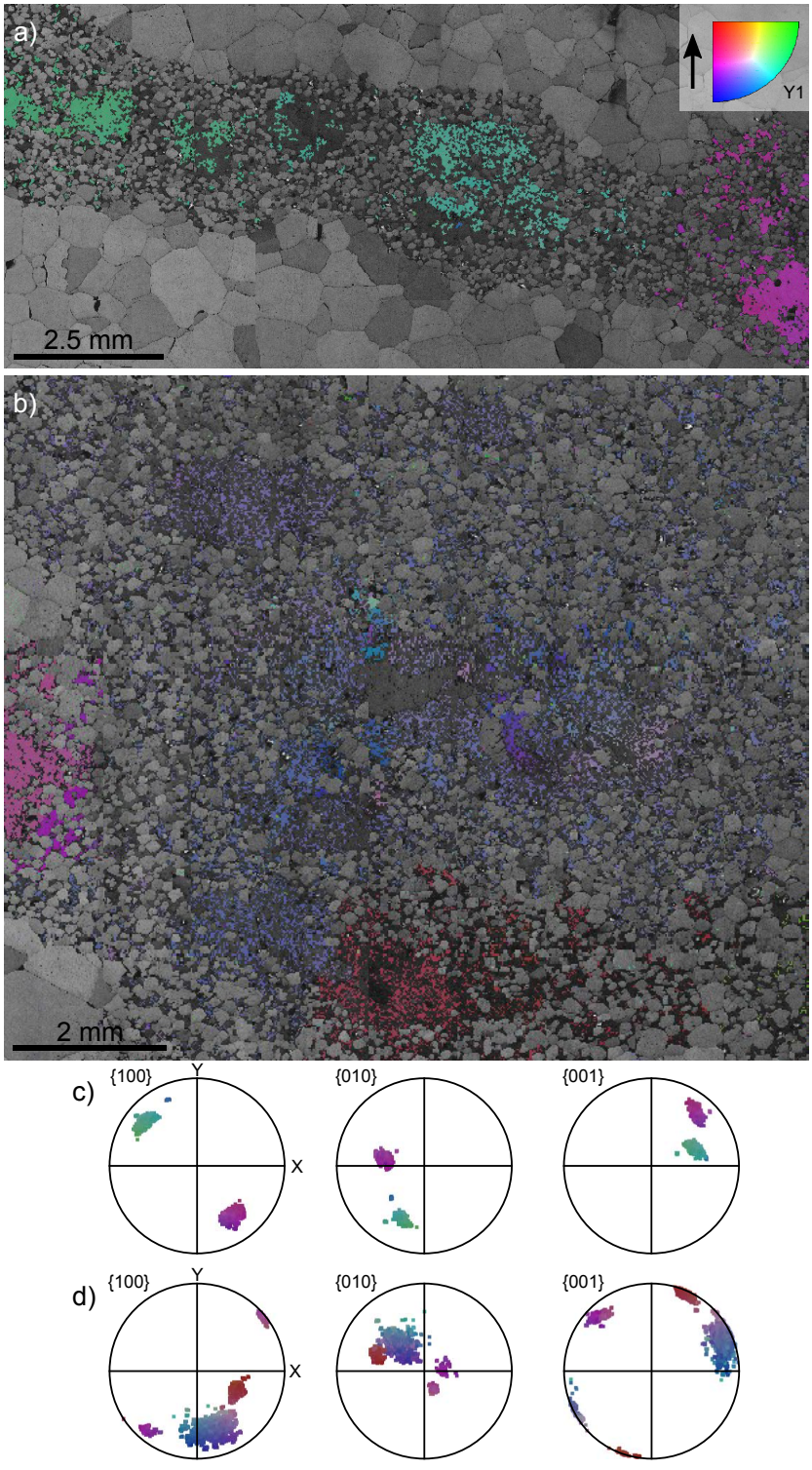

Figure 4.5: **a** and **b** EBSD inverse pole figure maps of orthopyroxene grains of the lower part of the MG1, superimposed on a band contrast map. **c** Orthopyroxene pole figure for map **a**. **d** Orthopyroxene pole figure for map **b**. Colour coding of the orthopyroxene pole figures correspond to the inverse pole figure map.

particular sample direction (examples are outlined with white lines in Fig. 4.4a). Most of these clusters with similar crystallographic orientations do not contain more than 4 to 5 grains per cluster (as viewed in thin section). While each cluster contains at least one common axis

along the x-direction of the sample reference frame (e.g. <110> in the case of cluster 2 shown in Fig. 4.4d), one cluster shown in Fig. 4.4d (labelled cluster 1) shares the common axis <001> in all three sample directions (Fig. 4.4d). The axis that most commonly occurs as a common direction relating the individual grains within a cluster is <100>, with <110> and <111> being progressively less common (Fig. 4.4). The inverse pole figure map for orthopyroxene reveals large areas with a single crystallographic orientation (Fig. 4.4a, b). Sample MG1-22 contains two adjacent oikocrysts whose (001) planes are offset by only a few degrees (Fig. 4.5c). Large orthopyroxene oikocrysts from MG1-5 are almost all in optical continuity (Fig. 4.5d).

CSD plots for chromite enclosed in poikilitic orthopyroxene (Fig. 4.6a) and chromite in granular chromitite (Fig. 4.6b) are both straight. However, that for granular chromite is rotated towards larger grains with a shallower slope compared to that for chromite enclosed by the oikocrysts.

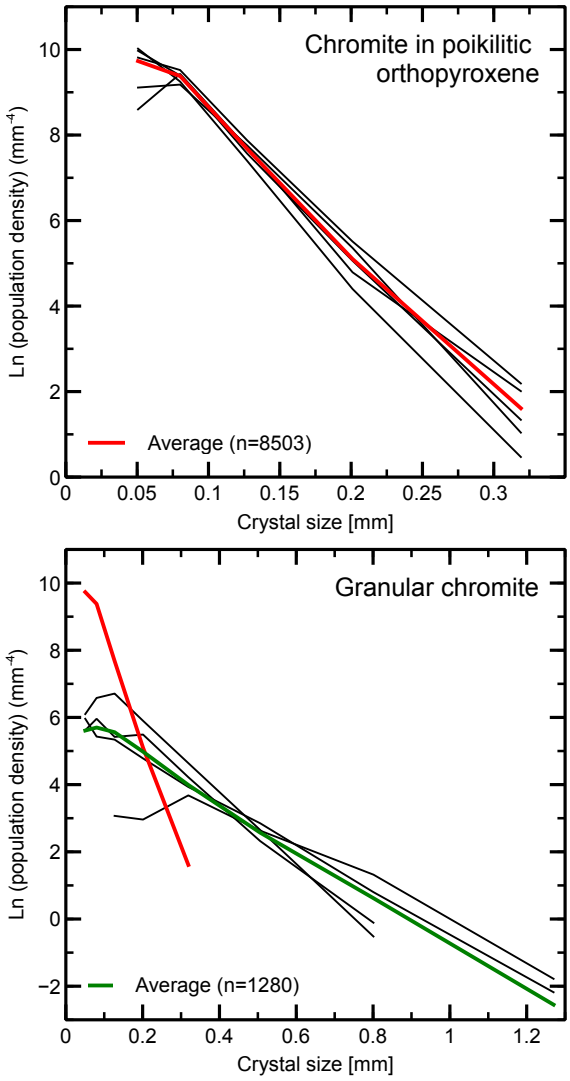

Figure 4.6: CSD diagram for **a** chromite enclosed in poikilitic orthopyroxene and **b** for chromite in granular chromitite.

4.4.3 Orthopyroxene and olivine composition

There are clear differences in the composition of orthopyroxene oikocryst core zones compared to the surrounding poikilitic aureoles (Tab. 4.1). Oikocryst core zones have lower Mg# (atomic ratio, $Mg/(Mg+Fe^{2+})$) and higher concentrations of minor (CaO, Al_2O_3) and trace elements (Zr) compared to poikilitic orthopyroxene (Fig. 4.7). Only TiO_2 concentrations display an opposing trend towards higher concentrations in poikilitic orthopyroxene (Fig. 4.7d). The composition of the orthopyroxene forming the outermost ∼100 µm of the core zones is intermediate between that of the centre of the core zones and that of the poikilitic aureoles. Ce/Yb ratios (Fig. 4.7f) reveal a similar behaviour for the REE concentrations in the poikilitic aureole and in the central and outermost part of the core zone, with the highest concentrations for light and heavy REE in the central part of the core zones. Orthopyroxene chemistry displays a decrease in trace element concentrations towards the top of the MG1 layer (light grey via medium grey towards black tone (e.g. Fig. 4.7f). Our data is in good agreement with other studies of orthopyroxene chemistry in the chromitite layers of the Bushveld Complex (e.g. Eales et al., 1993; Veksler et al., 2015).

For comparison we calculated the REE composition of orthopyroxene that would have crystallised from a postulated parental B1 magma, using the B1 composition of (Barnes et al., 2010) and partition coefficients for orthopyroxene from Sun and Liang (2013) and Yao et al. (2012) for 750° and 1250° C. The observed REE concentrations are notably higher in core zones compared to those expected from our calculations (Fig. 4.7f).

Similar trends can be observed in the REE signatures. Our results, normalised relative to the B1 magma, are shown in Fig. 4.8. In general, all measurements show a shift towards lower REE concentrations along the MG1 chromitite seam from bottom to top. Core zone, outer core zone and poikilitic aureole REE concentrations are clearly different. Poikilitic orthopyroxene has lower concentrations compared to oikocryst core zones, with intermediate compositions in the outer part of the core zones. Furthermore, the general slope of core zone and poikilitic aureole REE patterns vary: poikilitic orthopyroxene has a much steeper slope towards the light REE, as demonstrated by average Ce/Tb ratios of 12.327 in oikocryst core zones compared with ratios of 3.542 in poikilitic orthopyroxene for sample MG1-5 (Table 4.1). All patterns reveal a negative Eu anomaly, although this is less pronounced in the poikilitic aureoles.

The oikocryst core zones are clearly enriched in REE compared to expected values for orthopyroxene crystallising from B1 magma, regardless of the choice of temperature of crystallisation. Furthermore, the crystallisation temperature controls the slope of the REE pattern, with higher temperatures resulting in a flatter slope (red lines in Fig. 4.7). The observed composition of the poikilitic aureoles is roughly in agreement with that expected for crystallisation from the B1 magma, although some anomalous enrichment is still observed for the light REE.

The olivine inclusions in the oikocrysts are chemically homogenous. They are enriched in Ni (∼2800 ppm, Table 4.2) compared to both the orthopyroxene core zones (570–630 mm) and the poikilitic orthopyroxene aureoles (480–530 ppm). They are also enriched in Ni compared

with interstitial orthopyroxene (∼400 ppm) and with cumulus orthopyroxene in the silicate host rocks and pyroxenitic partings in the underlying LG6a and the overlying MG2 chromitite layer (unpublished data). Si and Ni distribution maps (Fig. 4.9) of the oikocryst core zones reveal no Ni-enrichment surrounding the olivine inclusions.

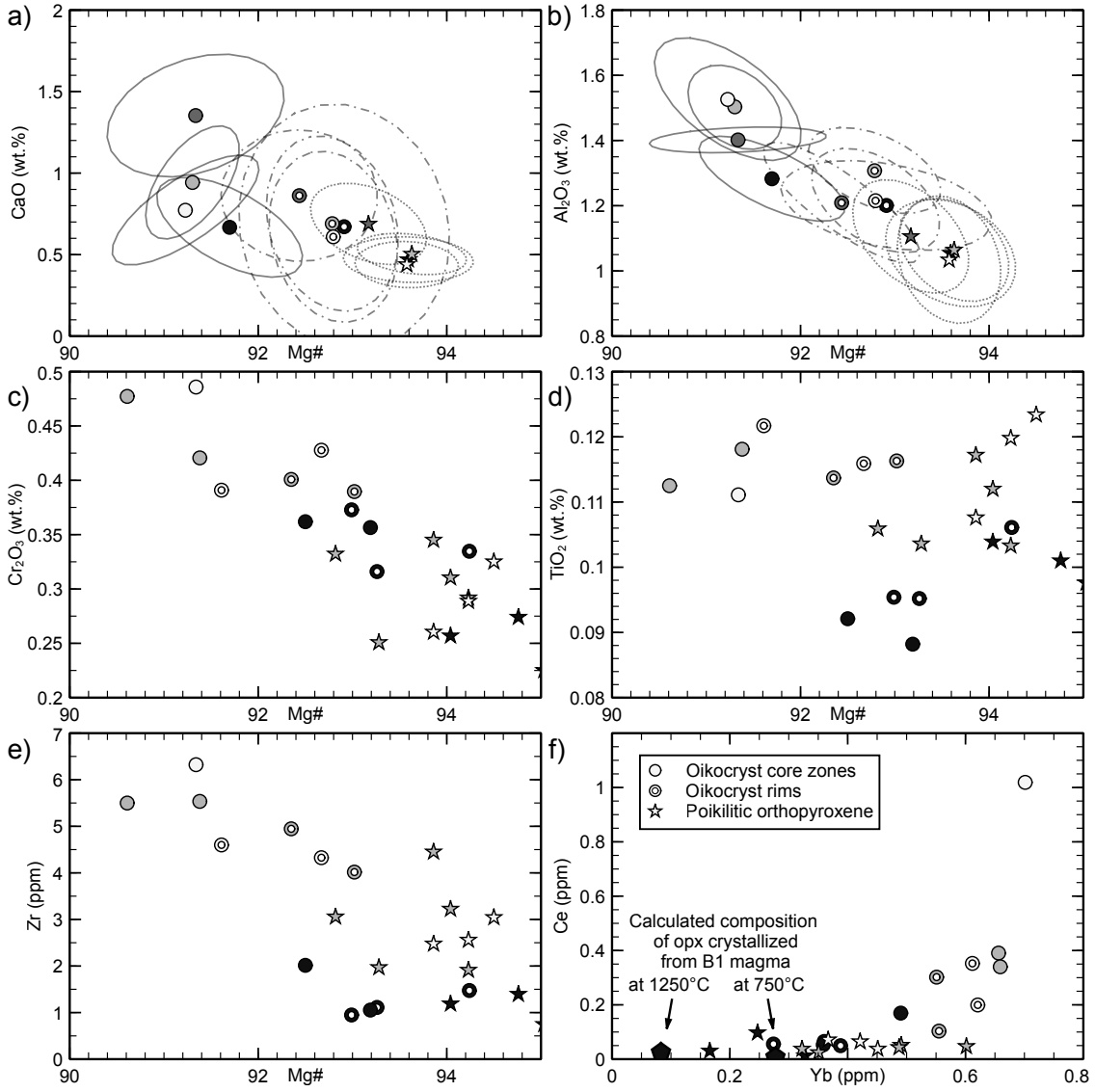

Figure 4.7: Variations in orthopyroxene chemistry **a** CaO, **b** Al_2O_3, **c** Cr_2O_3, **d** TiO_2, **e** Zr concentrations versus Mg# and **f** Ce/Yb ratio. Data in **a** and **b** were collected by electron microprobe, and that in **c**–**f** by LA-ICP-MS. Different grey scales display different heights along the MG1 (bright to dark from bottom to top). Filled circles represent orthopyroxene in oikocrysts core zones, open circles orthopyroxene along rims of oikocrysts core zones and stars poikilitic orthopyroxene. Ellipses indicate 66 % confidence intervals for each data set.

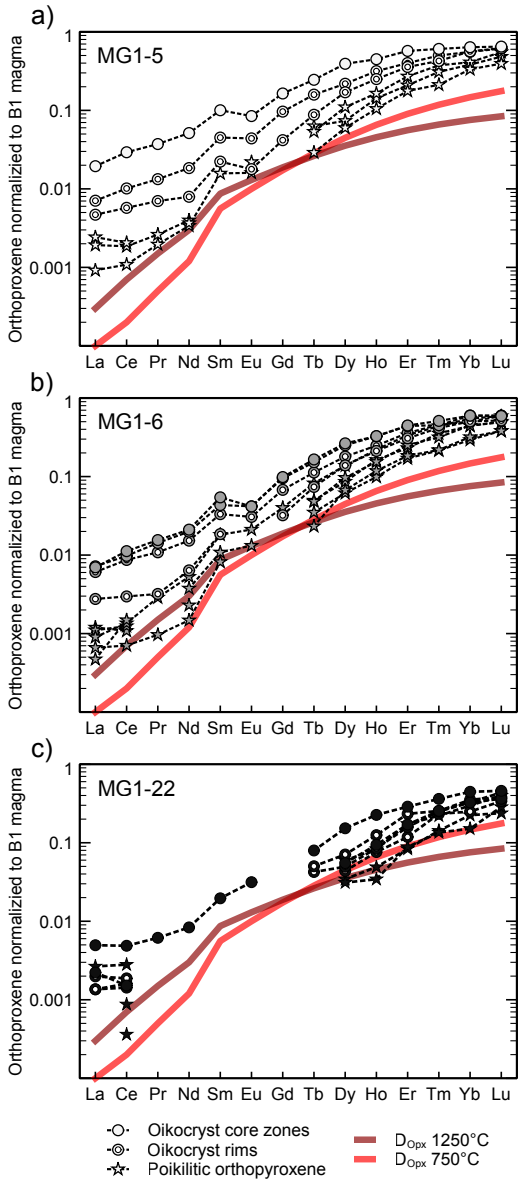

Figure 4.8: REE concentrations of orthopyroxene along the MG1 sample profile (bottom to top), normalised to a postulated B1 magma (Barnes et al., 2010).Red lines depict calculated partition coefficients taken from Sun and Liang (2013) and Yao et al. (2012).

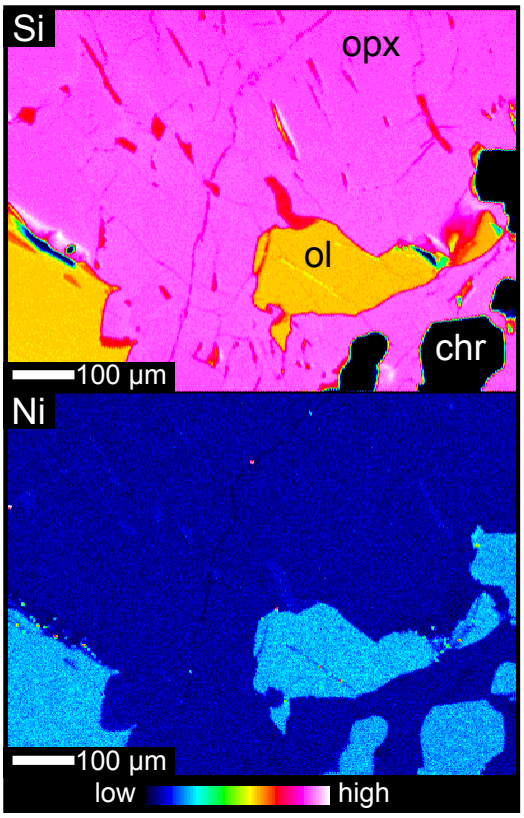

Figure 4.9: Electron microprobe Si and Ni distribution map of orthopyroxene oikocrysts. The relative concentrations are indicated by the colour bar.

4.4.4 Chromite composition

Chromite shows a clear correlation between texture and chemical composition of both major and trace elements Table. 4.3. Granular chromite grains have higher Mg# and lower Cr# (Cr/(Cr+Al)) as well as lower TiO_2 concentrations compared to chromite grains enclosed by poikilitic orthopyroxene (Fig. 4.10a, c). Calculated ferric/ferrous iron ratios reveal slightly higher values in grains enclosed by oikocrysts (Fig. 4.10b), especially in the upper and lower parts of the MG1 layer. A second minor trend can be observed closer to the middle of the MG1

layer, which contains chromite with almost constant Cr# and Fe^{3+}/Fe^{2+} ratios. Remarkably, the upper part of the MG1 is invariably chemically distinct from the lower part.

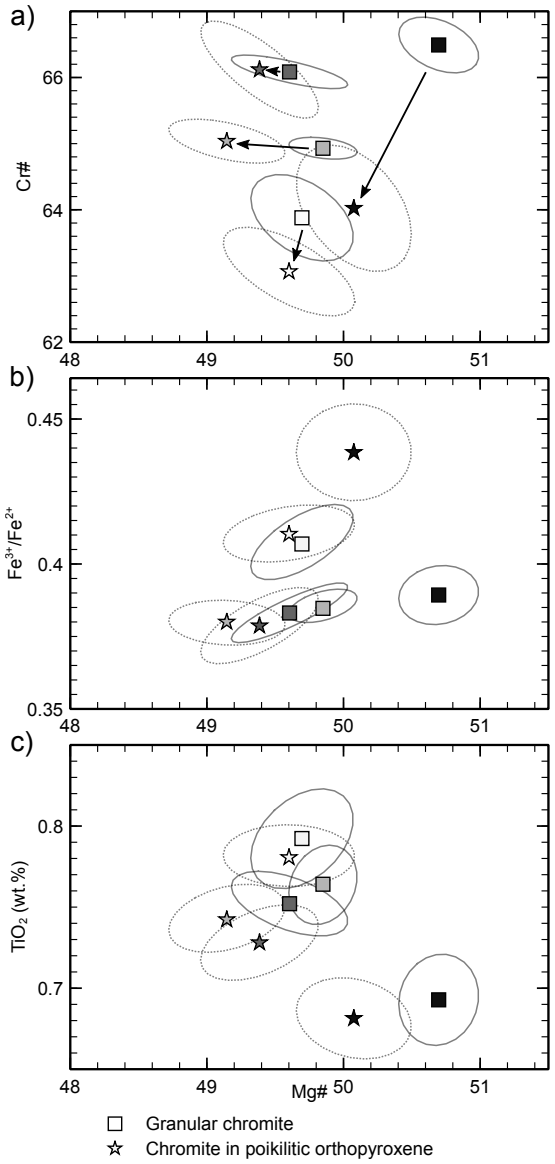

Figure 4.10: Variations in chromite chemistry. **a** Cr#, **b** Fe^{3+}/Fe^{2+} and **c** TiO_2 concentrations versus Mg# collected by electron microprobe. Different grey scales display different heights along the MG1 (bright to dark from bottom to top). Ellipses indicate 66 % confidence intervals for each data set.

4.5 Discussion

We will now assess the applicability of the two models of oikocryst formation in cumulate rocks, using our textural and chemical observations to evaluate which is most plausible for the orthopyroxene oikocrysts of the Bushveld MG1 chromitite. The critical observations that must be accounted for are:

1. Orthopyroxene oikocrysts contain almost chromite-free core zones, some of which contain olivine remnants, and have poikilitic aureoles containing euhedral to subhedral chromite chadacrysts (Figs. 4.2, 4.3d)

2. Oikocrysts occur as either single crystals, or form layer-parallel clusters and groups of several crystals (Figs. 4.2, 4.3a–b).

3. The chromitite hosting the oikocryst has a granular texture with only minor amounts of (hydrous) interstitial material. The microstructure of the chromitite is granular and coarse-grained, with 120° triple junctions and smoothly curved grain boundaries (Figs. 4.2, 4.3f, 4.6).

4. Chromite grains show no preferred crystal orientation, neither grains enclosed in poikilitic orthopyroxene nor grains in the granular chromitite, although some form small clusters in which individual grains show some evidence of crystallographic preferred orientations (Fig. 4.4a).

5. Oikocryst core zones and their poikilitic aureoles have the same crystallographic orientation. Oikocryst aggregates forming clusters and layers are commonly in the same crystallographic orientation (Fig. 4.5a, b).

6. Mineral chemistry of orthopyroxene core zones and poikilitic aureoles are different: core zones have lower Mg# and higher concentrations in incompatible trace elements, such as Zr and REE, compared to the poikilitic surroundings (Fig. 4.7).

7. The core zones are enriched in REE compared to the parental magma B1 and could not have crystallised in equilibrium with the surrounding minerals, whereas the composition of the poikilitic aureoles is consistent with growth from such a postulated parental magma (Fig. 4.8).

8. Granular chromite grains have lower Mg# and lower Cr# compared to chromite grains in poikilitic orthopyroxene (Fig. 4.10a).

Oikocrysts with partially similar characteristics have been reported from elsewhere in the Rustenburg Layer Suite: in MG1 several km northwards (I. Veksler, personal communication); the northern part of the Eastern Bushveld (Cameron, 1969; Cameron, 1975); and in the Stillwater Complex where Jackson (1961) described orthopyroxene oikocryst with replaced olivine inclusions in chromitite in great detail. This indicates that our observations may be of general relevance.

4.5.1 Post-cumulus origin of oikocrysts

The first of the post-cumulus models for oikocryst formation was proposed by Wager et al. (1960), who suggested that oikocrysts crystallise from interstitial melt in the cumulus chromite framework. Such an interstitial melt is likely to be relatively evolved and enriched in incompatible elements. Subsolidus re-equilibration of cumulus grains in contact with interstitial melt is thought to result in the post-cumulus enrichment in incompatible elements of cumulus phases, termed the trapped liquid shift effect (TLSE, Barnes, 1986b; Godel et al., 2011). This cannot explain why the later-crystallising poikilitic orthopyroxene has a composition consistent with growth from a more primitive magma (Fig. 4.8). Hence, a model involving entirely post-cumulus formation of the orthopyroxene oikocrysts is incompatible with our observations.

4.5.2 Cumulus formation of oikocrysts

The second main hypothesis for oikocryst formation is based on an origin at, or near, the magma–crystal mush interface (e.g. Mathison, 1987; Tegner and Wilson, 1995; Barnes et al., 2016). Accordingly, oikocrysts either form simultaneously with cumulus chromite by *in situ* growth at the magma–crystal mush interface, or form elsewhere and accumulate simultaneously by crystal settling (Hunter, 1996; Barnes et al., 2016). These two model variants can be distinguished microstructurally. *In situ* growth of grains in a gradient of either temperature or composition may lead to a preferred orientation of elongate crystals perpendicular to the magma-mush interface (e.g. the harrisites on Rum, Scotland: Wager et al., 1960; O'Driscoll et al., 2007). Conversely, crystal settling, with or without mechanical re-organisation of settled grains by magmatic currents, produces a preferred orientation of elongate grains parallel to the magma–crystal mush interface. Settling or deposition in magmatic currents may also result in grain sorting on the basis of size and/or density. Differing trace element compositions of orthopyroxene oikocryst cores and rims have also been used to argue for a cumulus origin of oikocrysts (Barnes et al., 2016).

Oikocryst core zones in the MG1 chromitite have shapes and orientations characteristic of grains accumulated during crystal settling (Figs. 4.2, 4.3b). Accordingly, the poikilitic orthopyroxene aureoles are therefore overgrowths on cumulus cores (Fig. 4.3a). The observed compositional differences between core zones and rims could then be explained if the cores zones were grown from a different magma to that in which they accumulated. However, this process cannot account for the observation that adjacent oikocrysts have the same crystallographic orientation. Our observations therefore support a two-stage growth history.

4.5.3 Oikocryst formation in the MG1 chromitite: an enhanced model

Our observations support a cumulus origin for the oikocryst core zones, but not as primary orthopyroxene. This is demonstrated by Fig. 4.3a in which the largest oikocryst core zone, pinched in the middle, contains two resorbed olivine grains, joined by a grain boundary located exactly at the waist of the oikocryst core, consistent with this having originally been two distinct olivine primocrysts. We conclude, therefore, that the core zones are former cumulus olivine crystals that have been replaced by orthopyroxene during peritectic reaction with a relatively Si-rich melt. With the exception of the few remaining remnants of olivine, the replacement was complete, as chemical characteristics of the cumulus olivine (e.g. high Ni concentrations, see Fig. 4.9 and Table 4.3) are no longer in evidence.

The presence of replacive orthopyroxene oikocrysts only a few cm above the base of the chromitite suggests that original cumulus olivine accumulated shortly after the MG1 layer began to form. While our data cannot be used to specify the process by which chromite accumulated, the aligned layers and clusters of former olivine crystals (Fig. 4.3a, b) are consistent with the hypothesis that olivine accumulated by crystal settling (Fig. 4.11a). The likelihood of both olivine and chromite accumulating simultaneously from the same overlying magma source can be assessed by comparing their settling velocities.

A rough estimation of settling velocities in a static liquid can be obtained from Stokes' Law, if we assume spherical grains and a low particle concentration:

$$V = \frac{2}{9}\frac{r^2 g(\rho_s - \rho_l)}{\eta}$$

where V is the settling velocity (cm/s), g is gravitational acceleration (981 cm/s^2, r is the radius of a spherical particle (cm), ρ_s is the density of the particle (g/cm^3), ρ_l the density of the liquid (g/cm^3) and η is the viscosity of the (assumed Newtonian) liquid (g/cm s). We used the following values of the parameters to calculate settling velocities for olivine and chromite: $r_{chr} = 0.02$ cm, $r_{ol} = 0.3$ cm, $\rho_{s\_chr} = 4.6$ g/cm^3, $\rho_{s\_ol} = 3.3$ g/cm^3, $\rho_l = 2.66$ g/cm^3 and $\eta = 520$ g/cm s. Values for the density and viscosity of the liquid were calculated according to Bottinga and Weill (1970) and Shawn (1972) respectively for the B1 magma at 1150° C. According to these values the settling velocity of olivine is ∼75 times faster than that of the co-existing chromite (3.3×10^{-6} cm/s for chromite grains and 2.4×10^{-4} cm/s for olivine).

We have assumed that the chromite grains settled individually: the limited evidence for clusters with similar crystallographic orientations in the granular chromitite suggests that at least some of the chromite grains were joined on low-energy faces to form clusters with a correspondingly larger Stokes' settling velocity. However, clusters appear to be rare, and are generally small (Fig. 4.4a) and so we argue that cluster formation was not sufficient to significantly affect the relative settling rates of chromite and olivine.

We have also assumed settling from a static liquid. However, our conclusion that olivine and chromite have significantly different settling velocities is relevant even if the magma were convecting. Martin and Nokes (1988) and Martin and Nokes (1989) showed that crystal settling occurs in convecting magmas in which the convective velocity exceeds the settling

velocity, when crystals enter the stagnant lower boundary layer. Settling from a convecting magma is slower than that from a static one, but in both situations larger denser crystals are more likely to settle faster than smaller lighter ones, to create a fining-upwards accumulation (Holness et al., 2017c). We note, however, that we did not detect such systematic changes in grain size.

While not arguing for accumulation of olivine primocrysts primarily by large-scale settling, we propose that the very different settling velocities support the hypothesis that the olivine primocrysts were introduced into the magma chamber by a crystal-bearing magma. A similar process was proposed by Barnes et al. (2016) to account for the oikocryst cores of the Ntaka Ultramafic Complex.

The second stage of our model is the peritectic replacement of the olivine primocrysts as a consequence of reaction with a more evolved (silica-rich) liquid in a solid-liquid reaction (e.g. Jackson, 1961; Nicholson and Mathez, 1991; Mathez, 1995; Mathez et al., 1997; Meurer and Boudreau, 1998b; Meurer and Boudreau, 1998a; Boorman et al., 2004; Barnes et al., 2016). The peritectic replacement of olivine primocrysts by orthopyroxene explains the observation that many cores have the same crystallographic orientation (i.e. several distinct olivine grains were replaced by a single orthopyroxene grain, attesting to a low nucleation rate for the replacive orthopyroxene, Fig. 4.5). It can also explain the negative Eu anomaly recorded by the oikocryst core zones, if the reactive liquid had already crystallised plagioclase. The high Mg# of the oikocryst core zones could be accounted for if the reactive liquid were evolved and oxidised, resulting in lower ferrous iron concentrations and the crystallisation of minerals with high Mg#.

The source of the infiltrating liquid is likely to have been the footwall pyroxenite (Fig. 4.11b). Upward flow may have been a consequence of gravitationally-driven viscous compaction. There is no evidence for dislocation creep in these rocks, so any compaction must have occurred by a more cryptic process such as melt-assisted diffusion creep (Holness et al., 2017a). Alternatively, upwards flow could have been driven by a reduction in density caused by *in situ* fractionation.

The poikilitic aureoles grew after olivine replacement (Fig. 4.11c), and their composition suggests that they grew from a different, less evolved, liquid, suggesting that by this point any upward flow from the footwall had ceased. Critically, the composition of the poikilitic aureoles is consistent with growth from a non-fractionated B1 magma, suggesting that they grew in a highly porous and permeable mush from interstitial liquid in effective chemical communication with the bulk magma overlying the crystal mush.

4.5.4 Post-accumulation microstructural modification of the chromitite mush

The final stages of solidification involved textural modifications of the chromite grains that are not enclosed by oikocrysts (Fig. 4.11d). The microstructure of the granular chromitite is significantly different to that of the chromite enclosed by the oikocrysts (Figs. 4.3f, 4.6). It also has a different composition (Fig. 4.10). These features have been observed in many of the Bushveld chromitite layers (Cameron, 1975; Hulbert and von Gruenewaldt, 1985; Nicholson and Mathez, 1991; Kottke-Levin et al., 2009; Voordouw et al., 2009; Junge et al., 2014). The reasons for these differences are not clear but we suggest they may involve a combination of

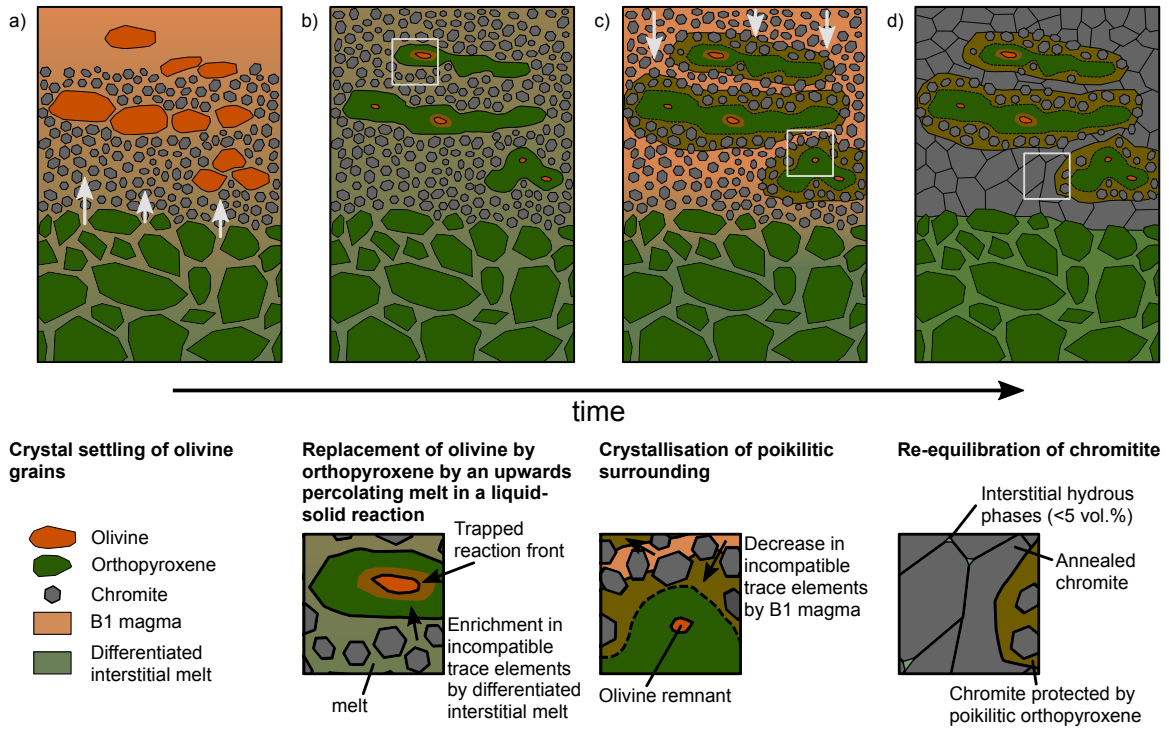

Figure 4.11: Proposed model for the formation of orthopyroxene oikocrysts in the MG1 chromitite layer. See text for further explanation.

adcumulus growth, textural modification and diffusional modification of composition: the relative balance of these processes is not known.

If the chromitite formed by grain settling, the maximum packing of the chromite (and thus the maximum mode) would be that for close packing of spheres, or 74 vol.%. More efficient packing can occur in accumulations with a range of grain sizes (Epstein and Young, 1962; Jerram et al., 2003), but the narrow range of sizes observed for the grains enclosed by orthopyroxene means that we cannot call on the effect of a strongly polydisperse grain population to increase the packing efficiency. Moreover, settling will result in a disordered grain arrangement. Random loose packing of single grains (defined as the loosest, mechanically stable packing state) results in 56–54 vol.% solids (Onoda and Liniger, 1990; Ciamarra and Coniglio, 2008; Zamponi, 2008; Farrell et al., 2010), and this packing can be reduced even further if grains settled as clusters (Heaney et al., 1995; Dong et al., 2006; Yang et al., 2007).

The evidence shown in Fig. 4.4 is supportive of the formation of at least some clusters of chromite grains. Clusters or chain formation by auto-nucleation or synneusis generally results in grains being joined by low-energy grain boundaries, resulting in a crystallographic relationship between the individual grains. Prichard et al. (2015) argue that inter-grain relationships within nodular chromite, in which grains in the central region share the same <110> axis as grains in the outer parts of the nodule indicate self-nucleation (of the outer grains on the inner grains). Such relationships are not evident in the MG1 chromitite. While some chromite grains share a 100 contact face (Fig. 4.4d, cluster 1), most of the clusters we examined share a common axis (Fig. 4.8d, e), but with no preference for any particular common axis (see the percentages for each axis given at the bottom of Fig. 4.4): these

features are most likely a result of cluster formation by synneusis. However, there are only few clusters in evidence in Fig. 4.4 and we argue that most of the chromite in the MG1 chromitite accumulated as single grains.

The chromite mode in the poikilitic orthopyroxene aureoles is 50–60 vol.%. This is in the range expected for a random loose packing of single monodisperse grains, and suggests that the spatial distribution and grain size population of chromite grains in the earliest stages of mush formation was preserved by early enclosure by the orthopyroxene. However, the almost 100 vol.% chromite mode in the granular chromitites demonstrates that they must have experienced some adcumulus growth.

Adcumulus growth of chromite grains in close proximity to interstitial orthopyroxene would necessitate the localised suppression of orthopyroxene nucleation and growth. The replacement of adjacent olivine primocrysts by single grains of orthopyroxene and the continued growth of the orthopyroxene grains into the chromite mush to form extended oikocrysts is certainly consistent with this. One possible mechanism to create the observed microstructure is therefore to have the interstitial liquid crystallising both chromite and orthopyroxene, with inhibition of orthopyroxene nucleation confining orthopyroxene growth to the immediate neighbourhood of olivine primocrysts. Adcumulus overgrowth of the chromite near the magma-mush interface would then have resulted in the densification of the chromite mush. The complete absence of plagioclase in the MG1 chromitite is consistent with this hypothesis. The last stages of solidification involved the crystallisation of a highly evolved, hydrous liquid to form the small amounts of biotite and hornblende.

The coarser grain size and granular microstructure of the chromite adcumulate would then be a simple consequence of its essentially monomineralic composition, permitting rapid grain boundary migration and the attainment of textural equilibrium, driven by the minimisation of interfacial energies (e.g. Hunter, 1987; Hunter, 1996; Holness and Vernon, 2015). Textural equilibration resulted in the smoothing of grain boundaries, the attainment of 120° triple junctions and the onset of normal grain growth driven by differences in grain boundary curvature (Thomson, 1887; Bulau et al., 1979; Holness, 2005; Holness et al., 2007). CSD data (Fig. 4.6) reveal a rotation consistent with normal grain growth, with a reduction in smaller grains and increase in larger grains in the granular chromitite compared to the population of grains enclosed in the orthopyroxene. The difference in composition between the granular chromitite and the chromite enclosed by oikocrysts (Fig. 4.10) could then be accounted for as the chromite enclosed by orthopyroxene would have equilibrated with the surrounding pyroxene, whereas the granular chromitite retained its original composition.

4.5.5 Implications for chromitite formation models

The focus of this paper has been on the oikocrysts within the chromitite, but our textural and chemical observations can also be used to shed some light on the formation of the chromitite layers themselves. Numerous models and ideas have been proposed to account for the formation of chromitite layers in layered intrusions (Maier et al., 2013; Cawthorn, 2015), including those based on the mobilisation of cumulate slurries (Maier et al., 2013). Importantly, we see no fining-upwards of the size in chromite grains enclosed in the oikocrysts (i.e. those most likely to retain their original size), suggesting that the slurry model cannot account for these particular chromitite layers.

4.6 Conclusions

Orthopyroxene oikocrysts in the MG1 chromitite layer of the western Bushveld Complex grew during a complex series of steps, involving the peritectic replacement of cumulus olivine triggered by an upwards percolating, incompatible element enriched, evolved melt. The core zones were then overgrown by poikilitic orthopyroxene in equilibrium with the parental melt B1 near the magma-crystal mush interface. Finally, post-cumulus adcumulus chromite growth followed by annealing of chromite crystals outside the oikocrysts led to the formation of granular chromitite.

Our integrated approach provides an understanding of different magmatic processes, controlling both the geochemical and the textural evolution of oikocrysts. Although this study describes small-scale phenomena, similar oikocrysts are observed in other parts of the Bushveld Complex, suggesting that the history we have outlined here may be common in layered mafic intrusions.

4.7 Acknowledgements

FEDK was supported by the German Federal Ministry of Education and Research (BMBF), Grant FKZ 033R119C, ZV by Marie Skłodowska-Curie Individual European Fellow grant. Cronimet Chrome Mining SA (Pty) Ltd. is thanked for provision of drill core material. We are grateful to M. Oeser-Rabe and S. Schuth for help with the LA-ICP-MS analyses, also assistance by K. Born and P. Czaja at the SEM and microprobe at the Museum für Naturkunde Berlin are greatly acknowledged. Fruitful discussions with M. C. Hoffmann and I. V. Veksler were highly appreciated. Helpful reviews by two anonymous reviewers and editor Chris Ballhaus greatly improved the original paper.

Associate editor: Chris Ballhaus

Table 4.1: Average orthopyroxene composition of *N* microprobe and *n* LA-ICP-MS analyses.

	MG1-5			MG1-6		
	Core	Rim	Poik	Core	Rim	Poik
N (n)	15 (1)	26 (2)	30 (3)	11 (2)	22 (2)	46 (5)
SiO_2	56.2	56.7	57.0	56.5	56.8	57.1
TiO_2	0.10	0.11	0.11	0.11	0.11	0.11
Al_2O_3	1.53	1.22	1.03	1.50	1.31	
Cr_2O_3	0.42	0.54	0.48	0.43	0.56	
MgO	33.8	34.8	35.4	33.9	34.8	35.4
MnO	0.17	0.16	0.15	0.18	0.16	0.15
FeO	5.80	4.81	4.33	5.75	4.82	4.30
CaO	2.25	2.28	2.35	2.16	2.24	2.35
Na_2O	7.82	6.86	6.44	7.69	6.84	6.41
Total	0.77	0.61	0.44	0.94	0.69	0.50
Mg#	91.2	92.8	93.6	91.3	92.8	93.6
Sc	34	34	29	33	34	31
Ti	666	712	701	691	689	650
V	87	71	50	75	66	49
Cr	3324	2801	1994	3071	2704	2094
Mn	1484	1359	1227	1491	1321	1214
Co	63	49	38	62	48	38
Ni	607	577	530	575	569	530
Zn	44	37	31	40	33	27
Rb	bdl	bdl	bdl	bdl	bdl	bdl
Sr	0.93	0.26	0.10	0.29	0.21	0.09
Y	4.52	2.70	1.39	3.36	2.42	1.56
Zr	6.32	4.46	2.69	5.52	4.48	2.92
Nb	0.037	0.034	0.025	0.036	0.039	0.024
Ba	bdl	bdl	bdl	0.117	0.110	0.171
La	0.350	0.106	0.032	0.127	0.080	0.016
Ce	1.019	0.276	0.058	0.365	0.203	0.041
Pr	0.155	0.042	0.010	0.062	0.029	0.008
Nd	0.796	0.204	0.057	0.317	0.168	0.050
Sm	0.281	0.094	0.044	0.137	0.072	0.035
Eu	0.069	0.025	0.016	0.034	0.025	0.014
Gd	0.394	0.166	bdl	0.233	0.120	0.096
Tb	0.083	0.042	0.016	0.053	0.031	0.016
Dy	0.745	0.369	0.154	0.489	0.302	0.171
Ho	0.170	0.108	0.052	0.124	0.087	0.057
Er	0.600	0.398	0.230	0.467	0.350	0.246
Tm	0.098	0.075	0.048	0.078	0.071	0.050
Yb	0.701	0.616	0.413	0.658	0.553	0.450
Lu	0.114	0.108	0.083	0.104	0.097	0.082
Hf	0.180	0.181	0.117	0.202	0.181	0.130
Pb	0.099	0.070	0.057	0.166	0.107	0.108
U	0.058	0.021	0.010	0.022	0.013	0.002
Ce/Tb	12.327	6.642	3.542	6.831	6.448	2.546

Main elements are given in wt.%, trace elements in ppm.
Core orthopyroxene oikocryst core zone, *rim* outermost ∼100 µm of the core zones, *poik* poikilitic orthopyroxene,
bdl below detection limit.

Table 4.1: (cont.) Average orthopyroxene composition of *N* microprobe and *n* LA-ICP-MS analyses, orthopyroxene in the section MG1–9 has not been analysed by LA-ICP-MS.

	MG1-9			MG1-22		
	Core	Rim	Poik	Core	Rim	Poik
N (n)	7 (0)	9 (0)	19 (0)	10 (2)	17 (2)	17 (3)
SiO_2	56.3	56.4	56.8	56.6	56.7	57.0
TiO_2	0.09	0.11	0.11	0.08	0.09	0.09
Al_2O_3	1.40	1.21	1.11	1.28	1.20	1.05
Cr_2O_3	0.48	0.50	0.51	0.38	0.43	0.47
MgO	33.5	34.3	35.0	34.3	34.8	35.4
MnO	0.18	0.15	0.16	0.17	0.16	0.15
FeO	5.66	5.01	4.57	5.53	4.74	4.32
CaO	2.08	1.96	2.09	2.09	2.17	2.28
Na_2O	7.53	6.77	6.45	7.41	6.69	6.37
Total	1.35	0.86	0.69	0.67	0.67	0.47
Mg#	91.3	92.4	93.2	91.7	92.9	93.6
Sc				30	29	27
Ti				540	593	604
V				64	56	44
Cr				2458	2334	1725
Mn				1384	1268	1157
Co				51	41	32
Ni				565	526	479
Zn				35	30	26
Rb				bdl	bdl	bdl
Sr				0.24	0.39	0.28
Y				1.35	0.89	0.59
Zr				1.53	1.18	1.11
Nb				0.031	0.035	0.034
Ba				bdl	bdl	bdl
La				0.065	0.028	0.048
Ce				0.111	0.057	0.047
Pr				0.026	bdl	bdl
Nd				0.129	bdl	bdl
Sm				0.055	bdl	bdl
Eu				0.026	bdl	bdl
Gd				bdl	bdl	bdl
Tb				0.027	0.016	bdl
Dy				0.197	0.104	0.079
Ho				0.061	0.036	0.021
Er				0.241	0.179	0.121
Tm				0.050	0.040	0.027
Yb				0.424	0.341	0.247
Lu				0.072	0.067	0.054
Hf				0.063	0.051	0.063
Pb				0.378	0.144	0.232
U				0.027	0.012	0.014
Ce/Tb				4.140	3.644	

Main elements are given in wt.%, trace elements in ppm.
Core orthopyroxene oikocryst core zone, *rim* outermost ∼100 µm of the core zones, *poik* poikilitic orthopyroxene,
bdl below detection limit.

Table 4.2: Average olivine composition of *N* microprobe analyses and *n* LA-ICP-MS analyses.

	MG1-5	MG1-22
N (n)	5 (4)	9 (0)
SiO_2	39.6	40.0
TiO_2	bdl	bdl
Al_2O_3	bdl	bdl
Cr_2O_3	bdl	bdl
MgO	48.2	49.2
MnO	0.15	0.11
FeO	11.6	10.1
CaO	0.02	0.03
NiO	0.36	0.36
Total	99.9	99.8
Mg#	88.1	89.7
Sc	4	
Ti	14	
V	1	
Cr	21	
Mn	1205	
Co	144	
Ni	2810	
Zn	36	
Rb	bdl	
Sr	bdl	
Y	0.03	
Zr	0.05	
Nb	bdl	
Ba	bdl	
La	bdl	
Ce	bdl	
Pr	bdl	
Nd	bdl	
Sm	bdl	
Eu	bdl	
Gd	bdl	
Tb	bdl	
Dy	bdl	
Ho	bdl	
Er	bdl	
Tm	bdl	
Yb	0.0349	
Lu	0.0108	
Hf	0.0038	
Pb	bdl	
U	bdl	

Main elements are given in wt.%,
trace elements in ppm.
bdl below detection limit.

Table 4.3: Average chromite composition of *N* microprobe analyses.

	MG1-5		MG1-6		MG1-9		MG1-22	
	Chromite in oikocrysts	Granular chromite	Chromite in oikocrysts	Granular chromite	Chromite in oikocrysts	Granular chromite	Chromite in oikocrysts	Granular chromite
N	40	37	40	27	21	31	19	25
TiO_2	0.78	0.79	0.74	0.76	0.73	0.75	0.68	0.69
SiO_2	0.05	0.01	0.04	0.00	0.03	0.01	0.03	0.02
Al_2O_3	17.2	16.9	16.4	16.5	15.9	15.9	16.6	15.7
Cr_2O_3	43.8	44.4	45.5	45.5	46.2	46.1	44.1	46.5
V_2O_3	0.28	0.28	0.26	0.26	0.25	0.25	0.27	0.26
Fe_2O_3	8.71	8.61	8.11	8.11	8.02	8.08	9.16	8.03
FeO	19.1	19.0	19.2	19.0	19.1	19.0	18.8	18.6
MnO	0.27	0.28	0.28	0.27	0.28	0.28	0.28	0.28
MgO	10.5	10.6	10.4	10.6	10.4	10.5	10.6	10.7
ZnO	0.06	0.05	0.06	0.06	0.05	0.05	0.05	0.05
NiO	0.16	0.16	0.14	0.14	0.15	0.15	0.16	0.13
Total	100.9	101.1	101.1	101.1	101.1	101.1	100.8	101.0
Mg#	49.6	49.7	49.1	49.8	49.4	49.6	50.1	50.7
Cr#	63.1	63.9	65.0	64.9	66.1	66.1	64.0	66.5

Main elements are given in wt.%.

Chapter 5

Lateral variations in the Unit 7-8 Cr-spinel seam of the Rum Layered Intrusion, NW Scotland[1]

The Rum Layered Intrusions, NW Scotland hosts lateral continuous Cr-spinel seams, which are present at the base of several peridotite-troctolite units. This study focuses on the Unit 7-8 boundary seam, detailed field observations are presented here together with microstructural and mineral chemistry analyses of the seam and its immediate footwall and hanging wall. Detailed mapping and sampling revealed significant lateral variations in structure and mineral composition. Although the Cr-spinel seam is continuous over almost 3 km, it is absent towards the centre and the margins of the intrusion. In addition, the compositional character of Cr-spinel and plagioclase phases varies systematically along strike, illustrating a trend of increasing fractionation with increasing distance from the centre and the main feeder.

Our combined observations suggest a chronology of replenishment events, which formed the Unit 7-8 seam package and help to refine the current model: we propose that the anorthosite layer underlying the Cr-spinel seam and the seam itself originated by two genetically linked, but separated replenishment steps. (1) The anorthosite layer formed due to assimilation of the Unit 7 troctolite crystal mush by intruding, picritic magma. (2) The Unit 7-8 Cr-spinel seam crystallised after the anorthosite layer on top of the crystal mush or due to injections within the anorthosite mush. Moreover, we suggest that the localised occurrence of the anorthosite and seam was spatially controlled and depended on a certain distance to the main feeder in the central part of the intrusion.

[1]This chapter is based on a manuscript that is almost ready for submission to *Contributions to Mineralogy and Petrology*: Kaufmann, F. E. D., O'Driscoll, B., Hecht, L. Lateral variations in the Unit 7-8 Cr-spinel seam of the Rum Layered Intrusion, NW Scotland.

5.1 Introduction

The presence of Cr-spinel seams in layered intrusions remains a controversial phenomenon in igneous petrology. Despite being the world's main reserve of Cr and associated platinum-group elements (PGE), their formation is still not well understood, and a variety of contrasting petrological models exist for their formation. These models include magma mixing of the residual melt with intruding primitive or assimilated felsic melts, changes in pressure or oxygen fugacity or the emplacement as chromite-rich slurries (see Namur et al., 2015, for detailed reviews). The Rum Layered Suite in NW Scotland is a classic example of a layered intrusion that hosts Cr-spinel seams (Harker, 1908; Brown, 1956). The Rum Cr-spinel seams have been the objects of careful petrological study for decades (Harker, 1908; Brown, 1956; Henderson and Suddaby, 1971; Henderson and Suddaby, 1971; Young, 1984; Volker and Upton, 1990; Emeleus, 1994; Emeleus and Hudson, 1997; O'Driscoll et al., 2009b; O'Driscoll et al., 2009a; O'Driscoll et al., 2010; Hepworth et al., 2017). This is due in part to the fact that some of the seams exhibit significant, albeit sub-economic, enrichment in the PGE (Butcher et al., 1999; Power et al., 2003; O'Driscoll et al., 2009a). In addition, the style of PGE mineralisation on Rum is quite similar to that of the economically significant Merensky Reef and UG2 chromitites (Bushveld Complex, South Africa), in that Cr-spinel seams apparently occur at unconformable boundaries in the cumulate section, often associated with anorthosite and mafic orthocumulate. Most previous work on the Rum intrusion Cr-spinel seams has focused on discrete vertical sections of the cumulate stratigraphy containing the Cr-spinel seams (Power et al., 2000; O'Driscoll et al., 2009b; O'Driscoll et al., 2009a). Unlike other significant PGE reefs (e.g., the Bushveld examples noted above), little information exists on the detailed petrology of the Rum Cr-spinel seams along strike, i.e., the degree to which they vary or appear similar laterally. The Rum Cr-spinel seams likely formed during some significant (intrusion-scale) replenishment of primitive magma (Dunham and Wadsworth, 1978; O'Driscoll et al., 2009a), so establishing the relationships between the Cr-spinel seams and their host rocks, and whether these vary laterally, could reveal valuable information on the nature and extent of the replenishment event that triggered precious metal enrichment in the Rum intrusion.

The aim of this study is to advance our understanding of the mechanisms that drive PGE-reef formation in layered intrusions, by characterising the Unit 7-8 Cr-spinel seam and hanging wall-footwall lithologies laterally across the extent of the intrusion. The Unit 7-8 Cr-spinel seam package contains a diverse assemblage of lithologies (anorthosite, deformed troctolite, multiple Cr-spinel seams) as well as the highest PGE abundances of any of the Rum PGE-reefs (O'Driscoll et al., 2009a). Here, we report detailed field observations, petrographic and mineral chemistry data to elucidate and quantify lateral variations in the macro-to-microstructural and mineral chemical character of the Unit 7-8 Cr-spinel seam and its host rocks.

5.2 Geological Setting

The Rum Layered Intrusion (Fig. 5.1) is a classic example of an mafic-ultramafic layered intrusion (Brown, 1956; Wager and Brown, 1967). It formed in response to opening of the North Atlantic (Emeleus et al., 1996), at ca. 60 Ma (Hamilton et al., 1998). The intrusion is subdivided into the Eastern Layered Intrusion (ELI), Western Layered Intrusion (WLI) and the Central Intrusion (CI). The comparatively well-studied ELI consists of 16 macro-rhythmic units of feldspatic peridotite-troctolite (±olivine gabbro), each of which varies considerably in thickness (Brown, 1956; Emeleus et al., 1996). The macro-rhythmic units of the ELI are generally interpreted to represent new batches of replenishing magma (Emeleus et al., 1996; O'Driscoll et al., 2009a) of basaltic-to-picritic composition (Upton et al., 2002). Cr-spinel seams occur at the bases of the 6-7, 7-8, 11-12 and 13-14 units (Brown 1956; O'Driscoll et al. 2009a). These seams are typically 2–5 mm thick and can be traced laterally over much of the 2–3 km extent of the ELI (Emeleus et al., 1996). Elevated PGE concentrations have been reported for the Cr-spinel seams of the ELI (Butcher et al., 1999; O'Driscoll et al., 2009a). O'Driscoll et al. (2009b) and O'Driscoll et al. (2010) reported that several of the 'main' Cr-spinel seams at unit bases are associated with other, thinner, subsidiary seams several centimetres above and below the unit boundary (e.g., Unit 7-8 and 11-12). Early studies proposed that the Cr-spinel seams formed by crystal settling on top of the solidifying crystal mush (Brown, 1956; Henderson and Suddaby, 1971; Dunham and Wilkinson, 1985), following new magma replenishment. However, more recently, it has been proposed that the ELI Cr-spinel seams crystallised *in situ*, due to assimilation of the troctolite footwall by picritic melt (O'Driscoll et al., 2009b; O'Driscoll et al., 2010). Variations of this model have subsequently gained traction for PGE-reef petrogenesis at other layered intrusions (Latypov et al., 2013; Latypov et al., 2015; Latypov et al., 2017a).

5.3 Field relations

The Unit 7-8 boundary was mapped and sampled in a number of localities across the extent of the ELI to assess lateral variation in the presence of the Cr-spinel seam and its immediate footwall and hanging wall (see Figure 5.1 for locality details). In very general terms, the Unit 7-8 boundary sequence comprises the Unit 7 troctolite footwall with ubiquitous elongated anorthosite autoliths and peridotite schlieren, overlain by a 1–20 cm thick layer of anorthosite, the 1–3 mm thick Cr-spinel seam and the Unit 8 feldspathic peridotite on top (Fig. 5.2a). However, from one locality to the next, significant structural and lithological variations are observed.

The Cr-spinel seam varies in thickness along strike (0.5–4 mm) with an average thickness ranging between 1–2 mm. The main Cr-spinel seam is generally located at the anorthosite-peridotite contact (Fig. 5.2a). However, the main seam may also transgress into the overlying peridotite (Fig. 5.3a, b). The Cr-spinel seam is undulose and frequently forms small depressions extending into the footwall (Fig. 5.2b), forming concentrated pockets of Cr-spinel (Fig. 5.3b, c).

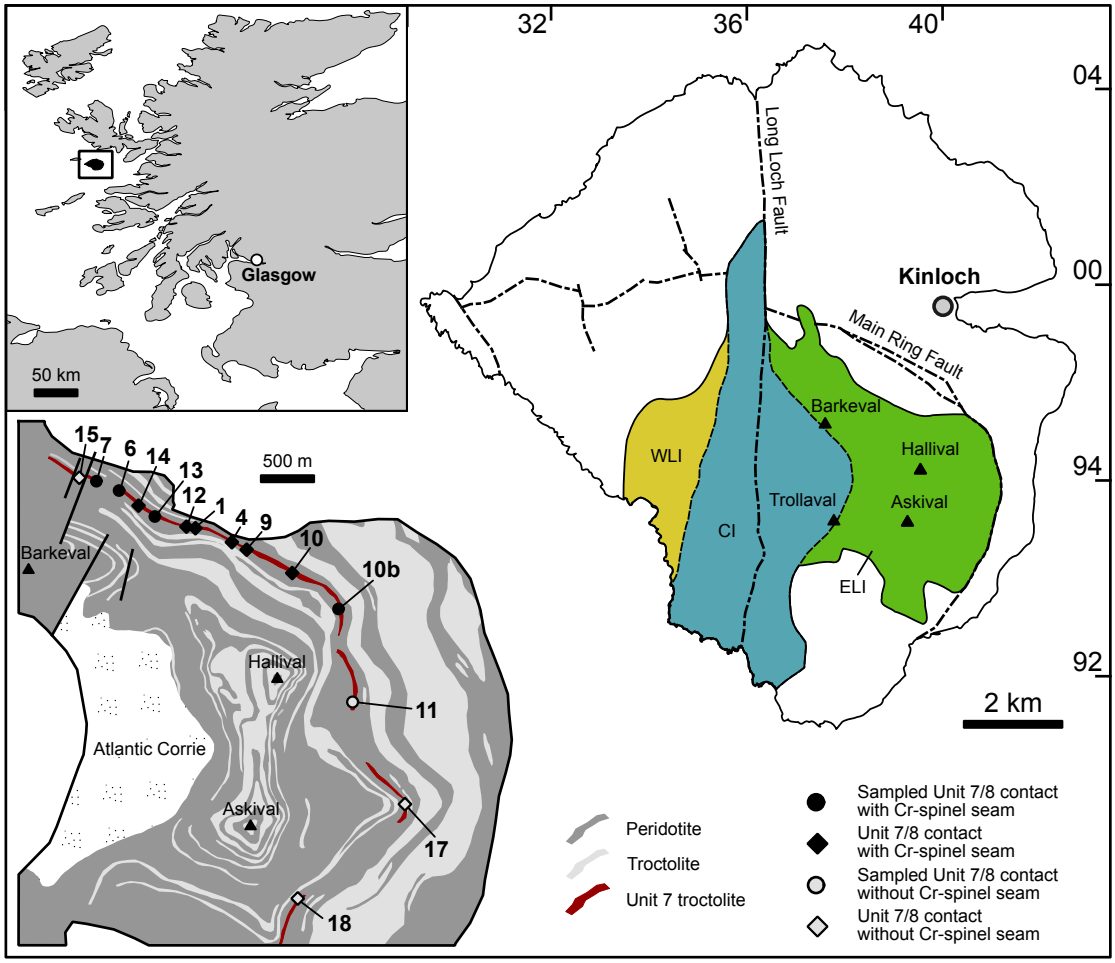

Figure 5.1: Location map of the Rum Layered Intrusion, NW Scotland and simplified geological map of the Rum Layered Intrusion, modified after Emeleus (1994). WLI, Western Layered Intrusion; CI Central Intrusion; ELI, Eastern Layered Intrusion.

These structures were referred to as 'cone-structures' by O'Driscoll et al. (2010). These cones are usually 1–2 cm in width, but can reach amplitudes of up to 10 cm and they may represent small-scale analogues of potholes frequently occurring in the chromitite layers of the Merensky Reef and UG2 chromitite of the Bushveld Complex. The main seam is often accompanied by additional seams occurring within or at the lower contact of the anorthosite layer (Fig. 5.2c, e). These subsidiary seams can be oriented parallel to the main seam (Fig. 5.2c), or may bifurcate (Figs. 5.2e, 3b). They are generally thinner (0.5–1 mm) than the main seams and are laterally discontinuous. The footwall anorthosite layer below the seam is a 2–20 cm thick (on average 2–6 mm), strongly foliated layer that overlies troctolite. It is present in most of the boundary sections studied, but locally it can be cut or pinched out by the overlying Cr-spinel seam and peridotite (Fig. 5.3a, b).

The footwall troctolite is a complex layer of deformed cumulates. It typically contains highly deformed diffuse schlieren of peridotite. The basal contact of the overlying anorthosite layer cross-cuts the foliation, structures and peridotite schlieren in the troctolite (Fig. 5.2d). Autoliths of anorthosite commonly occur throughout the upper 3–4 m of the troctolite (Fig. 5.2a), with the exception that they are not seen in the uppermost 5–10 cm immediately

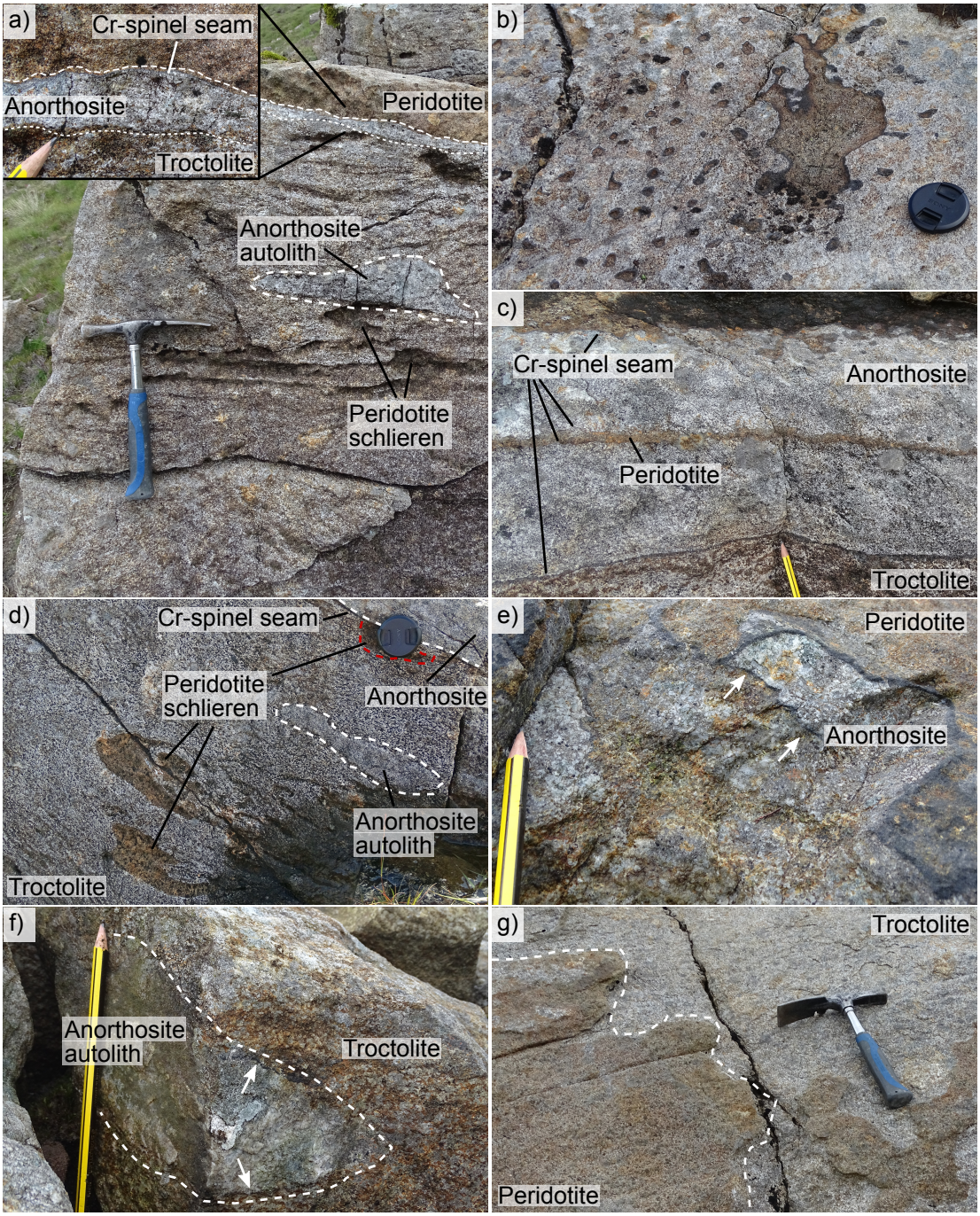

Figure 5.2: Field relations of the Unit 7-8 boundary. **a** Typical Unit 7-8 boundary with ca. 2 mm thick undulating Cr-spinel seam (*location 13*). **b** Plan view of Cr-spinel seam. The seam forms small depressions extending into anorthosite (*location 1*). **c** Complex Unit 7-8 boundary with thick anorthosite layer, a layer of peridotite and four Cr-spinel seams, which occur on all contacts (*location 12*). **d** Unit 7 troctolite footwall troctolite with lengthened anorthosite autolith and deformed peridotite schlieren, which can be cross-cut by the anorthosite layer, here marked in red (*location 1*). **e** Bifurcation of Cr-spinel seam, additional small seam is indicated by arrows (*location 6*). **f** Anorthosite autolith (dashed lines) in the footwall troctolite rimmed by small Cr-spinel seams (arrows). **g** Unit 7-8 boundary without Cr-spinel seam and anorthosite layer (*location 11*).

below the anorthosite layer. The autoliths are elongate and lie with their long-axis (as observed on the outcrop plane) oriented parallel to layering in the troctolite, forming a flat ellipsoid.

They vary in length from several mm to almost 0.5 m. The height of the anorthosite autoliths rarely exceeds 10 cm and most are in the range of 1–5 cm. A systematic change in shape or aspect ratio depending on the distance to the boundary is not apparent. Some anorthosite autoliths are rimmed by mm-thick rinds of Cr-spinel (Fig. 5.2f).

The Unit 7-8 boundary is well-exposed along the Barkeval-Hallival traverse and could be mapped continuously over large parts of the northern portion of the ELI (Fig. 5.1). The main Cr-spinel seam is present across the entirety (∼3 km) of this traverse. The seam in the locations to the northwest, close to Barkeval (Localities 6 and 7), displays the maximum thickness, while it generally thins out towards the northeast. To the northeast, east and south of Hallival, exposure of the Unit 7-8 boundary becomes poor (Fig. 5.1). In the latter areas, the main Cr-spinel appears to be absent at the Unit 7-8 boundary position (e.g., Localities 11, 17 and 18). There are other significant variations observed in the Unit 7-8 package across the entire traverse. For example, the anorthosite layer appears to be relatively thick in the northwest (>10 cm), but thins out to <1 cm thick in the northwest (i.e., Localities 6, 7, 13 and 14) and disappears entirely in the southeast (Locality 11 and further south). At its thickest, the lower contact of the anorthosite layer is bounded by a subsidiary seam (Localities 4 and 12), which can be traced for several tens of metres. To the northwest of Barkeval, exposure is poor and the Cr-spinel seam and anorthosite layer are missing or are highly discontinuous. At Locality 15, the Unit 7 troctolite is directly overlain by the Unit 8 peridotite (Figs. 5.2g, 5.4). Peridotite schlieren and anorthosite autoliths occur across the entirety of the traverse in the Unit 7 troctolite regardless of the presence of the anorthosite layer. Systematic lateral variations in distribution frequency or size of autoliths are not evident. Autoliths, rimmed by Cr-spinel rinds, could be observed in different localities (e.g., localities 6 and 11).

5.4 Petrography

The granular-textured Unit 8 peridotite comprises euhedral (cumulus) olivine, Cr-spinel and intercumulus plagioclase and clinopyroxene (Fig. 5.3c, d). In general, Cr-spinel is embedded in the intercumulus plagioclase, often in well-developed embayments in olivine crystals (Fig. 5.5a). Less commonly, Cr-spinel occurs as inclusions in clinopyroxene or olivine crystals. In the lowermost 1-5 cm of the peridotite, diffuse concentrations of Cr-spinel are locally developed in a chain-textured arrangement around the cumulus olivine framework. The proportion of Cr-spinel in the Unit 8 peridotite ranges between 1 and 7 vol.%, with an average of ∼3.5 vol.%.

Cr-spinel in the main seam is euhedral to subhedral, with a grainsize range of 0.01–0.5 mm (average ca. 0.15–0.25 mm). The overall proportion of Cr-spinel in the seam ranges between 55–65 vol.%. Cr-spinel seams are typically cemented by intercumulus plagioclase and to a lesser extent by intercumulus olivine oikocrysts (Fig. 5.5c). Cr-spinel often forms clusters or chains of several crystals, attached by shared grain boundaries. Such clusters exhibit an increase in average Cr-spinel grain size. Plagioclase from the underlying anorthosite layer and olivine from the overlying peridotite extend into the seam (Fig. 5.5a, c), as evidenced by optical continuity of these minerals across the seam boundaries. Thus, a given olivine or

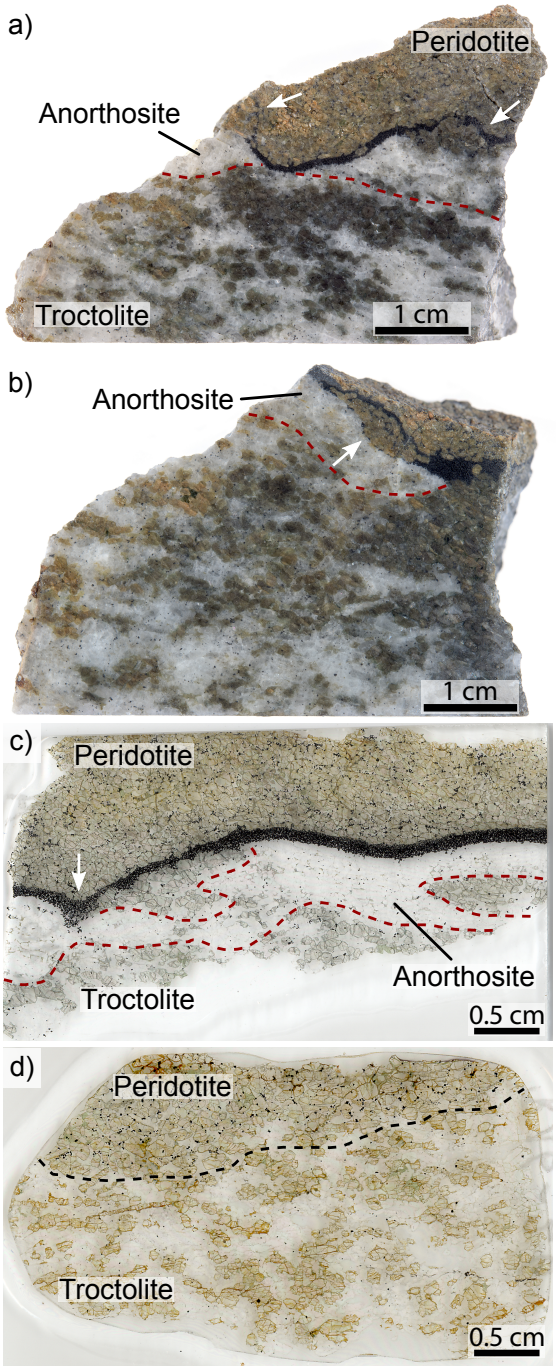

Figure 5.3: **a** Wavy Cr-spinel seam cross-cuts the underlying anorthosite and migrates into the overlying peridotite (white arrow). **b** Main seam in the Unit 8 peridotite, a small additional seam occurs at the peridotite/anorthosite contact (white arrow). **c** Typical thin-section of the Unit 7-8 boundary with Cr-spinel seam (*location 6*), with a thickened Cr-spinel cone (white arrow). **d** Thin-section scan of the Unit 7-8 boundary without Cr-spinel seam and anorthosite layer (*location 11*).

plagioclase crystal can have a primocrystic portion and an intercumulus portion. Cr-spinel in contact with olivine of the adjacent layers typically occurs in embayments in the olivine (Fig. 5.5e). Cr-spinel in the subsidiary seam and in rinds around anorthosite autoliths is petrographically similar to that in the main seam, although the latter seams are generally thinner (Fig. 5.5b). Base metal sulphides (BMS) occur throughout all varieties of Cr-spinel

seams (Fig. 5.5f). The BMS crystals are typically situated at the edges of one or more Cr-spinel crystals. More rarely the BMS occur as inclusions in Cr-spinel crystals. They vary in size (0.01–0.1 mm), but are typically in the range of ca. 0.3–0.5 mm.

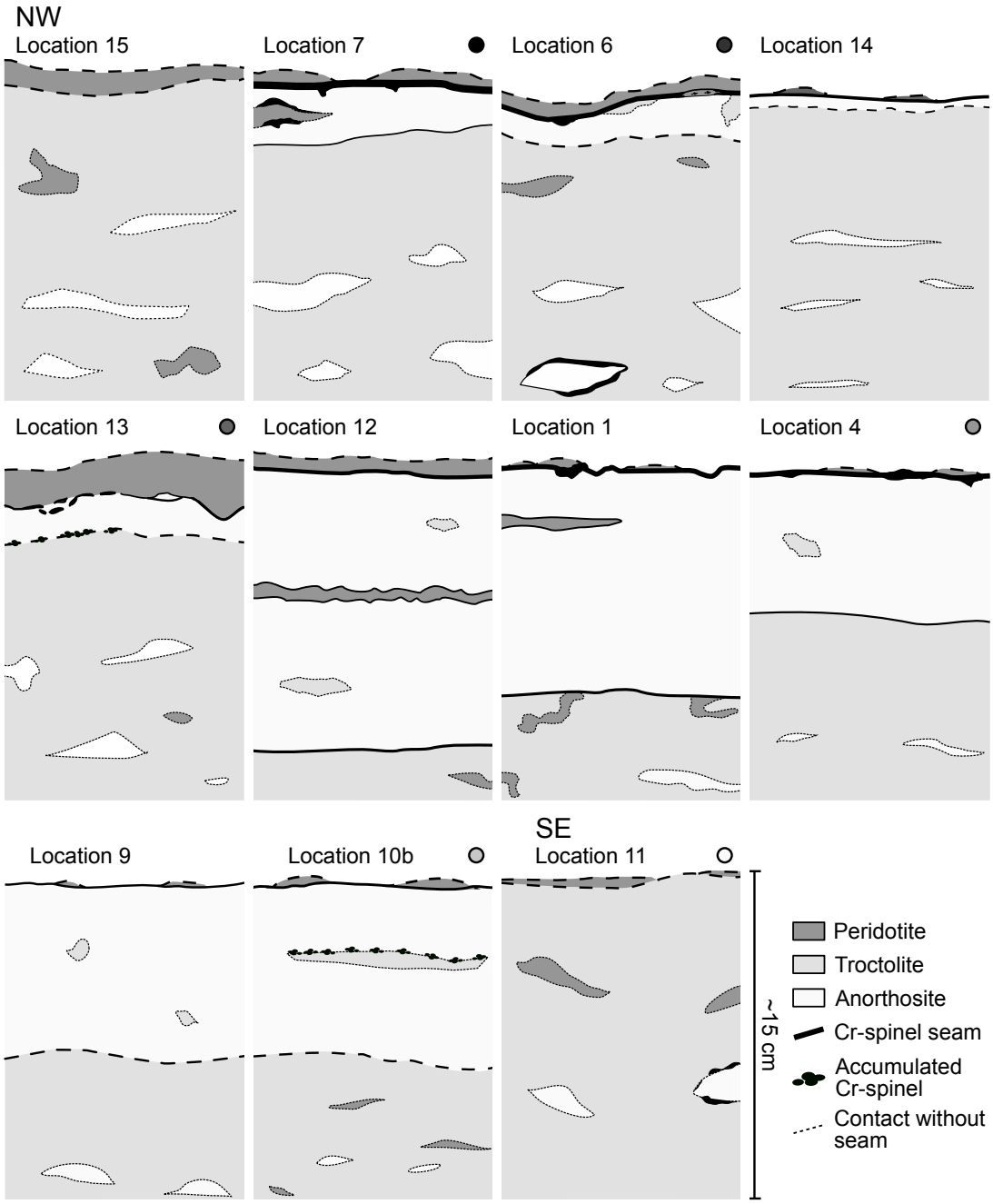

Figure 5.4: Sketches of the Unit 7-8 boundary along strike, for sample location see Fig. 5.1. Location 4 is the 'classic outcrop' described in by e.g. Young 1984; O'Driscoll et al. 2009b; O'Driscoll et al. 2010, Location 12 has been described by Bédard et al. (1988)

The anorthosite layer below the Cr-spinel seam is composed of strongly aligned plagioclase laths (Fig. 5.5d) and variable proportions of intercumulus olivine (0–15 vol.%). Cr-spinel is ubiquitous (up to 4 vol.%, with an average of 2.5 vol.%) in the layer. Plagioclase crystals are blocky to tabular and aligned parallel to the upper and lower contacts of the anorthosite

layer. Plagioclase grain size varies from 0.1–2 mm (long axis), with an average size of 0.25 mm. Compositional zoning is a common feature in these plagioclase crystals, ranging from distinct core-rim zonation to irregular patchy zoning (Fig. 5.5d). The anorthosite autoliths are petrographically similar to the anorthosite layer. Both comprise foliated plagioclase crystals, which are aligned parallel to the long axis of the autoliths, however plagioclase in the autoliths is often cemented by interstitial hornblende or clinopyroxene instead of olivine. Plagioclase grains in the anorthosite layer and autoliths are typically smaller at the direct contact to the hosting troctolite and overgrow existing, equant olivine crystals. Plagioclase in the autoliths reveals strongly developed compositional zoning; in most cases this appears to be normal zoning. Cr-spinel is less frequent in the autoliths relative to the massive anorthosite layer, with typical proportions of ∼1 vol.%. Apatite is a local accessory phase.

In the metre of stratigraphy below the anorthosite layer, the Unit 7 troctolite comprises unevenly distributed clusters of olivine and plagioclase (Fig. 5.3d). Plagioclase forms tabular laths that are oriented parallel to the layering. Olivine crystals are typically equant to tabular in shape. The plagioclase crystals are normally zoned, but this is much less well-developed compared to plagioclase in the anorthosite layer and autoliths. Intercumulus clinopyroxene oikocrysts occur close to olivine-rich portions of the troctolite. Disseminated Cr-spinel appears throughout the troctolite, but is less common (∼0.7 vol.%) than in the Unit 8 peridotite. Locally, hornblende can be observed as accessory phase.

5.5 Analytical techniques

5.5.1 Quantitative fabric analysis

Fabric and texture of plagioclase primocrysts in the Unit 7-8 boundary package was quantified to compare and evaluate the textural character of anorthosite lithologies compared to the hosting troctolite and thus understand the anorthosite layer and autoliths. In order to quantify the strength of the foliation in the troctolite, anorthosite layer and autoliths between 200–450 (on average 350) plagioclase primocrysts were outlined in digitised photomicrographs in crossed polarised light for each location. The major and minor axis length, size, orientation and spatial distribution were measured using the program ImageJ. Average aspect ratios were calculated using the major and minor axis lengths. Plagioclase crystal alignments in the samples were obtained using CSDCorrections 1.53 by Higgins (2000), which quantifies an alignment factor, ranging from 0 (no statistically significant alignment) to 100 (perfect alignment of grains) (see Meurer and Boudreau (1998b) and Boorman et al. (2004) for further information). We used the normalised grain size frequency of the length (i.e. major axis) and width (i.e. minor axis) of plagioclase to calculate the apparent grain size distribution, following the approach described by Holness (2014) and Holness et al. (2018). We did not calculate crystal size distributions (CSDs), because they are based on assumptions of the true crystal shape. Randomly-oriented sections are required for the most accurate assumption of the 3D shape of plagioclase. This is a potential source of uncertainty in this study, as our

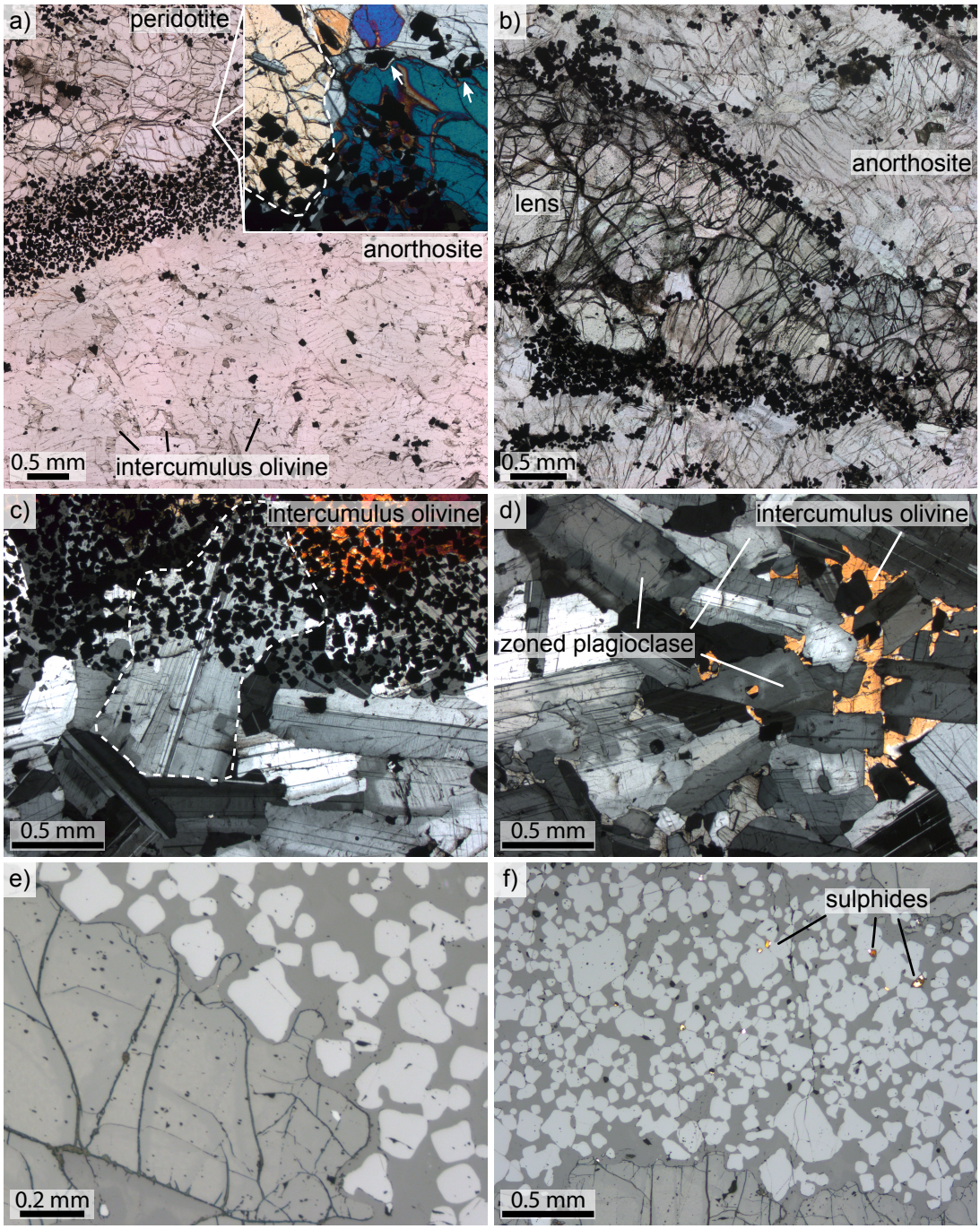

Figure 5.5: Photomicrographs in plain and crossed polarised light. **a** Plain polarised light image of a typical Unit 7-8 Cr-spinel overlain by peridotite and underlain by the anorthosite layer. Inset shows olivine primocrysts exceeding into the underlying Cr-spinel seam (indicated by dashed line) and the occurrence of Cr-spinel in embayment structures in olivine above the seam (highlighted by arrows). **b** Troctolite schlieren in the anorthosite layer, surrounded by a Cr-spinel rind. **c** Reflected light photomicrograph of plagioclase primocryst exceeding into the overlying Cr-spinel seam, indicated by dashed line. **d** Anorthosite layer below the Unit 7-8 seam with foliated plagioclase primocrysts and interstitial olivine. **e** Embayment structure of Cr-spinel into an olivine crystal. **f** Association of sulphide droplets in the Cr-spinel seam.

thin-sections were preferentially prepared perpendicular to the foliation (see Holness (2014) and Holness et al. (2018) for a more detailed description).

5.5.2 Mineral chemistry

The mineral chemistry of plagioclase, olivine and Cr-spinel in the Unit 7-8 package of rocks was investigated by electron microprobe (EMP) and LA-ICP-MS analyses in five different locations. These included one of the localities without a Cr-spinel seam (location 11). These measurements were conducted to assess if and how the presence of the Cr-spinel seam and anorthosite layer controls the mineral chemistry of the main phases and to potentially link the described lateral variations with their geochemical evolution of the analysed minerals.

EMP analyses were carried out at the Museum für Naturkunde Berlin on a JEOL JXA-8500F EMP equipped with a field emission cathode and five wavelength-dispersive spectrometers. Cr-spinel, olivine and plagioclase were analysed with the following conditions: 20 kV accelerating voltage for Cr-spinel and 15 kV for olivine and plagioclase measurements, 20 and 15 nA beam current for Cr-spinel and olivine and plagioclase, respectively. The spot size was set to 1 µm for Cr-spinel and olivine and a defocused beam spot size of 5 µm for plagioclase to minimize the effect of alkali loss. The measured intensities were calibrated against natural minerals of the Smithsonian international standard suite (Jarosewich et al., 1980) and pure metals of the Astimex metal standard. Analyses were processed by a ZAF routine by the JEOL series operating system to minimise matrix effects. Accuracy and reproducibility were checked regularly before and after each analysis session by measurements on minerals of the Smithsonian mineral standards (Cr-spinel, USNM 117075; Olivine San Carlos, USNM111312/444; Olivine Springwater meteorite, USNM 2566; Anorthite, USNM 137031; Anorthoclase, USNM 133868, Microcline, USNM 143966, Jarosewich et al. 1980). The ferric iron contents of Cr-spinel were calculated assuming ideal stoichiometry (Droop, 1987).

LA-ICP-MS analyses for trace element concentrations in olivine and plagioclase, focusing on the rare-earth elements (REE) distribution in the latter were performed at the Institut für Mineralogie of the Leibniz Universität Hannover (LUH) with a fast scanning-sector field-ICP-MS (ThermoScientific ElementXR) which is connected to a femtosecond (Ti-sapphire) laser ablation system. Further details of the fs-LA system are given in Oeser et al. (2014) and Lazarov and Horn (2015). In our study the laser operated at 30–40 Hz and the spot size was set to 40–50 µm diameter. Most analyses were performed in the raster mode, but the rims of plagioclase grains were ablated in line mode. Acquisition times of the background signal and the ablation signal were set to 40 s and 100 s, respectively. To avoid artefacts due to surface contamination sample surfaces of each spot were pre-ablated before measurement. Analyses were bracketed every 10–15 measurements by the standard reference material NIST610 to correct for internal instrumental drift. Further testing of the accuracy and reproducibility was undertaken by measuring silicate reference material (BCR-2G), which yielded an accuracy and reproducibility of 1–5 %. Si concentrations, obtained by EMP analyses, were used for the internal calibration of trace element concentrations for plagioclase and olivine. Data processing was performed with the SILLS program (Guillong et al., 2008).

5.6 Results

5.6.1 Quantitative fabric analysis

Plagioclase primocrysts in the anorthosite layer, anorthosite autoliths and the troctolite exhibit similar microstructural characteristics. Average aspect ratios of plagioclase in both types of anorthosite and the troctolite range between 2.2 and 2.5, with alignment factors that mostly range between 0.4 and 0.6 (Fig. 5.6a). Two outliers from the anorthosite layer plot at higher aspect ratios and alignment factors. The data are positively correlated, such that aspect ratios and alignment factors increase systematically. Across the lateral extent of the Unit 7-8 boundary, plagioclase in the anorthosite autoliths and the troctolite exhibits relatively constant alignment factors (Fig. 5.6b). Plagioclase fabric in the anorthosite layer is more variable, with a relatively low alignment factor observed at Locality 4 and a relatively high alignment factor at Locality 10b; the latter locality is close to the southeastern termination of the anorthosite layer. Grainsize frequency distributions (Fig. 5.7) for plagioclase (both long and short axes) are unimodal with a broader peak at 0.25 µm crystal length and a well-defined narrow peak at 0.15 mm crystal width. Interestingly, the plagioclase from the anorthosite layer, the anorthosite autoliths and the troctolite all show similar grain size distributions.

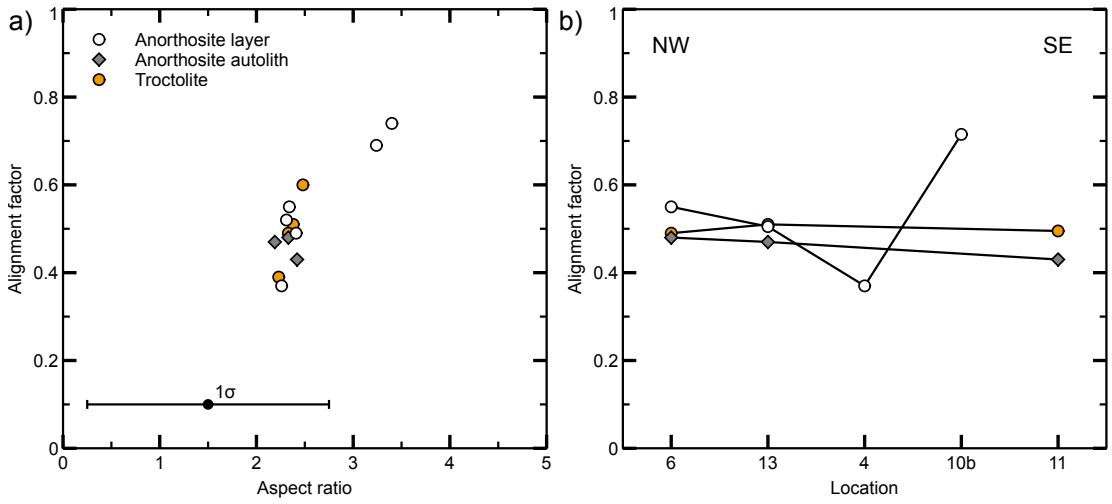

Figure 5.6: **a** Alignment factor against aspect ratio, average standard deviation is indicated exemplary of cumulated plagioclase crystals (Localities 4, 6, 10b, 11 and 13) in the anorthosite layer, autoliths and troctolite. **b** Development of alignment factor of plagioclase along strike, for sample location see Fig. 5.1.

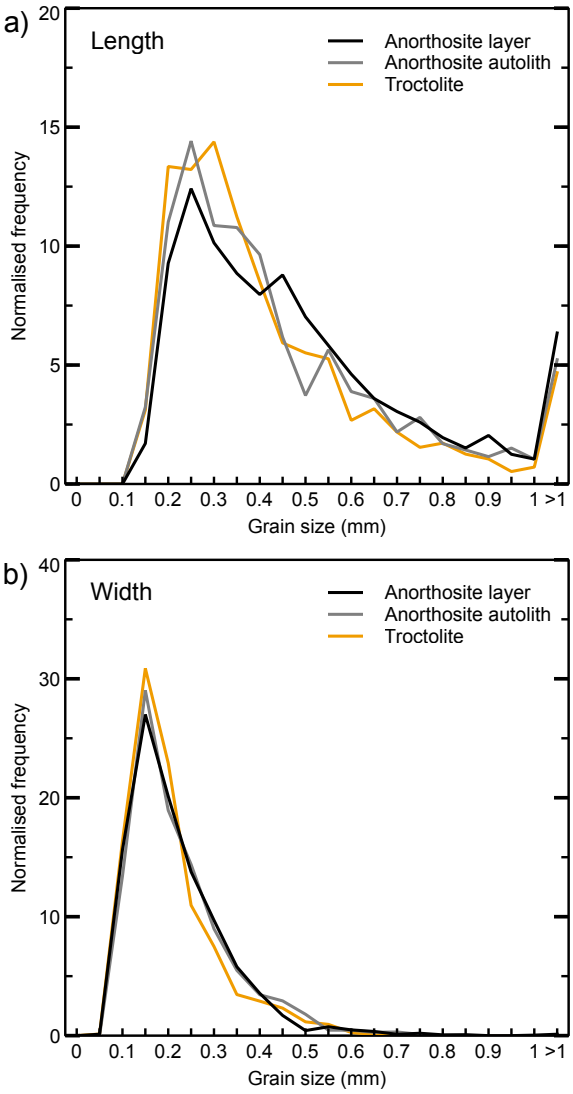

Figure 5.7: Normalised frequency plot for **a** long and **b** short axes of cumulated plagioclase crystals (Localities 4, 6, 10b, 11 and 13) in the anorthosite layer, autoliths and troctolite.

5.6.2 Mineral chemistry

Cr-spinel

The range of compositions revealed by Cr-spinel can broadly be subdivided into Cr–Al-dominated and Cr–Fe^{3+}-dominated varieties (Fig. 5.8). Cr-spinel in peridotite, Cr-spinel seams and troctolite are Cr–Al dominated spinels, following the Rum trend (Henderson, 1975). Cr-spinel compositions in the anorthosite layer and anorthosite autoliths are Cr–Fe^{3+} dominated and thus follow the FeTi-trend of Barnes and Roeder (2001). Cr-spinel exhibits a range of Mg# (atomic ratio, $Mg/(Mg+Fe^{2+})$) of between 5–72 and Cr# (atomic ration, Cr/(Cr+Al)) from 22 to 82 (Fig. 5.9). Anorthosite-hosted Cr-spinel generally has lower Mg# and Cr# relative to Cr-spinel in the other lithologies. Cr-spinel in the seams exhibits lower Cr# and higher Mg# compared to other lithologies. No apparent differences are observed in the composition of Cr-spinel crystals from the main seams versus the subsidiary seams. Cr-spinel TiO_2 concentrations range between ~0.2–6.25 wt.%. The Cr-spinel from Locality 11

generally has elevated TiO_2 contents compared to localities that contain a Cr-spinel seam. Cr-spinel crystals hosted in anorthosite reveal slight compositional differences depending on whether the crystals occur in the anorthosite layer or the autoliths in the Unit 7 troctolite. Specifically, Cr-spinel crystals in the autoliths have elevated TiO_2 contents and generally lower Mg#. Traverses across the Cr-spinel seam indicate that the compositional variations described above changes abruptly at the upper and lower contact of the seam. In addition, Cr-spinel in the seam depicts a slight increase in Mg#, which is followed by a slight decrease in Cr#. Similar compositional changes have been reported for the Unit 7-8 and Unit 11-12 Cr-spinel seams (O'Driscoll et al., 2009a; O'Driscoll et al., 2010) and for Cr-spinel seams of the Unit 10 peridotite (Hepworth et al., 2017). Moreover, Cr-spinel compositions in the peridotite and in the Cr-spinel seam suggest a systematic change along strike. In particular, Mg# and TiO_2 concentrations increase while Cr# decreases with increasing distance from the central part of the intrusion towards SE (from location 7 to 11, see Fig. 5.1).

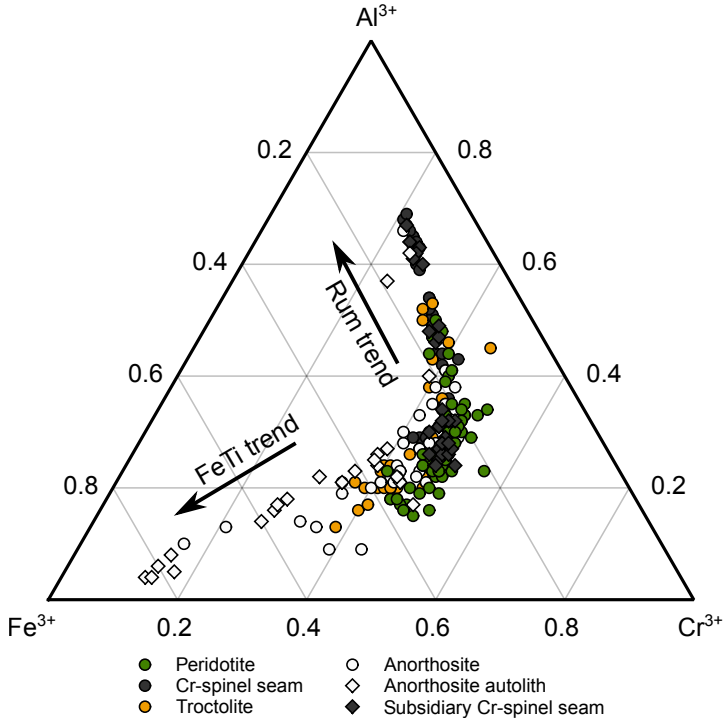

Figure 5.8: Trivalent cation (Al^{3+}-Cr^{3+}-Fe^{3+}) ternary plot for Cr-spinel, Rum trend and FeTi Trend (Henderson, 1975; Barnes and Roeder, 2001) are indicated by arrows.

Olivine

Olivine Mg# compositions range between 82–90, with Ni concentrations of ca. 1400–2600 ppm (Fig. 5.10). Olivine in peridotite has slightly higher Ni concentrations and generally shows a broader scatter compared to olivine in the troctolite and intercumulus olivine in the anorthosite layer. Olivine in the anorthosite has similar Mg# values, but lower Ni concentrations, an observation also made by O'Driscoll et al. (2009a). No compositional zoning was observed in olivine from any lithology, in either the primocrysts or in intercumulus crystals. LA-ICP-MS analyses confirm the trace element concentrations measured by EMP. As with the Cr-spinel

chemistry, a consistent lateral change in olivine composition is observed along the strike of the Unit 7-8 boundary package. Specifically, Mg# and Ni concentrations in all lithologies decrease towards the SE portion of the traverse. This trend is most pronounced for interstitial olivine in anorthosite. However, the locality without a seam (11) has an intermediate Mg# composition.

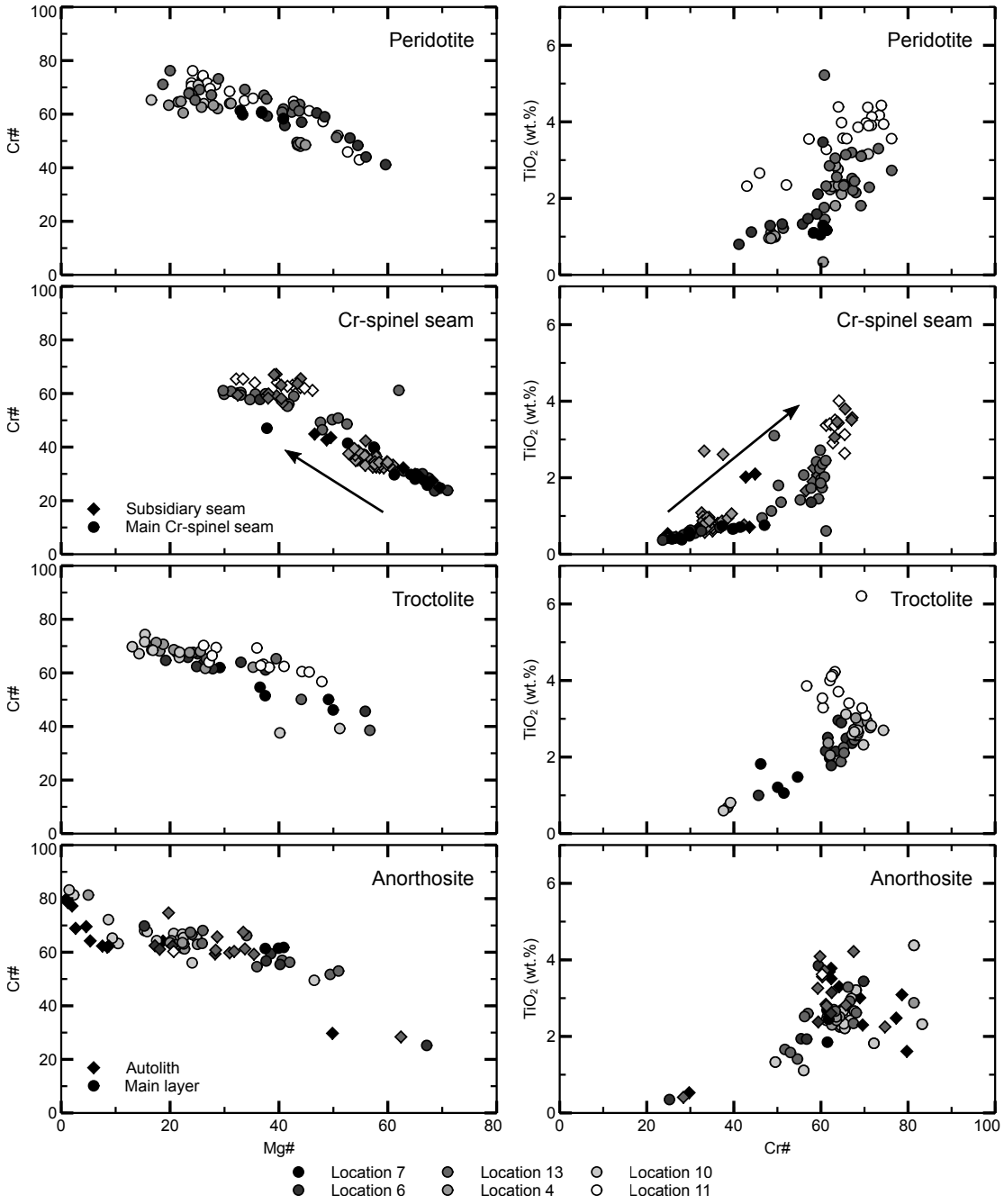

Figure 5.9: Variation in Cr-spinel composition. Data for location 4 was taken from O'Driscoll et al. (2009b).

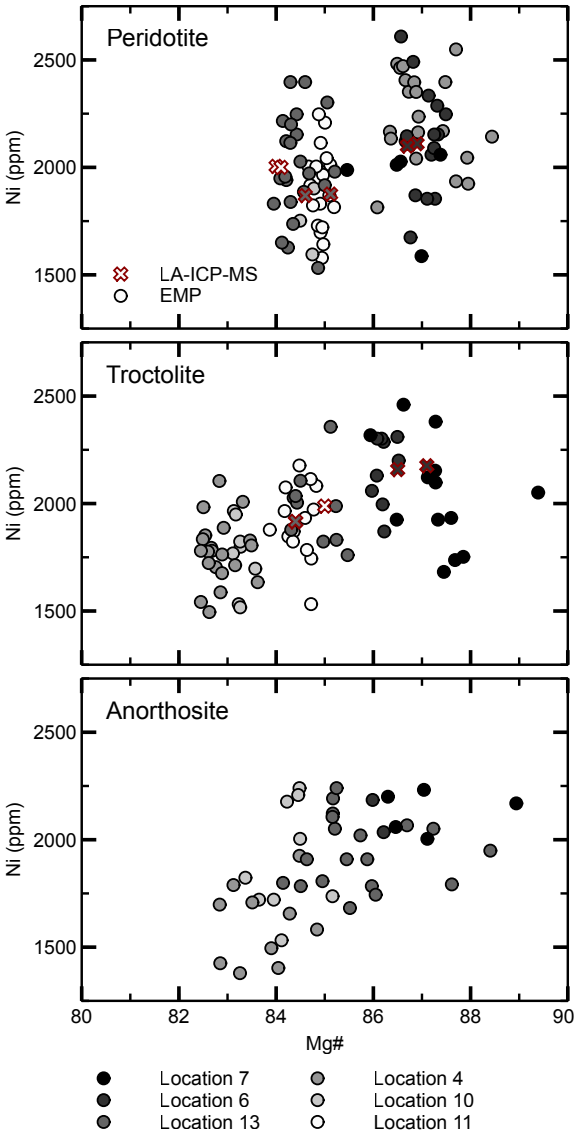

Figure 5.10: Variation in olivine composition, measured with EMP (circle) and LA-ICP-MS (cross). Data for location 4 was taken from O'Driscoll et al. (2009b)

Plagioclase

Plagioclase compositional data are illustrated in Fig. 5.11. Anorthite content in plagioclase (An) varies from An_{65} to An_{92} and K concentrations vary between being below detection limits to ∼1250 ppm. The plagioclase in peridotite and anorthosite typically has elevated K and Na, relative to the intercumulus plagioclase in the Cr-spinel seams and the primocrysts in the troctolite. Plagioclase from all lithologies reveals a broadly common trend of decreasing Ti concentration with increasing An content. Overall, Ti contents in plagioclase range from 100 to 680 ppm in all lithologies. Plagioclase in the autholiths and the subsidiary Cr-spinel seams has relatively low Ti and K concentrations and is more sodic compared to plagioclase in the anorthosite layer and the main seam. Additionally, the plagioclase compositions also exhibit lateral variation along strike. In particular, average plagioclase compositions in the

anorthosite layer, the troctolite and the main Cr-spinel seam evolve has lower An contents and higher K and Ti concentrations in the SE, compared to the NW.

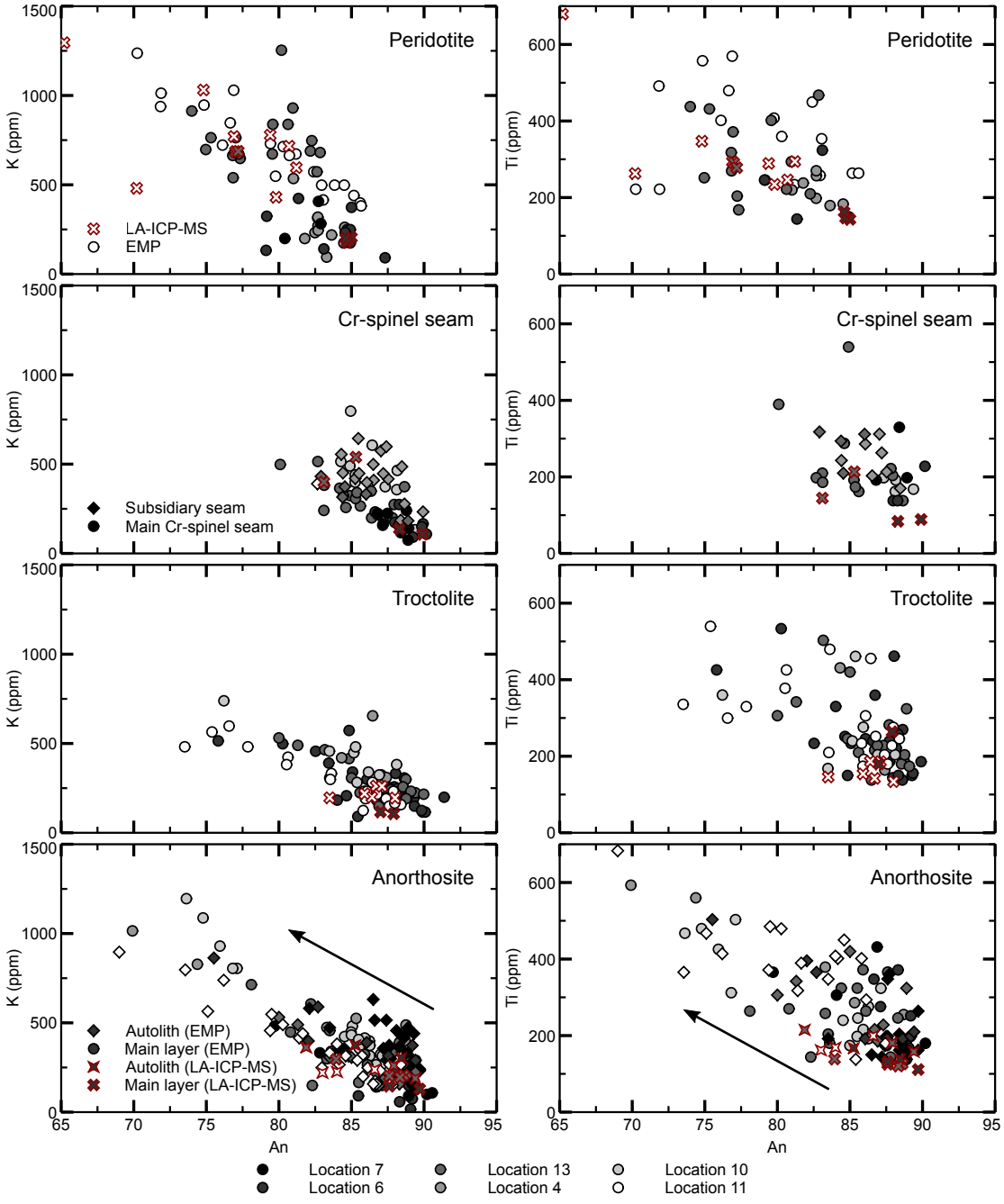

Figure 5.11: Compositional variations in plagioclase, measured with EMP (circle) and LA-ICP-MS (cross and star) with additional data for location 4 (O'Driscoll et al., 2009b).

Compositional zoning in plagioclase primocrysts is common, crystals typically show a pronounced normal zoning with calcic cores and sodic rims enriched in minor and trace elements. An content in primocryst rims generally differs by 5–10 mol.%, however single crystals can deviate by up to 18 mol.%. Core-rim differences of trace element concentrations range from ∼500–1000 ppm and ∼200–300 ppm for Ti and K, respectively. In addition,

intercumulus plagioclase in peridotite and in the Cr-spinel seams is occasionally zoned, showing similar trends, though less well developed compared to the zoning patterns observed in cumulus plagioclase (ΔAn 2–3 mol.%).

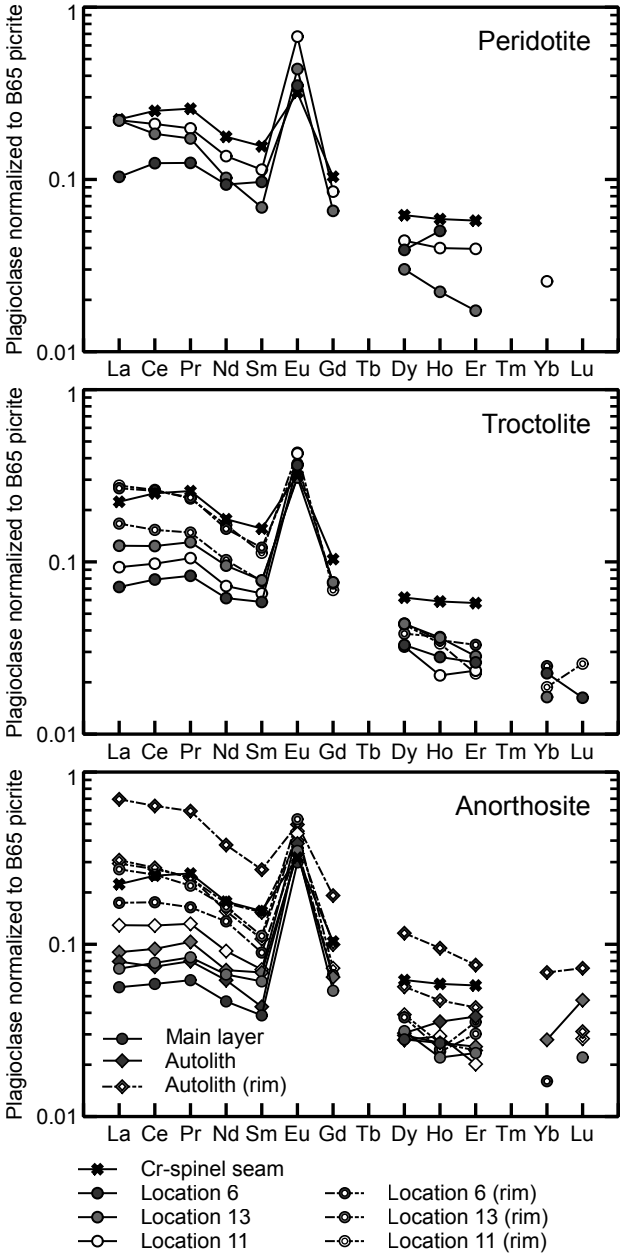

Figure 5.12: REE concentration of plagioclase normalised to the postulated parental magma B65 (Upton et al., 2002). Data from location 11 without a Cr-spinel seam are highlighted in red.

The REE element patterns of plagioclase from the different Unit 7-8 lithologies are shown in Figure 5.12. The patterns suggest that plagioclase in all lithologies broadly show similar average valuesfor the REE concentrations, however plagioclase in anorthosite depicts a broader scatter. All patterns reveal a relative enrichment in light REE (LREE) compared to heavy REE (HREE), a similar slope and a strong positive Eu anomaly, most pronounced in plagioclase from the anorthosite layer. Plagioclase in the anorthosite autoliths is clearly enriched in the

REE compared to those in the anorthosite layer, along the complete traverse. In addition, both plagioclase in the anorthosite layer and autoliths exhibits enrichment in REE concentrations towards the SE of the traverse with plagioclase in autoliths from Locality 11 revealing the highest REE contents. Rims of zoned primocrysts in troctolite and anorthosite are relatively enriched in REE, compared to crystal cores, an observation that is most prominent in the plagioclase compositions from the anorthosite layer and autoliths. Although the level of core-to-rim enrichment is variable, some plagioclase crystals in anorthosite have rims that are enriched by up to an order of magnitude, relative to cores.

5.7 Discussion

5.7.1 Chronology of the Unit 7-8 boundary formation

Our combined observations of field relations and petrography provide insights into the timing of the respective events which formed the Unit 7-8 boundary package. Cross-cutting relations in the central section of the traverse are graphically summarised in Figure 5.13. Notably, no lateral variations in cross-cutting relations were observed along strike, thus changes in the timing of events are not apparent. Taken together the following events were identified:

1. Emplacement of picritic melt in an undeformed or deforming crystal mush of the Unit 7 troctolite, which subsequently formed the peridotite schlieren. The presence of hot melt was likely connected to the deformation of the troctolite cumulates.

2. Formation of the anorthosite layer by assimilation of the troctolitic crystal mush due to new intruding magma.

3. Injection of picritic magma, which crystallised the Unit 7-8 Cr-spinel seam due to assimilation of the underlying anorthosite.

4. Subsequent crystallisation of the Unit 8 peridotite from this picritic melt.

Peridotite schlieren are an ubiquitous feature along the complete traverse of the Unit 7 troctolite (Figs. 5.2d, 5.13). Their embedded nature suggests that the schlieren formed due to infiltration of picritic melt into the troctolitic mush, either by porous flow through the mush from the overlying magma body or by dike-like melt channels. Moreover, the high degree of deformation indicates that they were emplaced before or during syn-magmatic deformation of the Unit 7 troctolite. Evidence for soft-sediment deformation on variable scales has been reported throughout the ELI (Volker and Upton, 1990; Emeleus et al., 1996; O'Driscoll et al., 2007; O'Driscoll et al., 2010). O'Driscoll et al. (2007) proposed that these deformation structures resulted from repeated sagging of the poorly consolidated troctolite mush towards the central part of the intrusion. Infiltration of hot melt by either possibilities would substantially change the rheology of the crystal mush due to increase of temperature and melt proportion, thus inducing or enhancing the syn-magmatic deformation of the unit 7 troctolite (O'Driscoll et al., 2010).

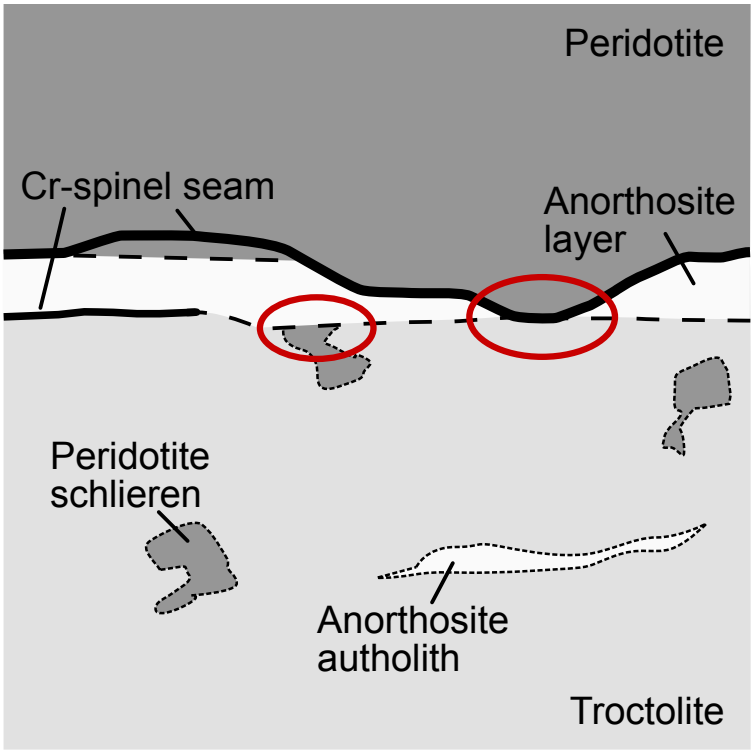

Figure 5.13: Graphic compilation of the most important field evidence indicating a chronology for the formation of the Unit 7-8 boundary package.

Cross-cutting of the peridotite schlieren by the overlying anorthosite layer (Figs. 5.2d, 5.13) indicate that the layer was formed after the picritic injections and the troctolite deformation. O'Driscoll et al. (2009; 2010) proposed that the anorthosite layer were formed due to thermo-chemical erosion, the unconsolidated troctolite were assimilated and partial melted by injections of new magma. Thus, the anorthosite layer below the Cr-spinel seam represents the remnant of this partial melting process. Our microstructural characterisation of the troctolite and the anorthosite layer support their model of a metasomatic origin of the anorthosite. Assessment of the plagioclase microstructure (Figs. 5.6, 5.7) demonstrates that both, the general alignment and the grain size distribution of plagioclase crystals in troctolite and the anorthosite layer, are similar indicating a similar evolution, i.e. metasomatic replacement.

The formation of the anorthosite layer was followed by the crystallisation of the Cr-spinel seam, which occasionally cross-cuts or pinches the underlying anorthosite (Figs. 5.3a, 5.13). We envisage Cr-spinel crystallisation due to assimilation of the unconsolidated anorthosite layer by an intruding picritic melt, which drove the contaminated picrite onto the spinel stability field, similar to O'Driscoll et al. (2009; 2010). However, based on the indicative field observations of the Cr-spinel seam cross-cutting the underlying anorthosite, we propose that the crystallisation step occurred after the anorthosite layer metasomatism. Small circular depressions of the seam into the anorthosite (Fig. 5.2b) are interpreted as small erosional features of the overlying magma. Injection of picritic magma into the anorthosite mush can also account for the reported peridotite apophyses, which are rimmed by subsidiary Cr-spinel seams (locations 4, 7, 12; Figs. 5.2, 5.4). The final step in the formation of the Unit 7-8 seam

package was the crystallisation of the Unit 8 peridotite form the overlying picritic magma sheet.

5.7.2 Lateral variations in structure and mineral chemistry along the Unit 7-8 boundary

In our study the Unit 7-8 boundary was mapped and sampled along strike across the extent of the ELI, revealing significant lateral variations in structure and geochemistry. The anorthosite layer thickens towards the central part of the investigated traverse (location 12 and 1, >10 cm), while it thins out (<1 cm) and finally disappears to the southeast and northwest (Fig. 5.4). The Cr-spinel seam overlying the anorthosite shows similar variations in structure. It displays its maximum thickness of about 5 mm near Barkeval (Localities 6 and 7), close to its first appearance, thins out towards the southeast and is absent near Hallival and the centre of the ELI where the presumable main feeder, the Long Loch Fault (LLF), is located (e.g. Volker and Upton, 1990; Emeleus et al., 1996). Strikingly, the changes in structure are also accompanied by compositional changes in mineral chemistry of Cr-spinel and plagioclase. In particular, Cr-spinel in the main seam depicts a gradual increase in Mg# and TiO_2 concentrations, while Cr# decreases with increasing distance from the central part of the ELI towards SE (Fig. 5.9). Plagioclase chemistry in the anorthosite layer follows a similar compositional trend, for both the main and trace elements (Figs. 5.1, 5.12): the An content decreases, while the K and trace elements like the REE depict an enrichment towards the SE. Taken together, the Cr-spinel seam and the anorthosite layer are apparently restricted to a certain part of the ELI, while the cumulus phases within these layers illustrate a trend of increasing fractionation with increasing distance from the LLF.

Based on these observations and the implications of the chronology described in the previous chapter, we suggest that the formation of the Cr-spinel seam and the anorthosite layer were controlled spatially, thus refining the current model for the Cr-spinel seam crystallisation in the ELI by O'Driscoll et al. (2009; 2010). No apparent lateral change was observed in occurrence, size or distribution of peridotite schlieren along the traverse, indicating that infiltration of picritic melt occurred uniformly throughout the ELI. Contrary, the anorthosite layer is restricted to the central part of the traverse, suggesting that the formation was likely depended on a certain distance to the LLF. The reason for this localised assimilation in the central part of the ELI remains uncertain, however we propose that it depends on a particular distance to the main feeder. In close proximity to the LLF, the erosional potential of the superheated magma (e.g. Upton et al., 2002; Holness and Winpenny, 2009) was too high, resulting in vivid, turbulent erosion, which prevent the formation of a restitic anorthosite ('too much or complete erosion'). With increasing distance to the main feeder the picrite magma influx cooled and therefore its capacity to sufficiently assimilate the troctolite ('too little erosion'). Thus, the potential to partially melt the troctolite mush efficiently was the highest in the central part, forming the thickest anorthosite portions. The crystallisation of the Cr-spinel seam resulted from a second influx of picritic magma, which spread, due to its higher density, at the crystal mush interface and resulted in assimilation of the anorthosite crystal mush. We attribute the general decrease in seam thickness towards the SE to a rather

thin magma sheet, which depleted in Cr and cooled below assimilation temperatures. This consideration is supported by the reported systematic changes in the plagioclase and Cr-spinel mineral chemistry in the Cr-spinel seam and the anorthosite layer. These lateral changes argue for crystallisation from a fractionating magma sheet, which becomes progressively enriched in incompatible trace elements (e.g. REE).

5.8 Conclusions

We investigated the Unit 7-8 Cr-spinel seam across the extent of the ELI by field observations as well as microstructural and mineral chemistry analyses, which showed significant lateral variations in the macro-to-microstructural and mineral chemical character. Our observations were used to elucidate the timing and connection to magmatic influxes of the Cr-spinel seam formation. The Unit 7-8 seam package was constructed by at least two genetically linked, but separated replenishment steps. While the first assimilated the Unit 7 troctolite and formed a restitic anorthosite cap, the second smaller influx crystallised the main Cr-spinel seam. Importantly, we could show that the nature and extent of the replenishing events and thus the interactions with the underlying cumulates (e.g. assimilation, Cr-spinel crystallisation) varied along the intrusion.

5.9 Acknowledgements

FEDK was supported by the German Federal Ministry of Education and Research (BMBF), grant FKZ 033R119C. Sampling permission by the Scottish National Heritage (SNH) is highly appreciated. We are grateful to M. Oeser-Rabe and S. Schuth for their support with the LA-ICP-MS analyses at the Leibniz University of Hannover and to K. Born and P. Czaja for their support at the SEM and electron microprobe at the Museum für Naturkunde Berlin.

Chapter 6

Discussion and Conclusion

The focus of this thesis is to enhance our knowledge and understanding on the processes of Cr-spinel accumulation and possible subsequent modification in layered intrusion. In order to unravel these processes, detailed field descriptions, textural and geochemical observations of two case studies, the Bushveld Complex and the Rum Layered Intrusion are presented. In the following chapter, the main results of Chapters 2, 3, 4 and 5 are briefly recapitulated and discussed in regards to the main two questions stated in Chapter 1.3. First, the process of post-cumulus modification of texture and composition in Cr-spinel seams will be summarised and discussed for both case studies. From this discussion, features reflecting the primary cumulus characteristics will be identified to decipher the primary processes involved in Cr-spinel accumulation. These cumulus formation processes will be reviewed on the basis of vertical and lateral variations described in the included studies. Finally, these implications result in generalized petrogenetical models for both case studies.

6.1 What is the significance of post-cumulus modification of Cr-spinel layers?

The potential of changes in texture and composition of cumulus phases due to post-cumulus modifications have been emphasised in both case studies. These post-cumulus modifications can provide important indications, for example for the closed or open behaviour of a crystal mush or the redistribution processes of precious metals like PGE. Textural observations of the LG and MG layers in the Bushveld Complex (Chapter 2), revealed a huge variety in texture from small disseminated grains to large massive ones (see Figure 6.1a for a representative comparison), indicating different degrees of post-cumulus modification. CSD and spatial distribution data of Cr-spinel in a defined area of textural similarity were used for the first time in these layers to measure and assess the extent of these modifications. It could be shown in Chapter 4 that CSD curves of Cr-spinel entrapped in oikocrysts provide an approximation of the original Cr-spinel texture. They are characterised by straight-lined CSD trend expected for primarily magmatic controlled crystallisation. In contrast, unprotected Cr-spinel in the LG and MG1 seams has a massive texture and CSD curves typically for textural equilibration, expressed by rotation of the curves and a reduction in the population density of small crystals. This is especially evident for the MG1 layer, which consist of almost pure Cr-spinel grains (up to 98 vol.%) aside from those trapped within orthopyroxene oikocrysts. The reasons for these significant differences in texture involve a combination of two processes, which are responsible for textural changes in a crystal mush: adcumulus growth and textural equilibration. Adcumulus growth (homogenous crystal growth regardless of the relative crystal

size) occurred near the magma–crystal mush interface in a permeable mush, which is in chemical communication with the overlying magma body (e.g. Chapter 4, Holness et al., 2017d; Holness et al., 2017a). Cr-spinel adcumulus growth in the mush depends on exchange of the intercumulus melt with the overlying magma body to provide sufficient Cr for crystal growth. Adcumulus growth was followed by textural equilibration, whereby small crystals were dissolved at the expense of larger ones. All CSD curves show a rotation towards coarser grain size, which is consistent with textural equilibration. Importantly, the lower layers (LG6-MG1) reveal a higher degree of post-cumulus equilibration, while the overlying MG2 layers show only patches of texturally re-equilibrated Cr-spinel. The main proportion of the MG2 layers shows a disseminated chromite texture closer to the primary kinetically controlled one (Higgins, 2002; Higgins, 2011). The reason for the decreasing grade of adcumulus growth and textural equilibration of Cr-spinel upwards stratigraphy (LG6 to MG2) could be a decreasing Cr concentration in the melt overlying the Cr-spinel crystal mush due to fractionation and thus progressively depletion of compatible Cr (Cameron, 1978; Cameron, 1980; Eales and Cawthorn, 1996). The last steps of solidification in the crystal mush had to occur in the presence of evolved, hydrous interstitial fluids: the remaining interstitial silicates in the massive Cr-spinel layers consist of biotite and hornblende and enrichment of incompatible trace elements in orthopyroxene oikocrysts (Chapter 4) suggest the presence of a more evolved liquid, which infiltrated the Cr-spinel mush. In addition, the presence of such evolved liquids is known to enhance textural equilibration (e.g. Matveev and Ballhaus, 2002). Late magmatic evolved fluids were also described for various parts of the Bushveld Complex (Chutas et al., 2012; Li et al., 2005; Boudreau, 1988; Boudreau, 2016), recently Schannor et al. (2018) highlighted the importance of fluid-interaction in the last post-cumulus stage of the UG2 formation.

Previous studies have emphasised the potential of compositional post-cumulus changes of cumulus crystals in general in layered intrusions (e.g. Barnes, 1986b; Lundgaard et al., 2006; Cawthorn, 2013; Cawthorn, 2015; Godel et al., 2011; Hulbert and von Gruenewaldt, 1985). One possibility to change of the primary composition of accumulated minerals by chemical post-cumulus re-equilibration was proposed by Barnes (1986b). Here, accumulated minerals in a closed system re-equilibration with the interstitial melt, which is known as trapped liquid shift effect (TLSE). The TLSE describes the concept that crystals in a closed cumulated interact with the surrounding liquid and thus consecutively exchange their composition. The TLSE has widely been proposed to be responsible for changes in the Fe-Mg ratio of ferromagnesian silicates and oxides (e.g. Barnes, 1986b; Cawthorn, 2015; Godel et al., 2011). However, a number of observations compiled in this thesis (Chapter 2) question that the Cr-spinel cumulate was a closed system. First, in a closed system all ferromagnesian phases (here: Cr-spinel and orthopyroxene) will chemically equilibrate with the interstitial liquid, but also the involved phases re-equilibrate their composition among each other. However, both phases mostly follow the same compositional fractionation trend with decreasing Mg-Fe ratios. In addition, mm-sized Cr-spinel layers depict a distinct chemical character compared to the surrounding Cr-spinel in pyroxenite, although it is almost impossible that these small layers acted as closed system. However, most importantly, the study on orthopyroxene oikocrysts (Chapter 4) demonstrated that the Cr-spinel crystal mush was an open system beyond the

cumulus stage, infiltrated by an upwards-percolating melt and successively by magma of the overlying magma sheet. In conclusion, this thesis proposes that the texture of Cr-spinel in the LG and MG layers of the Bushveld Complex was modified severely by adcumulus growth, followed by textural equilibration. However the textural post-cumulus changes were not necessarily accompanied by strong compositional ones (Chapter 2).

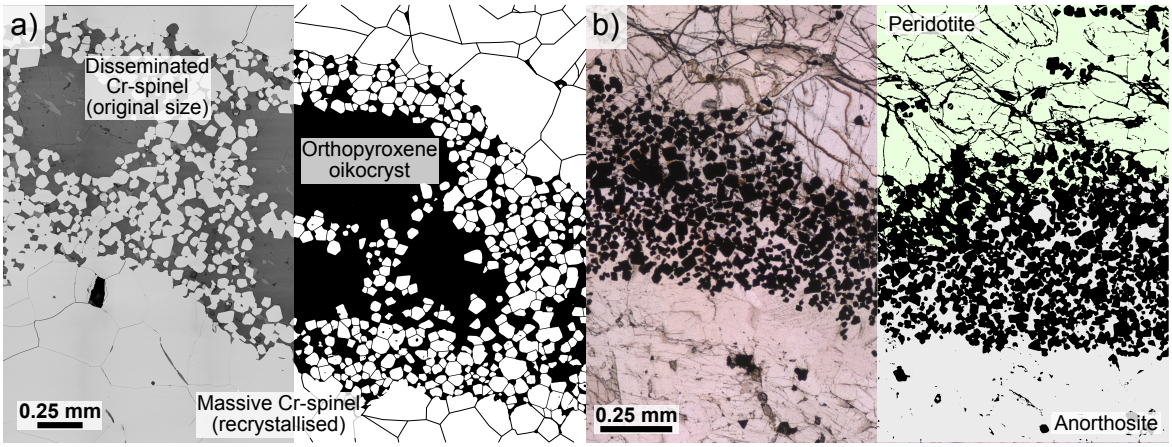

Figure 6.1: Exemplary comparison of Cr-spinel textures in both case studies illustrating the difference in textural post-cumulus modification. **a** MG1 layer, where orthopyroxene oikocrysts retained the original Cr-spinel grain size, while the surrounding Cr-spinel recrystallised due to adcumulus growth and textural equilibration. **b** Cr-spinel layer of the Rum Layered Intrusion, where Cr-spinel kept its original texture, possibly due to overgrowth of olivine and plagioclase, similar to **a**.

In contrast to the described Cr-spinel textures in the Bushveld Complex, the main Unit 7-8 Cr-spinel seam of the Rum Layered Intrusion is characterised by a more primary grain size distribution (Fig. 6.1b). This indicates that the layers exhibited less adcumulus growth and textural equilibration. These observations (Chapter 5) are supported by CSD curves published by previous studies (O'Driscoll et al., 2009b; O'Driscoll et al., 2010), which suggest a rather un-equilibrated character for Cr-spinel in the main seam. However the authors illustrated that additional Cr-spinel layers, located in the anorthosite below the main Cr-spinel layer (subsidiary layer), underwent adcumulus growth and textural equilibration, similar to those of the Bushveld Complex. Notably, Cr-spinel crystals of the main layer are overgrown by olivine of the overlying peridotite and plagioclase of the underlying anorthosite (Fig. 6.1b) in most locations described in Chapter 5, suggesting that they were protected from textural modifications similar to grains in oikocrysts of the MG1 (Chapter 4).

Compositional post-cumulus changes in Cr-spinel across the different lithologies have been reported and highlighted by numerous studies (e.g. Henderson, 1975; Henderson and Suddaby, 1971; O'Driscoll et al., 2009b; O'Driscoll et al., 2010; Power et al., 2000), however O'Driscoll et al. (2010) argued that the composition of Cr-spinel in the Cr-spinel layers maintained their primary signatures due to the high proportion of spinel, which buffered the system, while those crystals in anorthosite and troctolite changed their composition due to re-equilibration with the intercumulus melt. This chemical re-equilibration resulted in a clear enrichment in Fe^{3+} and Ti. Determination of the mineral chemistry in this thesis (Chapter 5) depicts similar trends. Thus, it can be concluded that Cr-spinel in the Cr-spinel layers kept their

primary composition, while grains in the anorthosite and troctolite follow a trend of chemical modification, suggesting interaction with the intercumulus melt.

In conclusion, the compiled data of this thesis as well as comparison with published studies suggest that the Cr-spinel layers of the Rum Layered Intrusions resembles a relatively original texture, while the seams of the Bushveld Complex show clear signs of textural changes along all investigated seams. Compositional changes in cumulus Cr-spinel in the silicate host rocks could be observed, especially in the Rum Layered Intrusions. However, Cr-spinel in the main seams in both intrusions display only minor changes in composition, possibly due to the amount of Cr-spinel, which buffered the system. The reasons for this disparity can likely be found in the different lateral and vertical extent of the two complexes: the enormous size of the Bushveld Complex resulted in a completely different thermal history compared to the Rum Layered Intrusion, Zeh et al. (2015) suggested that magma chamber of the Bushveld Complex completely solidified in ca. 870 000 a, equivalent to a few °C per ∼10 000 a, while Tepley III and Davidson (2003) proposed the cooling rates of 400–500 °C within a few thousand years for the Rum Layered Intrusion. Given the huge differences in the cooling rates, one would expect that the rocks of the Bushveld Complex were more prone to post-cumulus changes. However, it could be demonstrated, that careful and thorough examination of the Cr-spinel texture and composition offers the chance to identify and deduce the primary cumulus characteristics, which will be discussed in the next section in regards to cumulus formation processes.

6.2 How did magmatic processes result in Cr-spinel cumulus formation? Implications from vertical and lateral variations of Cr-spinel layers

6.2.1 Cumulus formation processes: Bushveld Complex

The combined observations of vertical variations in the LG and MG layers of the Bushveld Complex (Chapter 2) and the textural and geochemical study on orthopyroxene oikocrysts in Chapter 4 can be used to constrain the processes of Cr-spinel layer formation (see Chapter 1.2.1 for an overview on the currently discussed models). Considering the post-cumulus changes described and discussed in the previous section the following characteristics are thought to best reflect the original characteristics of a Cr-spinel cumulate layer. Macro-structural characteristics, best represented by lithostratigraphic columns, suggest that the mechanisms that lead to exclusive Cr-spinel crystallization had to operate relatively fast and repeatedly, in order to switch crystallisation 'on' and 'off' and thus form distinct mm-thick pyroxenitic partings within Cr-spinel layers and small Cr-spinel stringers in the silicate host rocks. The best explanation accounting for this key feature is offered by repeated magma replenishing events, which did not or only to a limited extent mix with the residual magma of the Bushveld Complex. Compositional analyses of Cr-spinel crystals across the Lower and Middle Group Cr-spinel layers support the replenishing hypothesis and indicate that additionally magmatic fractionation played a role in the construction of the respective layers. Consecutive

fractionation across single layers implies that crystallisation had to occur within the magma sheet in the Bushveld magma chamber and thus contradicts any model involving Cr-spinel crystallisation and concentration in a deeper magma chamber and injections of Cr-spinel-rich slurries (e.g. Maier and Barnes, 2008; Eales and Costin, 2012; Maier et al., 2013). Moreover, in the lights of the compositional similarity of chromite in the footwall and hanging wall (Chapter 2) any model is unlikely, where crystallization is induced by intermixing of crustal material or primitive magma (e.g. Irvine, 1975; Irvine, 1977; Scoon and Teigler, 1994; Schoenberg et al., 1999; Kinnaird et al., 2002; Spandler et al., 2005; Naldrett et al., 2009), because the resulting mixed magma would lead to a compositional different hanging wall. Similar considerations contradict models, which involve Cr-spinel crystallisation due to cumulate assimilation for example proposed for the Cr-spinel layers of the Rum Layers Intrusions (e.g. O'Driscoll et al., 2009b; O'Driscoll et al., 2010). Here, incorporation of dissolved cumulates by injected magmas result in Cr-spinel seams, however, due to mass balance calculations and the rapidly decreasing thermo-chemical potential to erode metres of cumulate rocks, this process cannot account for the LG and MG seams. Even if the lowermost part of the seams would crystallise due to cumulate assimilation and the upper part accumulated by a differing process, one would expect a compositional change, where this transition from one process to the other occurred. Nevertheless in none of the investigated seams such transition was observed.

The textural and geochemical study on orthopyroxene oikocrysts in Chapter 4 provide important insights into the formation process of Cr-spinel entrapped in oikocrysts, because the oikocrysts preserved the original size and texture of Cr-spinel in the earliest stages of the crystal mush formation. Importantly, entrapped Cr-spinel does not depict any change in grain size across the whole layer such as fining-upwards. Thus, chromite accumulation exclusively by large-scale crystal settling or by mobilisation of cumulate slurries proposed by Maier et al. (2013) cannot account for these particular Cr-spinel layers. Numerous studies have proposed *in situ* crystallisation of Cr-spinel seams instead of crystal settling in the Bushveld Complex (e.g. Latypov et al., 2015; Latypov et al., 2017b; Latypov et al., 2017a; Latypov et al., 2018; Mukherjee et al., 2017; Pebane and Latypov, 2017). However the presented data in Chapter 2 and 4 were collected from drill core material, which did not record steep or even overhanging Cr-spinel seams and thus cannot contribute to this debate. Taken together, accumulation of chromite by cumulate slurries, crystal settling on a large intrusion-wide scale or mixing did not play a major role in the formation of the investigated layers. Instead, the observations of this thesis can be explained by the recent model proposed by (Latypov et al., 2017b; Latypov et al., 2018). Here, ascending basaltic melts from the mantle get saturated in Cr-spinel only, due to decrease in pressure. Several replenishing events on an intrusion-wide scale resulted in the crystallization of Cr-spinel layers. This model offers a possible explanation for the described Cr-spinel characteristics in Chapter 2 and 4 and will be used as approach for the process of Cr-spinel accumulation in the Bushveld Complex.

The investigated lateral, compositional changes along strike presented in Chapter 3, can be used to advance our understanding on the formation of Cr-spinel seams in the Bushveld Complex. While the described changes in P and Si might be attributed to post-cumulus

depletion due to compaction, lateral variations in Mg# and Cr# are more likely to be explained by primary magmatic processes. This interpretation is corroborated by previous studies, which described structural and compositional changes along strike in the Critical and Main Zone of the Bushveld Complex (e.g. Klemm et al., 1985; Scoon and Teigler, 1995), arguing for lateral flow of new intruding magmas in the Bushveld magma chamber. The nature of the magmatic emplacement of the Bushveld Complex has been described by Kruger (2005) and Clarke et al. (2009). They proposed that the Bushveld magma chamber filled by subsequent influxes of new magmas, which formed sill-like sheets on top of the existing crystal mush. According to their studies these influxes propagated away from the main feeder, the Thabazimbi-Murchison-Lineament (TML) (Fig. 2.1), a massive, reactivated fault zone north of the complex, as fingered intrusion front (Clarke et al., 2009). These fingered intrusions initially followed existing structural unconformities or create their own due to thermo-chemical erosion. Such erosional magmatic features are typical circular, mm-dm sized depressions. They are ubiquitously found in Cr-spinel layers, where they are called potholes (e.g. Carr and I Groves, 1994; Carr et al., 1999; Latypov et al., 2017b; Latypov et al., 2017a). Broader kilometre-sized depressions, possibly confined by syn-magmatic faults, could thus result in lateral compositional changes of the main cumulus phase Cr-spinel, due to the differing thickness of the magma sheet on-top of the crystal mush, from which Cr-spinel crystallised. Similar conclusions were drawn by Scoon and Teigler (1995) for the LG6 in the eastern limb. Vertical compositional variations described in Chapter 2 support and refine the outlined formation model. Changes in the Cr-spinel chemistry indicate a general fractionation interrupted by repeated reversals (i.e. influx of primitive magma) upwards the lithostratigraphy. Similar fractionation and reversal trends of Cr-spinel layers have been described for various locations in the western and eastern limb (Naldrett et al., 2009; Naldrett et al., 2012). Moreover, compositional variations across single layers have been described in this thesis (Chapter 2) and are interpreted to represent one or more replenishing events, which initiated the accumulation of Cr-spinel, followed by subsequent differentiation. Notably, the reversals occur typically close to pyroxenitic parting within the seams. Therefore it is proposed that extensive, metre-sized seams like the MG1 and MG2 were constructed by a number of replenishing events, instead of a single one.

6.2.2 Cumulus formation processes: Rum Layered Intrusion

The Rum Layered Intrusion hosts several Cr-spinel seams (see Chapters 1.7.2 and 5 for a more detailed description), however, contrary to the first case study, they occur at the base of macro-rhythmic units and are much smaller in dimensions, typically 2–5 mm thick. These differences in position and thickness indicate that different processes were responsible for the formation of seams in the second case study.

Observations on the Unit 7-8 Cr-spinel layer of the Rum Layered Intrusion (Chapter 5) and previous studies O'Driscoll et al. (2009b) and O'Driscoll et al. (2010) argue for *in situ* crystallisation of Cr-spinel at the magma–crystal mush interface due to assimilation of unconsolidated troctolitic cumulate. In this model, infiltration of pricritic, crystal-poor magma resulted in thermo-chemical erosion of the troctolite footwall (similar to the process

proposed for the Bushveld Complex). The incorporation of dissolved troctolite drove the contaminated picrite onto the spinel stability field, which resulted in crystallisation of Cr-spinel to form continuous seams. Field relationships of these seams were used to argue for *in situ* crystallisation, because they are developed along an inclined or even overhanging topography (O'Driscoll et al., 2009b; O'Driscoll et al., 2010; Latypov et al., 2013). The anorthosite layer below the Cr-spinel seam represents the remnant of the partial melting and assimilation process, where most of the olivine and large portions of plagioclase were dissolved. Field descriptions, mineral chemistry and textural observations on a complete traverse of the Unit 7-8 Cr-spinel seam compiled in this thesis (Chapter 5) generally support this model on a broader scale, compared to the studies of O'Driscoll et al., which base upon a defined outcrop area. Moreover, the observed lateral changes provide deeper insights in the involved processes and thus aid in a refined model for C-spinel seam formation in the Rum Layered Intrusion.

In chapter 5 the Cr-spinel seam was mapped and sampled on a lateral continuous traverse across the extent of the Rum Layered Intrusion for the first time. Mapping showed that the typical Unit 7-8 seam package, consisting of hanging wall peridotite, Cr-spinel seam, anorthosite layer and footwall troctolite extend along large portions in the centre of the intrusions. Assessment of the plagioclase texture in the footwall troctolite and anorthosite layers depict similar crystal size and form. These observations in combination with recent studies (O'Driscoll et al., 2009b; O'Driscoll et al., 2010) argue for a similar origin by partial melting of the troctolite crystal–mush to produce a restitic anorthosite layer. Mapping and sampling of the Unit 7-8 traverse revealed the presence of a typical Unit 7-8 seam package along large portions, however, from one locality to the next, significant structural, lithological and compositional variations were observed (Chapter 5). The Cr-spinel seam is absent towards the margins (SE) and the central part of the intrusion (NW), where the main feeder is located (Long Loch Fault, LLF) (Fig. 5.1). In addition, the presence of the anorthosite layer, which typically underlies the Cr-spinel layer, is closely linked to the Cr-spinel layer and depicts similar structural changes. It appears to be relatively thick in the northwest, but thins out in the northwest and disappears entirely in the southeast. Here, both the anorthosite and the Cr-spinel layer are missing and the footwall troctolite are directly overlain by the hanging wall peridotite. Moreover, the compositional character of Cr-spinel in the Cr-spinel layer and the peridotite varies laterally along strike. In particular, Mg# and TiO_2 concentrations increase while Cr# decreases with increasing distance from the central part of the intrusion towards SE. As with the Cr-spinel chemistry, a consistent lateral change in plagioclase composition is observed along the strike, specifically Ab contents and K concentrations in plagioclase increase towards the SE. Thus, Cr-spinel and plagioclase illustrate a trend of increasing fractionation with increasing distance from the LLF.

The described lateral variations suggest the following refinements to the current model for Cr-spinel seam formation in the Rum Layered Intrusion. While O'Driscoll et al. (2009b) and O'Driscoll et al. (2010) envisaged one magmatic event to account for the metasomatic anorthosite layer formation and the Cr-spinel crystallisation, this study proposed two genetically linked, but separated replenishment steps. The first event was initiated by injections re-melting the troctolite cumulate by thermo-chemical erosion, which resulted in

the anorthosite 'restite' layer. The reasons for the localised re-melting in the central part remain uncertain, however here it is proposed that it depended on the distance to the main feeder. In close proximity to the LLF, the superheated magma (e.g. Holness, 1999; Upton et al., 2002) possibly resulted in vivid thermo-chemical erosion of the underlying crystal mush, preventing anorthosite formation ('too much erosion'). With increasing distance to the LLF the intruding magma cooled and thus its capacity to sufficiently erode the underlying crystal mush diminished ('too little erosion'). Thus, the potential to parially melt the underlying cumulates was the highest at the central part, forming the thickest anorthosite portions. A second influx of picritic magma (Upton et al., 2002) was injected and spread, due to its higher density, at the crystal mush interface and interacted with the anorthosite mush resulting in Cr-spinel crystallisation (similar to O'Driscoll et al., 2009b; O'Driscoll et al., 2010). Cross-cutting field relations suggest that this magma re-melted parts of the anorthosite mush layer forming small circular depressions, similar to potholes in the Cr-spinel layers of the Bushveld Complex. Systematic lateral changes in mineral chemistry described above suggest that the intruding magma was a rather thin sheet, facilitating fractionation along strike.

6.2.3 Generalised models for the formation of Cr-spinel layers

The considerations resulted in two generalised models for the formation of Cr-spinel layers in the Bushveld Complex (Fig. 6.2a–c) and the Rum Layered Intrusion (Fig. 6.1d–f): **(a)** the magma chamber of the Bushveld Complex was repeatedly fed by basaltic melt of slightly different composition (e.g. Zeh et al., 2015), due to melting of the subcontinental lithospheric mantle (SCLM) by a mantle plume. Fast ascent of these magmas along the TML possibly results in Cr-spinel saturation when the magmas entered the Bushveld magma chamber (Latypov et al., 2018). The magma chamber acted as an open system and was constantly filled with magma and discharged by basaltic lavas, which formed the Rooiberg Group. **(b)** Influx of Cr-spinel saturated, superheated magmas likely led to thermo-chemical erosion, possibly along syn-magmatic faults. This was followed by crystallisation of Cr-spinel layers, due to the Cr-spinel saturated nature of the magma. Depending on the respective thickness of the Cr-spinel layers, they were accumulated from a single or several successive magma injections. Although the replenishing magmas were generally crystal-poor, some batches carried olivine primocryst, which formed the nuclei of the oikocrysts described in Chapter 4. Post-cumulus modification of Cr-spinel by adcumulus growth started soon after accumulation, close to the magma–crystal mush interface. **(c)** Repeated replenishing resulted in the formation of the pyroxenite host rocks and additional Cr-spinel layers above the first one. The fact, that some replenishing events formed Cr-spinel layers, while others did not is not fully understood, however Zeh et al. (2015) emphasised the heterogeneity of the SCLM below the Bushveld Complex and suggested that different reservoirs (with varying Cr concentrations) were tapped in the process of the Bushveld Complex formation. Minor differences in the cumulate load could lead to minor lateral variations in P concentrations (Chapter 3).

(d) The cumulates of the Rum Layered Intrusion formed due to magma emplacement of partial mantle melts of picritic to basaltic composition (Upton et al., 2002) along the LLF. The layered series was constructed by several small influxes of these magmas, which formed

rather thin sheets of magma (Renner and Palacz, 1987; O'Driscoll et al., 2007) in an evolving sill-like complex (Emeleus and Troll, 2014). Importantly, some of these injections where placed within the unconsolidated cumulate pile, instead on top of the pile (e.g. Bédard et al., 1988; Hepworth et al., 2017). Similar to the Bushveld Complex, the magma chamber of the Rum Layered Intrusion was an open system in which magmas were released as basaltic lavas. Studies proposed that a volcanic complex was located on top of the intrusion, however most of the lavas are eroded nowadays (e.g. Troll et al., 2008). **(e)** Injection of primitive, superheated magma on top of the cumulate pile caused re-melting of the troctolite cumulate by thermo-chemical erosion and the formation of an anorthosite 'restite' layer via partial melting. **(f)** Finally, additional picritic magma intruded the magma–crystal mush package and interacted with the anorthosite layer and drove the contaminated picrite onto the spinel stability field (O'Driscoll et al., 2009b; O'Driscoll et al., 2010). Injections in the anorthosite crystal mush resulted in apophyses, which experienced a similar reaction, forming the Cr-spinel rims reported in Chapter 5.

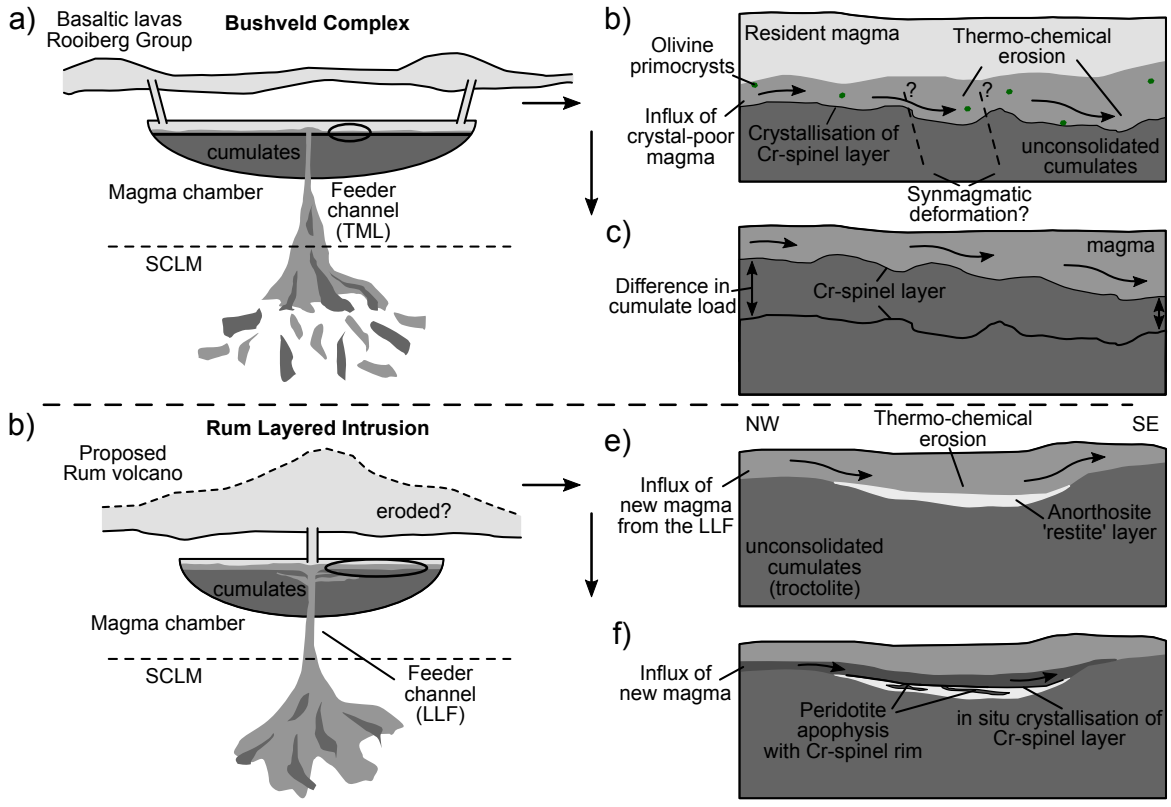

Figure 6.2: Generalised model for the formation of formation of the Cr-spinel layers of the Bushveld Complex **a-c** and the Rum Layered Intrusion **d-f**. Adapted after Zeh et al. (2015), Latypov et al. (2018), Troll et al. (2008), and O'Driscoll et al. (2010), see text for further explanation.

In the lights of the presented data this thesis proposes that Cr-spinel accumulation in both case studies was controlled by physico-chemical processes at or close to the crystal mush–magma interface and not by mechanical ones. The investigated Cr-spinel layers of the Bushveld Complex could have formed by chromite saturation and mainly *in-situ* crystallisation of adiabatic ascending magmas. The Cr-spinel layers of the Rum Layered Intrusions formed by

silicate rock assimilation due to repeated influxes of primitive magma. Despite the differences in the specific process, yet both are closely linked to one or repeated influxes of new magmas. In both case studies, these magmas operated on an intrusion-wide scale, where repeated influxes of primitive magma, assimilation of the underlying crystal mush, and fractionation resulted in lateral and vertical variations.

References

Albrecht, M., Derrey, I. T., Horn, I., Schuth, S., and Weyer, S. (2014). Quantification of trace element contents in frozen fluid inclusions by UV-fs-LA-ICP-MS analysis. *J Anal At Spectrom* 29, 1034–1041.

Allan, J. F., Sack, R. O., and Batiza, R. (1988). Cr-rich spinels as petrogenetic indicators; MORB-type lavas from the Lamont seamount chain, eastern Pacific. *Am Mineral* 73 (7-8), 741–753.

Arndt, N. T., Nelson, D. R., Compston, W., Trendall, A. F., and Thorne, A. M. (1991). The age of the Fortescue Group, Hamersley Basin, Western Australia, from ion microprobe zircon U–Pb results. *Aust J Earth Sci* 38 (3), 261–281.

Bachmann, K., Frenzel, M., Krause, J., and Gutzmer, J. (2017). Advanced Identification and Quantification of In-Bearing Minerals by Scanning Electron Microscope-Based Image Analysis. *Microsc Microanal* 23 (3), 527–537.

Barbey, P. (2009). Layering and schlieren in granitoids: A record of interactions between magma emplacement, crystallization and deformation in growing plutons. *Geol Belg* 12, 109–133.

Barnes, S. J. (1986a). The distribution of chromium among orthopyroxene, spinel and silicate liquid at atmospheric pressure. *Geochim Cosmochim Acta* 50 (9), 1889–1909.

Barnes, S. J. (1986b). The effect of trapped liquid crystallization on cumulus mineral compositions in layered intrusions. *Contrib Miner Petrol* 93, 524–531.

Barnes, S. J., Maier, W. D., and Curl, E. A. (2010). Composition of the Marginal Rocks and Sills of the Rustenburg Layered Suite, Bushveld Complex, South Africa: Implications for the Formation of the Platinum-Group Element Deposits. *Econ Geol* 105, 1491–1511.

Barnes, S. J., Mole, D. R., Le Vaillant, M., Campbell, M. J., Verral, M. R., Roberts, M. P., and Evans, N. J. (2016). Poikilitic Textures, Heteradcumulates and Zoned Orthopyroxenes in the Ntaka Ultramafic Complex, Tanzania: Implications for Crystallization Mechanisms of Oikocrysts. *J Petrol* 57 (6), 1171–1198.

Barnes, S. J. and Roeder, P. L. (2001). The range of spinel compositions in terrestrial mafic and ultramafic rocks. *J Petrol* 42 (12), 2279–2302.

Bédard, J. H. (2006). Trace element partitioning in plagioclase feldspar. *Geochim Cosmochim Acta* 70 (14), 3717–3742.

Bédard, J. H., Sparks, R. S. J., Renner, R., Cheadle, M. C., and Hallworth, M. A. (1988). Peridotite sills and metasomatic gabbros in the Eastern Layered Series of the Rhum complex. *J Geol Soc* 145 (2), 207–224.

Blundy, J. D. and Annen, C. J. (2016). Crustal magmatic systems from the perspective of heat transfer. *Elements* 12 (2), 115–120.

Boorman, S., Boudreau, A. E., and Kruger, F. J. (2004). The Lower Zone-Critical Zone Transition of the Bushveld Complex: a Quantitative Textural Study. *J Petrol* 45 (6), 1209–1235.

Bottinga, Y. and Weill, D. F. (1970). Densities of liquid silicate systems calculated from partial molar volumes of oxide components. *Am J Sci* 269 (2).

Boudreau, A. E. (1988). Investigations of the Stillwater Complex; 4, The role of volatiles in the petrogenesis of the J-M Reef, Minneapolis adit section. *Can Mineral* 26, 193–208.

Boudreau, A. E. (2016). The Stillwater Complex, Montana – Overview and the significance of volatiles. *Miner Mag* 80 (4), 585–637.

Boudreau, A. E., Ferré, E. C., O'Driscoll, B., and Ripley, E. M. (2016). Layered Mafic Intrusions and Associated Economic Deposits. *GSA Today,* 25–26.

Brown, G. M. (1956). The layered ultrabasic rocks of Rhum, Inner Hebrides. *Philos Trans R Soc London, Ser B* 240 (668), 1–54.

Bulau, J. R., Waff, H. S., and Tyburczy, J. A. (1979). Mechanical and thermodynamic constraints on fluid distribution in partial melts. *J Geophys Res B: Solid Earth* 84 (B11), 6102–6108.

Butcher, A. R., Pirrie, D., Prichard, H. M., and Fisher, P. (1999). Platinum-group mineralization in the Rum layered intrusion, Scottish Hebrides, UK. *J Geol Soc* 156 (2), 213–216.

Cameron, E. N. (1969). Postcumulus changes in the eastern Bushveld Complex. *Am Mineral* 54, 754–779.

Cameron, E. N. (1975). Postcumulus and subsolidus equilibration of chromite and coexisting silicates in the Eastern Bushveld Complex. *Geochim Cosmochim Acta* 39, 1021–1033.

Cameron, E. N. (1977). Chromite in the central sector of the Eastern Bushveld Complex, South Africa. *Am Mineral* 62, 1082–1096.

Cameron, E. N. (1978). The lower zone of the eastern Bushveld Complex in the Olifants River trough. *J Petrol* 19 (3), 437–462.

Cameron, E. N. (1980). Evolution of the Lower Critical Zone, central sector, eastern Bushveld Complex, and its chromite deposits. *Econ Geol* 75 (6), 845–871.

Campbell, I. H. (1968). The origin of heteradcumulate and adcumulate textures in the Jimberlana Norite. *Geol Mag* 105 (4), 378–383.

Campbell, I. H. (1987). Distribution of Orthocumulate Textures in the Jimberlana Intrusion. *J Geol* 95 (1), 35–53.

Campbell, I. H., Naldrett, A. J., and Barnes, S.-J. (1983). A model for the origin of the platinum-rich sulfide horizons in the Bushveld and Stillwater Complexes. *J Petrol* 24 (2), 133–165.

Carr, H. W. and I Groves, D. (1994). The importance of synmagmatic deformation in the formation of Merensky Reef potholes in the Bushveld Complex. *Econ Geol* 89 (6), 1398–1410.

Carr, H. W., Kruger, F. J., I Groves, D., and Cawthorn, R. G. (1999). The petrogenesis of Merensky Reef potholes at the Western Platinum Mine, Bushveld Complex: Sr-isotopic evidence for synmagmatic deformation. *Miner Deposita* 34 (4), 335–347.

Cashman, K., Sparks, R. S. J., and Blundy, J. D. (2017). Vertically extensive and unstable magmatic systems: A unified view of igneous processes. *Science* 355 (6331), 1–9.

Cawthorn, R. G. (1996). Models for incompatible trace-element abundances in cumulus minerals and their application to plagioclase and pyroxene compositions in the Bushveld Complex. *Contrib Miner Petrol* 123, 109–115.

Cawthorn, R. G. (2005). Pressure fluctuations and the formation of the PGE-rich Merensky and chromitite reefs, Bushveld Complex. *Miner Deposita* 40, 231–235.

Cawthorn, R. G. (2011). Geological interpretations from the PGE distribution in the Bushveld Merensky and UG2 chromitite reefs. *J S Afr Inst Min Metall* 111 (2), 67–79.

Cawthorn, R. G. (2013). Rare earth element abundances in apatite in the Bushveld Complex—A consequence of the trapped liquid shift effect. *Geology* 41 (5), 603–606.

Cawthorn, R. G. (2015). The Bushveld Complex, South Africa. *Layered Intrusions.* Ed. by B. Charlier, O. Namur, R. Latypov, and C. Tegner. Springer Geology. Dordrecht: Springer, 517–587.

Cawthorn, R. G. and Biggar, G. M. (1993). Crystallization of titaniferous chromite, magnesian ilmenite and armalcolite in tholeiitic suites in the Karoo Igneous Province. *Contrib Miner Petrol* 114 (2), 221–235.

Cawthorn, R. G. and Davies, G. (1983). Experimental data at 3 kbars pressure on parental magma to the Bushveld Complex. *Contrib Miner Petrol* 83 (1-2), 128–135.

Cawthorn, R. G. and Walraven, F. (1998). Emplacement and Crystallization Time for the Bushveld Complex. *J Petrol* 39 (9), 1669–1687.

Cawthorn, R. G. and Walsh, K. L. (1988). The use of phosphorus contents in yielding estimates of the proportion of trapped liquid in cumulates of the Upper Zone of the Bushveld Complex. *Miner Mag* 52 (364), 81–89.

Chutas, N. I., Bates, E., Prevec, S. A., Coleman, D. S., and Boudreau, A. E. (2012). Sr and Pb isotopic disequilibrium between coexisting plagioclase and orthopyroxene in the Bushveld Complex, South Africa: microdrilling and progressive leaching evidence for sub-liquidus contamination within a crystal mush. *Contrib Miner Petrol* 163 (4), 653–668.

Ciamarra, M. P. and Coniglio, A. (2008). Random very loose packings. *Phys Rev Lett* 101 (12), 128001.

Clarke, B., Uken, R., and Reinhardt, J. (2009). Structural and compositional constraints on the emplacement of the Bushveld Complex, South Africa. *Lithos* 111 (1-2), 21–36.

Collinet, M., Charlier, B., Namur, O., Oeser, M., Médard, E., and Weyer, S. (2017). Crystallization history of enriched shergottites from Fe and Mg isotope fractionation in olivine megacrysts. *Geochim Cosmochim Acta* 207, 277–2997.

Cooper, K. M. (2017). What Does a Magma Reservoir Look Like? The "Crystal's-Eye" View. *Elements* 13 (1), 23–28.

Cross, A. F. and Schlesinger, W. H. (1995). A literature review and evaluation of the. Hedley fractionation: Applications to the biogeochemical cycle of soil phosphorus in natural ecosystems. *Geoderma* 64 (3-4), 197–214.

Davis, D. W. (2008). Sub-million-year age resolution of Precambrian igneous events by thermal extraction–thermal ionization mass spectrometer Pb dating of zircon: Application to crystallization of the Sudbury impact melt sheet. *Geology* 36 (5), 383–386.

Dong, K. J., Yang, R. Y., Zou, R. P., and Yu, A. B. (2006). Role of interparticle forces in the formation of random loose packing. *Phys Rev Lett* 96 (14), 145505.

Droop, G. T. R. (1987). A general equation for estimating Fe^{3+} concentrations in ferromagnesian silicates and oxides from microprobe analyses, using stoichiometric criteria. *Miner Mag* 51 (361), 431–435.

Dunham, A. C. and Wadsworth, W. J. (1978). Cryptic variation in the Rhum layered intrusion. *Miner Mag* 42 (323), 347–356.

Dunham, A. C. and Wilkinson, F. C. F. (1985). Sulphide droplets-and the Unit 11/12 chromite band, Rhum: a mineralogical study. *Geol Mag* 122 (5), 539–548.

Eales, H. V. (2000). Implications of the chromium budget of the Western Limb of the Bushveld Complex. *S Afr J Geol* 103 (2), 141–150.

Eales, H. V. (2002). Caveats in defining the magmas parental to the mafic rocks of the Bushveld Complex, and the manner of their emplacement: review and commentary. *Miner Mag* 66 (6), 815–832.

Eales, H. V. and Cawthorn, R. G. (1996). The Bushveld Complex. *Layered Intrusions.* Ed. by R. G. Cawthorn. Elsevier, 181–229.

Eales, H. V. and Costin, G. (2012). Crustally contaminated komatiite: primary source of the chromitites and Marginal, Lower, and Critical Zone magmas in a staging chamber beneath the Bushveld Complex. *Econ Geol* 107 (4), 645–665.

Eales, H. V., de Klerk, W. J., and Teigler, B. (1990). Evidence for magma mixing processes within the Critical and Lower Zones of the northwestern Bushveld Complex, South Africa. *Chem Geol* 88, 261–278.

Eales, H. V., Teigler, B., and Maier, W. D. (1993). Cryptic variations of minor elements A1, Cr, and Mn in Lower and Critical Zone orthopyroxenes of the Western Bushveld Complex. *Miner Mag* 57, 257–264.

Egorova, V. and Latypov, R. (2013). Mafic–ultramafic sills: New insights from M-and S-shaped mineral and whole-rock compositional profiles. *J Petrol* 54 (10), 2155–2191.

Emeleus, C. H. (1994). *1: 20000 solid geology map of Rum.* Scottish Natural Heritage.

Emeleus, C. H., Cheadle, M. C., Hunter, R. H., Upton, B. G. J., and Wadsworth, W. J. (1996). The Rum layered suite. *Layered Intrusions.* Ed. by R. G. Cawthorn. Elsevier, 403–439.

Emeleus, C. H. and Hudson, J. D. (1997). *Geology of Rum and the adjacent islands.* Memoir of the British Geological Survey.

Emeleus, C. H. and Troll, V. R. (2011). Recent research developments on the Isle of Rum, NW Scotland. *Geol Today* 27 (5), 184–193.

Emeleus, C. H. and Troll, V. R. (2014). The Rum Igneous Centre, Scotland. *Miner Mag* 78 (4), 805–840.

Epstein, N. and Young, M. J. (1962). Random loose packing of binary mixtures of spheres. *Nature* 196 (4857), 885–886.

Fandrich, R., Gu, Y., Burrows, D., and Moeller, K. (2007). Modern SEM-based mineral liberation analysis. *Int J Min Proc* 84 (1), 310–320.

Farrell, G. R., Martini, K. M., and Menon, N. (2010). Loose packings of frictional spheres. *Soft Matter* 6 (13), 2925–2930.

Fisk, M. R. and Bence, A. E. (1980). Experimental crystallization of chrome spinel in FAMOUS basalt 527-1-1. *Earth Planet Sci Lett* 48 (1), 111–123.

Fletcher, I. R., Libby, W. G., and Rosman, K. J. R. (1987). Sm–Nd dating of the 2411 Ma Jimberlana dyke, Yilgarn Block, Western Australia. *Aust J Earth Sci* 34 (4), 523–525.

Francis, D. (2011). Columbia Hills-An exhumed layered igneous intrusion on Mars? *Earth Planet Sci Lett* 310 (1).

Gain, S. B. (1985). The geologic setting of the platiniferous UG-2 chromitite layer on the farm Maandagshoek, eastern Bushveld Complex. *Econ Geol* 80 (4), 925–943.

Godel, B. (2015). Platinum-group element deposits in layered intrusions: recent advances in the understanding of the ore forming processes. *Layered Intrusions.* Ed. by B. Charlier, O. Namur, R. Latypov, and C. Tegner. Springer Geology. Dordrecht: Springer, 379–432.

Godel, B., Barnes, S.-J., and Maier, W. D. (2011). Parental magma composition inferred from trace element in cumulus and intercumulus silicate minerals: An example from the Lower and Lower Critical Zones of the Bushveld Complex, South-Africa. *Lithos* 125, 537–552.

Guillong, M., Meier, D., Allan, M. M., Heinrich, C. A., and Yardley, B. W. D. (2008). SILLS: A MATLAB-based program for the reduction of laser ablation ICP-MS data of homogeneous

materials and inclusions. *Mineralogical Association of Canada Short Course 40, Vancouver, B.C.* 328–333.

Gunn, A. G. and Styles, M. T. (2002). Platinum-group element occurrences in Britain: magmatic, hydrothermal and supergene. *Appl Earth Sci* 111 (1), 2–14.

Haggerty, S. E. (1991). Oxide Mineralogy of the Upper Mantle. *Oxide Minerals: Petrologic and Magnetic Significance.* Ed. by D. H. Lindsley. Mineralogical Society of America, 355–416.

Hall, A. L. (1932). The Bushveld igneous complex of the central Transvaal. *Geol Surv S Afr Mem* 28 (544).

Hall, A. L. and Humphrey, W. A. (1908). On the occurrence of chromite deposits along the southern and eastern margins of the Bushveld Plutonic Complex. *S Afr J Geol* 11 (1), 69–77.

Hamilton, M. A., Pearson, D. G., Thompson, R. N., Kelley, S. P., and Emeleus, C. H. (1998). Rapid eruption of Skye lavas inferred from precise U–Pb and Ar–Ar dating of the Rum and Cuillin plutonic complexes. *Nature* 394 (6690), 260–263.

Harker, A. (1908). *The Geology of the Small Isles of Invernessshire: Memoir of the Geological Survey: Scotland.* Edinburgh.

Harmer, R. E. and Sharpe, M. R. (1985). Field relations and strontium isotope systematics of the marginal rocks of the eastern Bushveld Complex. *Econ Geol* 80, 813–837.

Harris, C., Pronost, J. J., Ashwal, L. D., and Cawthorn, R. G. (2005). Oxygen and hydrogen isotope stratigraphy of the Rustenburg Layered Suite, Bushveld Complex: constraints on crustal contamination. *J Petrol* 46 (3), 579–601.

Hartmann, J., Moosdorf, N., Lauerwald, R., Hinderer, M., and West, A. J. (2014). Global chemical weathering and associated P-release - The role of lithology, temperature and soil properties. *Chem Geol* 363, 145–163.

Heaney, D. F., German, R. M., and Ahn, I. S. (1995). The gravitational effects on low solid-volume fraction liquid-phase sintering. *J Mater Sci* 30 (22), 5808–5812.

Henderson, P. (1975). Reaction trends shown by chrome-spinels of the Rhum layered intrusion. *Geochim Cosmochim Acta* 39, 1035–1044.

Henderson, P. and Suddaby, P. (1971). The nature and origin of the chrome-spinel of the Rhum layered intrusion. *Contrib Miner Petrol* 33 (1), 21–31.

Hepworth, L. N., O'Driscoll, B., Gertisser, R., Daly, J. S., and Emeleus, C. H. (2017). Incremental Construction of the Unit 10 Peridotite, Rum Eastern Layered Intrusion, NW Scotland. *J Petrol* 58 (1), 137–166.

Hiemstra, S. A. (1985). The distribution of some platinum-group elements in the UG-2 chromitite layer of the Bushveld Complex. *Econ Geol* 80 (4), 944–957.

Hiemstra, S. A. (1986). The distribution of chalcophile and platinum-group elements in the UG-2 chromitite layer of the Bushveld Complex. *Econ Geol* 81 (5), 1080–1086.

Higgins, M. D. (2000). Measurement of crystal size distributions. *Am Mineral* 85, 1105–1116.

Higgins, M. D. (2002). A crystal size-distribution study of the Kiglapait layered mafic intrusion, Labrador, Canada: evidence for textural coarsening. *Contrib Miner Petrol* 144 (3), 314–330.

Higgins, M. D. (2006). *Quantitative Textural Measurements in Igneous and Metamorphic Petrology.* Cambridge University Press.

Higgins, M. D. (2011). Textural coarsening in igneous rocks. *Int Geol Rev* 53 (3-4), 354–376.

Higgins, M. D. (2015). Quantitative Textural Analysis of Rocks in Layered Mafic Intrusions. *Layered Intrusions.* Ed. by B. Charlier, O. Namur, R. Latypov, and C. Tegner. Springer Geology. Dordrecht: Springer, 153–181.

Hodson, M. E. (1998). The origin of igneous layering in the Nunarssuit syenite, South Greenland. *Geol Mag* 62 (1), 9–27.

Holness, M. B. (1999). Contact metamorphism and anatexis of Torridonian arkose by minor intrusions of the Rum Igneous Complex, Inner Hebrides, Scotland. *Geol Mag* 135 (5), 527–542.

Holness, M. B. (2005). Spatial Constraints on Magma Chamber Replenishment Events from Textural Observations of Cumulates: the Rum Layered Intrusion, Scotland. *J Petrol* 46 (8), 1585–1601.

Holness, M. B. (2014). The effect of crystallization time on plagioclase grain shape in dolerites. *Contrib Miner Petrol* 168 (5), 1–19.

Holness, M. B., Cawthorn, R. G., and Roberts, J. (2017a). The thickness of the crystal mush on the floor of the Bushveld magma chamber. *Contrib Miner Petrol* 172 (11-12), 102.

Holness, M. B., Farr, R., and Neufeld, J. A. (2017b). Crystal settling and convection in the Shiant Isles Main Sill. *Contrib Miner Petrol* 172 (1), 1–25.

Holness, M. B., Neufeld, J. A., Gilbert, A. J., and Macdonald, R. (2018). Orientation of tabular mafic intrusions controls convective vigour and crystallization style. *J Petrol.*

Holness, M. B., Nielsen, T. F. D., and Tegner, C. (2007). Textural Maturity of Cumulates: a Record of Chamber Filling, Liquidus Assemblage, Cooling Rate and Large-scale Convection in Mafic Layered Intrusions. *J Petrol* 48 (1), 141–157.

Holness, M. B., Tegner, C., Nielsen, T. F. D., and Charlier, B. (2017c). The thickness of the mushy layer on the floor of the Skaergaard magma chamber at apatite saturation. *J Petrol* 58 (5), 909–932.

Holness, M. B. and Vernon, R. H. (2015). The influence of interfacial energies on igneous microstructures. *Layered Intrusions.* Ed. by B. Charlier, O. Namur, R. Latypov, and C. Tegner. Springer Geology. Dordrecht: Springer, 183–228.

Holness, M. B., Vukmanovic, Z., and Mariani, E. (2017d). Assessing the role of compaction in the formation of adcumulates: a microstructural perspective. *J Petrol* 58 (4), 643–673.

Holness, M. B. and Winpenny, B. (2009). The Unit 12 allivalite, Eastern Layered Intrusion, Isle of Rum: a textural and geochemical study of an open-system magma chamber. *Geol Mag* 146 (3), 437–450.

Hulbert, L. J. and von Gruenewaldt, G. (1985). Textural and Compositional Features of Chromite in the Lower and Critical Zones of the Bushveld Complex South of Potgietersrus. *Econ Geol* 80, 872–893.

Hunter, R. H. (1987). Textural Equilibrium in Layered Igneous Rocks. *Origins of Igneous Layering.* Ed. by I. Parson. Dordrecht: Springer Netherlands.

Hunter, R. H. (1996). Texture Development in Cumulate Rocks. *Layered Intrusions.* Ed. by R. G. Cawthorn. Elsevier, 77–101.

Irvine, T. N. (1965). Chromian spinel as a petrogenetic indicator: Part 1. Theory. *Can J Earth Sci* 2 (6), 648–672.

Irvine, T. N. (1967). Chromian spinel as a petrogenetic indicator: Part 2. Petrologic applications. *Can J Earth Sci* 4 (1), 71–103.

Irvine, T. N. (1975). Crystallization sequences in the Muskox intrusion and other layered intrusions-II. Origin of chromitite layers and similar deposits of other magmatic ores. *Geochim Cosmochim Acta* 33, 991–1020.

Irvine, T. N. (1977). Origin of chromitite layers in the Muskox intrusion and other stratiform intrusions: A new interpretation. *Geology* 5, 273–277.

Ivanic, T. J., Nebel, O., Jourdan, F., Faure, K., Kirkland, C. L., and Belousova, E. A. (2015). Heterogeneously hydrated mantle beneath the late Archean Yilgarn Craton. *Lithos* 238, 76–85.

Jackson, E. D. (1961). *Primary Textures and Mineral Associations in the Ultramafic Zone of the Stillwater Complex, Montana.* US Geological Survey Professional Papers 358.

Jarosewich, E., Nelen, J. A., and Norberg, J. A. (1980). Reference samples for electron microprobe analysis. *Geostand Geoanal Res* 4 (1), 43–47.

Jerram, D. A., Cheadle, M. C., Hunter, R. H., and Elliott, M. T. (1996). The spatial distribution of grains and crystals in rocks. *Contrib Miner Petrol* 125 (1), 60–74.

Jerram, D. A., Cheadle, M. C., and Philpotts, A. R. (2003). Quantifying the building blocks of igneous rocks: are clustered crystal frameworks the foundation? *J Petrol* 44 (11), 2033–2051.

Junge, M., Oberthuer, T., and Melcher, F. (2014). Cryptic variation of chromite chemistry, platinum group element and platinum group mineral distribution in the UG-2 chromitite: an example from the Karee Mine, western Bushveld Complex, South Africa. *Econ Geol* 109 (3), 795–810.

Junge, M., Oberthuer, T., Osbahr, I., and Gutter, P. (2016). Platinum-group elements and minerals in the lower and middle group chromitites of the western Bushveld Complex, South Africa. *Miner Deposita* 51 (7), 841–852.

Kamenetsky, V. S., Crawford, A. J., and Meffre, S. (2001). Factors controlling chemistry of magmatic spinel: an empirical study of associated olivine, Cr-spinel and melt inclusions from primitive rocks. *J Petrol* 42 (4), 655–671.

Kaufmann, F. E. D., Vukmanovic, Z., Holness, M. B., and Hecht, L. (2018). Orthopyroxene oikocrysts in the MG1 chromitite layer of the Bushveld Complex: implications for cumulate formation and recrystallisation. *Contrib Miner Petrol* 173 (2), 1–20.

Kinnaird, J. A., Kruger, F. J., Nex, P. A., and Cawthorn, R. G. (2002). Chromite formation—a key to understanding processes of platinum enrichment. *Trans Inst Miner Min Metal* 111, 1–32.

Klemm, D. D., Ketterer, S., Reichhardt, F., Steindl, J., and Weber-Diefenbach, K. (1985). Implication of vertical and lateral compositional variations across the pyroxene marker and its associated rocks in the upper part of the main zone in the eastern Bushveld Complex. *Econ Geol* 80 (4), 1007–1015.

Kottke-Levin, J., Tredoux, M., and Graebe, P. J. (2009). An investigation of the geochemistry of the Middle Group of the eastern Bushveld complex, South Africa Part 1 – the chromitite layers. *Appl Earth Sci* 118 (3/4), 111–130.

Kruger, F. J. (2005). Filling the Bushveld Complex magma chamber: lateral expansion, roof and floor interaction, magmatic unconformities, and the formation of giant chromitite, PGE and Ti-V-magnetitite deposits. *Miner Deposita* 40 (5), 451–472.

Kuck, P. H. (2013). Nickel. *Minerals Yearbook.* Ed. by US Geological Survey.

Latypov, R., Chisyakova, S., Barnes, S. J., and Hunt, E. J. (2017a). Origin of platinum deposits in layered intrusions by in situ crystallization: evidence from undercutting Merensky Reef of the Bushveld Complex. *J Petrol* 58 (4), 715–761.

Latypov, R., Chisyakova, S., and Mukherjee, R. (2017b). A Novel Hypothesis for Origin of Massive Chromitites in the Bushveld Igneous Complex. *J Petrol.*

Latypov, R., Costin, G., Chisyakova, S., Hunt, E. J., Mukherjee, R., and Naldrett, A. J. (2018). Platinum-bearing chromite layers are caused by pressure reduction during magma ascent. *Nat Geosci* 462.

Latypov, R., Morse, S. A., Robins, B., Wilson, R., Cawthorn, R. G., Tegner, C., Holness, M. B., Lesher, C. E., Barnes, S. J., O'Driscoll, B., Veksler, I. V., Higgins, M. D., Wilson, A. H., Namur, O., Chisyakova, S., Naslund, H. R., and Thy, P. (2015). A fundamental dispute: A discussion of "On some fundamentals of igneous petrology" by Bruce D. Marsh, Contributions to Mineralogy and Petrology (2013) 166: 665–690. *Contrib Miner Petrol* 169 (20).

Latypov, R., O'Driscoll, B., and Lavrenchuk, A. (2013). Towards a model for the in situ origin of PGE reefs in layered intrusions: insights from chromitite seams of the Rum Eastern Layered Intrusion, Scotland. *Contrib Miner Petrol* 166, 309–327.

Lazarov, M. and Horn, I. (2015). Matrix and energy effects during in-situ determination of Cu isotope ratios by ultraviolet-femtosecond laser ablation multicollector inductively coupled plasma mass spectrometry. *Spectrochim Acta Part B At Spectrosc* 111, 64–73.

Lee, C. A. (1996). A review of mineralization in the Bushveld complex and some other layered Mafic intrusions. *Layered Intrusions.* Ed. by R. G. Cawthorn. Elsevier, 103–145.

Lee, C. A. and Parry, S. J. (1988). Platinum-group element geochemistry of the lower and middle group chromitites of the eastern Bushveld Complex. *Econ Geol* 83, 1127–1139.

Li, C., Ripley, E. M., Sarkar, A., Shin, D., and Maier, W. D. (2005). Origin of phlogopite-orthopyroxene inclusions in chromites from the Merensky Reef of the Bushveld Complex, South Africa. *Contrib Miner Petrol* 150, 119–130.

Lipin, B. R. (1993). Pressure Increases, the Formation of Chromite Seams, and the Development of the Ultramafic Series in the Stillwater Complex, Montana. *J Petrol* 34 (5), 955–976.

Lundgaard, K. L. L., Tegner, C., Cawthorn, R. G., Kruger, F. J., and Wilson, J. R. (2006). Trapped intercumulus liquid in the Main Zone of the eastern Bushveld Complex, South Africa. *Contrib Miner Petrol* 151 (3), 352–369.

Maier, W. D. (1995). Olivine oikocrysts in Bushveld Anorthosite; some implications for cumulate formation. *Can Mineral* 33, 1011–1022.

Maier, W. D. and Barnes, S.-J. (2008). Platinum-group elements in the UG1 and UG2 chromitites, and the Bastard reef, at Impala platinum mine, western Bushveld Complex, South Africa: Evidence for late magmatic cumulate instability and reef constitution. *S Afr J Geol* 111 (2-3), 159–176.

Maier, W. D., Barnes, S.-J., and I Groves, D. (2013). The Bushveld Complex, South Africa: formation of platinum– palladium, chrome- and vanadium-rich layers via hydrodynamic sorting of a mobilized cumulate slurry in a large, relatively slowly cooling, subsiding magma chamber. *Miner Deposita* 48 (1), 1–56.

Maier, W. D. and Hanski, E. J. (2017). Layered Mafic–Ultramafic Intrusions of Fennoscandia: Europe's Treasure Chest of Magmatic Metal Deposits. *Elements* 13 (6), 415–420.

Manoochehri, S., Schmidt, M. W., and Britz, W. (2015). Trapped Liquid, Paleo-porosity and Formation Time Scale of a Chromitite–(Ortho) pyroxenite Cumulate Section, Bushveld, South Africa. *J Petrol* 56 (11), 2195–2222.

Marks, M. A. W. and Markl, G. (2015). The Ilímaussaq Alkaline Complex, South Greenland. *Layered Intrusions.* Ed. by B. Charlier, O. Namur, R. Latypov, and C. Tegner. Springer Geology. Dordrecht: Springer, 649–692.

Martin, D. and Nokes, R. (1988). Crystal settling in a vigorously converting magma chamber. *Nature* 332 (6164), 534–536.

Martin, D. and Nokes, R. (1989). A fluid-dynamical study of crystal settling in convecting magmas. *J Petrol* 30 (6), 1471–1500.

Mathez, E. A. (1995). Magmatic metasomatism and formation of the Merensky Reef, Bushveld Complex. *Contrib Miner Petrol* 119 (2), 277–286.

Mathez, E. A., Hunter, R. H., and Kinzler, R. J. (1997). Petrologic evolution of partially molten cumulate: the Atok section of the Bushveld Complex. *Contrib Miner Petrol* 129 (1), 20–34.

Mathez, E. A. and Mey, J. (2005). Character of the UG2 Chromitite and Host Rocks and Petrogenesis of Its Pegmatoidal Footwall, Northeastern Bushveld Complex. *Econ Geol* 100, 1617–1630.

Mathison, C. I. (1987). Pyroxene oikocrysts in troctolitic cumulates-evidence for supercooled crystallisation and postcumulus modification. *Contrib Miner Petrol* 97 (2), 228–236.

Matveev, S. and Ballhaus, C. G. (2002). Role of water in the origin of podiform chromitite deposits. *Earth Planet Sci Lett* 203, 235–243.

McBirney, A. R. (1996). The Skaergaard Intrusion. *Layered Intrusions.* Ed. by R. G. Cawthorn. Elsevier, 147–180.

McBirney, A. R. and Noyes, R. M. (1979). Crystallization and Layering of the Skaergaard Intrusion. *J Petrol* 20 (3).

McDonough, W. F. and Sun, S. S. (1995). The composition of the Earth. *Chem Geol* 120 (3-4), 223–253.

McLaren, C. H. and De Villiers, J. P. R. (1982). The platinum-group chemistry and mineralogy of the UG-2 chromitite layer of the Bushveld Complex. *Econ Geol* 77 (6), 1348–1366.

Merkle, R. K. W. (1992). Platinum-group minerals in the middle group of chromitite layers at Marikana, western Bushveld Complex: indications for collection mechanisms and postmagmatic modification. *Can J Earth Sci* 29, 209–221.

Meurer, W. P. and Boudreau, A. E. (1998a). Compaction of Igneous Cumulates Part I: Geochemical Consequences for Cumulates and Liquid Fractionation Trends. *J Geol* 106, 281–292.

Meurer, W. P. and Boudreau, A. E. (1998b). Compaction of Igneous Cumulates Part II: Compaction and the Development of Igneous Foliations. *J Geol* 106, 293–304.

Meurer, W. P. and Claeson, D. T. (2002). Magma replenishment, and the significance of poikilitic textures, in the Lower Main Zone of the western Bushveld Complex, South Africa. *J Petrol* 43 (4), 607–629.

Mitchell, A. A. and Scoon, R. N. (2007). The Merensky Reef at Winnaarshoek, Eastern Bushveld Complex: a primary magmatic hypothesis based on a wide reef facies. *Econ Geol* 102 (5), 971–1009.

Molengraff, G. A. F. (1901). Geologie de la Republique Sud-Africaine du Transvaal. *Bull Soc Geol France* 1, 13–92.

Mondal, S. K. and Mathez, E. A. (2007). Origin of the UG2 chromitite layer, Bushveld Complex. *J Petrol* 48 (3), 495–510.

Morse, S. A. (2015). Kiglapait Intrusion, Labrador. *Layered Intrusions.* Ed. by B. Charlier, O. Namur, R. Latypov, and C. Tegner. Springer Geology. Dordrecht: Springer, 589–648.

Morse, S. A., Davidson, J. P., and Tepley III, F. J. (2017). Plagioclase Zonation: An Archive of Trapped Liquid and Crustal Contamination. *Elements* 13 (6), 403–408.

Moskalyk, R. R. and Alfantazi, A. M. (2003). Processing of vanadium: a review. *Min Eng* 16 (9), 793–805.

Mukherjee, R., Latypov, R., and Balakrishna, A. (2017). An intrusive origin of some UG-1 chromitite layers in the Bushveld Igneous Complex, South Africa: Insights from field relationships. *Ore Geol Rev.*

Mungall, J. E., Kamo, S. A., and McQuade, S. (2016). U–Pb geochronology documents out-of-sequence emplacement of ultramafic layers in the Bushveld Igneous Complex of South Africa. *Nat Commun,* 1–13.

Naldrett, A. J. (2004). *Magmatic sulfide deposits: Geology, geochemistry and exploration.* Springer.

Naldrett, A. J. and von Gruenewaldt, G. (1989). Association of platinum-group elements with chromitite in layered intrusions and ophiolite complexes. *Econ Geol* 84 (1), 180–187.

Naldrett, A. J., Wilson, A. H., Kinnaird, J. A., and Chunnett, G. (2009). PGE Tenor and Metal Ratios within and below the Merensky Reef, Bushveld Complex: Implications for its Genesis. *J Petrol* 50 (4), 625–659.

Naldrett, A. J., Wilson, A. H., Kinnaird, J. A., Yudovskaya, M. A., and Chunnett, G. (2012). The origin of chromitites and related PGE mineralization in the Bushveld Complex: new mineralogical and petrological constraints. *Miner Deposita* 47 (3), 209–232.

Namur, O., Abily, B., Boudreau, A. E., Blanchette, F., Bush, J. W. M., Ceuleneer, G., Charlier, B., Donaldson, C. H., Duchesne, J. C., Higgins, M. D., Morata, D., Nielsen, T. F. D., O'Driscoll, B., Pang, K. N., Peacock, T., Spandler, C., Toramaru, A., and Veksler, I. V. (2015). Igneous Layering in Basaltic Magma Chambers. *Layered Intrusions.* Ed. by B. Charlier, O. Namur, R. Latypov, and C. Tegner. Springer Geology. Dordrecht: Springer, 75–152.

Namur, O., Humphreys, M. C. S., and Holness, M. B. (2014). Crystallization of interstitial liquid and latent heat buffering in solidifying gabbros: Skaergaard intrusion, Greenland. *J Petrol* 55 (7), 1389–1427.

Naslund, H. R. and McBirney, A. R. (1996). Mechanisms of formation of igneous layering. *Layered Intrusions.* Ed. by R. G. Cawthorn. Elsevier, 1–44.

Nicholson, D. M. and Mathez, E. A. (1991). Petrogenesis of the Merensky Reef in the Rustenburg section of the Bushveld Complex. *Contrib Miner Petrol* 107, 293–309.

O'Driscoll, B., Butcher, A. R., and Latypov, R. (2014). New insights into precious metal enrichment on the Isle of Rum, Scotland. *Geol Today* 30 (4), 134–141.

O'Driscoll, B., Day, J. M. D., Daly, J. S., Walker, R. J., and McDonough, W. F. (2009a). Rhenium–osmium isotopes and platinum-group elements in the Rum Layered Suite, Scotland: Implications for Cr-spinel seam formation and the composition of the Iceland mantle anomaly. *Earth Planet Sci Lett* 286, 41–51.

O'Driscoll, B., Donaldson, C. H., Daly, J. S., and Emeleus, C. H. (2009b). The roles of melt infiltration and cumulate assimilation in the formation of anorthosite and a Cr-spinel seam in the Rum Eastern Layered Intrusion, NW Scotland. *Lithos* 111, 6–20.

O'Driscoll, B., Emeleus, C. H., Donaldson, C. H., and Daly, J. S. (2010). Cr-spinel Seam Petrogenesis in the Rum Layered Suite, NWScotland: Cumulate Assimilation and in situ Crystallization in a Deforming Crystal Mush. *J Petrol* 51 (6), 1171–1201.

O'Driscoll, B., Hargraves, R. B., Emeleus, C. H., Troll, V. R., Donaldson, C. H., and Reavy, R. J. (2007). Magmatic lineations inferred from anisotropy of magnetic susceptibility fabrics in Units 8, 9, and 10 of the Rum Eastern Layered Series, NW Scotland. *Lithos* 98, 27–44.

O'Driscoll, B. and VanTongeren, J. A. (2017). Layered intrusions: From petrological paradigms to precious metal repositories. *Elements* 13 (6), 383–389.

Oberthuer, T., Junge, M., Rudashevsky, N., de Meyer, E., and Gutter, P. (2016). Platinum-group minerals in the LG and MG chromitites of the eastern Bushveld Complex, South Africa. *Miner Deposita* 51 (1), 71–87.

Oeser, M., Weyer, S., Horn, I., and Schuth, S. (2014). High-Precision Fe and Mg Isotope Ratios of Silicate Reference. *Geostand Geoanal Res* 38 (3), 311–328.

Onoda, G. Y. and Liniger, E. G. (1990). Random loose packings of uniform spheres and the dilatancy onset. *Phys Rev Lett* 64 (22), 2727–2730.

Oppermann, L., Junge, M., Schuth, S., Schwarz-Schampera, U., and Sautheitl, L. (2017). Mobility and distribution of palladium and platinum in soils above Lower and Middle Group chromitites of the western Bushveld Complex, South Africa. *S Afr J Geol* 120, 511–524.

Osbahr, I., Oberthuer, T., Klemd, R., and Josties, A. (2014). Platinum-group element distribution in base-metal sulfides of the UG2 chromitite, Bushveld Complex, South Africa—a reconnaissance study. *Miner Deposita* 49 (6), 655–665.

Papp, J. F. (2014). Chromium. *Minerals Yearbook.* Ed. by US Geological Survey.

Parson, I. (1979). The Klokken Gabbro—Syenite Complex, South Greenland: Cryptic Variation and Origin of Inversely Graded Layering. *J Petrol* 20 (4), 653–694.

Pebane, M. and Latypov, R. (2017). The significance of magmatic erosion for bifurcation of UG1 chromitite layers in the Bushveld Complex. *Ore Geol Rev.*

Penberthy, C. J. and Merkle, R. K. W. (1999). Lateral variations in the platinum-group element content and mineralogy of the UG2 Chromitite Layer, Bushveld Complex. *S Afr J Geol* 102 (2), 240–250.

Polyak, D. E. (2015). Vanadium. *Minerals Yearbook.* Ed. by US Geological Survey.

Power, M. R., Pirrie, D., and Andersen, J. Ø. (2003). Diversity of platinum-group element mineralization styles in the North Atlantic Igneous Province: new evidence from Rum, UK. *Geol Mag* 140 (5), 499–512.

Power, M. R., Pirrie, D., Andersen, J. Ø., and Wheeler, P. D. (2000). Testing the validity of chrome spinel chemistry as a provenance and petrogenetic indicator. *Geology* 28 (11), 1027–1030.

Prichard, H. M., Barnes, S. J., Godel, B., Reddy, S. M., Vukmanovic, Z., Halfpenny, A., Neary, C. R., and Fisher, P. C. (2015). The structure of and origin of nodular chromite from the Troodos ophiolite, Cyprus, revealed using high-resolution X-ray computed tomography and electron backscatter diffraction. *Lithos* 218-219, 87–98.

Prior, D. J., Boyle, A. P., Brenker, F., Cheadle, M. C., Day, A., Lopez, G., Peruzzo, L., Potts, G. J., Reddy, S. M., Spiess, R., Timms, N. E., Trimby, P., Wheeler, J., and Zetterstroem, L. (1999). The application of electron backscatter diffraction and orientation contrast imaging in the SEM to textural problems in rocks. *Am Mineral* 84, 1741–1759.

Renner, R. and Palacz, Z. (1987). Basaltic replenishment of the Rhum magma chamber: evidence from unit 14. *J Geol Soc* 144, 961–970.

Ripley, E. M. (1979). Sulfide petrology of basal chilled margins in layered sills of the Archean Deer Lake Complex, Minnesota. *Contrib Miner Petrol* 69 (4), 345–354.

Roeder, P. L. (1994). Chromite; from the fiery rain of chondrules to the Kilauea Iki lava lake. *Can Mineral* 32 (4), 729–746.

Roeder, P. L. and Campbell, I. H. (1985). The effect of postcumulus reactions on composition of chrome-spinels from the Jimberlana intrusion. *J Petrol* 26 (3), 763–786.

Roelofse, F. and Ashwal, L. D. (2012). The Lower Main Zone in the Northern Limb of the Bushveld Complex-a> $1 \cdot$ 3 km thick sequence of intruded and variably contaminated crystal mushes. *J Petrol* 53 (7), 1449–1476.

Sack, R. O. (1982). Spinels as petrogenetic indicators: activity-composition relations at low pressures. *Contrib Miner Petrol* 79 (2), 169–186.

Sack, R. O. and Ghiorso, M. S. (1991). Chromite as a Petrogenetic Indicator. *Oxide Minerals: Petrologic and Magnetic Significance.* Ed. by D. H. Lindsley. Mineralogical Society of America, 323–354.

Schannor, M., Veksler, I. V., Hecht, L., Harris, C., Romer, R. L., and Manyeruke, T. D. (2018). Small-scale Sr and O isotope variations through the UG2 in the eastern Bushveld Complex: The role of crustal fluids. *Chem Geol.*

Schoenberg, R., Kruger, F. J., Nägler, T. F., Meisel, T., and Kramers, J. D. (1999). PGE enrichment in chromitite layers and the Merensky Reef of the western Bushveld Complex; a Re–Os and Rb–Sr isotope study. *Earth Planet Sci Lett* 172 (1-2), 49–64.

Scoates, J. S. and Friedman, R. M. (2008). Precise age of the platiniferous Merensky Reef, Bushveld Complex, South Africa, by the U-Pb zircon chemical abrasion ID-TIMS technique. *Econ Geol* 103 (3), 465–471.

Scoates, J. S. and Wall, C. J. (2015). Geochronology of Layered Intrusions. *Layered Intrusions.* Ed. by B. Charlier, O. Namur, R. Latypov, and C. Tegner. Springer Geology. Dordrecht: Springer, 3–74.

Scoon, R. N. and Mitchell, A. A. (1994). Discordant iron-rich ultramafic pegmatites in the Bushveld Complex and their relationship to iron-rich intercumulus and residual liquids. *J Petrol* 35 (4), 881–917.

Scoon, R. N. and Teigler, B. (1994). Platinum-group element mineralization in the critical zone of the western Bushveld Complex; I, Sulfide poor-chromitites below the UG-2. *Econ Geol* 89, 1094–1121.

Scoon, R. N. and Teigler, B. (1995). A new LG-6 chromite reserve at Eerste Geluk in the boundary zone between the central and southern sectors of the eastern Bushveld Complex. *Econ Geol* 90 (4), 969–982.

Scowen, P. A. H., Roeder, P. L., and Helz, R. T. (1991). Reequilibration of chromite within Kilauea Iki lava lake, Hawaii. *Contrib Miner Petrol* 107 (1), 8–20.

Sharpe, M. R. and Irvine, T. N. (1983). Melting relations of two Bushveld chilled margin rocks and implications for the origin of chromitite. *Yrbk Carnegie Inst Wash* 82, 295–300.

Shawn, H. R. (1972). Viscosities of magmatic silicate liquids; an empirical method of prediction. *Am J Sci* 272 (2), 870–893.

Shirley, D. N. (1986). Compaction of igneous cumulates. *J Geol* 94 (6), 895–809.

Smeck, N. E. (1973). Phosphorus: An indicator of pedogenetic weathering processes. *Soil Sci* 115 (3), 199–206.

South African Committee for Stratigraphy, ed. (1980). *Stratigraphy of Southern Africa. Part 1. Lithostratigraphy of South Africa, South West Africa/Namibia, and the Republics of Boputhatswana, Transkei, and Venda.* Geological Survey of South Africa.

Spandler, C., Mavrogenes, J., and Arculus, R. (2005). Origin of chromitites in layered intrusions: Evidence from chromite-hosted melt inclusions from the Stillwater Complex. *Geology* 33 (11), 893–896.

Sparks, R. S. J., Huppert, H. E., Kerr, R. C., McKenzie, D. P., and Tait, S. R. (1985). Postcumulus processes in layered intrusions. *Geol Mag* 122 (5), 555–568.

Sun, C. and Liang, Y. (2013). Distribution of REE and HFSE between low-Ca pyroxene and lunar picritic melts around multiple saturation points. *Geochim Cosmochim Acta* 119, 340–358.

Tegner, C., Thy, P., Holness, M. B., Jakobsen, J. K., and Lesher, C. E. (2009). Differentiation and compaction in the Skaergaard intrusion. *J Petrol* 50 (5), 813–840.

Tegner, C. and Wilson, J. R. (1995). Textures in a poikilitic olivine gabbro cumulate: evidence for supercooling. *Miner Petrol* 54, 161–173.

Teigler, B. (1990). Platinum group element distribution in the lower and middle group chromitites in the western Bushveld Complex. *Miner Petrol* 42, 165–179.

Tepley III, F. J. and Davidson, J. P. (2003). Mineral-scale Sr-isotope constraints on magma evolution and chamber dynamics in the Rum layered intrusion, Scotland. *Contrib Miner Petrol* 145, 628–641.

Thomson, W. (1887). On the division of space with minimum partitional area. *Acta Math* 11 (1-4), 121–134.

Troll, V. R., Nicoll, G. R., Donaldson, C. H., and Emeleus, C. H. (2008). Dating the onset of volcanism at the Rum Igneous Centre, NW Scotland. *J Geol Soc* 165 (3), 651–659.

Ulmer, G. C. and Gold, D. P. (1982). Monomineralicity and oikocrysts: keys to cumulus cooling rates? *Magmatic Processes of Early Planetary Crusts: Magma Oceans and Stratiform Layered Intrusions.*

Upton, B. G. J., Skovgaard, A. C., McClurg, J., Kirstein, L., Cheadle, M. C., Emeleus, C. H., Wadsworth, W. J., and Fallick, A. E. (2002). Picritic magmas and the Rum ultramafic complex, Scotland. *Geol Mag* 139 (4), 437–452.

Veksler, I. V., Reid, D. L., Dulski, P., Keiding, J. K., Schannor, M., Hecht, L., and Trumbull, R. B. (2015). Electrochemical Processes in a Crystal Mush: Cyclic Units in the Upper Critical Zone of the Bushveld Complex, South Africa. *J Petrol* 56 (6), 1229–1250.

Veksler, I. V., Sedunova, A. P., Darin, A. V., Anosova, M. O., Reid, D. L., Kaufmann, F. E. D., Hecht, L., and Trumbull, R. B. (2018). Chemical and textural re-equilibration in the UG2 chromitite layer of the Bushveld Complex, South Africa. *J Petrol.*

Vernon, R. H. (2004). *A practical guide to rock microstructure.* Cambridge University Press.

Volker, J. A. and Upton, B. G. J. (1990). The structure and petrogenesis of the Trallval and Ruinsival areas of the Rhum ultrabasic complex. *Trans R Soc Edinb, Earth Sci* 81 (1), 69–88.

von Gruenewaldt, G., Hatton, C. J., and Merkle, R. K. W. (1986). Platinum-group element-chromitite associations in the Bushveld Complex. *Econ Geol* 81 (5), 1067–1079.

von Gruenewaldt, G., Horsch, H., Dickst, D., and de Wet, J. (1990). PGE mineralization in the western sector of the eastern Bushveld Complex. *Miner Petrol* 42 (1-4), 71–95.

Voordouw, R., Gutzmer, J., and Beukes, N. J. (2009). Intrusive origin for Upper Group (UG1, UG2) stratiform chromitite seams in the Dwars River area, Bushveld Complex, South Africa. *Miner Petrol* 97, 75–94.

Voordouw, R., Gutzmer, J., and Beukes, N. J. (2010). Zoning of platinum group mineral assemblages in the UG2 chromitite determined through in situ SEM-EDS-based image analysis. *Miner Deposita* 45 (2), 147–159.

Vukmanovic, Z., Barnes, S. J., Reddy, S. M., Godel, B., and Fiorentini, M. L. (2013). Morphology and microstructure of chromite crystals in chromitites from the Merensky Reef (Bushveld Complex, South Africa). *Contrib Miner Petrol* 165, 1031–1050.

Vukmanovic, Z., Reddy, S. M., Godel, B., Barnes, S. J., Fiorentini, M. L., Barnes, S.-J., and Kilburn, M. R. (2014). Relationship between microstructures and grain-scale trace element distribution in komatiite-hosted magmatic sulphide ores. *Lithos* 184, 42–61.

Wadsworth, W. J. (1985). Terminology of postcumulus processes and products in the Rhum layered intrusion. *Geol Mag* 122 (05), 549–554.

Wager, L. R. (1961). A note on the origin of ophitic texture in the chilled olivine gabbro of the Skaergaard intrusion. *Geol Mag* 98 (5), 353–364.

Wager, L. R. and Brown, G. M. (1967). *Wager, Lawrence Rickard, and George Malcolm Brown. Layered igneous rocks.* WH Freeman.

Wager, L. R., Brown, G. M., and Wadsworth, W. J. (1960). Types of Igneous Cumulates. *J Petrol* 1 (1), 73–85.

Wagner, P. (1929). *Platinum deposits and mines of South Africa.* Edinburgh: Oliver and Boyd.

Webb, S. J., Ashwal, L. D., and Cawthorn, R. G. (2011). Continuity between eastern and western Bushveld Complex, South Africa, confirmed by xenoliths from kimberlite. *Contrib Miner Petrol* 162, 101–107.

Webb, S. J., Cawthorn, R. G., Nguuri, T., and James, D. (2004). Gravity modeling of Bushveld Complex connectivity supported by Southern African Seismic Experiment results. *S Afr J Geol* 107, 207–218.

Wilson, A. H. (2012). A Chill Sequence to the Bushveld Complex: Insight into the First Stage of Emplacement and Implications for the Parental Magmas. *J Petrol* 53 (6), 1123–1168.

Winter, J. D. (2009). *Principles of igneous and metamorphic petrology.* Pearson Education.

Yang, R. Y., Zou, R. P., Dong, K. J., An, X. Z., and Yu, A. (2007). Simulation of the packing of cohesive particles. *Comput Phys Commun* 177 (1), 206–209.

Yao, L., Sun, C., and Liang, Y. (2012). A parameterized model for REE distribution between low-Ca pyroxene and basaltic melts with applications to REE partitioning in low-Ca

pyroxene along a mantle adiabat and during pyroxenite-derived melt and peridotite interaction. *Contrib Miner Petrol* 164, 261–280.

Young, I. M. (1984). Mixing of supernatant and interstitial fluids in the Rhum layered intrusion. *Miner Mag* 48, 345–350.

Zamponi, F. (2008). Mathematical physics: packings close and loose. *Nature* 453 (7159), 606–607.

Zeh, A., Ovtcharova, M., Wilson, A. H., and Schaltegger, U. (2015). The Bushveld Complex was emplaced and cooled in less than one million years – results of zirconology, and geotectonic implications. *Earth Planet Sci Lett* 418, 103–114.

Appendix A

Supplementary information Chapter 2

A.1 CSD

Table A.1: CSD input and output data.

Lithology	Chromitite layer	Chromite fraction (vol.%)	No. of crystals	CSD maximum (mm)	Regression	
					Slope (mm-1)	Intercept ($\ln(mm^{-4})$)
Chromitite, massive	LG6a	90.0	920	0.06	-9.4	7.4
Spotted chromitite	LG6a	82.0	2339	0.08	-12.4	8.4
Pyroxenitic parting	LG6a	21.3	902	0.08	-18.6	8.7
Chromitite, massive	MG1	97.5	1280	0.08	-31.7	11.8
Chromitite, disseminated	MG1	58.4	8503	0.05	-7.2	6.4
Chromitite, massive	MG2	94.6	744	0.13	-11.1	8.1
Chromitite, disseminated	MG2	77.8	4031	0.08	-15.2	9.1
Spotted chromitite	MG2	50.0	1807	0.08	-21.7	10.1
Pyroxenitic parting	MG2	7.9	210	0.08	-19.6	8.9
Chromitite, massive	MG2 II	86.1	695	0.08	-13.2	8.9
Chromitite, disseminated	MG2 II	69.2	2004	0.06	-17.7	9.7

A.2 Chromite

Table A.2: Average chromite composition in the LG6 chromitite layer of *N* microprobe analyses. Main elements are given in wt.%.

	Footwall		Chromitite		Pyroxenitic parting		Hanging wall	
N	41		960		7		126	
	Av.	S.D.	Av.	S.D.	Av.	S.D.	Av.	S.D.
SiO_2	0.37	0.04	0.02	0.01			0.09	0.03
TiO_2	0.27	0.71	0.59	0.18	0.45	0.07	0.75	1.61
Al_2O_3	8.30	0.09	14.86	0.02	14.82	0.04	9.22	0.18
Cr_2O_3	49.58	0.03	47.53	0.00	47.69	0.01	48.93	0.04
V_2O_3	0.41	0.58	0.34	0.20	0.37	0.05	0.46	2.03
Fe_2O_3	8.79	0.04	7.44	0.03	7.18	0.00	9.11	0.03
FeO	28.37	1.39	19.51	0.26	20.05	0.09	26.59	1.18
MgO	3.18	0.02	9.86	0.01	9.43	0.00	4.67	0.03
MnO	0.40	0.93	0.29	0.25	0.30	0.09	0.38	2.05
ZnO	0.34	0.64	0.06	0.30	0.06	0.07	0.13	0.58
NiO	0.06	0.14	0.12	0.01	0.12	0.03	0.10	0.04
Total	100.06	0.46	100.60	0.17	100.52	0.02	100.43	0.13
Mg#	16.60	3.55	47.39	0.78	45.60	0.29	23.65	7.63
Cr#	80.03	1.49	68.21	0.36	68.34	0.11	78.21	4.06

Table A.3: Average chromite composition in the LG6a chromitite layer of *N* microprobe analyses. Main elements are given in wt.%.

	Footwall		Chromitite		Spotted chromitite		Pyroxenitic parting		Hanging wall	
N	44		132		93		28		77	
	Av.	S.D.	Av.	S.D.	Av.	S.D.	Av.	S.D.	Av.	S.D.
SiO_2	0.04	0.10	0.02	0.06	0.02	0.07	0.07	0.07	0.04	0.1
TiO_2	0.75	5.76	0.60	9.71	0.64	9.11	0.57	8.33	0.64	5.31
Al_2O_3	10.46	0.77	14.71	0.60	14.37	0.64	13.46	0.57	9.59	0.64
Cr_2O_3	48.70	0.35	47.55	0.28	47.27	0.29	47.61	0.31	49.59	0.36
V_2O_3	0.39	9.98	0.33	14.71	0.33	14.36	0.34	13.46	0.37	9.59
Fe_2O_3	8.71	0.40	7.23	0.33	7.55	0.33	7.80	0.34	8.64	0.37
FeO	24.52	48.93	19.59	47.55	20.45	47.24	21.46	47.61	25.48	49.59
MgO	6.09	0.12	9.71	0.12	9.14	0.12	8.33	0.12	5.31	0.1
MnO	0.35	24.95	0.28	19.59	0.29	20.51	0.31	21.46	0.36	25.48
ZnO	0.10	8.81	0.06	7.23	0.06	7.59	0.07	7.80	0.10	8.64
NiO	0.12	0.05	0.12	0.02	0.12	0.02	0.12	0.07	0.10	0.04
Total	100.24	100.22	100.22	100.22	100.27	100.28	100.15	100.15	100.24	100.24
Mg#	30.57	29.10	46.90	46.90	44.33	44.17	40.80	40.80	26.97	26.97
Cr#	75.83	76.71	68.44	68.44	68.82	68.82	70.42	70.42	77.69	77.69

Table A.4: Average chromite composition in the MG1 chromitite layer of *N* microprobe analyses. Main elements are given in wt.%.

	Footwall		Chromitite		Chromitite in oikocrysts		Pyroxenitic parting		Chromitite stringer		Hanging wall	
N	111		421		260		171		43		293	
	Av.	S.D.	Av.	S.D.	Av.	S.D.	Av.	S.D.	Av.	S.D.	Av.	S.D.
SiO_2	0.03	0.03	0.02	0.01	0.05	0.01	0.07	0.01	0.05	0.01	0.04	0.03
TiO_2	1.08	0.70	0.69	0.82	0.71	0.22	0.64	0.79	0.76	0.24	0.86	1.1
Al_2O_3	17.14	0.14	16.02	0.10	16.04	0.04	15.25	0.08	16.34	0.06	13.70	0.19
Cr_2O_3	37.98	0.01	46.16	0.03	46.08	0.00	46.59	0.01	44.58	0.00	45.04	0.01
V_2O_3	0.34	1.11	0.26	0.75	0.26	0.46	0.26	0.76	0.27	0.21	0.33	1.55
Fe_2O_3	11.86	0.03	7.90	0.01	7.99	0.01	7.13	0.01	8.15	0.00	9.15	0.04
FeO	24.89	1.26	19.20	0.91	18.92	0.96	22.25	0.27	21.24	0.51	24.79	0.76
MgO	6.76	0.01	10.33	0.02	10.55	0.01	8.22	0.01	9.06	0.01	6.46	0.02
MnO	0.30	1.05	0.28	1.10	0.28	0.34	0.32	1.10	0.29	0.35	0.33	1.49
ZnO	0.12	0.71	0.06	0.57	0.05	0.40	0.07	0.39	0.07	0.58	0.10	0.7
NiO	0.19	0.01	0.14	0.07	0.14	0.03	0.13	0.03	0.13	0.02	0.14	0.02
Total	100.69	0.12	101.06	0.32	101.08	0.12	100.93	0.10	100.93	0.19	100.93	0.18
Mg#	32.60	3.19	48.94	3.65	49.85	0.96	39.60	3.47	43.18	1.05	31.65	5.01
Cr#	59.84	2.08	65.90	1.54	65.84	1.11	67.28	1.18	64.69	0.23	68.88	2.67

Table A.5: Average chromite composition in the MG1 chromitite layer of *N* microprobe analyses. Main elements are given in wt.%.

	Footwall		Chromitite		Spotted chromitite		Pyroxenitic parting		Hanging wall	
N	136		516		103		22		78	
	Av.	S.D.	Av.	S.D.	Av.	S.D.	Av.	S.D.	Av.	S.D.
SiO_2	0.22	0.05	0.08	0.04	0.07	0.01	0.15	0.08	0.15	0.03
TiO_2	3.65	1.14	8.68	0.91	8.02	0.31	5.29	1.87	4.49	0.95
Al_2O_3	0.89	0.22	0.88	0.14	0.82	0.07	0.61	0.23	1.36	0.15
Cr_2O_3	0.39	0.03	0.29	0.02	0.31	0.01	0.36	0.03	0.35	0.01
V_2O_3	9.55	1.74	17.14	1.36	16.14	0.66	12.12	3.14	9.62	1.63
Fe_2O_3	0.66	0.07	0.43	0.02	0.42	0.03	0.48	0.04	0.54	0.05
FeO	47.79	1.36	43.54	0.36	44.02	0.33	45.98	1.41	45.84	0.7
MgO	0.10	0.02	0.13	0.00	0.13	0.01	0.11	0.03	0.13	0.01
MnO	28.24	1.36	21.82	1.09	22.60	0.38	25.91	2.17	27.27	1.29
ZnO	8.59	0.56	7.23	0.83	7.70	0.32	8.58	1.21	10.25	0.8
NiO	0.13	0.05	0.03	0.09	0.03	0.02	0.20	0.20	0.05	0.01
Total	100.20	0.20	100.25	0.42	100.27	0.11	99.79	0.69	100.06	0.16
Mg#	18.56	5.33	41.42	4.10	38.74	1.31	26.39	8.66	22.63	4.41
Cr#	77.15	3.45	63.08	2.06	64.68	1.08	72.09	6.01	76.28	3.03

Table A.6: Average chromite composition in the MG1 chromitite layer of *N* microprobe analyses. Main elements are given in wt.%.

	Footwall		Chromitite		Hanging wall	
N	133		215		116	
	Av.	S.D.	Av.	S.D.	Av.	S.D.
SiO_2	0.08	0.02	0.03	0.01	0.05	0.02
TiO_2	0.91	1.59	0.44	0.26	0.96	1.34
Al_2O_3	15.60	0.34	22.37	0.05	17.55	0.30
Cr_2O_3	41.38	0.02	42.81	0.01	38.47	0.01
V_2O_3	0.45	3.35	0.36	0.60	0.40	2.57
Fe_2O_3	9.36	0.09	4.46	0.01	10.41	0.07
FeO	25.77	3.21	17.76	0.59	25.33	2.90
MgO	5.75	0.07	11.65	0.01	6.29	0.06
MnO	0.34	2.05	0.29	0.35	0.34	1.86
ZnO	0.20	1.89	0.11	0.17	0.18	2.00
NiO	0.25	0.03	0.12	0.02	0.23	0.02
Total	100.09	0.25	100.39	0.08	100.22	0.10
Mg#	28.26	7.14	53.89	1.03	30.58	5.99
Cr#	64.25	6.17	56.22	0.99	59.65	4.80

A.3 Orthopyroxene

Table A.7: Average orthopyroxene composition in the LG6 chromitite layer of *N* microprobe analyses. Main elements are given in wt.%.

	Footwall		Interstitial chromitite		Pyroxenitic parting		Hanging wall	
N	181		392		18		117	
	Av.	S.D.	Av.	S.D.	Av.	S.D.	Av.	S.D.
SiO_2	55.36	0.18	56.75	0.63	56.43	0.58	55.29	0.2
TiO_2	0.09	0.01	0.09	0.01	0.07	0.02	0.10	0.01
Al_2O_3	1.06	0.08	1.20	0.08	1.18	0.18	1.07	0.21
Cr_2O_3	0.43	0.05	0.72	0.14	0.34	0.09	0.41	0.07
V_2O_3	0.03	0.00	0.03	0.01	0.02	0.01	0.03	0
Fe_2O_3	1.91	0.27	2.18	0.60	2.54	0.45	2.68	0.31
FeO	9.93	0.31	4.33	0.52	4.84	0.58	8.59	0.97
MgO	30.68	0.29	35.23	0.40	34.49	0.61	31.16	0.57
MnO	0.25	0.01	0.15	0.01	0.17	0.02	0.24	0.01
NiO	0.06	0.00	0.05	0.01	0.06	0.02	0.07	0
CaO	0.99	0.27	0.44	0.09	0.73	0.28	1.29	0.43
Na_2O	0.02	0.01	0.01	0.01	0.01	0.01	0.02	0.01
Total	100.81	0.20	101.19	1.02	100.90	0.72	100.95	0.26
Mg#	84.64	0.45	93.53	0.79	92.70	0.86	86.61	1.47

Table A.8: Average orthopyroxene composition in the LG6a chromitite layer of *N* microprobe and *n* LA-ICP-MS analyses. Main elements are given in wt.%, trace elements in ppm, bdl below detection limit.

	Footwall		Interstitial chromitite		Spotted chromitite		Pyroxenitic parting		Hanging wall	
N (n)	59 (10)		85 (3)		25 (8)		25 (9)		75 (3)	
	Av.	S.D.	Av.	S.D.	Av.	S.D.	Av.	S.D.	Av.	S.D.
SiO_2	55.38	0.17	56.37	19.34	55.86	0.14	55.72	0.15	55.67	0.2
TiO_2	0.11	0.00	0.10	0.03	0.10	0.01	0.09	0.01	0.10	0.01
Al_2O_3	1.23	0.06	1.26	0.44	1.48	0.06	1.46	0.11	1.21	0.08
Cr_2O_3	0.45	0.02	0.74	0.30	0.47	0.02	0.50	0.02	0.46	0.04
V_2O_3	0.03	0.00	0.03	0.01	0.02	0.01	0.02	0.00	0.03	0
Fe_2O_3	2.10	0.40	2.52	0.95	2.19	0.42	2.26	0.27	1.77	0.19
FeO	8.34	0.82	4.08	1.56	5.94	0.52	6.21	0.98	8.66	0.92
MgO	31.35	0.45	35.06	12.02	32.98	0.42	32.55	0.60	31.25	0.73
MnO	0.24	0.02	0.15	0.06	0.20	0.01	0.21	0.02	0.24	0.02
NiO	0.07	0.01	0.06	0.02	0.07	0.01	0.07	0.00	0.07	0.01
CaO	1.31	0.20	0.52	0.32	1.40	0.34	1.63	0.39	1.45	0.54
Na_2O	0.02	0.01	0.01	0.00	0.02	0.01	0.03	0.01	0.03	0.01
Total	100.63	0.16	100.90	34.62	100.73	0.23	100.75	0.18	100.94	0.16
Mg#	87.01	1.25	93.87	32.18	90.83	0.80	90.41	1.56	86.54	1.43
Sc	38	2	48	3	4486	4701	38	3	35	3.36
Ti	568	22	560	13	291	251	550	26	627	10.49
V	92	8	77	7	312	220	100	8	88	11.97
Cr	2966	231	3085	719	1618	1541	3653	567	3501	508.57
Mn	1702	116	1236	69	2803	1292	1625	124	1923	16.58
Co	71	13	37	3	58	6	68	12	92	1.41
Ni	573	14	525	13	558	14	586	19	580	4.74
Zn	46	11	24	3	42	7	50	10	65	0.56
Rb	bdl		bdl		bdl		bdl		bdl	
Sr	0.24	0.07	0.24	0.11	0.31	0.09	0.28	0.06	0.48	0.07
Y	2.86	0.40	3.77	2.28	4.45	1.09	4.88	1.42	3.56	0.78
Zr	4.33	0.98	5.39	1.75	5.63	0.52	5.76	2.08	5.04	1.61
Nb	0.05	0.01	0.04	0.01	0.06	0.01	0.06	0.02	0.08	0.04
Ba	0.10	0.04	0.19	0.02	0.18	0.07	0.20	0.12	0.54	0.17
La	0.090	0.040	0.015	0.000	0.141	0.070	0.179	0.070	0.353	0.17
Ce	0.343	0.150	0.050	0.020	0.647	0.330	0.777	0.300	1.363	0.7
Pr	0.063	0.030	0.018	0.010	0.122	0.060	0.144	0.060	0.228	0.12
Nd	0.359	0.140	0.133	0.050	0.736	0.300	0.824	0.340	1.132	0.58
Sm	0.157	0.050	0.124	0.050	0.327	0.110	0.373	0.140	0.346	0.13
Eu	0.029	0.010	0.023	0.000	0.045	0.010	0.042	0.010	0.051	0.02
Gd	0.259	0.060	0.325	0.090	0.477	0.140	0.523	0.190	0.438	0.22
Tb	0.053	0.010	0.063	0.040	0.093	0.020	0.106	0.030	0.085	0.03
Dy	0.432	0.060	0.559	0.300	0.723	0.170	0.802	0.250	0.588	0.18
Ho	0.108	0.010	0.150	0.080	0.164	0.040	0.186	0.060	0.143	0.02
Er	0.375	0.050	0.574	0.330	0.545	0.120	0.597	0.160	0.463	0.09
Tm	0.061	0.010	0.101	0.060	0.082	0.020	0.093	0.020	0.075	0.01
Yb	0.456	0.040	0.792	0.380	0.627	0.130	0.688	0.180	0.534	0.07
Lu	0.081	0.000	0.145	0.060	0.103	0.020	0.111	0.030	0.086	0.01
Hf	0.153	0.040	0.246	0.020	0.162	0.020	0.160	0.040	0.207	0.05
Pb	0.901	0.370	0.676	0.330	3.837	3.490	5.270	3.380	2.394	0.29
U	0.015	0.010	0.002	0.000	0.041	0.020	0.052	0.010	0.084	0.04

Table A.9: Average orthopyroxene composition in the MG1 chromitite layer of *N* microprobe analyses. Main elements are given in wt.%.

	Footwall		Interstitial chromitite		Oikocryst cores		Pyroxenitic parting		Chromitite stringers		Hanging wall	
N	86		297		130		147		26		278	
	Av.	S.D.	Av.	S.D.	Av.	S.D.	Av.	S.D.	Av.	S.D.	Av.	S.D.
SiO_2	55.49	0.76	56.78	0.38	56.37	0.32	56.15	0.39	56.02	0.11	55.46	0.19
TiO_2	0.13	0.02	0.11	0.02	0.10	0.01	0.10	0.02	0.11	0.00	0.12	0.02
Al_2O_3	1.68	0.82	1.16	0.15	1.38	0.09	1.37	0.10	1.46	0.01	1.39	0.05
Cr_2O_3	0.38	0.05	0.57	0.17	0.48	0.08	0.48	0.08	0.48	0.02	0.46	0.02
V_2O_3	0.03	0.00	0.02	0.00	0.02	0.00	0.02	0.00	0.02	0.00	0.03	0
Fe_2O_3	2.81	0.35	2.48	0.38	2.60	0.30	2.39	0.27	2.50	0.07	2.55	0.21
FeO	7.64	0.95	4.52	0.80	5.10	0.60	6.11	0.89	6.18	0.14	8.00	0.84
MgO	32.01	1.04	35.01	0.78	34.06	0.63	33.20	0.98	32.99	0.25	31.65	0.59
MnO	0.24	0.09	0.16	0.02	0.17	0.02	0.19	0.02	0.20	0.01	0.22	0.01
NiO	0.08	0.04	0.06	0.01	0.07	0.01	0.07	0.01	0.06	0.00	0.07	0.01
CaO	1.04	0.33	0.64	0.25	1.08	0.33	1.24	0.43	1.37	0.37	1.27	0.26
Na_2O	0.02	0.02	0.01	0.00	0.01	0.01	0.02	0.01	0.02	0.00	0.02	0.01
Total	100.01	5.33	101.51	0.30	101.44	0.25	101.35	0.35	101.42	0.09	101.24	0.18
Mg#	88.18	1.55	93.24	1.25	92.24	0.95	90.62	1.46	90.49	0.13	87.59	1.33

Table A.10: Average orthopyroxene composition in the MG2 chromitite layer of *N* microprobe and *n* LA-ICP-MS analyses. Main elements are given in wt.%, trace elements in ppm, bdl below detection limit.

	Footwall		Interstitial chromitite		Spotted chromitite		Pyroxenitic parting		Hanging wall	
N (n)	164 (1)		195 (4)		24 (4)		74 (8)		93 (6)	
	Av.	S.D.	Av.	S.D.	Av.	S.D.	Av.	S.D.	Av.	S.D.
SiO_2	54.68	0.26	55.60	0.22	55.10	0.17	54.84	0.21	54.49	0.22
TiO_2	0.02	0.02	0.01	0.02	0.01	0.01	0.02	0.02	0.02	0.03
Al_2O_3	1.06	0.17	1.53	0.08	1.62	0.05	1.36	0.20	1.18	0.11
Cr_2O_3	0.40	0.07	0.58	0.13	0.47	0.02	0.47	0.03	0.44	0.02
V_2O_3	0.04	0.00	0.03	0.01	0.03	0.00	0.03	0.01	0.03	0.00
Fe_2O_3	2.82	1.27	2.22	0.62	1.85	0.25	2.96	0.93	3.68	1.22
FeO	10.72	0.74	6.27	0.51	8.44	0.20	9.99	1.01	10.52	0.61
MgO	29.76	0.43	33.39	0.37	31.42	0.18	30.31	0.64	29.65	0.36
MnO	0.27	0.01	0.18	0.01	0.23	0.00	0.26	0.02	0.28	0.01
NiO	0.07	0.01	0.05	0.01	0.07	0.00	0.07	0.00	0.06	0.01
CaO	1.02	0.34	0.42	0.10	0.91	0.22	0.97	0.16	1.17	0.27
Na_2O	0.02	0.01	0.01	0.00	0.01	0.01	0.02	0.01	0.02	0.01
Total	100.99	1.03	100.42	0.48	100.25	0.14	101.41	0.94	101.67	1.06
Mg#	83.19	1.11	90.46	0.79	86.91	0.26	84.39	1.61	83.40	0.94
Sc	34		48	10	52	6	43	4	41	4
Ti	874		780	161	628	15	705	106	948	106
V	144		104	9	113	15	137	11	128	9
Cr	2751		2575	534	2911	479	3395	265	3817	646
Mn	2156		1452	74	1660	62	2036	161	2313	184
Co	116		43	3	55	5	99	21	114	10
Ni	610		466	47	543	33	600	26	615	30
Zn	109		33	2	35	4	77	28	92	17
Rb	bdl		bdl		bdl		bdl		bdl	
Sr	0.13		0.81	0.45	0.34	0.00	0.21	0.07	0.40	0.14
Y	2.67		1.14	1.10	3.81	0.92	4.75	1.30	3.59	0.48
Zr	3.61		4.47	1.33	6.88	2.19	6.52	2.22	5.37	0.76
Nb	0.037		0.033	0.000	0.032	0.010	0.038	0.010	0.043	0.010
Ba	bdl		0.696	0.530	0.168	0.000	0.134	0.000	0.259	0.080
La	0.065		0.020	0.000	0.020	0.000	0.073	0.020	0.104	0.030
Ce	0.221		0.040	0.020	0.039	0.010	0.234	0.130	0.412	0.120
Pr	0.032		bdl		bdl		0.055	0.020	0.074	0.020
Nd	0.227		bdl		0.085	0.000	0.377	0.180	0.439	0.130
Sm	0.097		0.085	0.010	0.072	0.020	0.208	0.110	0.190	0.070
Eu	bdl		bdl		bdl		0.031	0.000	0.033	0.000
Gd	0.197		bdl		0.206	0.030	0.360	0.190	0.292	0.080
Tb	0.049		0.025	0.010	0.055	0.020	0.087	0.030	0.065	0.020
Dy	0.427		0.316	0.090	0.519	0.120	0.691	0.220	0.558	0.090
Ho	0.115		0.090	0.020	0.140	0.020	0.179	0.050	0.139	0.020
Er	0.364		0.366	0.060	0.532	0.100	0.627	0.150	0.486	0.070
Tm	0.077		0.051	0.020	0.090	0.020	0.108	0.020	0.077	0.010
Yb	0.632		0.486	0.180	0.803	0.120	0.804	0.170	0.605	0.050
Lu	0.107		0.083	0.020	0.124	0.020	0.131	0.020	0.104	0.010
Hf	0.188		0.304	0.060	0.342	0.090	0.247	0.090	0.179	0.030
Pb	1.303		0.561	0.340	0.185	0.090	0.488	0.800	2.879	2.770
U	0.013		0.003	0.000	bdl		0.027	0.010	0.025	0.010

Table A.11: Average orthopyroxene composition in the MG2 II chromitite layer of *N* microprobe analyses. Main elements are given in wt.%.

	Footwall		Interstitial chromitite		Hanging wall	
N	96		58		72	
	Av.	S.D.	Av.	S.D.	Av.	S.D.
SiO_2	54.69	0.16	56.27	0.12	54.86	0.8
TiO_2	0.13	0.03	0.09	0.02	0.11	0.02
Al_2O_3	1.57	0.17	1.52	0.10	1.57	0.15
Cr_2O_3	0.42	0.05	0.56	0.08	0.40	0.06
V_2O_3	0.03	0.00	0.03	0.00	0.03	0
Fe_2O_3	4.13	0.26	3.15	0.42	3.98	0.76
FeO	8.89	1.17	4.34	0.44	8.44	1.73
MgO	30.66	0.81	34.82	0.23	31.13	1.34
MnO	0.24	0.01	0.17	0.01	0.23	0.02
NiO	0.13	0.03	0.06	0.01	0.10	0.03
CaO	1.15	0.29	0.50	0.05	0.99	0.35
Na_2O	0.02	0.01	0.02	0.01	0.03	0.01
Total	102.08	0.43	101.52	0.31	101.88	0.75
Mg#	86.01	1.88	93.47	0.66	86.77	2.74

A.4 Plagioclase

Table A.12: Average plagioclase composition in the LG6 chromitite layer of *N* microprobe analyses. Main elements are given in wt.%.

	Footwall		Chromitite		Hanging wall	
N	117		384		95	
	Av.	S.D.	Av.	S.D.	Av.	S.D.
SiO_2	52.81	2.65	48.91	0.94	52.82	1.62
TiO_2	0.01	0.00	0.02	0.00	0.01	0.01
Al_2O_3	29.85	1.88	32.34	0.63	29.68	0.95
Cr_2O_3	0.01	0.06	0.41	0.06	0.06	0.01
MgO	0.04	0.14	0.09	0.21	0.06	0.19
MnO	0.01	0.00	0.01	0.00	0.01	0.02
FeO	0.19	0.14	0.30	0.10	0.19	0.33
CaO	11.82	2.16	14.61	0.74	11.82	1.11
Na_2O	4.49	1.24	2.95	0.42	4.36	0.66
K_2O	0.22	0.03	0.01	0.07	0.09	0.02
SrO	0.21	0.01	0.22	0.01	0.20	0.01
Total	99.64	0.37	99.85	0.25	99.30	0.3
An	58.57	10.80	73.20	3.62	59.53	5.91

Table A.13: Average plagioclase composition in the LG6a chromitite layer of *N* microprobe and *n* LA-ICP-MS analyses. Main elements are given in wt.%, trace elements in ppm, bdl below detection limit.

	Footwall		Chromitite		Spotted chromitite		Pyroxenitic parting		Hanging wall	
N	44		132		93		28		77	
	Av.	S.D.	Av.	S.D.	Av.	S.D.	Av.	S.D.	Av.	S.D.
SiO_2	0.04	0.10	0.02	0.06	0.02	0.07	0.07	0.07	0.04	0.1
TiO_2	0.75	5.76	0.60	9.71	0.64	9.11	0.57	8.33	0.64	5.31
Al_2O_3	10.46	0.77	14.71	0.60	14.37	0.64	13.46	0.57	9.59	0.64
Cr_2O_3	48.70	0.35	47.55	0.28	47.27	0.29	47.61	0.31	49.59	0.36
V_2O_3	0.39	9.98	0.33	14.71	0.33	14.36	0.34	13.46	0.37	9.59
Fe_2O_3	8.71	0.40	7.23	0.33	7.55	0.33	7.80	0.34	8.64	0.37
FeO	24.52	48.93	19.59	47.55	20.45	47.24	21.46	47.61	25.48	49.59
MgO	6.09	0.12	9.71	0.12	9.14	0.12	8.33	0.12	5.31	0.1
MnO	0.35	24.95	0.28	19.59	0.29	20.51	0.31	21.46	0.36	25.48
ZnO	0.10	8.81	0.06	7.23	0.06	7.59	0.07	7.80	0.10	8.64
NiO	0.12	0.05	0.12	0.02	0.12	0.02	0.12	0.07	0.10	0.04
Total	100.24	100.22	100.22	100.22	100.27	100.28	100.15	100.15	100.24	100.24
Mg#	30.57	29.10	46.90	46.90	44.33	44.17	40.80	40.80	26.97	26.97
Cr#	75.83	76.71	68.44	68.44	68.82	68.82	70.42	70.42	77.69	77.69

Table A.14: Average plagioclase composition in the MG1 chromitite layer of *N* microprobe analyses. Main elements are given in wt.%.

	Footwall		Chromitite		Chromitite stringer		Hanging wall	
N	28		108		20		248	
	Av.	S.D.	Av.	S.D.	Av.	S.D.	Av.	S.D.
SiO_2	50,86	1,38	52,86	2,27	50,23	0,55	50,91	1,27
TiO_2	0,03	0,02	0,02	0,01	0,03	0,00	0,01	0,01
Al_2O_3	31,36	0,95	29,96	1,81	31,85	0,45	31,50	0,86
Cr_2O_3	0,04	0,06	0,16	0,10	0,28	0,07	0,08	0,06
MgO	0,10	0,13	0,08	0,07	0,13	0,02	0,05	0,04
MnO	0,01	0,02	0,01	0,00	0,01	0,01	0,01	0
FeO	0,24	0,15	0,19	0,07	0,29	0,01	0,19	0,05
CaO	13,51	1,14	11,91	2,02	14,07	0,47	13,71	1,05
Na_2O	3,85	0,63	4,64	0,41	3,55	0,28	3,78	0,6
K_2O	0,05	0,02	0,32	1,13	0,02	0,00	0,04	0,02
SrO	0,25	0,02	0,26	0,04	0,30	0,02	0,23	0,02
Total	100,30	0,20	100,39	0,33	100,74	0,15	100,51	0,19
An	65,82	5,61	57,57	9,80	68,60	2,42	66,56	5,18

Table A.15: Average plagioclase composition in the MG2 chromitite layer of *N* microprobe and *n* LA-ICP-MS analyses. Main elements are given in wt.%, trace elements in ppm, bdl below detection limit.

	Footwall		Chromitite		Spotted chromitite		Pyroxenitic parting		Hanging wall	
N (n)	103 (4)		323 (4)		62 (4)		48 (8)		71 (5)	
	Av.	S.D.	Av.	S.D.	Av.	S.D.	Av.	S.D.	Av.	S.D.
SiO_2	52,19	1,82	49,52	0,44	48,90	0,82	50,44	1,46	49,73	2,80
TiO_2	0,02	0,00	0,02	0,00	0,01	0,01	0,01	0,01	0,01	0,00
Al_2O_3	30,37	1,09	32,15	0,51	32,74	0,65	31,67	0,90	32,18	1,93
Cr_2O_3	0,01	0,14	0,18	0,08	0,12	0,15	0,02	0,25	0,01	0,12
MgO	0,05	0,07	0,04	0,04	0,03	0,04	0,06	0,08	0,04	0,07
MnO	0,01	0,00	0,01	0,01	0,00	0,01	0,01	0,00	0,01	0,00
FeO	0,20	0,09	0,19	0,04	0,17	0,07	0,21	0,12	0,17	0,06
CaO	12,43	1,33	14,43	0,43	15,06	0,69	13,86	1,05	14,50	2,24
Na_2O	4,15	0,75	3,20	0,29	2,83	0,38	3,53	0,61	3,10	1,22
K_2O	0,15	0,04	0,02	0,00	0,02	0,00	0,07	0,03	0,11	0,03
SrO	0,20	0,00	0,20	0,01	0,19	0,06	0,19	0,01	0,19	0,01
Total	99,78	0,25	99,96	0,23	100,09	0,37	100,08	0,15	100,05	0,28
An	61,78	6,83	71,27	2,40	74,52	3,40	68,15	5,48	71,63	11,17
Sc	bdl		bdl		bdl		bdl		bdl	
Ti	123,31	14,08	81,38	9,54	53,79	7,32	70,94	28,60	70,13	15,13
V	0,80	0,29	bdl		bdl		1,11	0,90	0,38	0,00
Cr	bdl		22,82	2,59	bdl		21,60	0,00	bdl	
Mn	7,49	0,41	5,15	0,32	9,78	3,89	9,23	1,24	15,43	6,33
Co	bdl		bdl		bdl		bdl		bdl	
Ni	bdl		bdl		bdl		bdl		bdl	
Zn	2,25	0,00	1,43	0,18	bdl		1,62	0,00	14,43	2,99
Rb	bdl		bdl		bdl		bdl		bdl	
Sr	434,90	9,17	512,70	13,86	451,54	85,50	409,37	26,61	456,79	36,09
Y	0,30	0,01	0,04	0,00	0,43	0,12	0,38	0,14	0,23	0,04
Zr	bdl		bdl		bdl		0,05	0,00	bdl	
Nb	bdl		bdl		bdl		0,03	0,00	bdl	
Ba	202,139	6,640	39,606	6,020	48,812	11,480	133,127	28,510	132,447	20,650
La	10,773	0,510	3,577	0,270	9,543	2,130	8,021	1,370	7,488	0,610
Ce	16,290	0,160	4,809	0,600	17,723	3,270	13,654	1,820	11,501	0,840
Pr	1,281	0,030	0,355	0,060	1,705	0,360	1,220	0,240	0,906	0,090
Nd	3,572	0,180	0,964	0,140	5,707	1,020	3,946	1,130	2,499	0,270
Sm	0,361	0,050	0,083	0,020	0,789	0,150	0,488	0,200	0,253	0,060
Eu	1,025	0,030	0,504	0,040	1,070	0,050	0,910	0,110	0,859	0,050
Gd	bdl		bdl		0,383	0,050	0,307	0,100	0,147	0,000
Tb	0,023	0,000	bdl		0,042	0,010	0,025	0,010	0,018	0,000
Dy	0,085	0,010	0,030	0,000	0,167	0,050	0,114	0,040	0,074	0,010
Ho	0,015	0,000	bdl		0,023	0,000	0,022	0,000	0,010	0,000
Er	bdl		bdl		0,048	0,000	0,045	0,010	0,021	0,010
Tm	bdl		bdl		bdl		0,007	0,000	bdl	
Yb	bdl		bdl		0,046	0,000	0,042	0,000	0,013	0,000
Lu	bdl		bdl		0,008	0,000	0,007	0,000	bdl	
Hf	bdl		bdl		bdl		0,022	0,000	bdl	
Pb	4,079	0,170	2,722	0,170	5,520	1,430	5,475	1,560	7,420	4,730
U	bdl		0,002	0,000	0,007	0,000	bdl		bdl	

Table A.16: Average plagioclase composition in the MG2 II chromitite layer of *N* microprobe analyses. Main elements are given in wt.%.

	Footwall		Chromitite		Hanging wall	
N	66		150		54	
	Av.	S.D.	Av.	S.D.	Av.	S.D.
SiO_2	50,50	1,23	49,37	0,73	48,33	3,09
TiO_2	0,01	0,00	0,01	0,01	0,01	0,01
Al_2O_3	31,36	0,82	32,26	0,46	32,70	2,08
Cr_2O_3	0,03	0,01	0,15	0,11	0,01	0,08
MgO	0,13	0,02	0,20	0,08	0,21	0,04
MnO	0,01	0,00	0,01	0,00	0,02	0,00
FeO	0,30	0,03	0,17	0,06	0,53	0,04
CaO	13,72	0,94	14,66	0,55	15,34	2,53
Na_2O	3,66	0,56	3,11	0,28	2,63	1,31
K_2O	0,07	0,07	0,05	0,00	0,05	0,03
SrO	0,22	0,01	0,22	0,02	0,22	0,01
Total	100,00	0,19	100,21	0,30	100,05	0,32
An	67,24	4,85	72,04	2,57	76,14	12,37

Appendix B

Supplementary information Chapter 5

B.1 Cr-spinel

Table B.1: Average Cr-spinel composition at location 7 of *N* microprobe analyses. Main elements are given in wt.%.

	Unit 8 Peridotite		Main Cr-spinel seam		Subsidiary seam		Unit 7 Troctolite		Anorthosite layer		Anorthosite autoliths	
N	4		10		10		5		3		11	
	Av.	S.D.	Av.	S.D.	Av.	S.D.	Av.	S.D.	Av.	S.D.	Av.	S.D.
SiO_2	0.15	0.08	0.07	0.05	0.05	0.03	0.11	0.11	0.11	0.02	0.20	0.07
TiO_2	1.15	0.09	0.58	0.14	0.85	0.61	1.51	1.51	2.33	0.12	2.72	0.60
Al_2O_3	15.94	0.77	32.22	5.47	33.29	5.66	18.80	18.80	13.44	0.21	6.12	0.89
Cr_2O_3	35.61	0.32	24.92	3.30	23.93	3.47	30.98	30.98	32.06	0.76	12.04	4.39
V_2O_3	0.25	0.02	0.17	0.03	0.20	0.06	0.32	0.32	0.51	0.02	0.95	0.32
Fe_2O_3	15.55	0.43	11.78	1.69	11.50	1.18	16.95	16.95	20.30	0.43	43.63	4.06
FeO	23.66	0.89	16.71	2.77	15.99	3.08	22.55	22.55	22.86	0.65	30.89	0.18
MgO	7.47	0.76	13.38	2.26	14.12	2.26	8.67	8.67	8.35	0.36	2.08	0.34
MnO	0.36	0.01	0.22	0.02	0.22	0.04	0.32	0.32	0.32	0.01	0.42	0.10
ZnO	0.08	0.04	0.07	0.04	0.06	0.03	0.11	0.11	0.06	0.03	0.08	0.05
NiO	0.18	0.01	0.24	0.02	0.25	0.01	0.24	0.24	0.34	0.03	0.40	0.32
Total	100.40	0.34	100.37	0.20	100.45	0.41	100.56	100.56	100.66	0.14	99.52	0.79
Mg#	35.98	3.18	58.54	8.37	60.96	8.50	40.44	40.44	39.42	1.69	9.99	1.65
Cr#	60.00	1.10	34.63	6.95	33.02	7.27	52.87	52.87	61.55	0.20	65.35	3.20

Table B.2: Average Cr-spinel composition at location 6 of *N* microprobe analyses. Main elements are given in wt.%.

	Unit 8 Peridotite		Main Cr-spinel seam		Unit 7 Troctolite		Anorthosite layer		Anorthosite autoliths	
N	13		11		9		5		4	
	Av.	S.D.	Av.	S.D.	Av.	S.D.	Av.	S.D.	Av.	S.D.
SiO_2	0.09	0.08	0.07	0.07	0.09	0.09	0.11	0.06	0.15	0.07
TiO_2	1.47	0.65	0.60	0.26	2.26	2.26	2.30	1.25	2.74	0.29
Al_2O_3	18.87	3.90	34.83	6.57	13.48	13.48	18.32	10.50	8.96	1.96
Cr_2O_3	34.02	2.41	22.98	4.02	31.48	31.48	27.51	4.13	21.03	3.69
V_2O_3	0.26	0.03	0.17	0.05	0.44	0.44	0.56	0.23	1.05	0.42
Fe_2O_3	14.48	1.15	11.28	1.88	20.12	20.12	19.16	4.22	32.74	4.74
FeO	20.95	2.67	15.07	2.99	25.79	25.79	22.77	5.24	28.42	1.23
MgO	9.73	2.11	14.70	2.51	6.37	6.37	8.75	4.09	4.25	0.95
MnO	0.32	0.05	0.21	0.05	0.37	0.37	0.31	0.07	0.41	0.02
ZnO	0.08	0.04	0.08	0.03	0.13	0.13	0.06	0.03	0.07	0.05
NiO	0.20	0.02	0.25	0.02	0.29	0.29	0.49	0.19	0.32	0.07
Total	100.47	0.39	100.22	0.30	100.82	100.82	100.34	0.62	100.14	0.32
Mg#	45.04	8.49	63.16	9.23	30.31	30.31	39.75	16.47	21.01	4.36
Cr#	55.09	6.48	31.39	9.17	61.74	61.74	53.32	14.93	61.33	1.24

Table B.3: Average Cr-spinel composition at location 13 of *N* microprobe analyses. Main elements are given in wt.%.

	Unit 8 Peridotite		Main Cr-spinel seam		Subsidiary seam		Unit 7 Troctolite		Anorthosite layer		Anorthosite autoliths	
N	20		19		13		8		10		9	
	Av.	S.D.	Av.	S.D.	Av.	S.D.	Av.	S.D.	Av.	S.D.	Av.	S.D.
SiO_2	0.15	0.20	0.07	0.05	0.16	0.06	0.08	0.08	0.09	0.06	0.09	0.07
TiO_2	2.58	0.83	1.86	0.61	2.49	0.88	2.89	2.89	2.36	0.58	3.01	1.16
Al_2O_3	12.20	3.09	16.65	3.46	14.94	3.69	14.43	14.43	14.39	3.93	12.99	8.61
Cr_2O_3	33.86	1.32	31.85	1.25	32.74	1.49	31.46	31.46	31.77	1.77	26.01	3.16
V_2O_3	0.46	0.06	0.35	0.07	0.40	0.07	0.44	0.44	0.45	0.14	0.73	0.23
Fe_2O_3	18.63	3.24	17.68	2.90	17.64	1.41	18.62	18.62	19.02	3.87	24.89	4.89
FeO	24.93	2.68	22.53	3.23	22.73	1.73	25.59	25.59	24.36	3.11	24.98	3.77
MgO	7.08	2.17	8.57	1.96	8.78	1.24	7.16	7.16	7.52	2.26	7.29	2.88
MnO	0.35	0.05	0.31	0.06	0.33	0.03	0.35	0.35	0.33	0.04	0.36	0.06
ZnO	0.10	0.06	0.09	0.04	0.05	0.04	0.10	0.10	0.07	0.04	0.08	0.05
NiO	0.22	0.03	0.22	0.04	0.24	0.03	0.23	0.23	0.24	0.05	0.24	0.04
Total	100.55	0.43	100.17	2.23	100.48	0.31	101.35	101.35	100.60	0.35	100.66	0.44
Mg#	33.32	9.24	40.34	9.00	40.71	5.16	32.62	32.62	35.26	9.77	33.83	11.64
Cr#	65.55	5.29	56.63	4.81	59.98	6.12	60.89	60.89	60.43	6.19	59.76	12.77

Table B.4: Average Cr-spinel composition at location 10 of *N* microprobe analyses. Main elements are given in wt.%.

	Unit 8 Peridotite		Main Cr-spinel seam		Unit 7 Troctolite		Anorthosite layer	
N	3		10		10		16	
	Av.	S.D.	Av.	S.D.	Av.	S.D.	Av.	S.D.
SiO_2	0.06	0.02	0.05	0.04	0.17	0.17	0.12	0.05
TiO_2	2.76	0.33	1.32	0.23	2.30	2.30	2.43	0.72
Al_2O_3	9.63	1.33	26.13	1.65	12.07	12.07	9.91	4.25
Cr_2O_3	28.57	0.83	28.01	0.80	26.71	26.71	27.70	3.18
V_2O_3	0.84	0.02	0.25	0.03	0.65	0.65	0.80	0.29
Fe_2O_3	17.75	5.90	13.78	0.65	25.27	25.27	25.69	5.34
FeO	25.48	2.42	18.69	0.49	28.14	28.14	29.29	2.97
MgO	4.20	0.97	11.92	0.39	4.75	4.75	3.64	2.24
MnO	0.37	0.08	0.25	0.01	0.41	0.41	0.44	0.10
ZnO	0.13	0.10	0.05	0.04	0.13	0.13	0.14	0.13
NiO	0.35	0.01	0.23	0.04	0.23	0.23	0.34	0.11
Total	90.14	9.29	100.66	0.18	100.83	100.83	100.50	1.03
Mg#	22.64	4.33	53.20	1.48	22.64	22.64	17.81	10.35
Cr#	66.70	3.00	41.89	2.23	63.01	63.01	66.60	7.74

Table B.5: Average Cr-spinel composition at location 11 of *N* microprobe analyses. Main elements are given in wt.%.

	Unit 8 Peridotite		Subsidiary seam		Unit 7 Troctolite	
N	20		10		12	
	Av.	S.D.	Av.	S.D.	Av.	S.D.
SiO_2	0.08	0.17	0.07	0.06	0.10	0.10
TiO_2	3.65	0.61	3.32	0.35	3.91	3.91
Al_2O_3	11.47	5.11	12.80	0.80	11.25	11.25
Cr_2O_3	30.57	1.80	32.94	0.63	29.35	29.35
V_2O_3	0.60	0.14	0.44	0.03	0.77	0.77
Fe_2O_3	21.00	3.84	18.62	0.60	22.14	22.14
FeO	25.17	3.40	23.08	1.50	24.61	24.61
MgO	7.41	2.52	8.78	1.14	7.94	7.94
MnO	0.34	0.04	0.33	0.02	0.33	0.33
ZnO	0.08	0.05	0.08	0.03	0.08	0.08
NiO	0.25	0.07	0.20	0.02	0.22	0.22
Total	100.61	0.50	100.66	0.30	100.69	100.69
Mg#	34.13	10.48	40.34	4.71	36.34	36.34
Cr#	65.52	9.14	63.35	1.34	63.95	63.95

B.2 Olivine

Table B.6: Average olivine composition at location 7 of *N* microprobe analyses. Main elements are given in wt.%.

	Unit 8 Peridotite		Unit 7 Troctolite		Anorthosite layer	
N	5		13		5	
	Av.	S.D.	Av.	S.D.	Av.	S.D.
SiO_2	39.38	0.17	39.56	0.15	39.53	0.21
TiO_2	0.01	0.02	0.02	0.01	0.01	0.01
Al_2O_3	0.03	0.02	0.06	0.09	0.05	0.04
Cr_2O_3	0.03	0.02	0.02	0.04	0.02	0.03
MgO	47.43	0.27	47.66	0.43	47.44	0.19
MnO	0.18	0.03	0.19	0.02	0.21	0.02
FeO	12.91	0.37	12.49	0.48	12.90	0.31
CaO	0.07	0.02	0.12	0.09	0.08	0.01
NiO	0.25	0.02	0.26	0.03	0.27	0.01
Total	100.29	0.25	100.39	0.31	100.52	0.21
Mg#	86.57	0.65	87.33	0.78	87.17	0.94

Table B.7: Average olivine composition at location 6 of *N* microprobe and *n* LA-ICP-MS analyses. Main elements are given in wt.%, trace elements in ppm, bdl below detection limit.

	Unit 8 Peridotite		Unit 7 Troctolite		Anorthosite layer	
N (n)	15 (2)		9 (2)		2	
	Av.	S.D.	Av.	S.D.	Av.	S.D.
SiO_2	39.13	0.17	39.52	0.33	39.02	
TiO_2	0.01	0.01	0.02	0.01	0.02	
Al_2O_3	0.02	0.01	0.03	0.02	0.04	
Cr_2O_3	0.02	0.01	0.01	0.01	0.00	
MgO	46.97	0.28	46.70	0.21	46.05	
MnO	0.20	0.03	0.21	0.02	0.21	
FeO	12.46	0.25	13.31	0.23	13.25	
CaO	0.10	0.01	0.09	0.02	0.09	
NiO	0.27	0.03	0.28	0.02	0.27	
Total	99.16	0.29	100.16	0.71	98.96	
Mg#	87.05	0.28	86.21	0.17	86.10	
Sc	9		8			
Ti	104		117			
V	5		3			
Cr	128		72			
Mn	1650		1706			
Co	173		177			
Ni	2105		2167			
Zn	77		83			
Rb	bdl		bdl			
Sr	bdl		bdl			
Y	0.37		0.23			
Zr	0.49		0.68			
Nb	bdl		bdl			
Ba	bdl		bdl			
La	bdl		bdl			
Ce	bdl		bdl			
Pr	bdl		bdl			
Nd	bdl		bdl			
Sm	bdl		bdl			
Eu	bdl		bdl			
Gd	bdl		bdl			
Tb	bdl		bdl			
Dy	bdl		0.0371			
Ho	0.0184		0.0091			
Er	0.0764		0.0544			
Tm	0.0136		0.0142			
Yb	0.1497		0.1506			
Lu	0.0259		0.0325			
Hf	0.0185		0.0263			
Pb	bdl		bdl			
U	bdl		bdl			

Table B.8: Average olivine composition at location 13 of *N* microprobe and *n* LA-ICP-MS analyses. Main elements are given in wt.%, trace elements in ppm, bdl below detection limit.

	Unit 8 Peridotite		Unit 7 Troctolite		Anorthosite layer	
N (n)	23 (2)		10 (1)		19	
	Av.	S.D.	Av.	S.D.	Av.	S.D.
SiO_2	39.15	0.14	39.37	0.16	39.40	0.20
TiO_2	0.02	0.02	0.02	0.02	0.02	0.02
Al_2O_3	0.03	0.05	0.01	0.01	0.05	0.04
Cr_2O_3	0.01	0.01	0.01	0.01	0.03	0.05
MgO	45.32	0.20	46.07	0.20	46.12	0.75
MnO	0.23	0.03	0.24	0.02	0.20	0.03
FeO	14.89	0.32	14.72	0.43	13.69	0.98
CaO	0.10	0.07	0.08	0.02	0.07	0.01
NiO	0.25	0.03	0.25	0.02	0.25	0.02
Total	99.99	0.30	100.77	0.38	99.83	0.25
Mg#	84.43	0.32	84.80	0.42	85.72	1.06
Sc	6		8			
Ti	96		148			
V	4		3			
Cr	95		47			
Mn	1844		1803			
Co	182		176			
Ni	2002		1988			
Zn	100		72			
Rb	bdl		bdl			
Sr	bdl		bdl			
Y	0.09		0.20			
Zr	0.10		0.52			
Nb	bdl		bdl			
Ba	bdl		bdl			
La	bdl		bdl			
Ce	bdl		bdl			
Pr	bdl		bdl			
Nd	bdl		bdl			
Sm	bdl		bdl			
Eu	bdl		bdl			
Gd	bdl		bdl			
Tb	bdl		bdl			
Dy	bdl		0.0178			
Ho	0.0045		bdl			
Er	0.0225		0.0524			
Tm	bdl		0.0174			
Yb	0.0569		0.1429			
Lu	0.0145		0.0224			
Hf	bdl		0.0203			
Pb	bdl		bdl			
U	bdl		bdl			

Table B.9: Average olivine composition at location 10 of *N* microprobe analyses. Main elements are given in wt.%.

	Unit 8 Peridotite		Unit 7 Troctolite		Anorthosite layer	
N	4		8		9	
	Av.	S.D.	Av.	S.D.	Av.	S.D.
SiO_2	38.89	0.18	39.37	0.15	38.92	0.16
TiO_2	0.02	0.01	0.02	0.01	0.02	0.01
Al_2O_3	0.02	0.02	0.01	0.01	0.04	0.02
Cr_2O_3	0.01	0.01	0.01	0.01	0.02	0.03
MgO	45.07	0.42	45.14	0.14	44.92	0.36
MnO	0.22	0.02	0.24	0.04	0.25	0.03
FeO	14.86	0.44	16.19	0.14	15.01	0.45
CaO	0.07	0.01	0.08	0.01	0.06	0.01
NiO	0.29	0.11	0.22	0.02	0.24	0.03
Total	99.45	0.19	101.29	0.26	99.48	0.28
Mg#	84.39	0.51	83.25	0.14	84.21	0.50

Table B.10: Average olivine composition at location 11 of *N* microprobe and *n* LA-ICP-MS analyses. Main elements are given in wt.%, trace elements in ppm, bdl below detection limit.

	Unit 8 Peridotite		Unit 7 Troctolite	
N (n)	19 (2)		14 (2)	
	Av.	S.D.	Av.	S.D.
SiO_2	38.75	0.20	38.79	0.15
TiO_2	0.03	0.02	0.02	0.01
Al_2O_3	0.01	0.01	0.02	0.09
Cr_2O_3	0.01	0.01	0.01	0.04
MgO	45.75	0.35	45.41	0.43
MnO	0.21	0.02	0.22	0.02
FeO	14.47	0.14	14.88	0.48
CaO	0.09	0.01	0.09	0.09
NiO	0.24	0.02	0.24	0.03
Total	99.56	0.43	99.68	0.31
Mg#	84.93	0.13	84.47	0.78
Sc	6		6	
Ti	140		170	
V	5		8	
Cr	64		78	
Mn	1760		1816	
Co	180		188	
Ni	1872		1916	
Zn	92		107	
Rb	bdl		bdl	
Sr	bdl		bdl	
Y	0.43		0.27	
Zr	0.84		0.89	
Nb	bdl		bdl	
Ba	bdl		bdl	
La	bdl		bdl	
Ce	bdl		bdl	
Pr	bdl		bdl	
Nd	bdl		bdl	
Sm	bdl		bdl	
Eu	bdl		bdl	
Gd	bdl		bdl	
Tb	bdl		bdl	
Dy	0.0433		bdl	
Ho	0.0144		0.0111	
Er	0.0962		0.0545	
Tm	0.0256		0.0178	
Yb	0.2014		0.1636	
Lu	0.0393		0.0355	
Hf	0.0347		0.0398	
Pb	bdl		bdl	
U	bdl		bdl	

B.3 Plagioclase

Table B.11: Average plagioclase composition at location 7 of *N* microprobe analyses. Main elements are given in wt.%.

	Unit 8 Peridotite		Main Cr-spinel seam		Anorthosite layer		Anorthosite autoliths	
N	3		8		16		25	
	Av.	S.D.	Av.	S.D.	Av.	S.D.	Av.	S.D.
SiO_2	47.31	0.30	45.65	0.27	45.99	0.71	46.17	0.40
TiO_2	0.01	0.01	0.02	0.02	0.03	0.02	0.03	0.01
Al_2O_3	33.98	0.03	35.10	0.21	34.89	0.55	34.83	0.25
Cr_2O_3	0.06	0.08	0.11	0.04	0.01	0.01	0.01	0.01
MgO	0.04	0.00	0.03	0.01	0.04	0.02	0.03	0.01
MnO	0.01	0.01	0.00	0.00	0.00	0.01	0.01	0.01
FeO	0.44	0.04	0.39	0.05	0.34	0.02	0.50	0.02
CaO	16.69	0.13	17.99	0.13	17.83	0.57	17.73	0.28
Na_2O	2.00	0.15	1.33	0.09	1.38	0.32	1.37	0.16
K_2O	0.04	0.01	0.02	0.01	0.03	0.01	0.05	0.01
SrO	0.17	0.01	0.17	0.02	0.18	0.02	0.18	0.02
Total	100.76	0.27	100.83	0.30	100.70	0.34	100.90	0.21
An	82.01	1.13	88.11	0.78	87.60	2.87	87.46	1.41

Table B.12: Average plagioclase composition at location 6 of *N* microprobe and *n* LA-ICP-MS analyses. Main elements are given in wt.%, trace elements in ppm, bdl below detection limit.

	Unit 8 Peridotite		Main Cr-spinel seam		Unit 7 Troctolite		Anorthosite layer		Anorthosite autoliths	
N (n)	10 (3)		10 (2)		32 (2)		9 (2)		9 (2)	
	Av.	S.D.	Av.	S.D.	Av.	S.D.	Av.	S.D.	Av.	S.D.
SiO_2	46.93	0.58	45.81	0.42	46.20	0.56	45.99	0.34	46.40	1.09
TiO_2	0.03	0.01	0.02	0.01	0.03	0.01	0.03	0.02	0.04	0.02
Al_2O_3	34.20	0.51	35.23	0.29	34.82	0.38	35.10	0.23	34.37	0.79
Cr_2O_3	0.01	0.03	0.11	0.05	0.00	0.01	0.01	0.01	0.01	0.01
MgO	0.06	0.02	0.04	0.01	0.05	0.03	0.04	0.03	0.04	0.02
MnO	0.01	0.02	0.01	0.01	0.00	0.01	0.00	0.00	0.01	0.01
FeO	0.44	0.06	0.44	0.04	0.40	0.02	0.38	0.02	0.45	0.05
CaO	16.95	0.50	17.95	0.22	17.61	0.35	17.92	0.24	17.34	0.90
Na_2O	1.84	0.29	1.28	0.14	1.46	0.22	1.32	0.15	1.60	0.47
K_2O	0.03	0.01	0.02	0.01	0.03	0.00	0.01	0.01	0.05	0.02
SrO	0.18	0.02	0.17	0.02	0.18	0.02	0.18	0.01	0.17	0.01
Total	100.67	0.48	101.08	0.09	100.79	0.25	100.98	0.17	100.48	0.16
An	83.41	2.57	88.43	1.25	86.78	1.88	88.14	1.32	85.45	4.33
Sc	0.48		0.44		0.57		0.55		0.62	
Ti	150.80		86.33		221.79		121.45		152.80	
V	1.64		0.58		1.69		2.60		2.82	
Cr	bdl		bdl		bdl		bdl		bdl	
Mn	9.39		8.96		10.31		15.88		25.74	
Co	bdl		bdl		bdl		bdl		bdl	
Ni	bdl		bdl		bdl		2.08		bdl	
Zn	bdl		bdl		bdl		bdl		bdl	
Rb	bdl		bdl		bdl		bdl		0.86	
Sr	313.87		292.38		309.18		309.14		325.95	
Y	0.41		0.68		0.56		0.30		0.29	
Zr	0.14		0.18		0.32		0.22		0.20	
Nb	bdl		bdl		bdl		bdl		bdl	
Ba	10.1576		8.8122		10.5309		4.7478		7.5431	
La	0.3046		0.6570		0.4904		0.1656		0.2334	
Ce	0.9996		2.0127		1.5795		0.4733		0.5963	
Pr	0.1447		0.2989		0.2376		0.0718		0.0926	
Nd	0.7065		1.3382		0.9108		0.3523		0.4681	
Sm	0.2188		0.3527		0.2706		0.0874		0.0981	
Eu	0.2947		0.2676		0.2566		0.2511		0.3233	
Gd	bdl		0.2823		0.2791		bdl		bdl	
Tb	bdl		0.0438		0.0314		bdl		0.0201	
Dy	0.1115		0.1774		0.1360		0.0803		0.0872	
Ho	0.0292		0.0342		0.0270		0.0155		0.0206	
Er	0.0341		0.0906		0.0658		bdl		0.0598	
Tm	bdl		0.0111		0.0132		bdl		bdl	
Yb	0.0365		0.0535		0.0420		bdl		bdl	
Lu	bdl		0.0051		bdl		bdl		bdl	
Hf	bdl		bdl		0.0136		bdl		bdl	
Pb	bdl		bdl		bdl		bdl		bdl	
U	bdl		bdl		bdl		bdl		bdl	

Table B.13: Average plagioclase composition at location 13 of *N* microprobe and *n* LA-ICP-MS analyses. Main elements are given in wt.%, trace elements in ppm, bdl below detection limit.

	Unit 8 Peridotite		Main Cr-spinel seam		Subsidiary seam		Unit 7 Troctolite		Anorthosite layer		Anorthosite autoliths	
N (n)	18 (2)		16 (2)		5		43		17 (4)		10 (3)	
	Av.	S.D.	Av.	S.D.	Av.	S.D.	Av.	S.D.	Av.	S.D.	Av.	S.D.
SiO_2	48.01	0.80	46.68	0.55	46.59	0.52	46.30	0.66	46.71	0.71	46.45	0.84
TiO_2	0.04	0.02	0.03	0.02	0.04	0.01	0.03	0.02	0.04	0.02	0.04	0.02
Al_2O_3	33.37	0.47	34.62	0.43	34.76	0.49	34.85	0.50	34.55	0.56	34.62	0.49
Cr_2O_3	0.02	0.03	0.12	0.07	0.15	0.08	0.01	0.05	0.01	0.01	0.01	0.01
MgO	0.07	0.05	0.12	0.26	0.06	0.02	0.05	0.03	0.05	0.02	0.05	0.02
MnO	0.01	0.01	0.01	0.01	0.00	0.01	0.01	0.01	0.00	0.01	0.01	0.02
FeO	0.48	0.15	0.53	0.08	0.49	0.08	0.45	0.08	0.37	0.03	0.45	0.03
CaO	16.00	0.49	17.29	0.50	17.33	0.41	17.63	0.49	17.29	0.58	17.39	0.57
Na_2O	2.33	0.32	1.66	0.23	1.62	0.22	1.48	0.26	1.67	0.33	1.58	0.34
K_2O	0.09	0.02	0.04	0.01	0.04	0.01	0.03	0.01	0.04	0.02	0.03	0.02
SrO	0.19	0.02	0.18	0.02	0.17	0.02	0.18	0.02	0.18	0.01	0.18	0.01
Total	100.61	0.31	101.28	0.32	101.25	0.27	101.03	0.40	100.91	0.22	100.81	0.29
An	78.74	2.73	85.03	2.12	85.35	2.03	86.67	2.37	84.94	2.96	85.75	3.05
Sc	0.64		0.59						0.59		0.62	
Ti	284.42		178.96						127.66		184.40	
V	3.07		1.51						2.53		3.38	
Cr	bdl		bdl						bdl		bdl	
Mn	14.06		11.36						16.32		17.74	
Co	bdl		bdl						bdl		bdl	
Ni	bdl		bdl						bdl		bdl	
Zn	bdl		bdl						bdl		bdl	
Rb	0.45		0.31						0.27		0.35	
Sr	386.78		347.11						324.25		298.77	
Y	0.20		0.35						0.30		0.36	
Zr	0.06		0.06						0.10		0.21	
Nb	bdl		bdl						bdl		bdl	
Ba	28.9423		23.8543						6.2595		7.9926	
La	0.6463		0.8882						0.2124		0.2647	
Ce	1.4790		2.1269						0.6270		0.7564	
Pr	0.2007		0.2857						0.0975		0.1199	
Nd	0.7719		1.2556						0.5049		0.5353	
Sm	0.1555		0.2428						0.1376		0.1551	
Eu	0.3678		0.3762						0.2927		0.2819	
Gd	0.1788		bdl						0.1462		0.1754	
Tb	0.0235		0.0251						0.0181		0.0229	
Dy	0.0860		0.0947						0.0896		0.0847	
Ho	0.0129		0.0167						0.0128		0.0155	
Er	0.0272		bdl						0.0367		0.0400	
Tm	bdl		bdl						0.0088		bdl	
Yb	bdl		0.0236						bdl		0.0385	
Lu	bdl		bdl						0.0044		0.0095	
Hf	bdl		bdl						0.0113		bdl	
Pb	bdl		bdl						bdl		bdl	
U	bdl		bdl						bdl		0.0035	

Table B.14: Average plagioclase composition at location 10 of *N* microprobe analyses. Main elements are given in wt.%.

	Main Cr-spinel seam		Unit 7 Troctolite		Anorthosite layer	
N	10		10		20	
	Av.	S.D.	Av.	S.D.	Av.	S.D.
SiO_2	46.25	0.52	46.62	0.75	46.92	1.08
TiO_2	0.02	0.01	0.03	0.02	0.04	0.03
Al_2O_3	34.83	0.37	34.69	0.61	34.30	0.81
Cr_2O_3	0.14	0.04	0.00	0.00	0.00	0.01
MgO	0.06	0.01	0.07	0.07	0.04	0.01
MnO	0.01	0.01	0.01	0.01	0.00	0.01
FeO	0.46	0.05	0.47	0.04	0.44	0.03
CaO	17.48	0.33	17.44	0.69	17.02	0.83
Na_2O	1.48	0.18	1.67	0.34	1.85	0.51
K_2O	0.06	0.02	0.05	0.02	0.06	0.03
SrO	0.18	0.02	0.19	0.02	0.19	0.02
Total	100.96	0.51	101.24	0.40	100.85	0.24
An	86.40	1.65	84.95	3.15	83.30	4.53

Table B.15: Average plagioclase composition at location 11 of *N* microprobe and *n* LA-ICP-MS analyses. Main elements are given in wt.%, trace elements in ppm, bdl below detection limit.

	Unit 8 Peridotite		Unit 7 Troctolite		Anorthosite autoliths	
N (n)	20 (8)		21 (6)		27 (3)	
	Av.	S.D.	Av.	S.D.	Av.	S.D.
SiO_2	47.99	1.14	46.94	1.00	47.02	1.35
TiO_2	0.05	0.03	0.05	0.02	0.05	0.03
Al_2O_3	33.53	0.83	34.31	0.81	34.13	0.98
Cr_2O_3	0.01	0.01	0.01	0.01	0.01	0.01
MgO	0.05	0.01	0.05	0.01	0.04	0.20
MnO	0.01	0.01	0.01	0.01	0.01	0.01
FeO	0.42	0.04	0.44	0.06	0.45	0.08
CaO	16.19	0.91	17.06	0.84	16.90	1.02
Na_2O	2.23	0.52	1.77	0.47	1.87	0.60
K_2O	0.08	0.03	0.04	0.01	0.04	0.02
SrO	0.19	0.02	0.19	0.02	0.18	0.02
Total	100.76	0.25	100.86	0.22	100.72	0.21
An	79.65	4.69	83.99	4.19	83.12	5.36
Sc	0.60		0.61		0.49	
Ti	330.88		157.99		176.43	
V	3.49		3.23		3.41	
Cr	bdl		bdl		bdl	
Mn	12.17		17.78		20.56	
Co	bdl		bdl		bdl	
Ni	2.85		bdl		bdl	
Zn	bdl		bdl		bdl	
Rb	0.80		0.23		0.23	
Sr	353.34		337.47		343.91	
Y	0.48		0.30		0.33	
Zr	0.20		0.15		0.08	
Nb	bdl		bdl		bdl	
Ba	29.4571		10.5314		15.3546	
La	0.6490		0.2739		0.3796	
Ce	1.6874		0.7848		1.0335	
Pr	0.2297		0.1220		0.1526	
Nd	1.0330		0.5471		0.6911	
Sm	0.2576		0.1482		0.1612	
Eu	0.5673		0.3575		0.3688	
Gd	0.2312		bdl		0.1442	
Tb	0.0315		0.0176		0.0171	
Dy	0.1262		0.0921		0.0796	
Ho	0.0232		0.0127		0.0170	
Er	0.0621		0.0367		0.0317	
Tm	0.0098		0.0044		0.0078	
Yb	0.0354		0.0251		0.0343	
Lu	bdl		0.0035		0.0059	
Hf	0.0190		0.0234		0.0100	
Pb	0.8071		bdl		bdl	
U	bdl		bdl		bdl	

Eigenständigkeitserklärung

Hiermit erkläre ich, dass ich die vorliegende Dissertation selbstständig verfasst habe und keine anderen als die angegebenen Hilfsmittel benutzt habe. Alle benutzten Hilfsmittel wurden durch entsprechende Angaben der Quellen kenntlich gemacht.

Diese Arbeit hat in gleicher oder ähnlicher Form noch keiner anderen Prüfungsbehörde vorgelegen.

Felix Kaufmann
Berlin, Mai 2018